UNIVERSITY OF COPENHAGEN

Towards Minimal Quantum Noise
Conditional broadband quantum noise reduction with negative mass spin oscillators

PhD thesis

Jun Jia

Center for Quantum Optics (QUANTOP)
Niels Bohr Institute
University of Copenhagen

Academic supervisors Prof. Eugene S. Polzik

Evaluation committee

External referee 1 : Prof. Klemens Hammerer

External referee 2 : Prof. Thomas Fernholz

Local referee : Prof. Leonardo Midolo

This thesis has been submitted to the PhD School of the Faculty of Science
University of Copenhagen

Abstract

Quantum sensing represents a significant research direction with Quantum Technologies, particularly promising in the acoustic frequency regime. This potential offers a wide range of scientific applications, including the detection of magnetic fields generated by the brain's activity, heartbeat, and the measurement of weak forces such as gravitational wave signals emitted by extreme astronomical events.

A principle challenge in enhancing the sensitivity of current gravitational wave detectors is managing two competing types of quantum noise; shot noise: which arises from the uncertainty associated with the arrival of photons, and quantum backaction noise: which results from the transfer of photon momentum to the test mass object as radiation pressure during the interaction. These noises, arise from the quantum nature of light, scale differently with the light power, and dominate at different frequencies. Their broadband reduction requires the injection of a squeezed vacuum source, with frequency-dependent rotation of the squeezed quadrature presently accomplished via a complex filter cavity.

This thesis explores an alternative approach for achieving broadband quantum noise reduction using polarized cesium atoms prepared in a higher energy ground state, oriented in an effective negative mass reference frame. Conditional reduction of broadband quantum noise is possible once the EPR entangled states are detected, with one arm positioned in a negative mass reference frame.

In this thesis, we report on the construction and characterization of an interaction-enhanced atomic system, consisting of polarized cesium atoms confined with a 2mm*2mm*80mm channel. These atoms are manipulated by a homogeneous, home-built magnetic coil system with an intrinsic decay of 30Hz, and are uniformly probed by a spatially shaped top hat beam. This setup has demonstrated quantum noise-limited performance and a quantum nondemolition (QND) based backaction dominance with a quantum cooperativity of approximately 3, across a wide range of Larmor frequencies. This is evidenced by the observed ponderomotive squeezing from - 4.9 dB at 1 MHz down to the upper acoustic frequency at 18 kHz. Additionally, experimental investigations into the virtual frequency shift of the atomic spin oscillator, facilitated by ponderomotive squeezing, have been conducted.

At lower acoustic frequencies, the dominance of quantum backaction noise is compromised by various classical noise sources and additional atomic spin noise at nearly DC levels. Experimentally investigating and mitigating these noise sources have enabled us to maintain the -3 dB squeezing down to 3 kHz, extending to -1.2 dB slightly below 1 kHz, thus bringing our proof-of-principle experiments

closer to the gravitational wave bandwidth

The thesis concludes with the discussion of our parallel achievement of $\sim$ - 7 dB nondegenerate entangled sources, which bridges the gap between the atomic system and gravitational wave detection, alongside the theoretical predictions for the broadband quantum noise reduction optimized using the well-calibrated experimental parameters. Additionally, I will also present our 'last-minute' preliminary experimental achievement of broadband quantum noise reduction at 50 kHz with the joint measurement of the hybrid systems. This results sets stage for our ongoing proof-of-principle frequency-dependent entangled source, aimed at broadband quantum noise reduction in the acoustic frequency regime. Furthermore, the established hybrid system signifies a step towards quantum-enhanced magnetic sensing and the potential for quantum entanglement and teleportation with this hybrid entangled light-atomic system.

Abstrakt

Kvantesansning repræsenterer en betydelig forskningsretning inden for kvanteteknologier, især lovende i det akustiske frekvensområde. Dette potentiale tilbyder en bred vifte af videnskabelige anvendelser, herunder detektion af magnetfelter genereret af hjernens aktivitet, hjerteslag og måling af svage kræfter som tyngdebølgesignaler udsendt af ekstreme astronomiske begivenheder.

En vigtig udfordring i forbedringen af følsomheden af nuværende tyngdebølgedetektorer er håndteringen af to konkurrerende typer kvantestøj; skudstøj: som opstår fra usikkerheden forbundet med ankomsten af fotoner, og kvantetilbageslagsstøj: som skyldes overførslen af fotonmomentum til probesensoren som strålingstryk under interaktionen. Denne støj, der opstår fra lysets kvantenatur, skalerer forskelligt med lysets styrke og dominerer ved forskellige frekvenser. Deres bredbåndsreduktion kræver injektion af en klemt vakuumkilde med frekvensafhængig rotation af den klemte kvadratur, som i øjeblikket opnås via et 300m langt filterhulrum.

Her vil jeg introducere et alternativt teoretisk forslag af E.S. Polzik og F. Ya. Khalili, i princippet kan vi samtidig opnå reduktion af kvantetilbageslagsstøj og skudstøj ved hjælp af polariserede cæsiumatomer, der er forberedt i en effektiv negativ masse referenceramme og opererer i et akustisk frekvensområde. Den betingede måling af atomar spin oscillator, ved hjælp af krydskorrelationen iboende i EPR-sammenfiltring, giver mulighed for at realisere forbedret bredbåndsfølsomhed for tyngdebølgedetektorer.

Preface
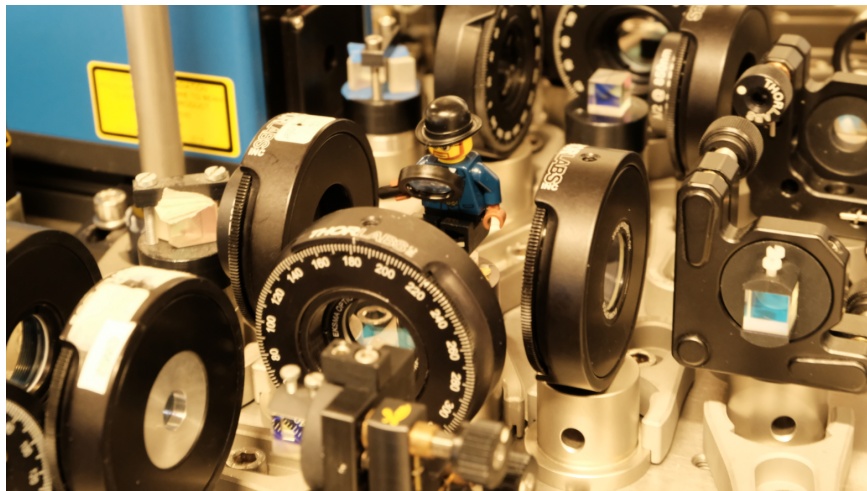
As I now reach the end of my PhD, I can confidently say that joining QUANTOP was the best decision I made. I have been incredibly fortunate to be part of this group, working on challenging yet extremely exciting projects, and meeting many friendly and intelligent people. Over the past four and a half years, I have received immeasurable support, and I could not have reached this stage alone. I am really grateful to a lot of people.

First and foremost, I would like to express my gratitude to Eugene Polzik for introducing me to the QUANTOP group and for creating such a warm and open environment. Your constant support and guidance have been invaluable whenever I needed help. Thank you for trusting us and being patient, allowing our team to develop and flourish into the wonderful team it is today.

The achievements we have made and will reach soon are incredible. The work I have presented in this thesis would not be the same without my wonderful colleagues. Túlio Brito Brasil, I am always amazed by the 'free jazz' you create while noise hunting and designing electronics. You are like a magician, with just a snap of your fingers, the noise is gone. Thank you for always inviting us to have fun together over the years. Valeriy Novikov, thank you for being such a great friend. I always enjoy discussing physics and anything else with you, and I am deeply grateful for your efforts in helping me with my thesis. Ryan Yde, thank you for being a wonderful colleague. I miss the happy times we worked together and am very happy you found an exciting new job. Maïmouna Bocoum, you are a true angel! I am so glad to have worked with you during my PhD, and I always enjoy our brain eruption sessions. We should automate everything in our setup! Andrea Grimaldi, our GWD master, thank you for showing me so many amazing calibration and characterization skills.

Besides my wonder GWD team, I also want to thank jörg Müller for being such a fantastic mentor, and It has been a privilege to develop my understanding of

physics with your guidance. Emil Zeuthen, our best theoretical master, thank you for always being willing to provide suggestions and advice. I cannot express enough gratitude for the many hours of discussion and the precious notes you have shared. I also want to thank Mikhail Balabas, our cell fabrication artist. Thank you for arriving at the perfect time to help us produce the most valuable cells for our project. I also want to thank Farid Khalili for helping me truly understand quantum noise in GWDs. I am very grateful for the invaluable help I received when I first arrived. Rodrigo Thomas, thank you for introducing me to the cell lab and guiding me through the first MORS measurement and many after. Your knowledge and experience have been crucial in pushing our system to its current state. Michal Parniak, you are one of the most knowledgeable people I have ever met, and I always learn new skills from you. Rebecca Schmieg, thank you for being such a great colleague; I learned so much from you when organizing my experimental work. There are many more QUANTOP members I would like to thank: Jean-Baptiste Sylvain Béguin, Chao Meng, Wengqiang Zhen, Heng Yan Wang, Ivan Galinskiy, Peyman Malekzadeh, Alkiviadis Zoumis, Jacob Thornfeldt Hansen, Sergey Fedorov, Michael Zugenmaier, Nikolaj Aagaard, Zi Hua Wang, Luiz Couto, and Christian F. Bærentsen. Thank you to all the amazing QUANTOP members.

Last but not least, I can never thank my parents enough. It is not easy to pursue a PhD abroad for many years. Thank you for being so supportive and for your unconditional love and care.

List of abbreviations

- Quantum nondemolition (QND)

- Gravitational-Wave Observatory (LIGO)

- Quantum backaction noise (QBAN)

- Shot noise (SN)

- Amplitude modulation (AM)

- Phase modulation (PM)

- Gravitational wave (GW)

- Parametric down conversion (PDC)

- Root-mean-square (RMS)

- Standard Quantum Limit (SQL)

- Power Spectral Density (PSD)

- Fabry-Perot (FP)

- Full width half maximum (HWHM)

- Einstein-Podolsky-Rosen (EPR)

- Polarized beam splitter (PBS)

- Spin noise spectroscopy (SNS)

- Thermal noise (TN)

- Top hat (TH)

- Acoustic-optic modulator (AOM)

- Polarization-maintaining (PM)

- Magneto Optical Resonance Signal (MORS)

- Coherently Induced Faraday rotation (CIFAR)

- Local oscillators (LOs)

- Optical parametric oscillator (OPO)

List of Publications

Jia, J., Novikov, V., Brasil, T. B., Zeuthen, E., Müller, J. H., Polzik, E. S. (2023). Acoustic frequency atomic spin oscillator in the quantum regime. Nature Communications, 14(1), 6396.
doi: https://doi.org/10.1038/s41467-023-42059-y.

Articles in preparation:
Frequency dependent rotation in EPR-entanglement via atomic spin oscillators.

Conference presentations

Continuously monitored quantum systems (CMONS 2023), 11-13 December 2023, Warsaw, Poland.

Press release:
Sensing the signature of life, Niels Bohr Institute.

Contents

Part I

Theoretical background

Introduction

1.1   Weak force measurement with interferometer
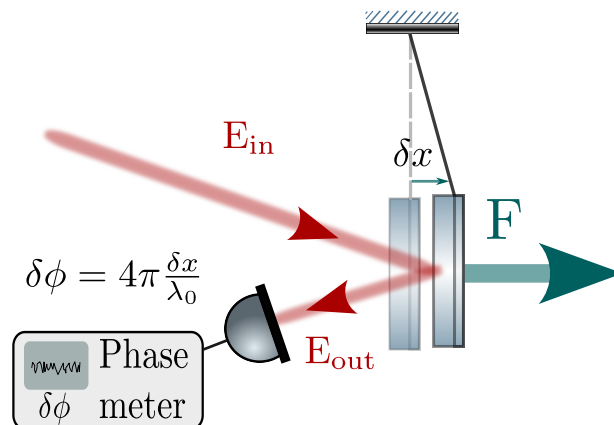
Figure 1.1: Scheme for measuring a weak force. An external force F pulls the mirror away from its equilibrium position, causing a displacement δx. This displacement then modulates the probe light and thus the signal force F can be measured by monitoring the phase shift of the probe light reflected from the mirror.

The measurement of weak forces remains a cornerstone in contemporary experimental physics. The core of these measurement systems lies a test mass device, which is coupled to a weak classical force and read out by a coherent optical field, as shown Fig.1.1. Assuming we would like to measure a weak classical force, denoted as F, the procedure begins by allowing it to act on a test object, and then followed by reading out the displacement of this object caused by the force. It is critical to minimize all forms of other extraneous information or noise during the measurement process, which may stem from both the test mass and the light. Additionally, isolating the system from other classical forces, such as thermal fluctuations, is essential to ensure that only the intended signal force F instead if thermal forces are detected. State-of-art laser interferometric gravitational-wave observatories exemplify the significant advancements in weak force measurement

technology, enabling us to measure tiny signals that is impossible to measure before. Specifically, the current generation of the gravitational wave observatories has reached its sensitivity threshold where the quantum noise in their systems becomes significant or even dominant across the targeted detection frequency bandwidth. The origin of this quantum noise is due to particles, such as photons in the probe light, randomly jumping in and out of empty space (referred to as vacuum fluctuations), creating background noise that adds uncertainty to the readout precision of laser-based measurements of the positions of nearly free test masses [1]. Consequently, reducing the quantum noise in gravitational wave observatories would enhance their astrophysics detection capabilities, improving sensitivity to extend their observational range from binary neutron stars to much heavier binary black holes [2].

The reduction of fundamental quantum noise in gravitational wave observatories can be achieved through the injection of the 'squeezed' light. This process can be visualized by imaging the uncertainty of noise as a balloon, which can be reduced by squeezing one side. The concept of squeezing was originated in the late 1970s with theoretical studies by Carlton Caves [3], Vladimir Braginsky, F. Ya. Khalili [4], and Kip Thorne [5, 6] and one of the first experimental demonstration in 1986 by H.Jeff Kimble [7]. Two decades later, researchers at the Laser Interferometer Gravitational-Wave Observatory (LIGO) discovered that the system, after many improvements, began to be limited by quantum noise. This led to the consideration of its implementation in the LIGO detector. In 2008, the first experimental demonstration was achieved at a 40-meter test system [8]. By 2010, researchers developed a LIGO squeezer and tested it at the real LIGO's Hanford interferometer[9], with parallel work conducted at the GEO600 detector in Germany [10]. In 2019, after extensive proof-of-principle testing, squeezing of one side of light's quantum noise was routinely applied in the advanced LIGO and VIRGO during their third observing run (O3) [11]. Squeezed states improved the sensitivity of signals above 50 Hz by up to 3dB, corresponding to around 40 % increase in the expected detection rate [12].

However, injecting a simple vacuum squeezed state can not improve the sensitivity across the full frequency range due to the quantum mechanics uncertainty principle. There is a trade-off when applying squeezing; as one side of 'balloon' is squeezed, the other side inevitably expands, leading to increased noise in the laser amplitude and causing more random rumbling of the mirror, known as the radiation pressure noise, which can evolve into additional quantum noise. Moreover, this noise level is frequency-dependent due to the frequency response of the test mass mirrors [13]. Optimal quantum noise reduction requires engineering the squeezed state of the vacuum according to the frequency range of gravitational waves and the frequency response of the LIGO interferometer. At the end of 2023, during the fourth observing run (O4), frequency-dependent squeezing was

4

first applied to gravitational wave detectors. This allowed for the simultaneous reduction of both the shot noise and quantum radiation pressure noise down to 30 Hz, further increasing the astrophysical detection rate by up to 65% at very low frequencies [14]. This remarkable frequency-dependent squeezing was achieved by reflecting the vacuum squeezed state from an additional 300-meter-long filter cavity with a finesse of 6700 and a full linewidth of 74 Hz.

The aim of this thesis is to introduce an alternative approaches that, instead of using a very long filtering cavity [15] to match the required cavity linewidth and compensate for the frequency-dependent rotation of the squeezing ellipse imposed by the ponderomotive squeezing of the interferometer, utilizes a collective spin oscillator prepared in a negative mass reference frame. This joint measurement of both systems with EPR entanglement and atomic ensemble can potentially perform a similar function and eliminate both the quantum backaction noise (QBAN) and shot noise (SN) in the gravitational wave detectors.

1.2 Classical nature of light

To understand the influence of quantum noise on gravitational wave detection systems, it would be better to familiarize ourselves with the mathematical description of the probe light, its propagation, its interaction with sensing objects such as movable mirrors, and the recording of its information.

1.2.1 Light propagation

Let's consider a plane monochromatic linearly polarised light propagating in the positive direction of the x-axis. This forward propagation field can be described as a sinusoidal function of a variable $\beta = t - \frac{x}{c}$. and can be written in three equivalent forms, as discussed since page 16 of [16]:

$$E(\beta) = \mathcal{E}_0 \cos\left[\omega_0 \beta - \phi_0\right] \equiv \mathcal{E}_c \cos \omega_0 \beta + \mathcal{E}_s \sin \omega_0 \beta \equiv \frac{\mathcal{E} e^{-i\omega_0 \beta} + \mathcal{E}^* e^{i\omega_0 \beta}}{\sqrt{2}}. \quad (1.1)$$

All three interpretations can be related by the following transformations:

$$
\begin{aligned}
\mathcal{E}_0 &= \sqrt{\mathcal{E}_c^2 + \mathcal{E}_s^2} = \sqrt{2}|\mathcal{E}| & \tan \phi_0 &= \mathcal{E}_s/\mathcal{E}_c = \arg \mathcal{E}, \quad \phi_0 \in [0, 2\pi] \\
\mathcal{E}_c &= \frac{\mathcal{E}+\mathcal{E}^*}{\sqrt{2}} = \sqrt{2}\,\mathrm{Re}[\mathcal{E}] = \mathcal{E}_0 \cos \phi_0 & \mathcal{E}_s &= \frac{\mathcal{E}-\mathcal{E}^*}{i\sqrt{2}} = \sqrt{2}\,\mathrm{Im}[\mathcal{E}] = \mathcal{E}_0 \sin \phi_0, \\
\mathcal{E} &= \frac{\mathcal{E}_c+\mathcal{E}_s}{\sqrt{2}} = \frac{\mathcal{E}_0}{\sqrt{2}} e^{i\phi_0} & \mathcal{E}^* &= \frac{\mathcal{E}_c-i\mathcal{E}_s}{\sqrt{2}} = \frac{\mathcal{E}_0}{\sqrt{2}} e^{-i\phi_0}.
\end{aligned}
$$

$$(1.2)$$

The first method, amplitude-phase, is our traditional description. The latter two interpretations of the electromagnetic field, known as the cosine and sine quadrature amplitudes, and complex amplitudes, are more often applied to analyze wave propagation. Particularly, the quadrature amplitudes interpretation is frequently

used in quantum noise calculations within the GW community, especially after [17] chosen it as the foundation for developing the two-photon formalism for describing the quantum fluctuations of light. I will demonstrate its convenience in the following section.

1.2.2 Amplitude and Phase modulation of light

In the previous section, we have seen that in the process of weak force measurement, a signal manifests itself by modulating the reflected light. Therefore, it is important to understand how the modulation of phase and amplitude happens during the probe propagation. Let's assume a monochromatic carrier field propagates with frequency ω_0, amplitude $\mathcal{E}_0$ and initial phase $\phi_0 = 0$:

$$E_{carrier}(t) = \mathcal{E}_0 \cos(\omega_0 t) = Re[\mathcal{E}_0 e^{-i w_0 t}]. \tag{1.3}$$

1.2.3 Amplitude modulation

The modulation of the carrier field amplitude with frequency Ω in the slow oscillation regime (i.e., $\Omega \ll \omega_0$) can be described as:

$$E_{AM}(t) = \mathcal{E}_0 (1 + \epsilon_m \cos(\Omega t + \phi_m)) \cos(\omega_0 t). \tag{1.4}$$

Where $\epsilon_m \ll 1$ is the modulation depth and ϕ_m represents the phase relationship between the carrier and the modulation. More interestingly, in the cosine-sine quadrature picture, the transformed expression is as follows (this is also the reason why this cosine quadrature is often referred to as amplitude quadrature):

$$\mathcal{E}_{c,AM}(t) = \mathcal{E}_0 (1 + \epsilon_m \cos(\Omega t + \phi_m)) \quad and \quad \mathcal{E}_{s,PM}(t) = 0. \tag{1.5}$$

We could also calculate the modulated light spectrum as following :

$$E_{AM}(t) = \text{Re} \left[\mathcal{E}_0 e^{-i\omega_0 t} + \frac{\mathcal{E}_0 \epsilon_m}{2} e^{-i\phi_m} e^{-i(\omega_0 + \Omega)t} + \frac{\mathcal{E}_0 \epsilon_m}{2} e^{i\phi_m} e^{-i(\omega_0 - \Omega)t} \right]. \tag{1.6}$$

From Eq. (1.6), the spectrum is discrete and contains three components, the harmonic at carrier frequency ω_0 (light blue arrow) and two small satellites (teal arrows) at frequencies $\omega_0 \pm \Omega$ as shown in Fig.1.2 (known as modulation sidebands). Here, the carrier field as well as two side-bands are represented by rotating vectors on a complex plane Fig.1.2 (a). The carrier field vector with length $\mathcal{E}_0$ rotates clockwise (Im $\rightarrow$ Re) with the rate ω_0, while the two sidebands in the frame of carrier field counter-rotate relative to each other at a rate of Ω as shown in Fig.1.2(c). The sum of these three vectors yields a complex vector, and its projection on the real axis leads to the amplitude modulated light as in Fig.1.2(b).
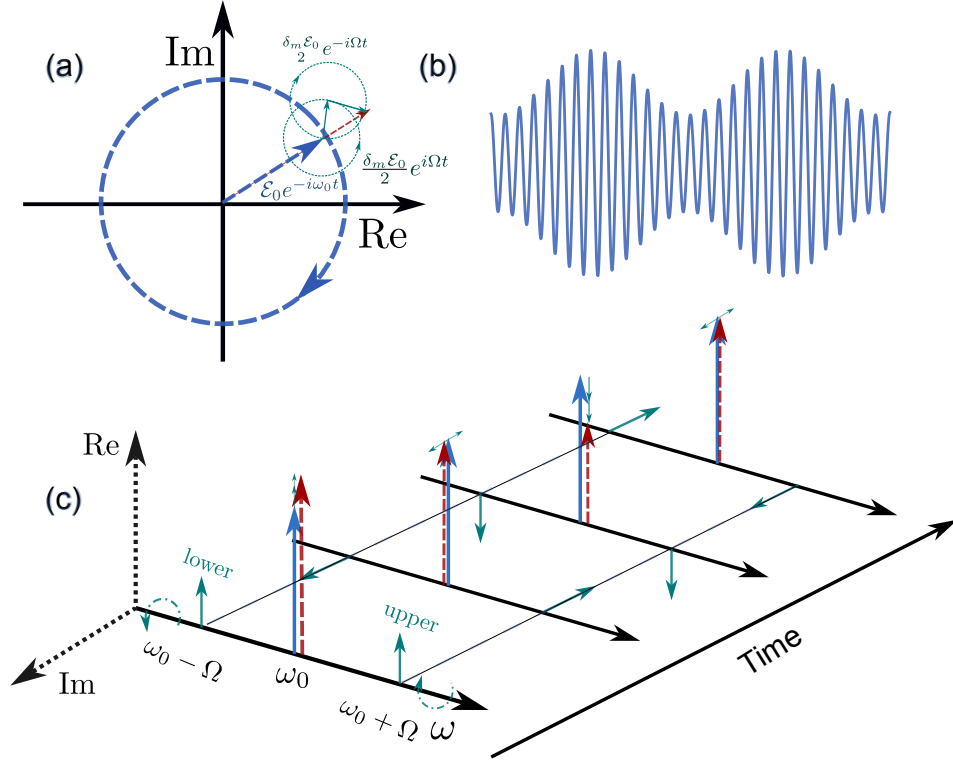
Figure 1.2: Amplitude modulation (AM) of light. Amplitude Modulation (AM) of light can be visualized using a phasor diagram in the complex plane. In this representation, the carrier field is depicted by a blue vector arrow rotating clockwise at a rate of ω_0. The modulation sidebands, indicated by teal arrows, have frequencies $\omega_0 \pm \Omega$ and rotate in time clockwise for the upper sideband and counter-clockwise for the lower sideband. Unlike the sidebands, the carrier (blue arrow) remains stationary in its rotation. The lower panel, labeled as (c), shows the time evolution of each sideband. These sidebands interfere with the carrier in such a way that only the amplitude of the resulting field (red arrow) changes, leaving the phase unaffected. The time dependent electric field strength of the AM light is plotted in the upper right corner, marked as (b).

1.2.4 Phase modulation

As we discussed in the section on amplitude modulation, the feature of this modulation on light is to create the modulated side-bands in the spectrum of this light. Now, let's use the same principle and explore phase modulation of a light, which can be expressed as:

$$E_{PM}(t) = \mathcal{E}_0 \cos[\omega_0 t + \delta_m \cos(\Omega t + \phi_m)], \tag{1.7}$$

and in cosine-sine quadrature where the modulation frequency Ω is much smaller than the carrier frequency ω_0:

$$\mathcal{E}_{c,PM}(t) = \mathcal{E}_0 \cos[\delta_m \cos(\Omega t + \phi_m)] \; and \; \mathcal{E}_{s,PM}(t) = \mathcal{E}_0 \sin[\delta_m \cos(\Omega t + \phi_m)]. \tag{1.8}$$

7

Especially, in the limit of weak modulation ($\delta_m \ll 1$), the above equations can be approximated (small angle approximation $\sin(\delta) \approx \delta$) as :

$$\mathcal{E}_{c,PM}(t) \approx \mathcal{E}_0 \ and \ \mathcal{E}_{s,PM}(t) \approx \delta_m \mathcal{E}_0 \cos(\Omega t + \phi_m). \qquad (1.9)$$

This also explains us why this sine quadrature is usually referred to as phase quadrature. In order to also get the spectrum of phase modulated light, with the help of Bassel function [16] and small δ_m limit, we could obtain a similar expression as:

$$E_{\mathrm{PM}}(t) = \mathrm{Re}\left[\mathcal{E}_0 e^{i\omega_0 t} + i\frac{\mathcal{E}_0 \delta_m}{2}\left[e^{i[(\omega_0+\Omega)t+\phi_m]} + e^{i[(\omega_0-\Omega)t-\phi_m]}\right]\right]. \qquad (1.10)$$

Again, we are facing the situation in which modulation creates a pair of side-
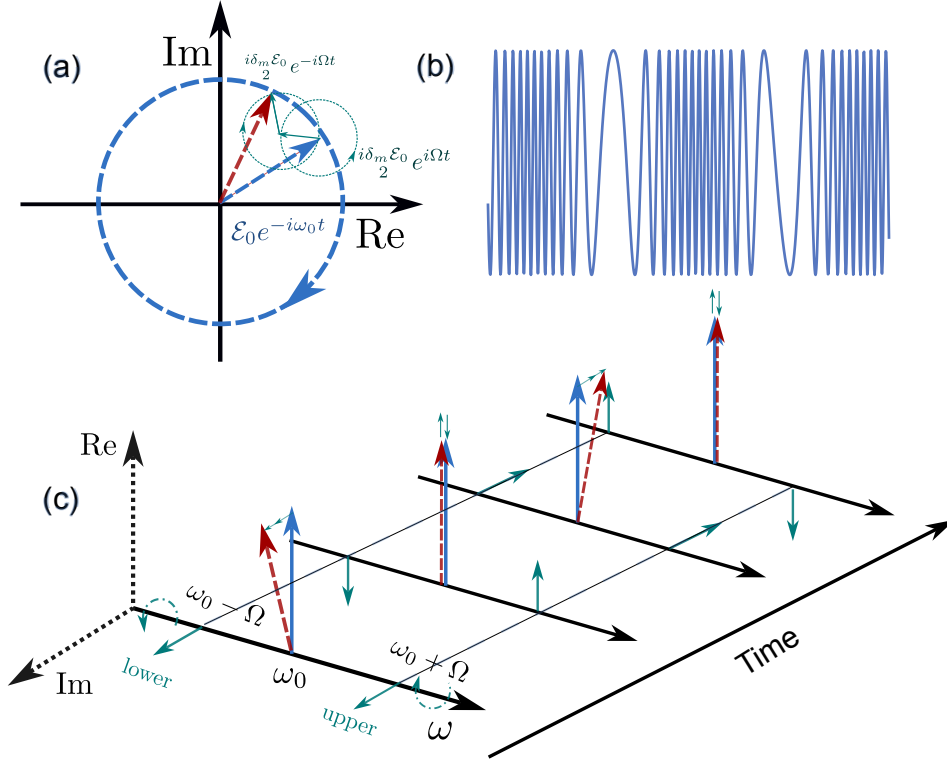
Figure 1.3: Phase modulation(PM) of light. In the case of phase modulation, the phasor diagram in the complex plane reveals some unique characteristics. Specifically, the sidebands experience a $\frac{\pi}{2}$ phase shift relative to the carrier field. This phase shift is due to the imaginary unit i present in the modulation term. As a result, the vector sum of the two sidebands (represented by the teal arrow) influences the orthogonal component of the carrier field vector (the blue arrow). Consequently, the modulated field (depicted by the red arrow) has roughly the same magnitude as the carrier field but oscillates faster or slower depending on the modulation frequency Ω. This behavior is illustrated in panel (c). Additionally, the time-dependent electric field strength of the phase-modulated (PM) light is plotted in the upper right corner, labeled as (b).

bands around the carrier frequency also shown in Fig. 1.3 (c). The difference from the amplitude modulation case is that these sidebands behave on the complex plane and always have $\frac{\pi}{2}$ phase shift relative to the carrier field (due to the factor i). Therefore, the sum of all three contributions results in the modulated oscillation vector that preserves a length close to the carrier field vector, yet experiences periodic phase shifts at the modulation frequency Ω as in Fig. 1.3 (b). The result of the PM oscillation on the real axis of the complex plane is presented in Fig. 1.3 (b).

1.3 Quantum nature of light
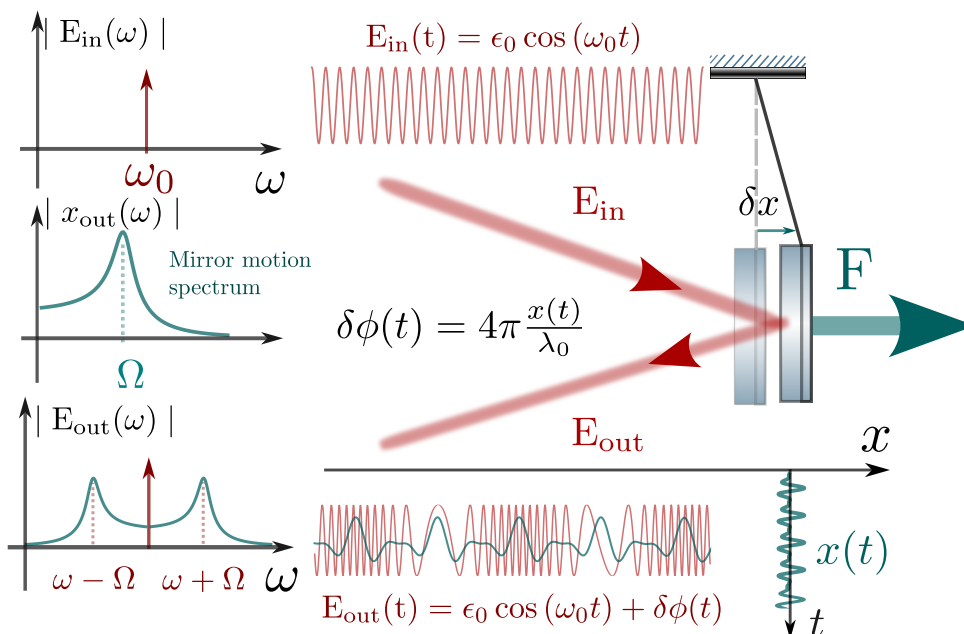
Figure 1.4: Schematic view of light modulated by mirror motion driven by a weak force F. The phase of the reflected probe light is modulated by the mechanical mirror motion, so that the mode of the outgoing field contains two sidebands, involving all the information about the mirror motion $x(\omega)$. The left panel shows spectra representation of the initial incident light with carrier frequency ω_0, the mirror mechanical motion $x(t)$ or $x(\omega)$, and the encoded phase information of mirror motion on the reflected light via the modulation by this mirror motion $\delta\phi(t)$. **Picture adapted from Farid Khalili (replotted).**

As previously mentioned, we explored the classical amplitude and phase modulation of light. This study allows for a deeper understanding of how a classical force signal is transferred into the probe laser. As illustrated in Fig.1.4, mirror displacement caused by an external force **F** leads to a phase modulation in the reflected light field. Notably, this modulation affects only the sine-quadrature, which is commonly referred to as the 'phase quadrature.' When analyzing the spectrum of

the phase-modulated field, we observe two additional sidebands superimposed on the monochromatic wave with a carrier frequency ω_o. These sidebands $\delta\phi$ mirror the spectral shape of the mirror's motion δx, as shown in left panel.

However, we must also account for the quantum nature of our real world. The electromagnetic field used to record signal information is not immune to quantum noise. This noise can become a dominant factor in our detection frequency spectrum, impacting the detected signal sensitivity. Consequently, a significant focus of our work is to understand and find ways to mitigate this quantum noise, potentially enhancing signal sensitivity.

To thoroughly grasp the effects of quantum noise on weak force signal measurements, an understanding of the probe light field's quantum dynamics is crucial. In this section, I present the background on the quantum noise of a probe light, explore various quantum states of this light, and discuss the formalism utilized in this thesis. For those interested in a more comprehensive review of quantum optics and noise, I recommend referring to the page 34-47 of [16].

We can begin by quantizing the probe light field. We focus on an electromagnetic field that propagates freely along the z-axis. Each spatial position is characterized by a location vector $\vec{r} = (x, y, x)$, in terms of its quantized form, we turn to the Heisenberg picture. In this representation, the electric field operator $\hat{E}(\vec{r}, t)$ can be written as:

$$\hat{E}(\vec{r}, t) = u(x, y, z) \int_0^{+\infty} \frac{d\omega}{2\pi} \sqrt{\frac{2\pi \hbar \omega}{\mathcal{A}c}} \left[\hat{a}_\omega e^{-i\omega t} + \hat{a}_\omega^\dagger e^{+i\omega t} \right]. \tag{1.11}$$

where $\hat{a}_\omega$ and $\hat{a}_\omega^\dagger$ are the single photon creation and annihilation operators with a mode of the field at sidebands frequency ω, respectively. $\mathcal{A}$ represents the cross-sectional area of the optical beam; $u(x, y, z)$ describes the spatial mode shape.

1.3.1 Two photon formalism

We have previously explained that the recorded signal information is encoded as two phase-modulated upper and lower sidebands added to the probe field's carrier frequency, as detailed in [18]. To analyze the influence of quantum noise around these sideband frequencies, it is advantageous to introduce operators specific to these frequencies. This approach, used to study the quantum light field in gravitational wave (GW) interferometers, is known as the 'two-photon formalism'. The operators for the modulated upper and lower sidebands are defined as follows:

$$\hat{a}_+ = \hat{a}_{\omega 0 + \Omega}, \ \hat{a}_- = \hat{a}_{\omega 0 - \Omega}, \tag{1.12}$$

with a set of commutation relations [19]:

$$\left[\hat{a}_+, \hat{a}_+'^\dagger\right] = \left[\hat{a}_-, \hat{a}_-'^\dagger\right] = 2\pi i \delta \left(\Omega - \Omega'\right), \tag{1.13}$$

from there in the limit of $\omega_o \gg \Omega$, we can define the amplitude quadrature $\hat{a}_c$ and phase quadrature $\hat{a}_s$ as follows:

$$\begin{aligned}
\hat{a}_c(\Omega) &= \frac{\hat{a}_+ + \hat{a}_-^\dagger}{\sqrt{2}} \Longleftrightarrow \hat{a}_c(t) = \int_{-\infty}^{\infty} \frac{d\Omega}{2\pi} \frac{\hat{a}_+ + \hat{a}_-^\dagger}{\sqrt{2}} e^{-i\Omega t}, \\
\hat{a}_s(\Omega) &= \frac{\hat{a}_+ - \hat{a}_-^\dagger}{i\sqrt{2}} \Longleftrightarrow \hat{a}_s(t) = \int_{-\infty}^{\infty} \frac{d\Omega}{2\pi} \frac{\hat{a}_+ - \hat{a}_-^\dagger}{i\sqrt{2}} e^{i\Omega t}.
\end{aligned} \tag{1.14}$$

they represent coherently create one photon in the lower sidebands and annihilate one photon in the upper sidebands. The newly defined two-photon quadrature operators satisfy the following commutation relations in the frequency domain, assuming we are measuring the photon number flux:

$$\left[\hat{a}_c(\Omega), \hat{a}_s^\dagger\left(\Omega'\right)\right] = \left[\hat{a}_c^\dagger(\Omega), \hat{a}_s\left(\Omega'\right)\right] = 2\pi i \delta \left(\Omega - \Omega'\right), \tag{1.15}$$

and all others vanish:

$$[\hat{a}_c(\Omega), \hat{a}_c\left(\Omega'\right)] = \left[\hat{a}_c(\Omega), \hat{a}_c^\dagger\left(\Omega'\right)\right] = \left[\hat{a}_c^\dagger(\Omega), \hat{a}_c^\dagger\left(\Omega'\right)\right] = [\hat{a}_c(\Omega), \hat{a}_s\left(\Omega'\right)] = 0, \tag{1.16}$$

such commutations can also be expressed in time domain:

$$[\hat{a}_c(t), \hat{a}_s\left(t'\right)] = i\delta \left(t - t'\right), \quad \text{and} \quad [\hat{a}_c(t), \hat{a}_c\left(t'\right)] = [\hat{a}_s(t), \hat{a}_s\left(t'\right)] = 0. \tag{1.17}$$

The electric field can be rewritten in a form very close to the classical phase-amplitude quadrature picture, expect it retains the classical terms (A_c, A_s) and incorporates the additional quantum noise terms $(\hat{a}_c, \hat{a}_s)$ as follows:

$$\hat{E}(x, y, z, t) = u(x, y, z)\sqrt{\frac{4\pi \hbar \omega_0}{\mathcal{A}c}} \left[(A_c + \hat{a}_c(t)) \cos \omega_0 t + (A_s + \hat{a}_s(t)) \sin \omega_0 t\right]. \tag{1.18}$$

1.3.2   Quantum state of light

Now we have defined a quantum Heisenberg operator of the electric field, and introduced quantum operators of two-photon quadrature. To fully describe the quantum noise in gravitational wave (GW) interferometers; a prominent example of weak force measurement. But first, we still need to define the quantum states of light, and they will help us to understand the magnitude and correlations of the amplitude and phase fluctuations of the probe light. In the following section, we will consider vacuum and coherent states of light, and also squeezed and Bi-particle entangled states. Same as the classical phase and amplitude modulation,

all the quantum noise and squeezed states of light will be visualized in phasor picture.

Vacuum states

We will start with a trivial but important quantum state, vacuum state, denoted as $|0\rangle$. The quantum state of the travelling wave can be viewed as a quantum harmonic oscillator. The vacuum state with frequency ω is the ground state of this oscillator with minimum energy $E_{vac} = \hbar\omega/2$. The mean amplitude of the vacuum state is zero, i.e:

$$\langle vac|\hat{a}_c(\Omega)|vac\rangle = \langle vac|\hat{a}_s(\Omega)|vac\rangle = 0. \tag{1.19}$$

Despite having a zero mean amplitude, the vacuum state still has noise in its amplitude and phase quadrature as indicated by the black arrows in Fig.1.5 (a) in the right plot. The second moments (variance) of quadrature amplitude as well as their cross-spectral density [20] are equal to: [1] [2]

$$\langle \hat{a}_c(\Omega) \circ \hat{a}_c(\Omega)\rangle = \langle \hat{a}_s\Omega) \circ \hat{a}_s(\Omega)\rangle = \frac{1}{2} \text{ and } \langle \hat{a}_c(\Omega) \circ \hat{a}_s(\Omega)\rangle = 0. \tag{1.20}$$

Therefore, Fig.1.5 (a) represents a vacuum state in complex phase picture where the area of the red circle equals to $\frac{1}{2}$ in dimensionless unit with a radius of $\frac{1}{\sqrt{2}}$. This area limits the minimal uncertainty product for canonical conjugate observable-The Heisenberg uncertainty relation. When considering the most well known non-commuting observables, position $\hat{X}$ and momentum $\hat{P}$ in $\hbar$ unit ;

$$\Delta\hat{X} \cdot \Delta\hat{P} \geq \frac{1}{2}\left|[\hat{X}, \hat{P}]\right| = \frac{1}{2}. \tag{1.21}$$

it is understood that these two observables cannot be measured with arbitrary precision simultaneously.

---

[1] The variance of an arbitrary observable $\hat{o}(t)$ in double side power spectrum density: $\text{Var}[\hat{o}(t)] \equiv (\Delta\hat{o})^2 = \langle\hat{o}^2(t)\rangle - \langle\hat{o}(t)\rangle^2 = \int_{-\infty}^{\infty} \frac{d\Omega}{2\pi}\overline{S}_o(\Omega)$. Normally, the noise sources are analyzed in single side power spectrum density $\overline{S}_o^+(\Omega)$, the connection between these two are $\overline{S}_o^+(\Omega) = 2\overline{S}_o(\Omega)$ for $\Omega \geq 0$.

[2] $\langle\hat{a}_i(\Omega) \circ \hat{a}_j(\Omega')\rangle \equiv \frac{1}{2}\left\langle\hat{a}_i(\Omega)\hat{a}_j(\Omega')^\dagger + \hat{a}_j(\Omega')\hat{a}_i(\Omega)^\dagger\right\rangle \equiv 2\pi\overline{S}_{ij}(\Omega)\delta(\Omega - \Omega')$

where $\overline{S}_{ij}$ represents the cross power spectral densities (CPSD) of the corresponding two quadrature amplitudes, which describes how the power of one signal at a particular frequency is correlated with the power of another signal at the same frequency.

Coherent states

Another important quantum state of light is the coherent state, it can be introduced by shifting the vacuum ground state along one direction by certain distance $\alpha = |\alpha| \, e^{iarg(\alpha)}$ in a complex plane. This shift is analogous to a classical effective force on a oscillator. Such a shift is effected by a displacement operator $\hat{D}$, and its action on a ground state $|\alpha\rangle$ can be written as

$$|\alpha\rangle = \hat{D}[\alpha] \, |0\rangle = e^{\alpha\hat{a}^\dagger - \alpha^*\hat{a}} \, |0\rangle \, . \tag{1.22}$$

It is also an eigenstate of the annihilation operator:

$$\hat{a} \, |\alpha\rangle = \alpha \, |\alpha\rangle \, . \tag{1.23}$$

Since the coherent state can be achieved by superimposing a vacuum states with a mean values on this corresponding operator. The variance and cross-spectral density of a coherent state are identical to those of a vacuum state as shown in Fig1.5 (b). It is worth noting that in the case of a freely propagating monochromatic laser with an emission frequency (ω_e), which also serves as the carrier frequency (ω_0), only the mode at ω_0 will be in a coherent state. while all other modes will remain in their ground vacuum state.

Squeezed state of light

One more interesting quantum state of light is squeezed state. Comparing with previous two quantum states with minimal uncertainty and equal noise across their quadratures, a squeezed state, on the other hand, displays unique characteristics. Specifically, one quadrature can be reduced by a certain factor, while the other conjugate quadrature is increased by the same factor. Therefore, the product of these two quadratures still fulfill the Heisenberg uncertainty principle as presented in Fig.1.5. Squeezed states of light are commonly generated through the parametric down conversion (PDC) with the Hamiltonian that describes the creation or annihilation of a two-photon process [16]:

$$\hat{H} = \hat{H}_0 + \frac{i\,\hbar\kappa}{2} \left[\hat{a}_+^\dagger \hat{a}_-^\dagger \hat{a}_p - \hat{a}_+ \hat{a}_- \hat{a}_p^\dagger \right] , \tag{1.24}$$

where $\hat{a}_p$ is the annihilation operator of the pump field and $\hat{a}_\pm$ correspond to the two produced sidebands. We commonly assume the pump field is a strong coherent state that does not get depleted, as a result, one could replace the pump operator with its coherent amplitude. $\kappa = \rho e^{2i\theta}$ is a complex coupling constant that depends on the crystal second-order susceptibility and experimental parameters such as pump field amplitude. If we operate the above Hamiltonian to a field over a time duration t, the annihilation $\hat{a}_\pm$ for the $\pm\Omega$ sideband frequencies

(a) Vacuum state

(b) Coherent state

(c) Bright amplitude squeezed state
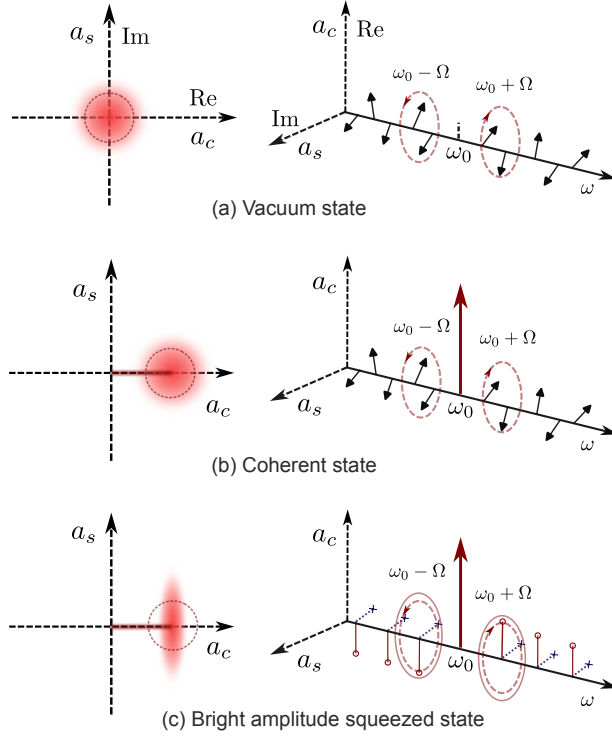
Figure 1.5: Quantum vacuum state (a), coherent state (b) and bright phase squeezed state (c) in phase (ball-stick) and side-bands picture. For all states their quantum uncertainties are illustrated as circles or a ellipses around their amplitude. Both the coherent state and bright phase squeezing state possess an amplitude of α. The side-bands diagram represents one snapshot in time with two upper and lower side-bands around the carrier frequency ω_o, which rotate in opposite directions along the complex axis.

can be described as following:

$$\hat{S}(\rho, \theta)\hat{a}_\pm \hat{S}^\dagger(\rho, \theta) = \hat{a}_{(\pm, in)} \cosh \rho t + \hat{a}^\dagger_{(\mp, in)} e^{2i\theta} \sinh \rho t. \qquad (1.25)$$

Where $\hat{S}(\rho, \theta)$ is the squeeze operator:

$$\hat{S}[\rho t, \theta] \equiv \exp\left\{ \rho t \left(\hat{a}_+ \hat{a}_- e^{-2i\theta} - \hat{a}^\dagger_+ \hat{a}^\dagger_- e^{2i\theta} \right) \right\}. \qquad (1.26)$$

Now, by introducing a squeezing factor $r = \rho t$, we can express the generate transformation of the phase-amplitude quadrature operators in terms of the squeeze operator [16] with the help of Bloch-Messiah reduction [21, 22] :

$$\hat{\mathbf{b}} = \begin{pmatrix} \hat{b}_c \\ \hat{b}_s \end{pmatrix} = \hat{S}[r, \theta]\hat{\mathbf{a}} = \hat{R}[-\theta]\hat{S}[r, 0]\hat{R}[\theta]\hat{\mathbf{a}}$$

$$= \begin{pmatrix} \cos\theta & \sin\theta \\ -\sin\theta & \cos\theta \end{pmatrix} \begin{pmatrix} e^r & 0 \\ 0 & e^{-r} \end{pmatrix} \begin{pmatrix} \cos\theta & -\sin\theta \\ \sin\theta & \cos\theta \end{pmatrix} \begin{pmatrix} \hat{a}_c \\ \hat{a}_s \end{pmatrix}. \qquad (1.27)$$

From the general transformation, we could know the squeezing at an arbitrary squeezed angle θ can be understood as a sequence of operations: first, a counterclockwise rotation by θ, followed by squeezing and anti-squeezing of two conjugate quadratures, and finally a clockwise rotate back by θ. A bright phase squeezed state is visualised in Fig.1.5 (c), where the amplitude quadrature $\hat{a}_c$ is reduced below the level of vacuum noise (indicated by the red dashed circle). In the sideband phasor picture, the squeezed state corresponds to a spectrum of correlated sideband pairs with spectrum frequencies $\omega_o \pm \Omega$. These correlations would allow the two sidebands interfere destructively for the squeezed quadrature and constructively for the anti-squeezed quadrature, introducing additional quantum noise.

For better illustrating the time evolution of quantum noise, we set the axes to correspond with the amplitude and phase quadrature operators. As shown in Fig.1.6 , we focus on an example of a vacuum amplitude squeezed state, achieved by removing the carrier amplitude at ω_0. Two correlated photon side bands are presented at $\pm\Omega$ frequency. Each of these sidebands has greater uncertainty compared to the vacuum state but also shows either correlations or anti-correlations, as depicted by the symbols '+' and 'o' in the upper panel at initial time $T = 0$.

Similar to the classical phase modulation, the amplitude quadrature of the two sidebands remain anti-correlated through their evolution. This leads to destructive interference when summing the two sidebands, which in turn reduces the variance of the amplotude quandrature's quantum noise in single sideband quadrature representation, in contrast, the total quantum noise in phase quadrature increases.

Interestingly, applying a phase shift to only one sideband (e.g., lower sidebands) does not disrupt the existing quantum correlation but does alter the squeezed angle of the field's overall quantum noise. As shown in the bottom panel of Fig.1.6, a frequency-dependent squeeze angle ranging from 0 to $\pi/2$ can be achieved by applying a phase transition across the three sidebands frequencies (Ω, 2Ω, 3Ω) from 0 to $\pi/2$ and then to π.

In the absence of losses, the produced squeezing state is normally quantified in decibels (dBs) that can be directly related to the squeezing factor r in squeezing operator. This relationship is expressed as follows:

$$r_{dB} = 10\log_{10}e^{2r} \Longleftrightarrow r = r_{dB}/(20\log_{10}e).$$ (1.28)

For instance, a generated squeezed state of 10 dB is equivalent to a squeezed factor of r = 1.15.
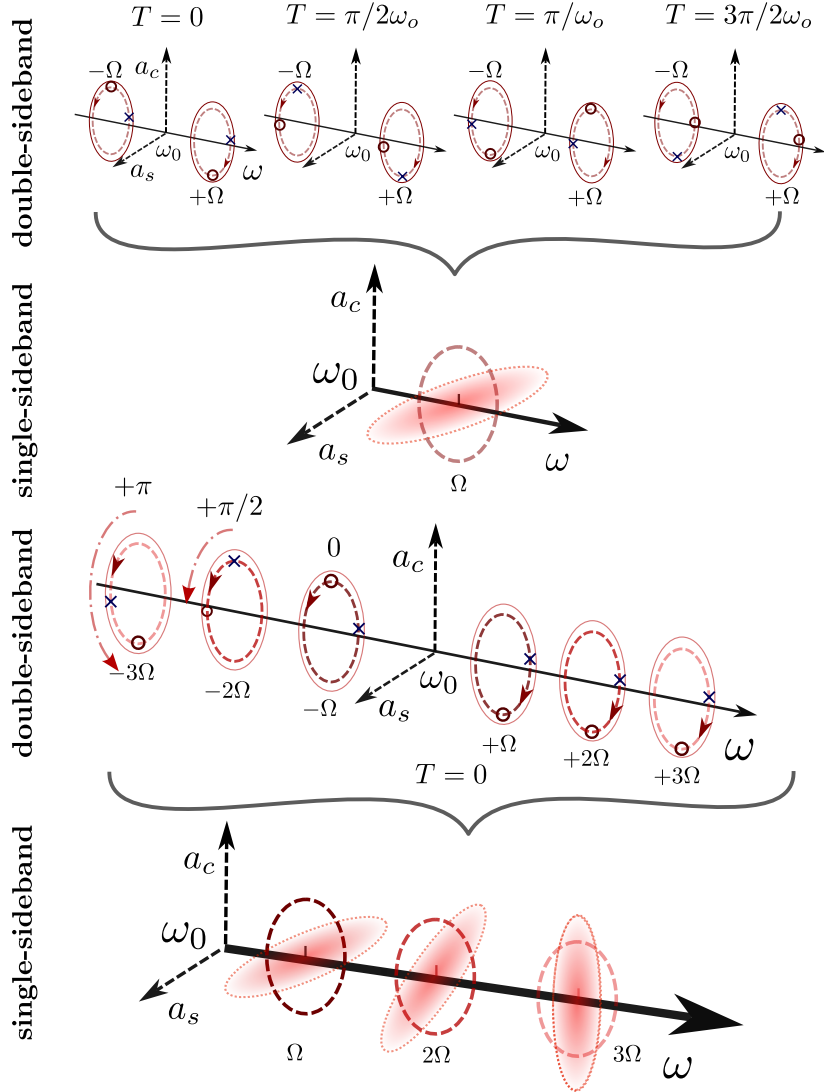
Figure 1.6: Phasor picture for amplitude (cosine) squeezed vacuum state in a rotating frame for frequency ω_0. In the quantum system, noise manifests differently in the upper and lower side-bands. The quantum noise rotates clockwise in the upper sidebands at a frequency of $(\omega_o + \Omega)$. In contrast, it rotates counterclockwise in the lower side-bands over time. Since we are dealing with a vacuum state, no carrier is present. The upper and lower sidebands exhibit quantum correlations, which can arise from processes like the down-conversion. These correlations are indicated by different symbols: a plus $(+)$ for the amplitude (cosine) quadrature sidebands and a circle (o) for the phase (sine) quadrature ones at initial time. Importantly, the uncertainty in each of these side-bands exceeds that of the vacuum state, as shown by a dashed red circle. The lower panel shows a single side-bands spectrum. Due to the correlation of quantum noise in two side-bands picture, the quantum noise is squeezed in the amplitude quadrature, but anti-squeezed in phase quadrature. In the bottom panel, the lower side-bands at frequencies of $(\omega_0 - \Omega)$, $(\omega_0 - 2\Omega)$, $(\omega_0 - 3\Omega)$ have a phase transition from 0 to π with respect to the initially amplitude squeezed state. These transitions lead to a rotation of squeezing ellipse from 0 to $\pi/2$ at single side-bands picture.

16

Non degenerate two-mode squeezed states of light

When a non-linear crystal is pumped at a frequency of $2\omega_0$, the upper and lower sidebands around the half pump frequency ω_0 are correlated and their sum result in a squeezed state around this carrier frequency ω_0. Parametric down conversion can also be used to generate entangled states, known as twin beam states, when operating in a non-degenerate fashion. With the same pump at frequency $2\omega_0$, an entangled pair consisting of a signal frequency ω_s and an idler frequency ω_i is generated and satisfying phase-match condition $\omega_p = 2\omega_0 = \omega_s + \omega_i$, as illustrated by the energy level diagram in Fig.1.7 (a). The non-degenerate parametric down-conversion can be characterized by the following Hamiltonian:

$$\hat{H} = \hat{H}_0 + \frac{i\hbar\kappa}{2}\left\{\left[\hat{a}^\dagger_{s,+}\hat{a}^\dagger_{i,-} + \hat{a}^\dagger_{s,-}\hat{a}^\dagger_{i,+}\right]\hat{a}_p - \left[\hat{a}_{s,+}\hat{a}_{i,-} + \hat{a}_{s,-}\hat{a}_{i,+}\right]\hat{a}^\dagger_p\right\}, \quad (1.29)$$

where the interaction introduces four sidebands at $\pm\Omega$ around either the signal or idler carrier frequencies (ω_s and ω_i, respectively). As illustrated in Fig.1.7 (b), we have entanglement between $\omega_s - \Omega$ and $\omega_i + \Omega$, as well as between $\omega_s + \Omega$ and $\omega_i - \Omega$. These four sidebands are denoted as:

$$\hat{a}_{s,\pm} = \hat{a}_s(\omega_s \pm \Omega), \ \hat{a}_{i,\pm} = \hat{a}_i(\omega_i \pm \Omega). \quad (1.30)$$

Following a similar approach to the one used for demonstrating the transformation of sideband operators in the single-mode squeezed state, we can derive the evolution of the operator for the two modes entangled states.

$$\begin{aligned}
\hat{a}_{(s,\pm)} &= \hat{a}_{(s\pm,in)}\cosh r + \hat{a}^\dagger_{(i\mp,in)}e^{2i\theta}\sinh r, \\
\hat{a}_{(i,\pm)} &= \hat{a}_{(i\pm,in)}\cosh r + \hat{a}^\dagger_{(s\mp,in)}e^{2i\theta}\sinh r,
\end{aligned} \quad (1.31)$$

with the newly defined two-mode (TM) squeezing operator, which we include for both positive and negative sidebands:

$$\hat{S}_{TM}(r,\theta) = \exp\left[r(\hat{a}_{s,+}\hat{a}_{i,-}e^{-2i\theta} - \hat{a}^\dagger_{s,+}\hat{a}^\dagger_{i,-}e^{2i\theta}) + r(\hat{a}_{s,-}\hat{a}_{i,+}e^{-2i\theta} - \hat{a}^\dagger_{s,-}\hat{a}^\dagger_{i,+}e^{2i\theta})\right].$$

$$(1.32)$$

In terms of amplitude quadrature $\hat{a}_c$ and phase quadrature $\hat{a}_s$ for the signal and idler fields, we can express the conversion from signal sidebands operator to quadrature operator as $\hat{a}_{s,c} = \frac{\hat{a}_{(s,+)} + \hat{a}^\dagger_{(s,-)}}{\sqrt{2}}$ for the signal amplitude quadrature and $\hat{a}_{s,s} = \frac{\hat{a}_{(s,+)} - \hat{a}^\dagger_{(s,-)}}{i\sqrt{2}}$ for the signal phase quadrature, with analogous expressions for the idler quadrature operators.

We can then calculate the covariance matrix for the quadrature operators $\hat{a}_{s,c}, \ \hat{a}_{s,s}, \ \hat{a}_{i,c}, \ and \ \hat{a}_{i,s}$ to gain a deeper understanding of the correlation among

these sidebands. The covariance matrix $\overline{\mathbf{S}}^3$ is given by:

$$
\overline{\mathbf{S}} = \begin{pmatrix} S_{sc\ sc} & S_{ss\ sc} & S_{ic\ sc} & S_{is\ sc} \\ S_{sc\ ss} & S_{ss\ ss} & S_{ic\ ss} & S_{is\ ss} \\ S_{sc\ ic} & S_{ss\ ic} & S_{ic\ ic} & S_{is\ ic} \\ S_{sc\ is} & S_{ss\ is} & S_{ic\ is} & S_{is\ is} \end{pmatrix}
$$

$$
= \begin{bmatrix} \cosh 2r & 0 & -\cos 2\theta \sinh 2r & \sin 2\theta \sinh 2r \\ 0 & \cosh 2r & \sin 2\theta \sinh 2r & -\cos 2\theta \sinh 2r \\ -\cos 2\theta \sinh 2r & \sin 2\theta \sinh 2r & \cosh 2r & 0 \\ \sin 2\theta \sinh 2r & -\cos 2\theta \sinh 2r & 0 & \cosh 2r \end{bmatrix}.
$$
(1.33)

In the special case when the squeezing angle is chosen to be $\theta = \pi/2$, corresponding to the phase squeezing quadrature, the covariance matrix simplifies to :

$$
\overline{\mathbf{S}}\Big|_{\theta_s = \pi/2} = \begin{bmatrix} \cosh 2r & 0 & \sinh 2r & 0 \\ 0 & \cosh 2r & 0 & -\sinh 2r \\ \sinh 2r & 0 & \cosh 2r & 0 \\ 0 & -\sinh 2r & 0 & \cosh 2r \end{bmatrix}.
$$
(1.34)

We observe that the quadratures in signal and idler fields are correlated, indicating quantum entanglement, as evidenced by the nonzero off-diagonal terms in the covariance matrix. These correlations between the entangled pairs enable the idler's measurements to serve as estimators, potentially reducing the uncertainty of the signal measurements, and vice versa. This conditional variance of signal uncertainty, represented by $\hat{a}_s \equiv (\hat{a}_{sc}, \hat{a}_{ss})$, can be derived by using the principle of conditional probability :

$$
P\left(\hat{a}_s \mid \hat{a}_{i,\phi}\right) = \frac{P\left(\hat{a}_s, \hat{a}_{i,\phi}\right)}{P\left(\hat{a}_{i,\phi}\right)}.
$$
(1.35)

For example, assuming the signal is measured at the phase quadrature, the conditional covariance matrix $\mathbf{S}^{\text{cond}}_{a_s a_s}$ is then:

$$
\overline{\mathbf{S}}^{\text{cond}}_{a_s a_s} = \overline{\mathbf{S}}_{a_s a_s} - \frac{\overline{\mathbf{S}}_{a_s a_{i,\phi}} \overline{\mathbf{S}}_{a_{i,\phi} a_s}}{\overline{\mathbf{S}}_{a_{i,\phi} a_{i,\phi}}} = R_{-\phi} \begin{bmatrix} e^{-2r_{\text{eff}}} & 0 \\ 0 & e^{2r_{\text{eff}}} \end{bmatrix} R_{\phi},
$$
(1.36)

where R_{ϕ} and $R_{-\phi}$ are rotation matrices. In this context (as depicted in middle panel of Fig.1.7 (c)), the detection of the idler field quadrature at $\hat{a}_{i,\phi}$, which is described as $\hat{a}_{i,\phi} = \hat{a}_{i,c} cos\phi + \hat{a}_{i,s} sin\phi$. This enables us to accurately predict the signal quadrature at $\hat{a}_{s,-\phi} = \hat{a}_{s,c} cos\phi - \hat{a}_{s,s} sin\phi$, through the off-diagonal

---

[3]Covariance is a measure of how much two variables vary together: $\overline{S}_{AB} = \text{Cov}(\hat{A}, \hat{B}) = \frac{1}{2}\left\langle \hat{A}\hat{B} + \hat{B}\hat{A} \right\rangle - \left\langle \hat{A} \right\rangle \left\langle \hat{B} \right\rangle$. Here, the angle brackets $\langle \rangle$ denote the quantum mechanical expectation value.

terms in covariance matrix while not providing any information for $\hat{a}_{s,\pi/2-\phi}$. The effective squeezing factor r_{eff} is defined as $e^{r_{eff}} \equiv \cosh 2r$. For significant squeezing, where $r_{eff} \gg 1$, the signal field conditional squeezed state exhibits only 3dB less squeezing compared with a single-mode squeezed state. In Fig.1.7 (d), when $\phi = 0$, we could observe the direct correlation or anti-correlation along these four quadrature operators, as represented by the equations.

$$\overline{S}_{(\hat{a}_{s,c}\pm\hat{a}_{i,c})/\sqrt{2}} = e^{\pm 2r_{eff}}, \quad \overline{S}_{(\hat{a}_{s,s}\pm\hat{a}_{i,s})/\sqrt{2}} = e^{\mp 2r_{eff}}. \tag{1.37}$$
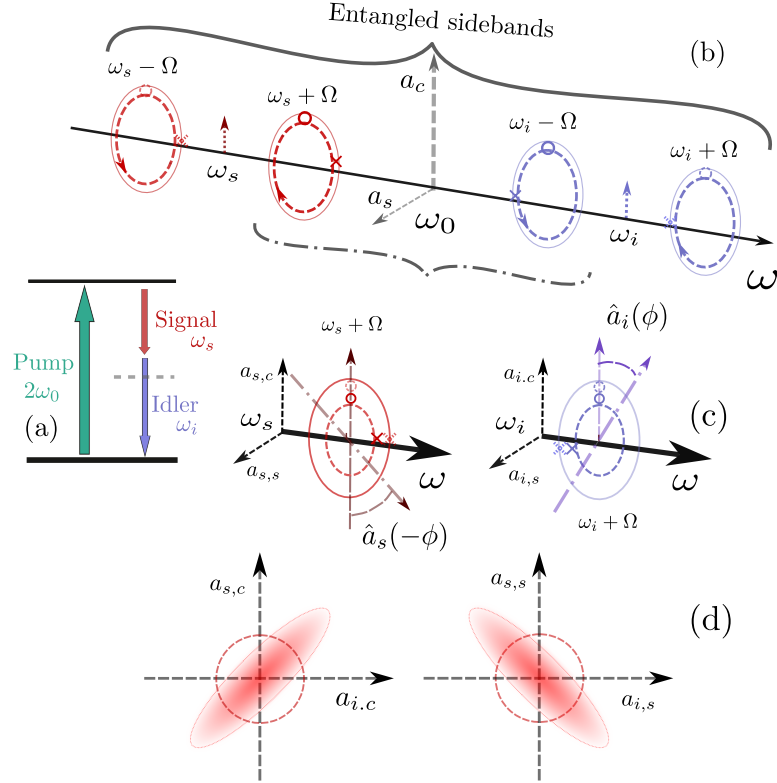
Figure 1.7: Phasor representation of two-mode entangled states in a rotating frame for frequency ω_0. (a), the generation of two-mode entangled fields (signal and idler) through the non-degenerate parametric down conversion. (b), the annihilation of the pump field with $2\omega_0$ creates two lower energy photons within entangled sidebands ($\omega_s - \Omega$ and $\omega_i + \Omega$) or ($\omega_s + \Omega$ and $\omega_i - \Omega$). (c), the mode of each quadrature in single sidebands picture is symmetric thermal state with the uncertainties (indicated by the large red circles) larger than those of the ground vacuum state (indicated by the small dashed circles). However, given the measured data of the idler quadrature, the corresponding signal beam quadrature will exhibit conditionally squeezing by a factor of 1/cosh (2r) due to the optimal correlation in two-mode squeezed vacuum. (d), In the two-mode squeezed state, the amplitude quadratures ($\omega_{s,c}$, $\omega_{i,c}$) are correlated, and the phase quadratures are anti-correlated ($\omega_{s,s}$, $\omega_{i,s}$), therefore, the joint measurement of two quadrature modes with properly selected quantum correlations can surpass the limits of the ground vacuum state.

1.4 Detecting signal and quantum states

In this section, I will discuss the detection of the encoded phase shifts in the output optical field, which contains interesting external force signals such as gravitational wave (GW) along with the quantum noise inherent in the optical field. A photo-detector is a device employed to sense the optical photons and converts them into an electrical current, governed by the equation:

$$
\begin{aligned}
i = \frac{e\eta_{pd}}{\hbar\omega}P &= e\eta_{pd}\left(|\alpha|^2 + |\alpha|\left(\hat{a} + \hat{a}^\dagger\right) + \hat{a}^\dagger\hat{a}\right) \\
&\approx e\eta_{pd}\left(|\alpha|^2 + |\alpha|\delta\hat{a}_c\right).
\end{aligned}
\tag{1.38}
$$

Considering a high conversion efficiency ($\eta_{pd} \approx 1$), and since the last term $\hat{a}^\dagger\hat{a}$ is significantly smaller than the light amplitude α, ($\hat{a}^\dagger\hat{a} \ll \alpha$), this term can be omitted. Direct detection with a photodetector allows measurement of the optical power $|\alpha|^2$ together with the fluctuation $\delta\hat{a}_c$ in amplitude quadrature of the same field . However, it cannot measure fluctuations of other quadrature, such as $\hat{a}_s$, of the same field.
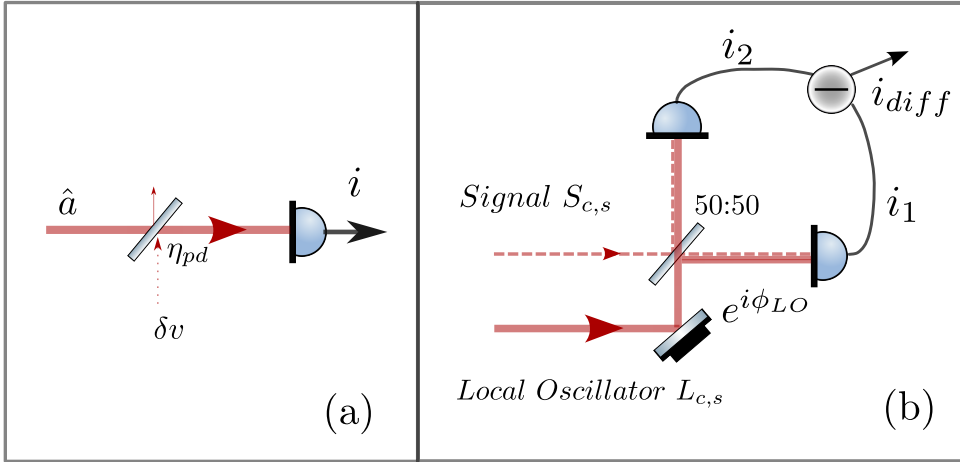
Figure 1.8: Schematic of direct and homodyne detection of an optical field (a) a photodetector with imperfect quantum efficiency modelled as a partial beam splitter. (b) A weak signal field and bright local oscillator field are combined with a 50:50 beam splitter (BS). The superposed fields at the output of the BS are detected with two photodetectors and their subtracted photocurrents are sent for further analysis.

Homodyne detection

In order to acquire the phase quadrature (or an arbitrary quadrature) information of the optical field, we need to perform a quadrature measurement of this optical field instead of measuring its power. This can be achieved by using an interferometric method known as homodyne detection, where the output signal

field is mixed with a bright local oscillator (LO) on a 50/50 beam splitter with a relative phase ϕ_{LO}. The two outputs from the beam splitter are detected with two photodiodes, and the resulting photocurrents are subtracted. This subtraction helps separate the quadrature fluctuation from the steady-state optical power.

In homodyne detection, both the fields in signal arm and LO arm share the same carrier frequency ω_0. We could write the weak signal wave (the DC amplitude of signal $S_{c,s}^{(0)} \approx 0$) as:

$$S(t) = S_c(t) \; \cos\omega_0 t + S_s(t) \; \sin\omega_0 t, \tag{1.39}$$

where we assume the signal field contains both the interested force signal $F_{c,s}(t)$ and quantum noise $\delta\hat{S}_{c,s}(t)$ in two quadratures for the general case:

$$S_{c,s}(t) = F_{c,s}(t) + \delta\hat{S}_{c,s}(t). \tag{1.40}$$

And the local oscillator field is given by:

$$L(t) = L_c(t) \; \cos\omega_0 t + L_s(t) \; \sin\omega_0 t, \tag{1.41}$$

with the local oscillator being a bright laser light with field amplitudes $L_{c,s}^0(t)$ and laser classical noise $l_{c,s}(t)$ (classical amplitude modulation):

$$L_{c,s}(t) = L_{c,s}^0(t) + l_{c,s}(t). \tag{1.42}$$

After the homodyne detection, the resulting two photocurrents $i_{1,2}$ are proportional to the intensities $I_{1,2}$ of the two output optical fields, where $\mathrm{L}_{c,s}^0 = |\mathrm{L}_c^0 \; \cos\omega_0 t + \mathrm{L}_s^0 \; \sin\omega_0 t|$:

$$
\begin{aligned}
i_1 \propto I_1 \propto \overline{\frac{(L+S)^2}{2}} &= \frac{L_0^2}{2} + |L_0|(F_c + l_c + \delta\hat{S}_c) \cos\phi_{LO} \\
&+ |L_0|(F_s + l_s + \delta\hat{S}_s) \sin\phi_{LO} + \mathcal{O}[F_{c,s}^2, l_{c,s}^2, \delta\hat{S}_{c,s}^2], \\
i_2 \propto I_2 \propto \overline{\frac{(L-S)^2}{2}} &= \frac{L_0^2}{2} - |L_0|(F_c - l_c + \delta\hat{S}_c) \cos\phi_{LO} \\
&- |L_0|(F_s - l_s + \delta\hat{S}_s) \sin\phi_{LO} + \mathcal{O}[F_{c,s}^2, l_{c,s}^2, \delta\hat{S}_{c,s}^2].
\end{aligned}
\tag{1.43}
$$

Again we omit the much smaller second-order terms in the balanced homodyne detection scheme, the differential photocurrent i_{diff} will contain only the force signal $F_{c,s}(t)$ and quantum noise $\delta\hat{S}_{c,s}$ of the signal field $\hat{S}_{c,s}(t)$:

$$i_{diff} = i_1 - i_2 \propto 2|L_0| \left[(F_c + \delta\hat{S}_c)\cos\phi_{LO} + (F_s + \delta\hat{S}_s)\sin\phi_{LO} \right]. \tag{1.44}$$

Thus, a bright LO optical field effectively amplifies the signal and quantum noise of the weak signal field, enables the readout of either the amplitude or phase quadrature by tuning the ϕ_{LO}. And the classical LO laser noise $l_{c,s}(t)$ does not contribute to the subtracted photocurrents due to the large common mode

rejection of the balanced detector. However, due to challenging technical difficulties, such as ultra-low noise LO light phase control system, the gravitational communities still employ another approach known as DC readout. This method intentionally offsets the two balanced interferometer arms from the dark fringe initially, using a small leakage of the bright intracavity laser to carry the signal information. The main disadvantage of the DC readout is that it cannot remove the influence of the classical laser noise, which is not a concern for the homodyne detection scheme [16].

1.5 is there a measurement precision limit further imposed by quantum mechanics?

The pursuit of more effective gravitational wave (GW) detection is a key objective in experimental physics. Current GW observatories, such as LIGO and Virgo, utilize high-precision laser interferometry as a weak force sensor, achieving gravitational wave strain sensitivities of 10^{-21}. As shown in Fig.1.9(a), this approach involves using a coherent laser with wavelength λ_0 to detect the displacement of test mass mirrors due to the passing GW. The GW amplitude h(t) stretches the interferometer by h(t)·L while compressing the other. This results in a relative change in the lengths of the two arms, consequently, a phase shift in the interferometer 's light fields, and this shift converts into a power change after the combing beam splitter at the output of interferometer [23]:

$$P_{out} = \frac{1}{2}P_{in}(1 + \sin(2\delta\phi)) \approx \frac{1}{2}P_{in}\left(1 + \sin\left(2\pi\frac{L}{\lambda_0}h(t)\right)\right). \qquad (1.45)$$

However, the interferometric GW detectors are subject to various noise sources that limit their further sensitivity improvements, such as seismic noise and electronic noise. Although these noises can be mitigated through several techniques, quantum noise that arises due to the Heisenberg uncertainty principle and quantum fluctuations of the probing light, increasingly predominates in the detection frequency bandwidth of advanced second-generation interferometers. This quantum noise imposes a fundamental limit on the precision of test mass displacement measurements.

Imprecision Noise (Shot Noise)

After discussing the physical background of quantum states of light, we now examine how quantum noise affects the detection system and its sensitivity. One source of quantum noise arises from the inherent uncertainty in arrival times of photons at the detector. Despite a constant average number of photons per time interval, these arrivals are subject to statistical fluctuation, characterized by a
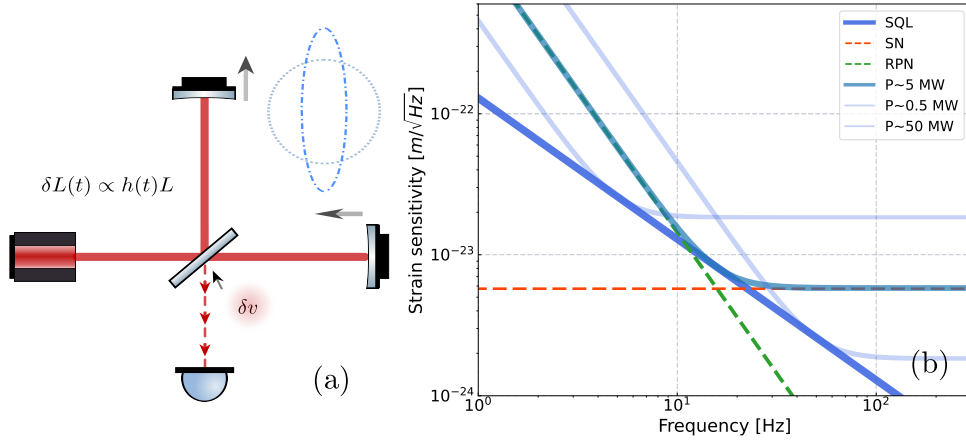
Figure 1.9: Schematic of a conventional Michelson Interferometer. (a) When the interferometer operates at the dark fringe, the leakage from the dark port carries the displacement signal of the interferometer. Simultaneously, vacuum noise can enter the interferometer, driving the test mass mirror as the radiation pressure noise. (b) The strain sensitivity for a conventional Michelson interferometer encompasses both shot noise (SN: red dashed curve) and radiation pressure noise (RPN: green dashed curve). Changing the laser power only shifts the minimum quantum noise along the standard quantum limit curve but cannot surpass this limit.

Poisson distribution. The root-mean-square (RMS) fluctuation of this distribution (denoted as $\sqrt{N} \propto \sqrt{P}$, the power of light is related to the average amount of photons), leads to a fractional error in phase measurement, known as imprecision noise (or shot noise, SN). Notably, this measurement imprecision noise variance is inversely proportional to the photons count in the detector (optical power) $(\propto \frac{1}{P})$ and is spectrally flat, where the carrier frequency $\omega_0 = 2\pi c / \lambda_0$:

$$\overline{S}_{\text{SN}} = \frac{\hbar c^2}{2\omega_0 P}. \tag{1.46}$$

Radiation Pressure (Backaction) Noise

Another significant source of quantum noise involves the fluctuation of photons transferring their momentum to the test-mass as random radiation pressure forces $(\delta F_{RPN} = \propto P)$, which induces additional vibration. This radiation pressure noise scales with the optical power; higher power leads to increased momentum being transferred to the test-mass, causing it to react and thus induce additional displacement. This reaction is characterized by its mechanical susceptibility $\chi_m(\Omega) = -1/m\Omega^2$ for a free mass object, which acts as a transfer function from force to displacement. The spectral density of the radiation pressure force and its consequent impact on the mirror displacement, can be expressed as:

$$\overline{S}_{\text{RPN}} = \frac{\hbar \omega_0 P}{m^2 \Omega^4 c^2}. \tag{1.47}$$

23
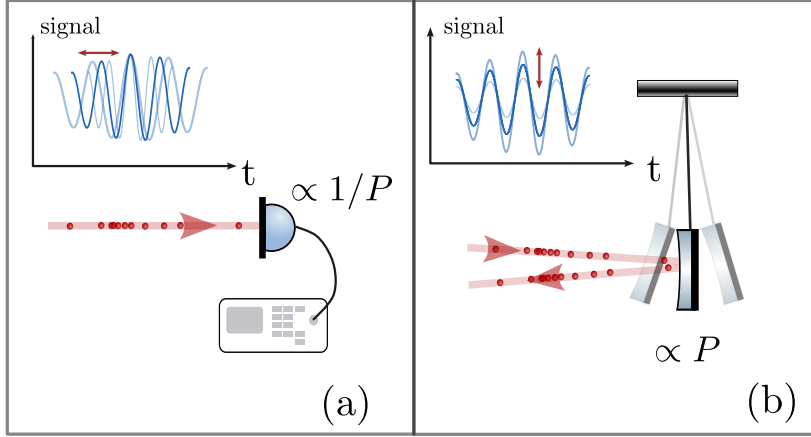
Figure 1.10: Diagram of shot and radiation pressure noise (a) Shot noise originates from the uncertainty in the simultaneous arrival of photons, compromising the phase precision required to distinguish the force signal at the detection quadrature. (b) Radiation pressure noise results from the random photons bombarding the mirrors. These induced vibrations of mirror will, in turn, distort the amplitude precision of the measured force signal.

Here, m is the mass of the test object, and Ω is the frequency of the mechanical susceptibility, and c is the speed of light. The combined effect of these two independent quantum noise sources results in total quantum noise that limits the sensitivity of the detection system:

$$\overline{S}_{\text{tot}} = \overline{S}_{\text{SN}} + \overline{S}_{\text{RPN}} = \frac{\hbar c^2}{2\omega_0 P} + \frac{\hbar \omega_0 P}{m^2 \Omega^4 c^2}. \tag{1.48}$$

These two uncorrelated quantum noise sources can be transferred into the relative strain $h(t) = \frac{\delta L(t)}{L}$ in a conventional Michelson interferometer, such as $\frac{\delta L(t) \sim 10^{-19}}{L \sim 4000} \sim 10^{-22}$ depicted in Fig.1.9 (a) (where the radiation pressure effect is considered twice for the differential mode of interferometer output [24, 25]. They together establish a lower bound of the total noise at each given optical power, as shown in Fig.1.9 (b) (blue curves), increasing the light power reduces the shot noise but enlarges the radiation pressure noise. The minimal noise point is reached with equal contributions of measurement imprecision and radiation pressure noise to the total quantum noise. Consequently, there exists an optimal power level for achieving maximum strain sensitivity (minimized quantum noise) at each frequency, defining the Standard Quantum Limit (SQL) (royal blue curve). These constraints set a theoretical boundary that classical sensors cannot surpass, but which quantum sensors aim to overcome. Thus, we can establish an ultimate lower bound independent of the optical power across the detection

| | Parameters for GW configurations | |
Parameter	Notation	Value
Mirror mass, kg	M	40
Arm length, km	L	4
Laser wavelength, nm	λ_p	1064
Optical power in each arm, MW	P_c	(0.5, 5, 50)
Power transmissivity (input mirror)	T	(0.014, 0.054)
Effective detector bandwidth, Hz	γ	(260, 1000)

Table 1.11: Parameters used for modeling the strain sensitivity of the gravitational wave detector throughout this thesis

bandwidth[4].

$$h_{\mathrm{SQL}} = \sqrt{\frac{1}{L^2}S_{\mathrm{SN}} + \frac{4}{L^2}S_{\mathrm{RPN}}} \geq \sqrt{\frac{4\hbar}{m\Omega^2 L^2}}. \tag{1.49}$$

In tab.1.11, the parameters used to numerically simulate the quantum noise and strain sensitivity for gravitational wave observatories are shown. These parameters were adapted based on a review paper by Khalili [ref] and detuned EPR entanglement paper [26]. These parameters will be used throughout this thesis. In the next chapter, we will explore various quantum techniques designed to surpass the Standard Quantum Limit (SQL) and achieve quantum-enhanced detection sensitivity.

1.6   Thesis overview

Before moving to the next chapter on quantum-enhanced measurement, allow me to present a brief overview of the thesis structure. The aim of this thesis is to demonstrate broadband quantum noise reduction techniques by combing EPR-entangled light and an atomic spin oscillator prepared in a negative reference frame.
This thesis is divided into three parts:

1. **Theoretical Background**: Introduced in Chapter 1,2, and 3.

2. **Experimental Setup and Calibration Techniques**: Detailed in Chapter 4, 5, and 6, focusing on the atomic spin system.

3. **Hybrid Quantum System and Conclusions**: Discussed in Chapter 7 and 8, covering conditional squeezing of entangled light and collective

---

[4]SQL will changes to $\sqrt{\frac{8\hbar}{m\Omega^2 L^2}}$ with cavities

atomic spin oscillators, along with numerical simulations of frequency-dependent squeezed source for the joint measurement of the hybrid system.

In more details:

Chapter 1: Introduces quantum noise, focusing on quantum backaction and shot noise in laser-based weak force measurements. This chapter discusses how quantum noise sets the standard quantum limit, which prevents the improvement of measurement sensitivity, such as in gravitational wave observatories.

Chapter 2: Covers various quantum engineering techniques to reduce quantum noise, such as variational readout and frequency-dependent squeezed vacuum, achieved by a detuned filter cavity or utilizing the interferometer as a filter cavity with detuned EPR-entangled pairs. It also explores how an atomic spin oscillator prepared in an effective negative mass reference frame can achieve broadband quantum noise reduction.

Chapter 3: Provides the theoretical background for cesium atoms used to prepare the collective atomic spin oscillator. It introduces the input-output relations for light-spin interaction and the figure of merit parameter, quantum cooperativity, to quantify the dominance of quantum backaction that will be used for quantum noise reduction.

Chapter 4: Describes the experimental setup for preparing the spin oscillator.

Chapter 5: Discusses the thorough calibration of the atomic spin system, including measurement readout rate, decoherence, atomic thermal noise, and broadband noise. The spin quantum cooperativity is cross-validated with the observation of ponderomotive squeezing of the probe light.

Chapter 6: Presents technique improvements and explore additional atomic alignment responses at ultra-high frequencies, maintaining the dominance of quantum backaction evidenced by ponderomotive squeezing down to the acoustic frequency range.

Chapters 7 and 8: Conclude the thesis by demonstrating the theoretical prediction of the frequency-dependent EPR-entangled source, optimized using the Wiener filter gain within the combined hybrid system. Additionally, future steps and our very recent experimental achievements are discussed.

GWD Quantum Theory

2.1 Quantum noise in GW interferometer

In the previous chapter, we introduced the quantum noise as one of the dominant noise sources within the GW detection bandwidth, establishing the standard quantum limit (SQL) prevents further sensitivity improvements. This chapter aims to theoretically model these quantum noises in two practical GW detector configurations : the conventional free mass and tuned Fabry-Pérot interferometer. More importantly, we will explore several quantum-enhanced approaches that can potentially help us to surpass this standard quantum limit.

2.1.1 I/O relations for simple Michelson Interferometers

We begin by revisiting the simple Michelson interferometer discussed in Fig.1.9 of the previous chapter . Here, we provide a theoretical model to describe the input-output relationship for a GW detector. The transformation, also known as the input output relation of a conventional interferometer, can be written in the general form as [27]:

$$
\begin{pmatrix} \hat{b}_c(\Omega) \\ \hat{b}_s(\Omega) \end{pmatrix} = \underbrace{e^{2i\beta_m} \begin{pmatrix} 1 & 0 \\ -\kappa(\Omega) & 1 \end{pmatrix} \begin{pmatrix} \hat{a}_c(\Omega) \\ \hat{a}_s(\Omega) \end{pmatrix}}_{\text{Quantum noise}} + \underbrace{e^{i\beta_m} \sqrt{2\kappa(\Omega)} \begin{pmatrix} 0 \\ 1 \end{pmatrix} \frac{h}{h_{SQL,m}}}_{\text{GW signal}},
$$

$$(2.1)$$

where $\hat{a}_{c,s}$ and $\hat{b}_{c,s}$ are the input and output of the amplitude and phase light quadratures, respectively. The variable h is the gravitational wave strain amplitude, and h_{SQL}^m represents the free mass standard quantum limit (SQL) in terms of strain sensitivity for a simple Michelson interferometer. When the interferometer operates in a dark fringe, the gravitational wave signal manifests solely in the phase quadrature of the output light. The SQL for a simple Michelson is

expressed as :

$$h_{SQL,m} = \sqrt{\frac{4\hbar}{m\Omega^2 L^2}}, \quad \beta_m = \arctan\left(\frac{2\Omega L}{c}\right), \quad \kappa = \frac{4P_0\omega_0}{mc^2\Omega^2}. \qquad (2.2)$$

Here, β_m is the round-trip phase accumulated on the laser sideband frequency, and κ denotes the optomechanics coupling factor. This factor is crucial in transferring vacuum quantum noise in the amplitude quadrature from the dark port of beam splitter into the interferometer as radiation pressure noise [28], a phenomenon that is predominant at low frequencies and depends on the laser power P_0, mass of the mirrors m and the susceptibility of the end mirrors. Additionally, vacuum fluctuations remain in the phase quadrature of the output field and limit the GW strain sensitivity as quantum shot noise. The strain sensitivity, defined as the smallest GW signal that an interferometer can measure across the detection bandwidth, is determined by the ratio of the total output quantum noise to the gravitational wave signal transfer function. Assuming the Power Spectral Density (PSD) of the vacuum noise in a single sideband picture is unitary, i.e., we only consider Gaussian quantum state of light[23], the PSD of the quantum-noise limited strain sensitivity for a simple Michelson interferometer (in h normalization [16]) can be expressed as follows (Here, I use κ to represent the optomechanical coupling factor for a free-mass $\kappa(\Omega)$ and K(Ω) for a tuned Fabry-Pérot interferometer:

$$\overline{S}_h^m = \frac{h_{SQL,m}^2}{2}\left(\frac{1}{\kappa(\Omega)} + \kappa(\Omega)\right). \qquad (2.3)$$

2.1.2   I/O relations for Fabry –Pérot Michelson

The sensitivity of a gravitational wave detector can be enhanced by increasing the circulating laser power within the interferometer's arms. This can be achieved, for example, by inserting Fabry-Perot (FP) cavities within the interferometer's arms to significantly boost the circulating power, as presented in Fig.2.1 (a). The input-output relation for the FP-Michelson (also known as tuned) interferometer is very similar to conventional Michelson:

$$\begin{pmatrix} \hat{b}_c(\Omega) \\ \hat{b}_s(\Omega) \end{pmatrix} = e^{2i\beta} \underbrace{\begin{pmatrix} 1 & 0 \\ -K(\Omega) & 1 \end{pmatrix}}_{\text{Quantum noise}} \begin{pmatrix} \hat{a}_c(\Omega) \\ \hat{a}_s(\Omega) \end{pmatrix} + e^{i\beta}\sqrt{2K(\Omega)}\begin{pmatrix} 0 \\ 1 \end{pmatrix}\frac{h}{h_{SQL}},$$

$$(2.4)$$

where [29]:

$$K(\Omega) = \frac{16\omega_0 P_0}{mLc}\frac{2\gamma}{\Omega^2(\Omega^2 + \gamma^2)}, \quad \gamma = \frac{Tc}{4L}, \quad \beta(\Omega) = \arctan\left(\frac{\Omega}{\gamma}\right). \qquad (2.5)$$

28
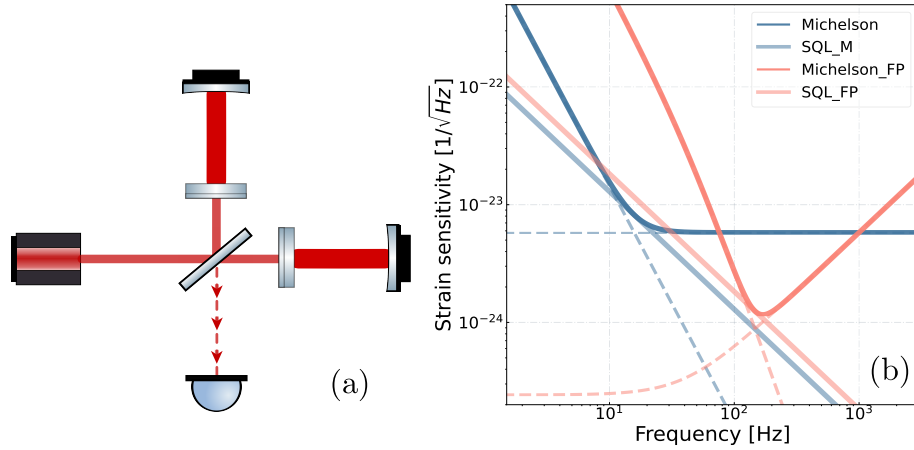
Figure 2.1: Comparison of strain sensitivity: conventional Michelson vs. Fabry-Perot (Tuned) Michelson. (a) By inserting Fabry-Perot (FP) within the interferometer arms, the circulating power can be significantly increased. (b) In the tuned Michelson interferometer, the signal sensitivity is notably enhanced by the FP cavities (illustrated by the red curve), compared to the conventional interferometer (shown by the blue curve). However, this improvement results in an increased standard quantum limit (SQL) and a reduced detection bandwidth. This reduction is due to the rolling up of shot noise and radiation pressure noise beyond the cavity bandwidth, affecting both low and high frequency ranges.

In this context, γ represents the half-width-half-maximum bandwidth of the arm cavities, β now is the phase accumulated within the arm cavities, and K is the new optomechanical coupling factor (kimble factor). The incident light, initially with uncorrelated phase and amplitude noise, has its amplitude noise ($\hat{a}_c$) impacting the momentum of the test mass mirror through the off-diagonal term in the matrix. This noise will later evolves into position noise of the mirror and project into the phase quadrature ($\hat{a}_s$) of the output light. In the specific case of phase quadrature readout out, $\phi_{LO} = \pi/2$, the expression simplifies as follows:

$$\overline{S}^h = \frac{h_{\mathrm{SQL}}^2}{2}\Big[\frac{1}{K(\Omega)} + K(\Omega)\Big] \geq h_{\mathrm{SQL}}^2 \equiv \overline{S}_{SQL}^h. \tag{2.6}$$

The standard quantum limit is now elevated by a factor of $\sqrt{2}$ compared to the previous configuration:

$$h_{SQL} = \sqrt{\frac{8\,\hbar}{m\Omega^2 L^2}}. \tag{2.7}$$

Fig.2.1 (b) illustrates the resonant enhancement of the strain sensitivity with FP cavities (depicted by the red curves) in comparison to the conventional Michelson interferometer (shown by the blue curves). The shot noise is reduced, but there is an increased radiation pressure noise due to the enhanced circulating power inside the arm cavities. However, both the strain sensitivity, and the noises, including

29

shot noise and radiation pressure noise, exhibit a significant roll-up beyond the cavity's bandwidth, affecting both the low and very high spectral frequency.

2.1.3 Ponderomotive squeezing due to Quantum back-action

When we consider the impact of the gravitational interferometer on the output state of light. An interesting reinterpretation emerges regarding the optomechanical transfer matrix as presented in Eq.(2.4). This matrix can be expressed in terms of the previously defined squeeze and rotation operators, thus the transfer matrix $\mathbf{T}$ can be mathematically represented as [30–32]:

$$\hat{b} = \mathbf{T} \cdot \hat{a} = e^{2i\beta} \mathbf{R}[\phi_{pond}] \mathbf{S}[r_{pond}] \mathbf{R}[\theta_{pond}] \hat{a}, \tag{2.8}$$

$e^{2i\beta}$ is the phase accumulated from the interferometer, $\mathbf{R}$ remains the rotation matrix and $\mathbf{S}$ is identified as the squeezing matrix (named as ponderomotive squeezing). This ponderomotive squeezing is characterized by the factor r_{pond}, squeezing quadrature angle ϕ_{pond} and rotation angle θ_{pond}:

$$e^{r_{\text{pond}}} = \sqrt{1 + \left(\frac{K(\Omega)}{2}\right)^2} + \frac{K(\Omega)}{2}, \tag{2.9}$$

$$\phi_{\text{pond}} = \frac{\pi}{2} + \theta_{\text{pond}} = -\frac{1}{2}\arctan\left(\frac{K(\Omega)}{2}\right) - \frac{\pi}{4}. \tag{2.10}$$
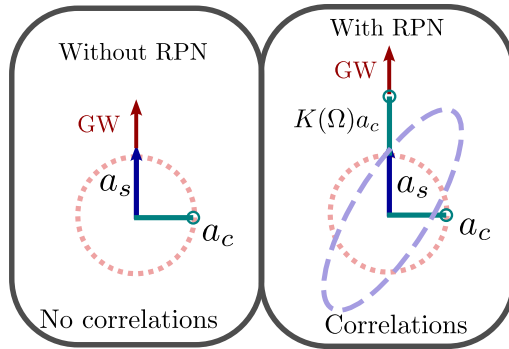
Figure 2.2: Generation of quantum correlation induced by the radiation pressure noise. In both the amplitude and phase quadrature of light, uncorrelated shot noise is present. The quantum back-action effectually transmits amplitude fluctuations of light to the phase quadrature, where the gravitational wave signal resides, through interacting with a suspended mirror, thereby generating quantum cross-correlations between these two quadratures. The ponderomotive squeezing is depicted by the purple noise ellipse, emerging when two light quadratures are mixed at the output. Both the squeezing factor and squeezing angle are modified by the frequency-dependent optomechanical factor $K(\Omega)$.

In contrast to the frequency-independent squeezing produced by parametric down

conversion, the ponderomotive squeezing effect arises from the fluctuating radiation pressure due to the amplitude quantum noise of light on the suspended test mass mirrors. This interaction subsequently causes additional phase fluctuations through the ponderomotive nonlinearity, as depicted in Fig.2.2. This additional fluctuation exhibits a frequency-dependent gain (various degrees of anti-squeezing for different sideband frequencies) and rotation, both modified by the optomechanical coupling factor $\mathbf{K}(\Omega)$. At higher frequencies, beyond the range of optomechanics interaction, the output quantum noise in phase quadrature is only dominated by the vacuum fluctuations. Such ponderomotive squeezing can be observed when these two quadrature are mixed during the measurements, such as homodyne detection or in detuned cavities.

This significant aspect of how the quantum backaction noise, resulting in the ponderomotive squeezing, plays a crucial role in engineering the quantum noise with the injection of squeezed state. This rotation also highlights why a frequency-dependent squeezing injection is important for achieving broadband quantum noise suppression, instead of just employing a phase-squeezed light in the read-out port.

2.2 Sub-SQL with the art of quantum noise engineer

2.2.1 Quantum noise cancellation with cross-correlation (variational readout)

Previously, we have discussed the standard quantum limit (SQL) that exists due to the independent contributions of shot and back action noise to the total quantum noise in the phase quadrature of probe light, where the gravitation wave signal resides, however, if we can smartly engineer these two types of quantum noise to induce a destructive quantum interference through the cross-correlation. This strategy might enable us to surpass the standard quantum limit.

$$\overline{S}^h = \overline{S}^h_{\text{SN}} + \overline{S}^h_{\text{BAN}} - 2\overline{S}^h_{\text{SN}-\text{QBAN corr}}. \tag{2.11}$$

One approach involves utilizing the correlation from the ponderomotive effect by deviating the detection quadrature from the pure phase quadrature (a method also known as variational readout). The power spectral density of the strain sensitivity, involving different detection angle, is now written as [16, 33]:

$$\overline{S}^h = \frac{h^2_{\text{SQL}}}{2}\left[\frac{1}{K(\Omega)} + \frac{[K(\Omega) - \cot\phi_{LO}]^2}{K(\Omega)}\right]. \tag{2.12}$$

As illustrated in Fig.2.3, in an ideal losses scenario, detection from the pure phase quadrature can lead to a narrower strain sensitivity (as shown in yellow curves).

More significantly, this approach can lead to detection with reduced quantum noise, even below the SQL at certain sideband frequencies due to the interference of the correlated quantum noise.

The variational readout approach can be understood as the mixed homodyne detection. It enables the original, uncorrelated back-action and shot noise in the phase quadrature to interfere with the shot noise in amplitude quadrature. Since both the back-action noise and shot noise in amplitude quadrature stem from the same noise source, this can result in destructive interference. Despite the partial loss of gravitational signal, by strategically choosing the detection spectrum frequency and homodyne angle, one can still enhance the signal strain sensitivity below SQL as shown in Fig.2.3 (b). Moreover, the reduction in signal strain can be compensated by employing higher circulating laser power. When
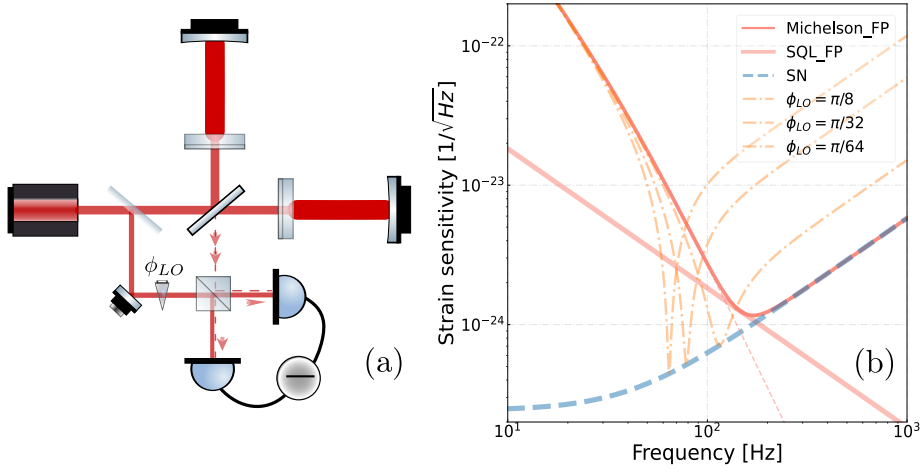
Figure 2.3: Quantum noise reduction with variational readout. (a) Quantum noise reduction is achieved by mixing the two light quadratures through the homodyne detection angle ϕ_{LO}. (b) In the absence of optical losses, strain sensitivity can surpass the SQL by strategically selecting the detection homodyne angle, thereby achieving maximum strain sensitivity at a specific sideband frequencies (yellow curves) (also known as post-filtering). When the detection angle angle is optimized for each sideband frequency, the quantum backaction quantum can potentially be removed completely, leaving the strain sensitivity only limited by the shot noise in the phase quadrature (blue curve).

the frequency dependent homodyne angle is optimized (where $K(\Omega) = \cot \phi_{LO}$), a lossless variational readout scheme can reduce the total quantum noise below the SQL across the entire back action dominant regime. The system 's limitation is primarily the residual shot noise in the phase quadrature, as expressed by :

$$\overline{S}^h = \frac{h_{\mathrm{SQL}}^2}{2} \Big[\frac{1}{K(\Omega)} \Big]. \tag{2.13}$$

This approach can be implemented by inserting a post-filter cavity at the interferometer output. However, the high sensitivity of both correlation and gravitational wave signal to optical loss makes this variational readout approach technically

demanding, especially in terms of optical loss management and phase control precision of the post-filtering cavity. More details are discussed in page 105 of Khalili's review paper [30] and page 9 of Valerii's thesis [33].

2.2.2 Quantum noise reduction with squeezed state injection

From the input-output transformation matrix of GW interferometry, it is clear that vacuum fluctuations enter the dark port of interferometer, thereby limiting the signal strain sensitivity due to quantum noise. By replacing the input vacuum fluctuation with a noise reduced quantum state, such as squeezed vacuum state. The output quantum noise of light after the interferometer can be effectively modified or even mitigated with the injection of an appropriate squeezed state. Assuming we are measuring the phase quadrature of light ($\phi_{LO} = \pi/2$), the quantum noise spectral density can be expressed as follows [30]:

$$\overline{S}^h(\Omega) = \frac{h_{\mathrm{SQL}}^2}{2K(\Omega)} \left[e^{-2r} \left(\sin\phi_{sq} - K(\Omega)\cos\phi_{sq} \right)^2 + e^{2r} \left(K(\Omega)\sin\phi_{sq} + \cos\phi_{sq} \right)^2 \right],$$

$$(2.14)$$

where r is the squeezing factor, and ϕ_{sq} is the squeezing angle. The strain sensitivity of Fabry-Perot (tuned) gravitational wave interferomter with a squeezed state injection, as illustrated in Fig.2.4, can be improved significantly. Fig.2.5 illustrates simple schematic representations of quantum noise engineering. For a squeezed injection angle $\phi_{sq} = \pi/2$, there is a reduction in shot noise within phase quadrature, without actually boosting the circulating power which could cause heat and deformation in the test mass mirrors. The quantum noise spectral density under this squeezed angle is now given by:

$$\overline{S}^h = \frac{h_{\mathrm{SQL}}^2}{2} \left[\frac{1}{K(\Omega)} e^{-2r} + K(\Omega)e^{2r} \right]. \qquad (2.15)$$

This squeezed state injection results in a reduced shot noise at high frequencies while elevated radiation pressure noise at low frequencies, as shown in Fig.2.4 (c, blue dashed curve). Conversely, selecting a squeezing angle at $\phi_{sq} = 0$ (tomato dashed curve) decreases the radiation pressure noise at the expense of the increased shot noise. Both scenarios are equivalent to change the circulating power inside the interferometer and thus only moving the sensitivity curve along the tuned SQL curve. An interesting case arises with $\phi_{sq} = \pi/4$ (as shown in purple curve), where both the shot noise and radiation pressure noise increase at very low and high sideband frequencies. However, the strain sensitivity can be improved and even surpass the SQL in a narrow band range, thanks to the quantum correlations induced by the injected squeezing light. This happens at frequencies where the contribution of both quantum noises nearly equalize, allowing efficient destructively interference.

To achieve a broadband reduction of quantum noise across the detection band-
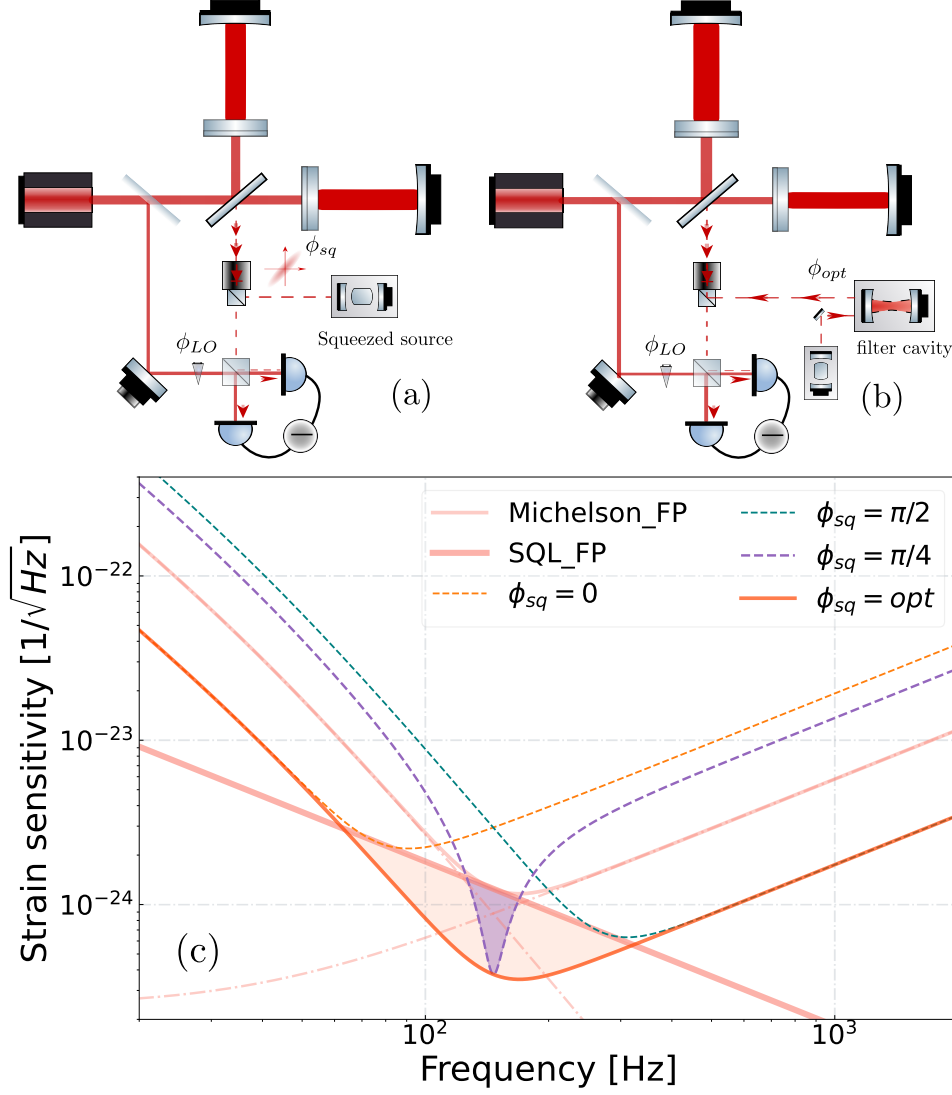
Figure 2.4: Strain sensitivity of tuned FP-interferometer with squeezed state injection at different squeezing angle. (a) The vacuum fluctuation at the interferometer's dark port is injected with a vacuum squeezed state, characterized by a fixed squeezed angle (ϕ_{sq}). (b) The squeezing angle can be modified in a frequency dependent manner through the reflection of a filter cavity. (c) The panel in the bottom illustrates the quantum noise curves with -10dB (r = 1.15) squeezed vacuum state injection at different squeezing angles. Notably, an optimized frequency dependent squeezed angle yields a broadband sensitivity improvement (depicted in orange curve), and this enhancement of strain sensitivity below the SQL is marked with orange area.

width, employing a frequency-dependent squeezed state is essential. At high frequencies, $\phi_{sq} = \pi/2$ minimizes the shot noise, while $\phi_{sq} = 0$ reduces the radiation pressure noise at low frequencies. The optimized angle for minimal quantum noise across a broadband frequencies are expressed as [33]:

$$\phi_{sq,opt} = \text{arccot}(-K(\Omega)), \tag{2.16}$$
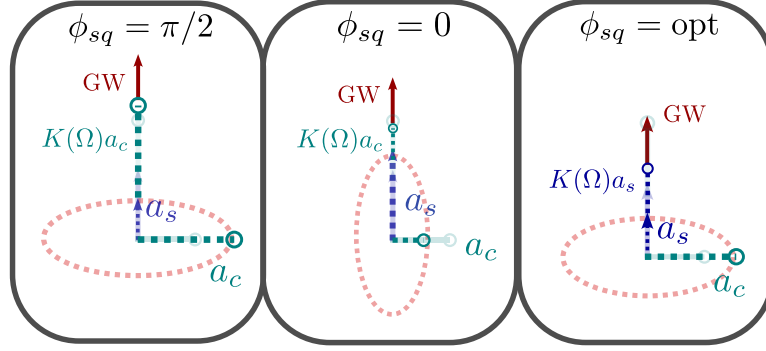
Figure 2.5: Engineering quantum noise with various squeezed vacuum state injections. In the phase quadrature of probe light where harbours the GW signal, a reduction in shot noise in phase quadrature (indicated by a blue arrow) is achieved using a phase squeezed vacuum ($\phi_{sq} = \pi/2$). This approach, however, results in anti-squeezing in the amplitude quadrature (denoted by a enlarged green arrow), consequently amplifying the back-action noise $\mathrm{K}(\Omega)\hat{a}_c$. Conversely, the injection of squeezed state with $\phi_{sq} = 0$ leads to the opposite effect. In an optimized frequency dependent squeezing scenario, a filtering cavity with an optimized phase allow both the shot and back-action noise to originate from the optical phase quadrature, by intergrating this with phase squeezed state injection, this scheme can in principle mitigate both shot and back-action noise at each sideband frequency.

which results in the optimized strain sensitivity with frequency-dependent squeezed vacuum injection:

$$\overline{S}^h = \frac{h_{\mathrm{SQL}}^2}{2}\Big[\frac{1}{K(\Omega)} + K(\Omega)\Big]e^{-2r}. \tag{2.17}$$

In reality, the frequency dependent squeezing can be achieved by sending the squeezed vacuum field through filter cavities, also called pre-filtering. There specifically designed Fabry-Perot cavities, tailored with appropriate bandwidth and very well-control losses to prevent degradation of squeezing, are made for this purpose, as detailed in the referenced work [34, 35], the optimal frequency dependent rotation can be expressed as follows:

$$\phi_{opt}(\Omega) = \mathrm{arccot}\left[\frac{2\delta_f\gamma_f}{\gamma_f^2 - \delta_f^2 + \Omega^2}\right], \tag{2.18}$$

where γ_f is the bandwidth (HWHM) of the filter cavity and δ_f is the detuning of the input quadrature relative to the cavity resonance. The role of the filter cavity is to substitute the shot noise in amplitude quadrature of light, denoted as $(K(\omega)\hat{a}_c)$ with the corresponding noise from the phase quadrature($K(\omega)\hat{a}_s$). Consequently, both the shot noise and radiation pressure noise originate from the same noise sources $(a_s + K(\omega)\hat{a}_s)$. As demonstrated in the introduction chapter regarding the frequency dependent squeezed state in the phasor picture, these rotational effects are attributed to the noise in the carrier field's upper and lower

sidebands, which acquire different phase shifts upon reflecting from a detuned filter cavity as depicted in Fig.2.6. Subsequently, an optimized frequency-dependent squeezed state, characterized by tailored cavity bandwidth and detuning, is injected to the dark port of interferometer. This process is instrumental in achieving the broadband strain sensitivity enhancement, as shown in Fig.2.4 (c).

However, ideal frequency dependent squeezing are not easy to produce. The requisite number of filter cavities is determined by the detection bandwidth of gravitational interferometer [30]. The current interferometer bandwidth requires filter cavities with lengths on the order of 100 meters [36], meanwhile, when the detector is quantum noise limited over the entire detection band, additional rotations of the squeezing ellipse can appear due to the detuned interferometer cavity and optical spring resonance. In such scenarios, at least two filter cavities are required to produce the optimal frequency dependent squeezing angle. Furthermore, considering the vulnerability of squeezed states to the optical losses, it becomes imperative to minimize these losses with better optics coating and an ideal spatial mode match of the filter cavity. A good phase noise control system is also important to reach the target sensitivity improvement [37].
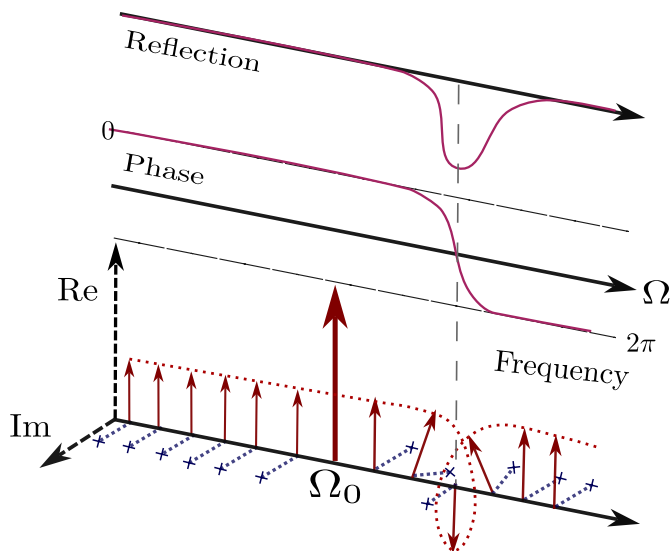
Figure 2.6: Observation of frequency-dependent quadrature rotation arising from the reflection off a detuned filter cavity. In the two-photon sideband phasor representation, upper sideband photons at each frequency accumulate distinct phases due to the reflection from a detuned filter cavity. This accumulation, combined with the photons in low sideband, results in the frequency-dependent rotation of the squeezing ellipse.

Moreover, in an ideal scenario where the losses can be effectively managed, the variational readout method could be employed to fully suppress the quantum backaction noise. Following this, the injection of phase squeezed vacuum would be sufficient to attenuate the shot noise, thereby improving the strain sensitivity to the level depicted by the yellow curve in Fig.2.7. it's strain sensitivity can now

be expressed as [34]:

$$\overline{S}^h = \frac{h_{\mathrm{SQL}}^2}{2}\big[\frac{1}{K(\Omega)}\big]e^{-2r}. \tag{2.19}$$

2.2.3 Conditional quantum noise cancellation with detunned EPR entanglement
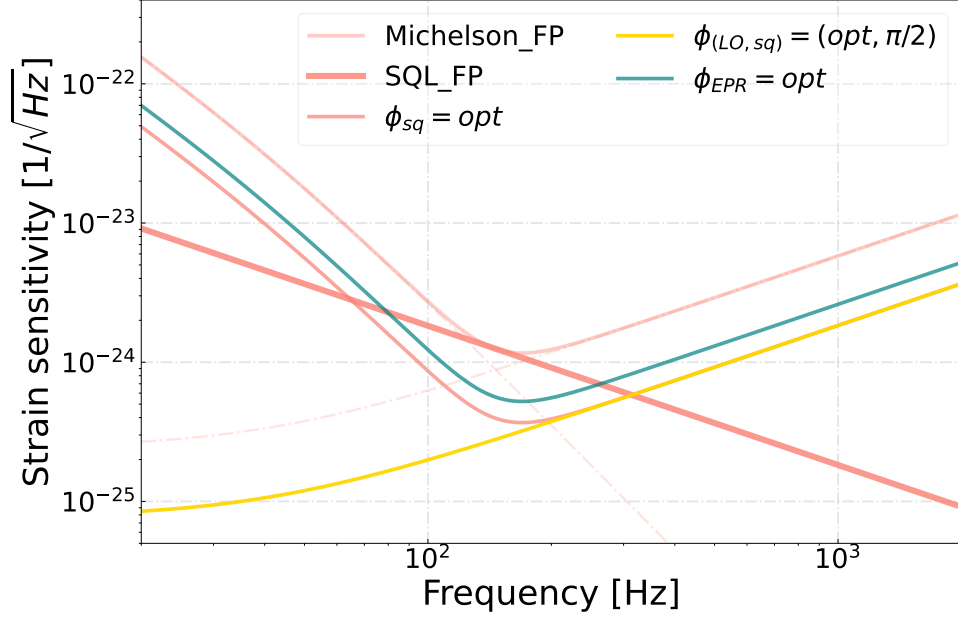
Figure 2.7: Quantum noise reduction with squeezed variational readout and detuned EPR entanglements scheme. Phase-squeezed vacuum injection paired with variational readout (yellow curve) can eliminate back-action noise under ideal conditions. Nondegenerate EPR entangled pairs used for conditional squeezing (green curve) achieve comparable strain sensitivity improvements, with a 3dB penalty. Traditional frequency-dependent squeezing (tomato curve), which is twice as effective as the EPR entangled pairs, is provided for reference. All comparisons are made with an injected squeezing level of 10dB (r = 1.15).

In 2017, Ma.et al. [29] introduced a different approach to achieve broadband quantum noise reduction below the SQL without relying on multiple filtering cavities. Instead of employing additional filter cavities to rotate the squeeze angle, this method uses the gravitational wave interferometer as a filter cavity to perform the require frequency dependent rotation. In contrast to the deployment of a single-mode squeezed state, where the center frequency aligns with the carrier frequency of interferometer, this proposal utilize the EPR entangled pairs. In this approach, while the signal field resonates with interferometer, the idler field, on the other hand, is slightly detuned by a few MHz, encountering a frequency-dependent phase shift contingent upon the relative detuning Δ and the bandwidth of the interferometer. As previously discussed, the quantum cor-

relation within these entangled EPR pairs enables the joint measurement and can create a conditional squeezing. This mechanism allows for the reduction of the signal uncertainty (fluctuations) by appropriately measuring the quadrature of the idler beam, and vice versa. The strain sensitivity for the detuned EPR proposal with optimized conditional measurement (shown in Fig.2.7) (teal curve) can be expressed as:

$$\overline{S}^h_{EPR} \approx \frac{h^2_{\text{SQL}}}{2\cosh 2r}\left[\frac{1}{K(\Omega)} + K(\Omega)\right]. \tag{2.20}$$

In the scenarios of strong correlation, the improvement factor $\cosh 2r \approx e^{2r}/2$, exhibits 3dB less than the single-mode squeezed vacuum injection due to the lack of the correlation between both the upper and lower sidebands of the signal and idler fields,. This proposal without necessitating of additional filter cavities and would be even compatible with detuned GW interferometers [38].

However, in practical applications, such scheme achieves sub-optimal suppression, as the interferometer, functions merely as a single filter cavity and thus does not yield the perfectly optimal phase for the idler beam across the entire detection bandwidth. Moreover, this scheme requires two readout channels, which imposes greater demands on minimizing the output losses in the detection systems. In 2020, two parallel groups successfully demonstrated this concept through the proof-of-principle experiments employing 1m filter cavities [39, 40]. Their experiments presented the necessary frequency dependent rotation on idler field, and the quantum noise impacting on the signal field at sub MHz side-band frequency was successfully mitigated. This reduction is conditional on the appropriate measurement of noise in idler field with additional 3dB penalty as anticipated. However, they couldn't adjust the relative weight between the two entangled arms due to system limitations. Furthermore, they illustrated that selecting suitable idler detuning could potentially counteract the additional phase shift when the signal recycling cavity operates in the detuned interferometer configuration. Despite the inherent 3dB penalty, the relaxing of need for additional expensive filter cavities make this approach as a highly practical option.

2.3 Quantum noise cancellation with hybrid negative mass oscillator

In the previous section, we discussed how the quantum noise in the gravitational wave interferometers can be reduced using the quantum correlations in non-classical states of light, such as frequency-dependent squeezed vacuum or detuned Einstein-Podolsky-Rosen (EPR) entanglement.

In this section, we will explore a relatively different approach aimed at improving the GW interferometer sensitivity. This method involves coupling the interferom-

eter to another quantum system. When the probe light simultaneously interacts with these new hybrid systems, a exciting new effect can be observed if this new quantum system is prepared in an effective negative-mass reference frame. It introduces radiation pressure noise but with an opposite sign relative to the test mirrors in GW detector. This hybrid setup allows for the suppression of the quantum back-action noise in the interferometer by reshaping its optomechanical response through the new reference system. Consequently, this new hybrid approach can counteract the ponderomotive squeezing effect, which is induced by light radiation pressure noise, without degrading the detection system's response to the GW signal as the variational readout technique does. Such an enhancement in sensitivity can be achieved without the necessity for both quantum squeezed states and filter cavities.

The negative-mass system can be realised by inserting a negative dispersion medium, either before or after the interferometer. If the optomechanical susceptibility of this negative mass oscillator is precisely aligned with the response transfer function of light radiation pressure force on the test mass mirrors in the GW detector, but with an opposite sign across the detection frequency band, then the back-action noise of the two systems can mutually cancel. This can effectively reverse the ponder-motive squeezing from the test mass mirrors, leading to so called backaction free measurement. In this scenario, the original fundamentally non-commuting quadratures of position and momentum of the text mass mirror, denoted by $[X(t), P(t)] = i$, are replaced by an entangled hybrid system with a commuting combination of two variables $[X(t) - X_{neg}(t), P(t) + P_{neg}(t)] = 0$. This allows for arbitrary precision in measuring the relative position $X(t) - X_{neg}(t)$ or momentum $P(t) + P_{neg}(t)$ of the two system oscillators, as referenced in [41]. In other words, this approach enables a quantum noiseless trajectory of the mean relative position of the two combined hybrid system at any measurement time t.

$$X(t) - X(t)_{neg} = X(0) - X(0)_{neg} + t[P(0) + P(0)_{neg}]/m. \qquad (2.21)$$

Therefore, for force signal such as gravitational wave that can disturb the relative position $(X(t) - X_{neg}(t))$ at time t, these hybrid systems, in principle, are capable of sensing such signals with a precision surpassing the SQL, free from the constraints of probe induced quantum back-action noise. An exciting aspect of these hybrid systems is is the possibility of operating two systems remotely, with atoms placed at a considerable distance from the mechanical system.

One experimental approaches to creating an effective negative mass oscillator involves interaction with a collective atomic spin oscillator [42], the resonance frequency of which is tunable via a bias magnetic field. An experiment demonstrating the reduction of back-action in a membrane cavity optomechanics system, oscillating at MHz sideband frequency, was conducted by Muller in 2018 [43]. Furthermore, the proof of EPR entanglement between these two hybrid sys-

tems is documented in the later paper [44], enabling the prediction of mechanical membrane system trajectories within the reference frame of the atomic spin oscillator, approximately 20% below the standard quantum limit (SQL). Building upon these findings, Eugene and Khalili proposed the use of this negative mass atomic ensemble in Gravitational wave (GW) detection systems for achieving broadband quantum noise reduction across their detection bandwidth [45–47].

The atomic spin ensemble offers several unique features that are particularly advantageous for optomechanical systems like GW interferometers. In specific scenarios, particularly when considering the coupling to the internal state of atomic spins [48], the dynamics of polarization rotation of probe light, which couples to the atomic hyperfine or Zeeman spin states, can be precisely modeled using an ordinary harmonic oscillator. Both the sign and magnitude of the eigenfrequency of this effective harmonic oscillator can be adjusted via the orientation and strength of the bias magnetic field. Additionally, the Faraday rotation measurement of the spin states with light results in a quantum back-action effect similar to that of a movable mirror in optomechanics, but with a modifiable sign.

Each spin in atomic ensemble can be described by the total angular momentum vector $\hbar \times \left[\hat{F}_x, \hat{F}_y, \hat{F}_z \right]$. Imagine that this atomic ensemble is optimally pumped to the highest energy state along the x-axis and is placed in a strong bias magnetic field B aligned in the same direction. Consequently, the ensemble, consisting of N atoms, now behaves as a collective macroscopic spin, expressed as $F_x = \sum_{i=1}^{N} \hat{F}_x^i$. When the energy of this collective spin corresponds to a large positive value, $\hbar \Omega_S F_x$, where Ω_S represents the Larmor precession frequency. Relative weak excitations from the highest energy state reduce the total energy and can be effectively modeled using the effective Hamiltonian [49]:

$$\hat{H}_S = \hbar \Omega_S F_x - \frac{\hbar \Omega_S}{2} \left(\hat{X}_S^2 + \hat{P}_S^2 \right), \tag{2.22}$$

in this context, the magnitude of the mean longitudinal spin, $F_x = |\langle \hat{F}_x | \hat{F}_x \rangle|$, is significantly larger than the transverse collective spin components, $\hat{F}_y$ and $\hat{F}_z$. These two transverse components can later be mapped to effective position and momentum variables of a harmonic oscillator. It is important to note there is a minus sign associated with the momentum variables:

$$\hat{X}_S = \frac{\hat{F}_z}{\sqrt{F_x}}, \quad \hat{P}_S = -\frac{\hat{F}_y}{\sqrt{F_x}}. \tag{2.23}$$

With the standard commutation relation $\left[\hat{X}_S, \hat{P}_S \right] = i$, these variables correspond to a harmonic oscillator that exhibits a negative frequency, denoted as $-\Omega_S$. Consider a scenario where a linearly polarized probe light, aligned along the x-axis, interacts with the collective spin. This interaction occurs far from the atomic resonance frequency, where the absorption of probe light by the atoms is

almost negligible. In this context, the only effective position, $\hat{X}_S$ of the spin oscillator is read out through the Faraday interaction (or QND in our group), a topic we will elaborate on in the following chapter. In this case, the interaction Hamiltonian, which considers only the vector interaction term, can be approximated as :

$$\hat{H}_{QND} \approx \hbar g_S a_1 \hat{S}_z \hat{F}_z = \hbar \sqrt{\Gamma_s} \hat{a}_S^c \hat{X}_S, \tag{2.24}$$

In this equation, g_S represents the single atom-photon coupling rate, a_1 is the vector interaction factor of the atomic polarizability, and $\hat{S}_z$ is one of the Stokes operators of light, which can be re-expressed in terms of the cosine quadrature of the polarized light $\hat{a}_{c,S}$, as $\hat{S}_z = \hat{a}_{c,S}/\sqrt{|S_x|}$, once the LO phase is properly selected. Γ_S is known as the readout rate, which represents the interaction strength of the light-atom quadrature:

$$\Gamma_S = g_S^2 a_1^2 S_x F_x. \tag{2.25}$$

The interaction described here closely resembles the standard dispersive coupling between the light and a mechanical object. The input-output relationship for the QND measurement of the atomic oscillator in the Fourier domain [1] can be expressed as follows [20, 30, 33, 49, 50] :

$$\begin{pmatrix} \hat{b}_{c,S}(\Omega) \\ \hat{b}_{s,S}(\Omega) \end{pmatrix} = \underbrace{\begin{pmatrix} 1 & 0 \\ \Gamma_S \chi_S(\Omega) & 1 \end{pmatrix} \begin{pmatrix} \hat{a}_{c,S}(\Omega) \\ \hat{a}_{s,S}(\Omega) \end{pmatrix}}_{\text{Quantum Noise}}$$
$$+ \underbrace{\sqrt{\Gamma_S \gamma_S} \begin{pmatrix} 0 & 0 \\ \rho_S(\Omega) & \chi_S(\Omega) \end{pmatrix} \begin{pmatrix} \hat{F}_S^X \\ \hat{F}_S^P \end{pmatrix}}_{\text{Thermal Noise}}, \tag{2.26}$$

where $\hat{a}_{(c,s),S}$ denote the cosine and sine quadrature of the incident light, while $\hat{b}_{(c,s),S}$ represent the corresponding quadrature of the outgoing light. The subscript 'S' in these variables signifies the input-output relationship of light interacting with atomic spins. Additionally, $\hat{F}_S^X$ and $\hat{F}_S^P$ are defined as effective stochastic Langevin forces, contributing to the system's dynamics. In this context, it is observed that the atomic spin oscillator exhibits decay phenomena in both $\hat{X}_S$ and $\hat{P}_S$ spin quadratures, attributable to the de-excitation of collective spins. (Unlike optomechanical systems, where the oscillator's momentum undergoes decay due to velocity-dependent damping, the atomic system demonstrates a distinct set of dynamical characteristics.)

---

[1]The angular Fourier transform is used as: $F(\Omega) = \frac{1}{2\pi} \int_{-\infty}^{+\infty} f(t) e^{i\Omega t} \, dt$, where $F(\Omega)$ represents the transformation of function f(t) in frequency domain.

$$\chi_S(\Omega) = \frac{\Omega_S}{\Omega_S^2 - \Omega^2 - i\gamma_S\Omega + (\frac{\gamma_S}{2})^2}, \tag{2.27}$$

$$\rho_S(\Omega) = \frac{\frac{\gamma_S}{2} - i\Omega}{\Omega_S^2 - \Omega^2 - i\gamma_S\Omega + (\frac{\gamma_S}{2})^2}. \tag{2.28}$$

χ_S and ρ_S are the effective spin susceptibilities of the atomic spin system with γ_S representing the total spin linewidth.

It's important to note that in real experiments, the light-atom interaction is considerably more complex than this model presents. We will delve into more detailed aspects of this interaction in next chapter.

2.3.1 Quantum backaction evading with negative mass spin oscillator in sequential scheme

Inspired by the experimental demonstration referenced in [43], a hybrid system employing a negative reference frame can be realized by first allowing the probe light to interact with the negative mass atomic spin system before its injection into the main interferometer. This interferometer is used to measure the test mass mirror's displacement, induced by the gravitational wave signal as depicted in Fig.2.9 (a). The output light from the interferometer is subsequently measured using homodyne detection. In this configuration, the primary role of the negative oscillator is to reduce quantum back-action noise, as presented in Fig.2.8, where the transfer function of quantum backaction is mitigated to $|\Gamma_S\chi_S(\Omega) - K(\Omega)|$. Additionally, injecting phase-squeezed vacuum can further reduce shot noise fluctuations in the phase quadrature. While this scheme shares similarities with the frequency dependent squeezing using a filter cavity, it differs in its nonlinear ponderomotive response. In contrast to utilizing the linear, frequency-dependent phase dispersion in a detuned filter cavity to rotate the light quadratures, together with the application of quantum squeezed light specifically modifies quantum fluctuations based on the prevailing dominance of either shot noise or back-action noise. Even yielding analogous outcomes, the atomic ensemble directly impacts the interferometer's response to light's radiation pressure. This modification actively adjusts or counteracts the ponderomotive squeezing effect originating from the test mass mirrors of the interferometer.

To demonstrate the fundamental aspects of this hybrid scheme, we initially disregard optical losses in both the atomic spin system and the interferometer. Readers seeking a more comprehensive analysis of optical losses are referred to [33, 45, 46]. Additionally, the atomic system exhibits unique imperfections, such as intrinsic damping of the atomic spin oscillator, the quantum noise arising from the imaginary part of atomic susceptibility, and spin projection noise associated with the atom number fluctuations, which results in effective thermal noise. These imperfections will be incorporated into our analysis of quantum noise reduction.

Consider the simplest case of a resonance-tuned interferometer, with the detailed input-output relationship in an ideal lossless scenario described in section.2.1.2. In the sequential scheme described in Fig.2.9(a), we have $\hat{a}_{(c,s),S} = \hat{b}_{(c,s),I}$, where S, I represent the spin oscillator and interferometer, respectively. Employing the input-output relationship for both systems, we deduce the output phase quadrature $\hat{b}_{s,out}$ of light via a homodyne detection after its interaction with the two systems:

$$\hat{b}_{s,out} = \hat{a}_{s,in} + (\Gamma_S \chi_S(\Omega) - K(\Omega)\hat{a}_{c.in}$$
$$+ \left[\sqrt{K(\Omega)} \frac{h}{h_{SQL}} + \sqrt{\Gamma_S \gamma_S}(\chi_S(\Omega)\hat{F}_S^P + \rho_S(\Omega)\hat{F}_S^X) \right]. \qquad (2.29)$$

After normalizing the quantum noise with respect to the gravitational wave (GW) strain signal h, we obtain the power spectral density of the strain sensitivity in the sequential negative mass spin oscillator scheme, which is now written as:

$$\overline{S}_{seq}^h = \frac{h_{\mathrm{SQL}}^2}{2} [\underbrace{\frac{1}{K(\Omega)}}_{SN} + \underbrace{\frac{|\Gamma_S \chi_S(\Omega) - K(\Omega)|^2}{K(\Omega)}}_{QBAN} + \underbrace{\frac{\Gamma_S \gamma_S(|\chi_S(\Omega)|^2 + |\rho_S(\Omega)|^2)\sigma_{th,S}}{K(\Omega)}}_{TN}].$$
$$(2.30)$$

Here, the term γ_S is the total decoherence rate of atomic oscillator. The resonant frequency of the atomic spin oscillator Ω_S, is commonly known as the Larmor frequency. In parallel, the optomechanical coupling factor $K(\Omega)$ is defined as $\frac{4P_0\omega_0}{mc^2\Omega^2}$ for a conventional free mass interferometer and $\frac{16\omega_0 P_0}{mLc} \frac{2\gamma}{\Omega^2(\Omega^2+\gamma^2)}$ for a tuned Fabry-Perot interferometer. The power spectral density of the effective thermal bath, $\sigma_{th,S}$, is described by $\sigma_{th,S} = \langle \hat{F}_S^X(\Omega) \circ \hat{F}_S^X(\Omega') \rangle = \langle \hat{F}_S^P(\Omega) \circ \hat{F}_S^P(\Omega') \rangle = (1/2 + n_S)\delta(\Omega - \Omega')$. In the limit of narrow spin decoherence $\gamma_S \ll \Omega_S$, the susceptibilities can be approximated as $\rho_S(\Omega) \sim -i\chi_S(\Omega)$. Under this approximation scenario, the spectral density of the effective thermal bath, arising from two collective components, can be combined into the single thermal bath, with the noise spectrum represented as: $2\Gamma_S\gamma_S|\chi_S(\Omega)^2|(n_S + 1/2)$. [2] This approximation proves effective in the high side-band frequency regime, as demonstrated in [43, 44]. However, for low frequency applications, such as the quantum noise reduction in GW interferometers, it would be essential to take into account the complete susceptibility function.

In Fig.2.9, the quantum noise spectral densities for the hybrid system, compris-

---

[2]When only concentrate around the spin resonance ($\Omega \sim \Omega_S$), the above susceptibilities can be further simplified as:

$$\chi_S(\Omega) = \frac{1}{2} \frac{1}{\Omega_S - \Omega - i(\gamma_S/2)}, \; \rho_S(\Omega) \sim -i\chi_S(\Omega),$$

and the absolute squares of these equations follow a Lorentzian function.
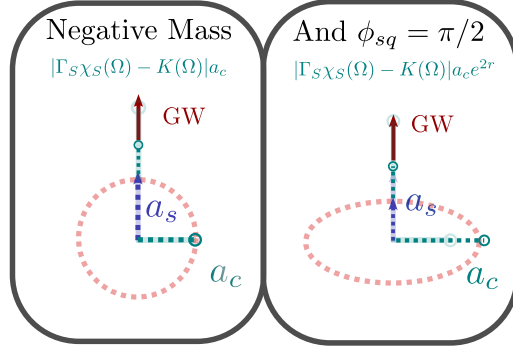
Figure 2.8: Engineering quantum noise with effective negative mass atomic ensembles. Within the phase quadrature of the output light, the quantum backaction transfer function is altered by $|\Gamma_S\chi_S(\Omega) - K(\Omega)|$. Ideally, when the two susceptibilities match perfectly such that $\Gamma_S\chi_S(\Omega) = K(\Omega)$, it becomes possible to maximally mitigate the quantum backaction noise (or ponderomotive effect). To further reduce quantum fluctuations in the phase quadrature, one simply needs to introduce phase-squeezed light. However, the injection of a squeezed state might also amplify the residual quantum backaction noise due to imperfect matching.

ing a sequential negative mass spin oscillator and a tuned interferometer, are plotted for two scenarios: without a squeezed state (green curve) and with a 10 dB phase-squeezed vacuum (blue curve). In an ideal setup, where two systems are perfectly matched, the hybrid system is primarily limited by the light's shot noise, as indicated by the yellow curve. However, imperfect cancellation due to the Fabry-Perot response instead of a free mass oscillator may compromise the quantum noise reduction efficiency. Nonetheless, significant quantum backaction noise cancellation is still observable, even falling below the standard quantum limit (SQL) at certain side-band frequencies that are unreachable by frequency-dependent squeezing. Additionally, the introduction of a squeezed state imposes more stringent matching requirements between the two system, as evidenced by the amplified quantum noise in the blue curve under the identical parameter conditions.

The strain sensitivity of the hybrid systems, when enhanced by an injection of phase squeezed state, can be expressed as follows:

$$\overline{S}_{seq}^{h} = \frac{h_{\text{SQL}}^2}{2}\Big[\frac{1}{K(\Omega)}e^{-2r} + \frac{|\Gamma_S\chi_S(\Omega) - K(\Omega)|^2}{K(\Omega)}e^{2r} + \frac{\Gamma_S\gamma_S(|\chi_S(\Omega)|^2 + |\rho_S(\Omega)|^2)\sigma_{th,S}}{K(\Omega)}\Big].$$

(2.31)

In reality, the atomic spin oscillator also exhibits intrinsic decay, introducing dissipative coupling via the imaginary part of the susceptibility function, as depicted by the green solid curve in Fig.2.10 (a). Unlike the high-Q suspension systems in GW interferometers, where the imaginary contributions are almost negligible, the imaginary part of atomic susceptibility in our case affects the matching of the two quantum systems, as shown in Fig.2.10 (b). This mismatch leads to

44
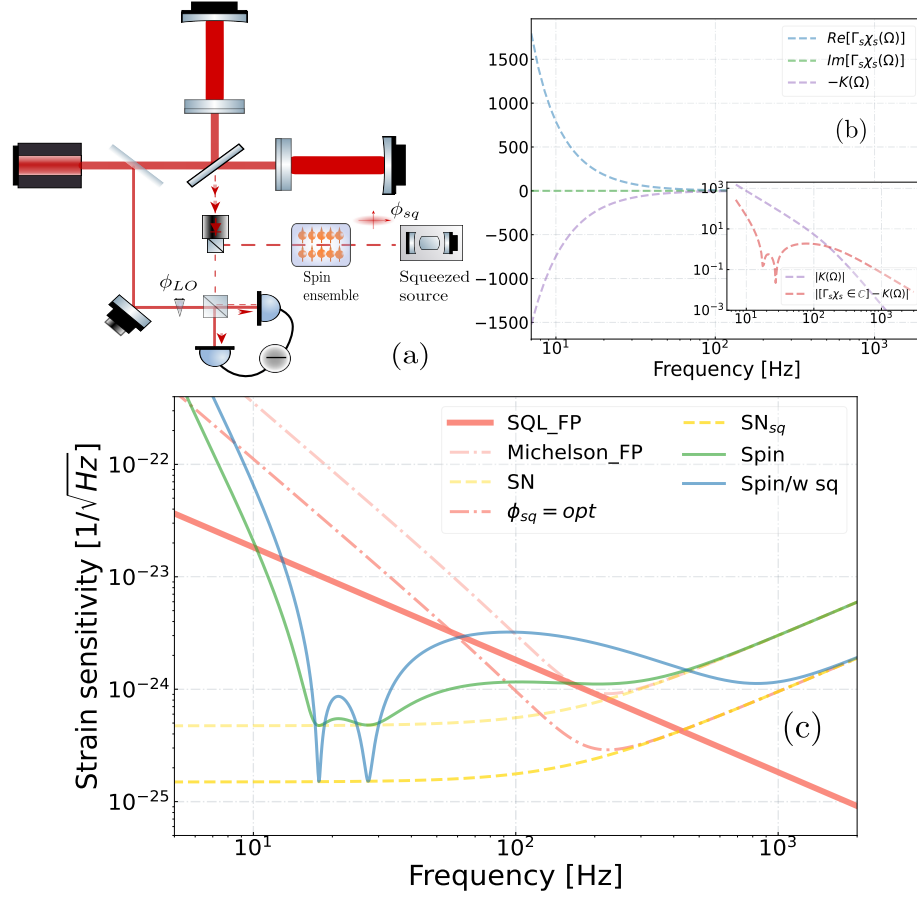
Figure 2.9: Quantum noise reduction with negative mass spin oscillator in sequential scheme. (a) Schematic of the setup for sequential measurement using a negative mass spin oscillator. (b) Susceptibility of atomic spin oscillator and optomechanical coupling factor as a function of Fourier frequency, with the absolute value of residual difference between the two displayed in the inner plot. (c) The strain sensitivity of the sequential hybrid system, excluding the atomic intrinsic decay, is shown as the green (without squeezing injection) and blue (with squeezing injection) curves. For reference, traditional frequency-dependent squeezing is shown by tomato dashed dot curve. Meanwhile, the shot noise in phase quadrature of output light, both with and without the squeezed state injection, is represented by the yellow curves. All comparisons are based on an injected squeezing level of 10dB (r = 1.15). The atomic decay: $\gamma_S/2\pi$ =0 Hz, the atomic readout rate : $\Gamma_S/2\pi = 23$ kHz, and the Larmor frequency: $\Omega_S/2\pi = 3$ Hz. Additional detailed parameters for GW interferometer are presented in the table.1.11. Since this plot, all curves are simulated with a 1000 Hz detector bandwidth.

additional quantum noise, compromising the overall quantum noise reduction, as illustrated by the blue and green solid curves in Fig.2.10 (c) . The reduction of strain sensitivity becomes evident when adding a 2 Hz intrinsic decay. Furthermore, including the atomic projection (and thermal) noise further degrades the performance of the quantum noise reduction in the gravitational wave frequency regime, as evidenced in Fig.2.10 (c). While the quantum back noise from
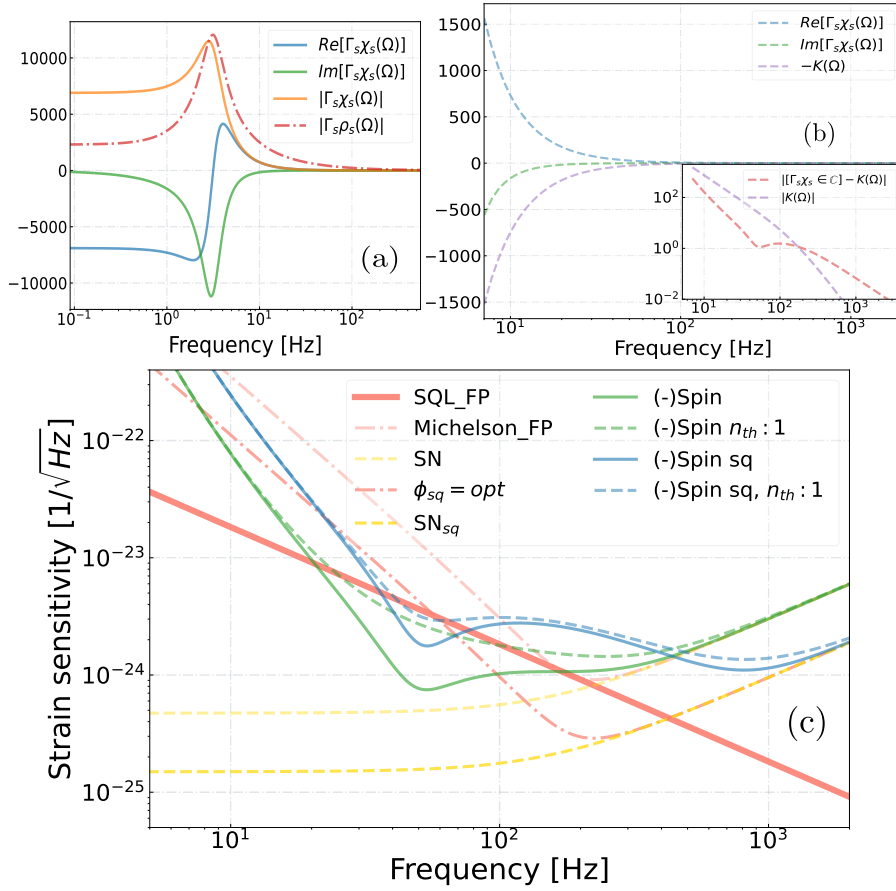
Figure 2.10: Quantum noise reduction including the experimental imperfections. (a) Atomic susceptibilities with Larmor frequency ($\Omega_S = 3$ Hz) and intrinsic decay ($\gamma_S = 2$ Hz). It is observed that the thermal bath, arising from the $\hat{F}_S^X$ and transferred through the $\rho_S(\Omega)$, exerts a more significant influence (illustrated by the red curve) on the spin noise above the Larmor frequency compared to the impact of another thermal bath contribution, $\chi_S(\Omega)$ (depicted by the orange curve). (b) This is followed by the matching of two susceptibilities involving the imaginary part of atomic system, represented by $|\text{Re}[\Gamma_s\chi_S(\Omega)] - K(\Omega) + i \cdot \text{Im}[\Gamma_s\chi_S(\Omega)]|$. (c) Finally, the strain sensitivity is analysed, incorporating experimental imperfections such as finite atomic center frequency, intrinsic decoherence, and the presence of two atomic thermal baths ($n_s = 1$).

the right wing of the atomic transfer function helps cancel the interferometer's quantum back action, these hybrid system also contends with the extra noise from two atomic thermal baths, illustrated as non-overlapping red and orange curves. This additional atomic thermal noise, compromising the overall quantum noise reduction as shown by the blue and green dashed curves, necessitates careful preparation of the negative atomic system. Fortunately, despite these realistic imperfections, the system can still achieve better sensitivity improvement compared to ideal frequency dependent squeezing at certain sideband frequencies.

2.3.2 Quantum backaction evading with negative mass spin oscillator in parallel scheme
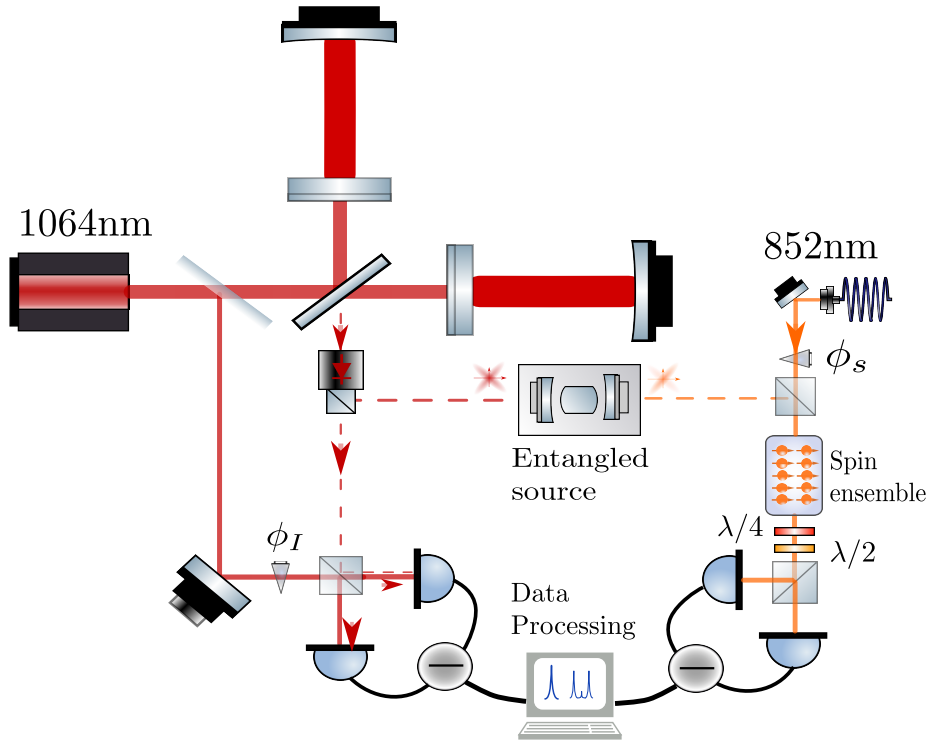
Figure 2.11: Scheme of broadband quantum noise reduction with conditional negative mass spin oscillator. This setup separates and injects entangled EPR pairs into the GWD interferometer and atomic spin oscillators, respectively. The quadrature of light can be adjusted through the homodyne phase (ϕ_I) and by using quarter and half-wave plates on the atomic side. Meanwhile, one can tune the injected phase (ϕ_S) before the atomic ensemble to effectively shift the atomic resonance frequency. This approach, known as the virtual rigidity effect, helps to better match two systems, even when they have different resonance frequencies.

In the sequential scheme, the hybrid systems would function optimally if both two systems could simultaneously couple to the same probe light. Given that the probe interacts with the internal state of atomic spin ensemble, the optical transition of the cesium atoms enables efficient interaction with a light wavelength of $\approx$ 850 nm. However, contemporary GW detector typically operates at wavelengths like 1064 nm, and even longer wavelengths are planned for future interferometers. Fortunately, this apparent wavelength mismatch can be addressed by utilizing non-degenerated EPR entangled pairs to conduct conditional squeezing measurements, as described in previous section. In the parallel hybrid system depicted in Fig.7.1, this scheme relies on the high degree of cross-correlation between the two entangled beams generated by the non-degenerate parametric-down conversion (PDC) process. This setup can align with the operational wavelength requirements of both the GW detector and atomic optical

47

transition. Each entangled beam interacts with the corresponding subsystem, allowing for the combined homodyne detection of both output signals with optimal weighting. The high cross-correlation mentioned above, enables a reduction in both the shot noise and quantum backaction noise of the interferometer, conditioned on the measurement results from the atomic arm. The conceptual framework for this scheme was initially proposed in [45], with a more comprehensive analysis incorporating practical parameters later presented in [46, 47]. Before delving into the total quantum noise of this scheme, let's first revisit the spectral densities of the entangled beams' variance, along with their non zero cross-correlations, which can be expressed as follows :

$$\overline{S}\left[\hat{a}_{(c,I)}\hat{a}_{(c,I)}\right] = \overline{S}\left[\hat{a}_{(s,I)}\hat{a}_{(s,I)}\right] = \overline{S}\left[\hat{a}_{(c,S)}\hat{a}_{(c,S)}\right] = \overline{S}\left[\hat{a}_{(s,S)}\hat{a}_{(s,S)}\right] = \cosh 2r,$$
$$\overline{S}\left[\hat{a}_{(c,I)}\hat{a}_{(c,S)}\right] = \sinh 2r, \quad \overline{S}\left[\hat{a}_{(s,I))}\hat{a}_{(s,S)}\right] = -\sinh 2r.$$
$$(2.32)$$

Assuming that both systems are measured at the sine (phase) quadrature of the output fields $\hat{b}_{(s,I)}$ and $\hat{b}_{(s,S)}$, and considering the input-output relationships for both the gravitational wave interferometer (GWI) and atomic oscillator, we can derive the following equations for the combined output signal, as demonstrated in [30]:

$$\hat{b}_{s,I}(\Omega) + g(\Omega)\hat{b}_{s,S}(\Omega) = \left[\overbrace{\hat{a}_I^s(\Omega) - K(\Omega)\hat{a}_I^c(\Omega) + \sqrt{K(\Omega)}\frac{h}{h_{SQL}}}^{GWI}\right]$$
$$+ g(\Omega)\left[\underbrace{\hat{a}_S^s(\Omega) + 2\Gamma_S\chi_S(\Omega)\hat{a}_S^c(\Omega) + \sqrt{2\Gamma_S\gamma_S}(\chi_S(\Omega)\hat{F}_S^P + \rho_S(\Omega)\hat{F}_S^X)}_{Atom}\right].$$
$$(2.33)$$

With $g(\Omega)$ representing the optimal choice of a weighted gain that can be modified for improved matching. We proceed to calculate the spectral densities of the interferometer and atomic spin ensembles in shot noise unit, denoted as σ_I and σ_S, respectively. Additionally, σ_{IS} corresponds to the cross-spectral density:

$$\sigma_I(\Omega) = \left[1 + K^2(\Omega)\right]\cosh 2r,$$
$$\sigma_S(\Omega) = \left[1 + \Gamma_S^2|\chi_S(\Omega)|^2\right]\cosh 2r + \Gamma_S\gamma_S(|\chi_S(\Omega)|^2 + |\rho_S(\Omega)|^2)\sigma_{th,S}, \quad (2.34)$$
$$\sigma_{IS}(\Omega) = [1 + K(\Omega)\Gamma_S\chi_S(\Omega)]\sinh 2r.$$

When the value of $g(\Omega) = \frac{\sigma_{IS}^*}{\sigma_S(\Omega)}$ is selected, we can derive the power spectral density (PSD) of strain sensitivity for this parallel hybrid system as follows (here

we need to use the expression $\cosh^2(2r) - \sinh^2(2r) = 1$:

$$\overline{S}_{par}^h(\Omega) = \frac{h_{SQL}^2}{2K(\Omega)} \left[\sigma_I(\Omega) - 2\mathrm{Re}(g(\Omega)\sigma_{IS}(\Omega)) + |g(\Omega)|^2\sigma_S(\Omega) \right]$$

$$= \frac{h_{SQL}^2}{2K(\Omega)} \left[\sigma_I(\Omega) - \frac{|\sigma_{IS}(\Omega)|^2}{\sigma_S(\Omega)} \right]$$

$$= \frac{h_{SQL}^2}{2K(\Omega)\sigma_S(\Omega)} \left\{ \left(1 + K^2(\Omega)\right) \left[1 + \Gamma_S^2|\chi_S(\Omega)|^2 + \overbrace{\Gamma_S\gamma_S(|\chi_S(\Omega)|^2 + |\rho_S(\Omega)|^2)\sigma_{th,S}}^{TN} \cosh 2r \right] \right.$$

$$\left. + \underbrace{|\Gamma_S\chi_S(\Omega) - K(\Omega)|^2}_{QBAN} \sinh^2 2r \right\}.$$

$$(2.35)$$

This formula may initially appear intimidating, but it is crucial to recognize that our primary goal is to cancel out the quantum backaction noise (QBAN), while realizing that the atomic thermal noise (TN) will compromise the overall quantum noise reduction. By simplifying this extensive equation under certain approximations, we can gain a clearer understanding of this scheme. First, if we neglect the atomic intrinsic damping term γ_S and presume that the susceptibilities of both systems perfectly match such that we can completely discard the quantum backaction noise. Second, if we consider the thermal decoherence contribution from atomic oscillator as negligible. Under these ideal conditions, the strain sensitivity of the system can be represented as follows:

$$\overline{S}_{par}^h = \frac{h_{SQL}^2}{2\cosh 2r} \left[\frac{1}{K(\Omega)} + K(\Omega) \right]. \qquad (2.36)$$

In the strong entanglement case, the $\cosh 2r \approx e^{2r}/2$ is only 3 dB less than that achieved with single mode squeezing injection. This approach could offer a comparable level of broadband quantum noise suppression to that of frequency dependent squeezing with optimally detuned EPR entanglement. However, it has advantages of simpler readout, an easier phase control system (eliminating the need to stabilize relative detuning in the detuned EPR states [39, 40]), and less optical losses, since only one arm of the entanglement beams is injected into the gravitational wave interferometer. Furthermore, while the detuned EPR entanglement scheme can only operate as a single frequency-dependent filter cavity, achieving the full gravitational wave signal frequency band quantum noise reduction typically requires at least two filter cavities in the detector. These additional filter cavities are implemented to counterbalance the optical spring effect and extra phase accumulation operated in the detuned signal recycling cavity configuration [30]. Revisiting the hybrid system in parallel scheme, where the conditional measurement on atomic arm allows for the engineering of gain and interaction dynamics, including high order tensor interactions (we will elaborate more in the

next chapter), this hybrid approach may offer better quantum noise reduction performance compared to the detund EPR in practical gravitational wave detection systems. From the perspective of fundamental physics, it is also interesting to consider the creation of quantum entanglement between a small atomic ensemble to a kilometer-scale gravitational wave interferometer. The spectral density of conditional broadband quantum reduction scheme, employing more realistic parameters for an atomic oscillator including the imperfect cancellation due to the imaginary part and additional atomic thermal noise, is depicted in Fig.2.12. In the ideal scheme, both the conditional squeezing measurement with a parallel atomic ensemble (represented by the light blue curve) and the detuned EPR state achieve the same level of sensitivity improvement, which is indeed 3dB less than that attained frequency dependent squeezing with filter cavities (tomato curve). if we closely examine the quantum backaction term in eq.(7.3), it becomes apparent that the matching of two systems is actually the product of the readout rate Γ_S and atomic susceptibility ($\chi_S(\Omega)$) subtracted from a fixed interferometer coupling factor $K(\Omega)$: $|\Gamma_S(\text{RE}[\chi_S(\Omega)] + i \times \text{Im}[\chi_S(\Omega)]) - K(\Omega)|$. Although this approach may result in diminished performance at very low spectral frequencies, one can relax the necessity for a large atomic readout rate (now is around 700 Hz) by increasing the Larmor frequency, for example up to 40Hz in fig.2.12(a), thereby still achieve substantial quantum noise reduction.

The inclusion of the atomic intrinsic damping $\gamma_S/2\pi = 10$ Hz begins to degrade the quantum noise reduction (as shown by the dark purple curve), primarily due to the imaginary part contribution (illustrated by the red curve in Fig.2.12(b)). Further incorporation of atomic projection & thermal noise keep degrading the reduction in quantum noise, as indicated by the light purple curve. However, despite these degradation, the improvement in strain sensitivity across the detection bandwidth can still be observable, and the system can maintain performance below the standard quantum limit (SQL).

Comparing the parallel approach with the negative mass spin oscillator in the sequential scheme, it's interesting to note that even with a less optimal intrinsic damping rate, a significantly higher Larmor frequency, and the same atomic thermal noise, the parallel approach can still achieve superior sensitivity improvement. This might be attributed to the additional weighted gain that allows for better matching between two systems.
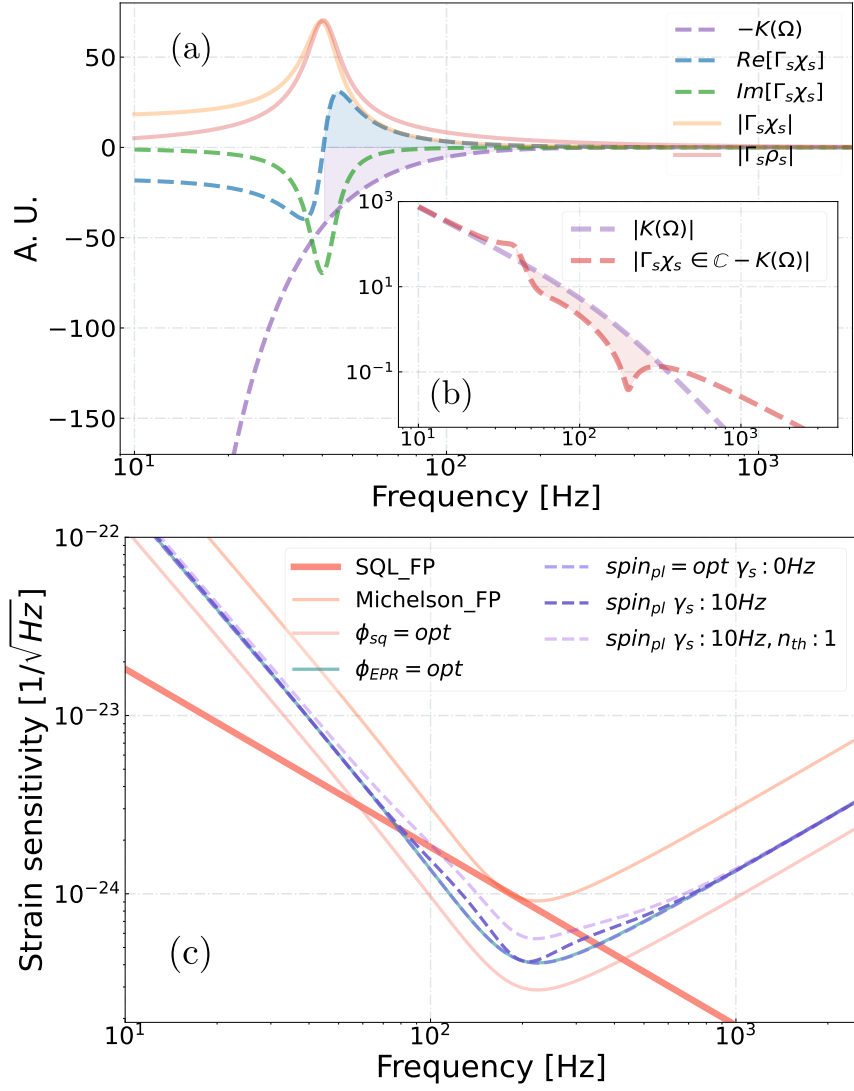
Figure 2.12: Strain sensitivity with conditional negative mass spin oscillator.
(a) Here we present the optomechanical coupling factor $K(\Omega)$, together with the real and imaginary parts of atomic susceptibility $\chi(\Omega)$, as functions of the Fourier frequency. The dynamic responses of two forms of thermal noise (χ_S and ρ_S) are also presented. The shaded blue and purple areas illustrate the potential for mutual cancellation of these two responses. (b) This part illustrates the matching of two susceptibilities in absolute value. The region shaded in red, where the red curve lies beneath the purple curve, signifies the mutual cancellation of responses. (c) The optimized strain sensitivity with conditional measurement of the atomic spin oscillator is shown by the light purple curve, achieving the same level of sensitivity improvement as the injection of detuned EPR entanglements (teal curve). The dark purple line highlights how the additional intrinsic decay compromise the quantum noise reduction as evidenced by the imaginary response (green curve in (a)), and is further slightly degraded by the atomic thermal noise. In the context, the Larmor frequency is $\Omega_S/2\pi = 40$ Hz, intrinsic decay: $\gamma_S/2\pi = 10$ Hz, and the readout rate is $\Gamma_S/2\pi = 700$ Hz.

Additionally, readers seeking a deeper understanding of parameter imperfections,

such as optical losses and optimal squeezing factors for a given system, are referred to further detailed discussions in Valeriy's PhD thesis [33].

Overcoming the imperfections with the Virtual rigidity

The application of a virtual rigidity shift, which emerges from the destructive interference between quantum shot noise and backaction noise, can also be employed to reduce the constraints on the readout rate and ultra-low Larmor frequency. Moreover, this approach has the potential to mitigate the effects of the imaginary component of susceptibility and atomic thermal noise. We will explore this in more detail in the following chapter.

2.3.3 Summary

In this chapter, we introduced the concept of quantum noise in gravitational wave interferometers and reviewed several quantum engineering approaches aimed at reducing this noise to improve the sensitivity within their operational bandwidth. Our discussion included analysis of the quantum noise and input-ouput relationships in both conventional free mass and tuned Fabry-Pérot interferometers. We explored quantum noise reduction techniques such as variational readout, the injection of squeezing and frequency-dependent squeezing, and utilization of detuned EPR state injection. Additionally, we examined innovative method like the sequential use of negative mass atomic ensembles and phase-squeezed state injection, as well as conditional squeezing utilizing negative atomic spin oscillators in a parallel scheme. These approaches collectively represent a comprehensive approach to enhancing the detection capabilities in the gravitational wave interferometers.

Spin Oscillator Theory

In the previous sections, we have explored various theoretical approaches for reducing quantum noise in gravitational wave detection systems. We have shown that atomic spin oscillators, when functioning in an effective negative mass domain, have the potential to create an innovative hybrid system. Moreover, simultaneous measurements of these systems could lead to the creation of EPR entangled systems, as discussed at the end of the previous chapter, significantly boosting the sensitivity of gravitational wave detectors. In the upcoming chapter, we will delve into the theoretical aspects of atomic oscillator, illustrating how such atomic spin oscillators can be achieved using an ensemble of cesium-133 atoms.

Our focus will be on several critical processes for controlling a collective atomic spin oscillator: tuning the resonant frequency of the spin oscillator, controlling its effective mass, analyzing the light-atom interactions, and addressing the additional noise, including atomic projection noise and even thermal fluctuations. Additionally, we will investigate atomic spins with various decay modes (fast and slow) as they interact with probe light. Finally, we will introduce the theoretical framework for calibrating a quantum noise-limited spin oscillator, highlighting potential applications, such as employing virtual frequency shift (virtual rigidity) to enhance the quantum-noise reduced measurements.

3.1   Cesium atom and Zeeman splitting

In our experiment, we work with the Cesium-133, the only stable isotope of Cesium. Cesium atom is famous for its relatively simple atomic structure, which includes only one valence electron in its outermost shell, and a melting point of $28.6\,°C$ leads to high vapour density at room temperature. These attributes, combined with well-developed laser systems, make this neutral atom an attractive option for room temperature-based atomic experiments, such as atomic magnetometry [51, 52], quantum teleportation[53], and quantum memory applications [54–56]. Additionally, Cesium atoms are also employed as a standard in defin-

ing current time in atomic clocks[57]. Now, we will briefly review the electronic
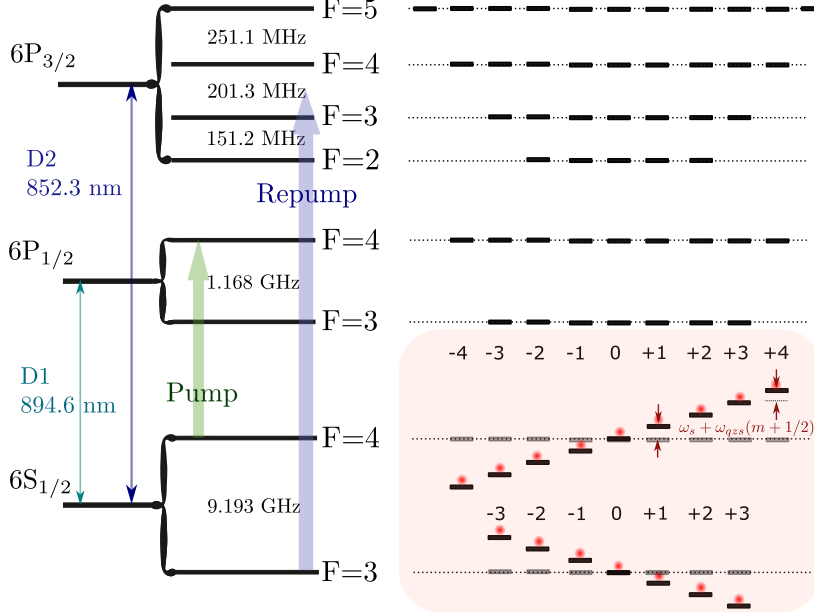
Figure 3.1: Cesium and its Zeeman Level Structure. (The transition from $6S_{1/2}$ to $6P_{1/2}$ is referred to as the D_1 line, which is utilized for optical pumping in our experiments. Meanwhile the transition from $6S_{1/2}$ to $6P_{3/2}$ is known as the D2 line and serves both as the optical repumping and probe. On the right, we present subsets of the Zeeman levels. The shaded orange area is the atomic states that we focus on in this thesis. In the weak of a low bias magnetic field, the Larmor frequency, which describes the energy difference between each m_F level, is also presented. Without optical pumping, the atoms are equally distributed across the Zeeman levels, indicating an atomic thermal state.

level structure of Cesium. Readers seeking more detailed information are recommended to Cesium atom D line datasheet [58, 59]. The cesium atom, with its one valence electron, has a ground state occupying the $S_{1/2}$ level. Given that Cesium also possesses a nuclear spin of $I = 7/2$, the hyperfile interaction $(I \pm S)$ results in two possible ground states, $F = \{3, 4\}$, with an energy split of $\Delta E_{hfs} = \hbar \cdot v_{hfs} = \hbar \cdot 9.193 \text{GHz}$. In the first excited state, where the orbital angular momentum $L = 1$, the coupling between the orbital and electron spin also yields two total angular momentum states $J = L \pm S = \{1/2, 3/2\}$. This results in the splitting of the first excited state into $F_{D1} = \{3, 4\}$ and $F_{D2} = \{2, 3, 4, 5\}$, respectively. Consequently, this splitting generates two transitions for the first excitation: the D1 line from $6S_{1/2} \rightarrow 6P_{1/2}$ at a wavelength of $\lambda : 894$ nm, and another D2 line transition from $6S_{1/2} \rightarrow 6P_{3/2}$ at a wavelength of $\lambda : 852.3$ nm. Owing to the substantial energy gap ($\approx \hbar \cdot 300$ THz) between the ground state and excited state, as depicted in Fig.3.1, all atoms typically reside in the ground state unless acted by special operations, like optical pumping. Therefore, our analysis primarily focuses on the dynamics of atoms in the ground state in the presence of external magnetic fields. When applying an external bias magnetic field, the nucleus, electronic spins, and the orbital angular momentum, each with

its own magnetic moment μ, collectively contribute to the total magnetic moment of the atom. In scenarios where the energy shift caused by the B fields is much smaller compared to the hyperfine splitting, particularly for the atomic ground state, the relevant quantum numbers are the total angular momentum F and its projection m_F on the quantization axis. The energy E_{F,m_F} of a given level is described by the Breit-Rabi formula [58]:

$$E_{F,m_F} = -\frac{hv_{\text{hfs}}}{2(2I+1)} + g_I\mu_B m_F B \pm \frac{hv_{\text{hfs}}}{2}\sqrt{1 + \frac{4m_F}{2I+1}x + x^2}, \qquad (3.1)$$

Where v_{hfs} is the hyperfine splitting, μ_B is the Bohr magneton, B indicates the bias magnetic field strength and $g_I \approx 4 \times 10^4$ is the nuclear g-factor. The parameter 'x' represents the Zeeman splitting strength, normalized to the hyperfine splitting, and is expressed as:

$$x = \frac{(g_J - g_I)\mu_B B}{\hbar v_{\text{hfs}}}. \qquad (3.2)$$

Here, $g_J \approx 2$ denotes the spin-orbit g-factor. In our experiments, we usually work with an external B field of less than ~ 10 G, making x$\sim 10^{-3}$. Therefore, in this condition the Zeeman splitting strength can be considered as a small perturbation, we can expand the Zeeman strength equation x around x = 0 up to second order. Accordingly, the Zeeman level energies for the ground states can now be described as follows:

$$E_{m_F} = \hbar\Omega_S m_F + \hbar\Omega_{qzs} m_F^2. \qquad (3.3)$$

Here, the first order Larmor frequency, denoted as Ω_S and the quadratic Zeeman splitting Ω_{qzs} are expressed as:

$$\begin{aligned}\frac{\Omega_S}{2\pi} &= v_S = \frac{g_F\mu_B B}{h}, \\ \frac{\Omega_{\text{qzs}}}{2\pi} &= v_{\text{qzs}} = \frac{2v_S^2}{v_{\text{hfs}}}.\end{aligned} \qquad (3.4)$$

The hyperfine landé g-factor is

$$g_F = \begin{cases} 0.250390 & \text{for F} = 4, \\ -0.251194 & \text{for F} = 3. \end{cases} \qquad (3.5)$$

The Larmor frequency scales approximately as 350 kHz/G, with variation ranges from a few Hz up to MHz in our experiments. Considering a scenario where the atomic processing at 350 kHz corresponding to a 1 Gauss bias magnetic field, one would observe a quadratic Zeeman splitting of 26 Hz. Due to the sign and slight difference in g_F, the two ground state hyperfine levels F = 3,4 shift oppositely

with the external magnetic field. Notably, the energy levels of F = 3 manifold are approximately 0.3% higher than those of F = 4 manifold, These details will be further presented in the atomic calibration Chapter 5. In our experiments, the probe laser induces the transition between the ground Zeeman levels, and assuming our primary focus is the neighboring transitions $\Delta m_F = \pm 1$, where the splitting behavior is described as follows:

$$\frac{E_{m+1} - E_m}{\hbar} = \Omega_S + \Omega_{qzs}(1 + 2m_F). \tag{3.6}$$

It is noteworthy that in the scenario where the quadratic Zeeman splitting surpasses the transition decoherence ($\Omega_{qzs} > \gamma_S$), the ground state dynamics will present resolved 2F resonances. This phenomenon can be employed to characterize the population distribution of optically pumped spin states.

3.2 Holstein-Primakoff approximation, and effective oscillator masses

Before delving into the quantum state of the atomic ensemble, allow me to briefly introduce our atomic setup. In our experiments, illustrated in the schematic Fig.3.2, Cesium atoms are confined within a vapor cell and placed in a homogeneous DC magnetic field aligned along the x -axis. The optical pumping lasers (pump and repump), with circular polarization, propagating collinearly with the bias field, prepare the atoms in one of the extreme Zeeman sub levels ($m_F = \pm 4$). Consequently, the atomic spins are quantized, aligning either parallel or antiparallel to the magnetic field. A linearly polarized probe light, with an input polarization angle α relative to the quantization axis (x-axis), travels orthogonally (along the z axis) to the quantized atomic spins , thereby reading out the transverse components of atomic spin into the polarization states of the light. This probe light with atomic signal is subsequently detected with the balanced polarimetric homodyne detection, where the detection quadrature angle is adjusted using quarter and half-waveplates.

We aim to theoretically describe the quantum state of atomic ensemble in an external magnetic field, let us consider an atomic ensemble comprising of N independent atoms. The quantum state of this ensemble can be characterized by the collective spin operator, denoted as $\hat{F} = \sum_{k=1}^{N} \hat{f}_k$, where $\hat{f}_k$ represents the spin of the k-th atom, and $\hat{F}$ is the total angular momentum of the ensemble spins. Therefore, a complete angular momentum basis for this collection of N spins can
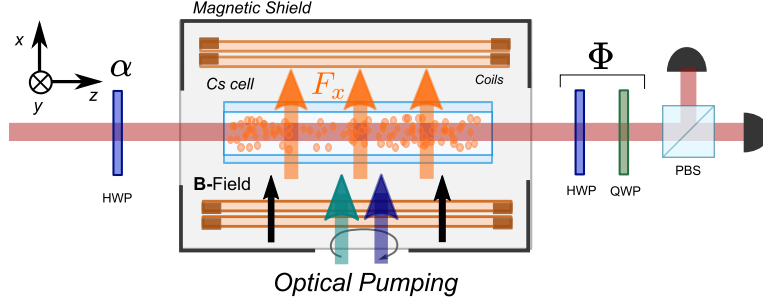
Figure 3.2: Illustrative Schematic of the Atomic Setup. The cesium atoms are situated in a homogeneous bias magnetic field and are optically pumped to the extreme Zeeman sublevels. This leads to the generation of a macroscopic collective spin oscillator F_x, precessing around the quantization axis x. The interaction with the spin oscillator is facilitated by linearly polarized light at the angle α relative to x-axis. The resulting atomic signal is detected using balanced polarimetry, with the detection quadrature controlled through a combination of half-wave and quarter-wave plates.

be formulated, as detailed in [49]:

$$
\begin{aligned}
\hat{F}_x &\equiv \sum_N \hat{f}_x^{(i)} = \sum_N \sum_m m \hat{A}_{mm}^{(i)}, \\
\hat{F}_y &\equiv \sum_N \hat{f}_y^{(i)} = \frac{1}{2} \sum_N \sum_m c(F,m) \left(\hat{A}_{m+1,m}^{(i)} + \hat{A}_{m,m+1}^{(i)} \right), \\
\hat{F}_z &\equiv \sum_N \hat{f}_z^{(i)} = \frac{1}{2i} \sum_N \sum_m c(F,m) \left(\hat{A}_{m+1,m}^{(i)} - \hat{A}_{m,m+1}^{(i)} \right), \\
\hat{F}_0 &\equiv \sum_N \hat{f}_0^{(i)} = \sum_N \sum_m \hat{A}_{mm}^{(i)},
\end{aligned}
\tag{3.7}
$$

where the coefficients are given by c (F, m) = $\sqrt{F(F+1) - m(m+1)}$, and the atomic spin operators $\hat{A}_{a,b}^{(i)} = |F,a\rangle \langle F,b|^{(i)}$ determine the relative weights of the atomic coherences in the angular momentum basis. These operators follow the commutation relations $[\hat{F}_i, \hat{F}_j] = i\hat{F}_k$ (where i, j, and k represent Levi-Civita symbols), exemplified by $[\hat{F}_y, \hat{F}_z] = i\hat{F}_x$. In this framework, if we neglect the additional quadratic Zeeman shift previously mentioned, the energy of the collective spins, quantized along the x-axis due to the magnetic dipole interaction, can be written as follows:

$$
\hat{H}_{B,S}/\hbar = \Omega_S \hat{F}_x.
\tag{3.8}
$$

In our experiments, which typically involve a highly polarized spin ensemble with a total atom number around 10^{11}, these large numbers enable the application of a technique known as the Holstein-Primakoff approximation [60]. In this approach, the spin operator aligned along x-axis, $\hat{F}_x$, is treated as a classical variable, such that $F_x \sim \left| \langle \hat{F}_x \rangle \right| = FN$. Conversely, the transverse spin components, $\hat{F}_z$, $\hat{F}_y$, are considered as quantum variables with zero mean values and second moment variances, quantified as $\Delta \hat{F}_z = \Delta \hat{F}_y = \sqrt{|F_x|/2}$ which are much less than $\left| \langle \hat{F}_x \rangle \right|$.

57

This approximation facilitates the mapping of the spin variables, $\hat{F}_{\pm} = \hat{F}_y \pm i\hat{F}_z$ with the above complex commutation relation to bosonic creation and annihilation operators $\hat{b}^{\dagger}$ and $\hat{b}$ respectively, satisfying the standard simple commutation relationship $[\hat{b}, \hat{b}^{\dagger}] = 1$. The transition between these representations are given by $\hat{F}_+ \sim \sqrt{F_x}\hat{b}$ and $\hat{F}_- \sim \sqrt{F_x}\hat{b}^{\dagger}$, which presents 'creating' or 'annihilating' nearly a single atom spin from the collective atomic spins along x-axis. Under this transformation, the original spin component $\hat{F}_x$ can be written as :

$$\hat{F}_x = F_x - \frac{\hat{b}^{\dagger}\hat{b}}{2}. \tag{3.9}$$

In the regime of low excitations $\langle \hat{b}^{\dagger}\hat{b}\rangle \ll F_x$, we can write the number of bosonic excitation in the system as:

$$\hat{b}^{\dagger}\hat{b} = \frac{\hat{F}_-\hat{F}_+}{F_x} \sim \frac{\hat{F}_y^2 + \hat{F}_z^2}{F_x}. \tag{3.10}$$

When revisiting the energy analysis of the collective spins, the magnetic dipole ($m_F = 4$) interaction can now be reformulated as:

$$\hat{H}_{B,S} = \hbar\Omega_S\hat{F}_x \sim \hbar\Omega_S F_x - \frac{\Omega_S}{2}(\hat{X}_S^2 + \hat{P}_S^2). \tag{3.11}$$

A similar approach can be applied to ($m_F = -4$) spin state. Here, we redefine the spin variables for both scenarios as follows:

$$\hat{X}_S = \hat{F}_z/\sqrt{F_x}, \ \hat{P}_S = \mathbf{sgn}(\pm F_x) \ \hat{F}_y/\sqrt{F_x}, \tag{3.12}$$

with the commutation relationship given by $[\hat{X}_S, \hat{P}_S] = i$. The first part in the above equation represents the spins energy before the excitation. The symbol $\pm$ refers to the orientation of the collective spin F_x , either parallel or anti-parallel to the bias magnetic field, soon we will discuss that these two different orientations can be treat as a harmonic oscillator with the effective 'positive' or 'negative' masses, respectively. This configuration describes the precession of two transverse components around the direction of the quantization magnetic field, whether clockwise or counterclockwise, is determined by the orientation of the collective spin relative to the B field as shown in Fig.3.3. Furthermore, with closer examination, it becomes evident that the newly defined, approximate spin variables correspond to the canonical position and momentum operators[1] [44, 49, 61]:

$$\hat{X}_S = \frac{b - b^{\dagger}}{\sqrt{2}i} = \frac{\hat{F}_+ - \hat{F}_-}{\sqrt{2}i}, \ \hat{P}_S = \frac{b + b^{\dagger}}{\sqrt{2}} = \frac{\hat{F}_+ + \hat{F}_-}{\sqrt{2}}. \tag{3.13}$$

This approximation enables us to treat the ensemble's collective spin in a bias

---

[1]Here we use the normalization from Rodrigo's thesis, is inverted relative to operators used in Brain's thesis

magnetic field B as a harmonic oscillator. Consequently, the two different interactions, characterized by different effective masses, can be written as follows:

$$\hat{H}_{S,B}/\hbar = \begin{cases} -\Omega_S F_x + \frac{\Omega_S}{2}(\hat{X}_S^2 + \hat{P}_S^2) & \text{for } \textbf{Positive Mass}, \\ \Omega_S F_x - \frac{\Omega_S}{2}(\hat{X}_S^2 + \hat{P}_S^2) & \text{for } \textbf{Negative Mass}. \end{cases} \tag{3.14}$$
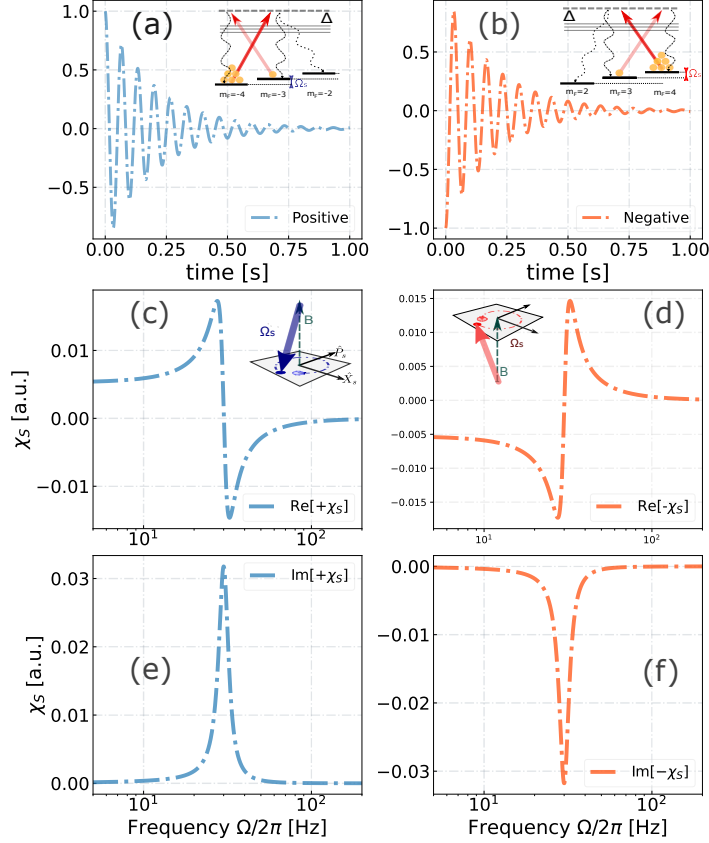
Figure 3.3: Positive and negative mass of spin oscillator. In an optimal system with ideal optical pumping and a quantization axis defined by the external magnetic field B, all atomic spins are transferred to the extreme Zeeman levels $m_F = \pm 4$, which correspond to the minimum (or maximum) ground state energy. Introducing an excitation transfers a few atoms to adjacent Zeeman level, denoted as the excited state, resulting in either an increase or decrease in the energy $\hbar\Omega_S$. This dynamic is analogous to the dynamic of a harmonic oscillator with the sign of the oscillator's effective positive (a) and negative (b) masses. We present the oscillation of the macroscopic spin oscillator with both positive and negative masses in the time domain (a,b), along with their driven responses in the frequency domain (c-f). Although the amplitudes of the oscillations in the time domain are identical for both configurations, they exhibit π phase shift relative to each other. Consequently, these phase differences affect both the real (c,d) and imaginary (e,f) components of atomic susceptibilities, offering a method for the potential cancellation of one oscillator's response in the reference frame of another.

In our experiment, the effective mass of spin system can be selectively determined

by either adjusting the polarization of circularly polarized pump and re-pump lasers or by altering the orientation of the bias magnetic field relative to the direction of pump and repump propagation. As depicted in Fig.3.3 , the plots in the top panel show the slowly decaying oscillations of the positive or negative masses oscillator over time. Notably, these oscillators exhibit a π phase shift relative to each other, due to the sign of spin momentum operator $\hat{P}_S$. Furthermore, the middle (c,d) and bottom (e,f) panels of figure demonstrate the real and imaginary components of the driven responses of the spin oscillator. The opposite sign of these responses opens up an opportunity: by using one response (e.g. from the negative mass) as a reference, it is possible to cancel out the response of another when they are perfectly matched.

3.3   Stokes operators and its measurement

We now shift our attention from the collective atomic spin to the domain of light polarization. This is a crucial component for understanding the interaction between light and atoms. We would like to note that the light polarization domain, which couples to atomic ensembles through various light polarizations, is distinct from the quadrature phase and amplitude of a linearly polarized light, as discussed in the first introduction chapter. Again if we consider a wave propagating along the z-axis, we may write a general field with arbitrary polarization as:

$$\vec{E} = \vec{E}_x \cos(\omega_0 t - kz + \phi_x) + \vec{E}_y \cos(w_0 t - kz + \phi_y). \qquad (3.15)$$

Here, $\vec{E}_x$ and $\vec{E}_y$ denote the complex amplitudes of wave, each has both the magnitudes and phases. Then, we could separate the phases into an overall phase of two waves and the relative phase difference between $\vec{E}_x$ and $\vec{E}_y$ expressed as $\phi_x - \phi_y$. We focus primarily on the relative phase and magnitude ratio, as these parameters help us to specify the light polarization, whether it is linear or circular. Furthermore, the polarization of a light beam can be effectively visualized using Stokes vectors on a Poincareé sphere, as depicted in Fig.3.4 and described by four Stokes parameters:

- S_0: The total intensity of the light.

- S_x: The intensity difference between horizontally and vertically polarized light.

- S_y: The intensity difference between light polarized at $+45°$ and $-45°$.

- S_z: The intensity difference between right-handed and left-handed circularly polarized light.

Based on the above stokes vectors, one could quantize the electric fields as follows:

$$\hat{E} \sim \mathbf{e}_x(\hat{a}_x(t)e^{-i(\omega_0 t - kz + \phi_x)} + \hat{a}_x^\dagger(t)e^{i(\omega_0 t - kz + \phi_x)}) + \mathbf{e}_y(\hat{a}_y(t)e^{-i(\omega_0 t - kz + \phi_y)} + \hat{a}_y^\dagger(t)e^{i(\omega_0 t - kz + \phi_y)}),$$

$$(3.16)$$

and acquire the stokes operator in quantum regime as shown in Fig.3.4 with a new quantum Poincaré sphere radius , $\langle \hat{S} \rangle = \left\langle \hat{S}_0^2 + 2\hat{S}_0 \right\rangle^{1/2}$:

$$\begin{aligned}
\hat{S}_o(z,t) &= \frac{1}{2}\left(\hat{a}_x^\dagger \hat{a}_x + \hat{a}_y^\dagger \hat{a}_y\right) = \frac{1}{2}\left(\hat{n}_x + \hat{n}_y\right), \\
\hat{S}_x(z,t) &= \frac{1}{2}\left(\hat{a}_x^\dagger \hat{a}_x - \hat{a}_y^\dagger \hat{a}_y\right) = \frac{1}{2}\left(\hat{n}_x - \hat{n}_y\right), \\
\hat{S}_y(z,t) &= \frac{1}{2}\left(\hat{a}_x^\dagger \hat{a}_y + \hat{a}_y^\dagger \hat{a}_x\right) = \frac{1}{2}\left(\hat{n}_{+45} - \hat{n}_{-45}\right), \\
\hat{S}_z(z,t) &= \frac{1}{2i}\left(\hat{a}_x^\dagger \hat{a}_y - \hat{a}_y^\dagger \hat{a}_x\right) = \frac{1}{2}\left(\hat{n}_R - \hat{n}_L\right).
\end{aligned}$$

$$(3.17)$$

These Stokes operators fulfill the commutation relations similar to the spin angular momentum operators F: $[\hat{S}_i, \hat{S}_j] = i\hat{S}_k$
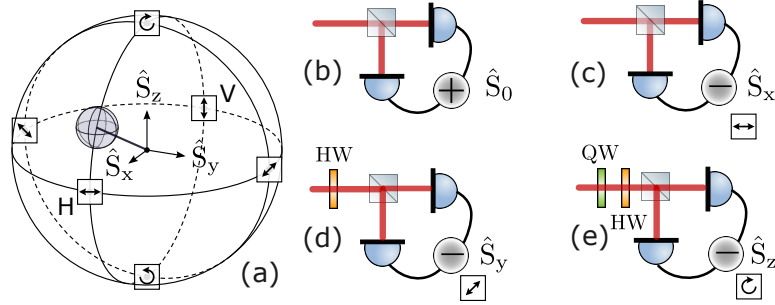
Figure 3.4: Illustration of Stokes vectors and their detection. (a) The Stokes operators on a Poincaré sphere. The small ball at the end of the vector represents the quantum noise associated with a Stokes vector. (b - e) Schematic of the detection scheme required to measure each Stokes operator. This figure has been adapted based on Oestfeldt's thesis

This definition enables the measurement of light operators through the photon number difference, which can be easily accessed through a polarized beam splitter (PBS) and a balanced photo-detector [62]. For instance, to measure $\hat{S}_y$, a half-wave plate is applied to rotate linearly polarized light (initially aligned along x) by 45°. Subsequently, the PBS decomposes this beam into x and y polarizations. The resulting photo-currents from each polarization are then subtracted to obtain the desired measurement. Based on the supplementary details described in [45], the measurement of $\hat{S}_z$ and $\hat{S}_y$ operators can be equivalent to the quadrature measurement of y-polarized light amplified by the amplitude of light in x-polarization, let us consider a light linearly polarized along the x-axis, with the classical amplitude A_x replacing the quantum operator $\hat{a}_x$ denoted as $\hat{a}_x = iA_x$, and $\hat{a}_x^\dagger = -iA_x$, where i represents a $\pi/2$ relative phase shift between

the x and y polarized waves $(\phi_x - \phi_y = \pi/2)^2$. In the scenario of far-off resonance relative to the hyperfine transition, such that the spin oscillator symmetrically affects the light plus and minus sidebands, we could simplify the two-photon formalism previously established to the symmetric one-photon formalism. Under this approximation, the expression for the light operators in the time domain and in the z and y directions can be reformulated as follows:

$$
\begin{aligned}
\hat{S}_z(z,t) &= \frac{1}{2i}\left(\hat{a}_x^\dagger \hat{a}_y - \hat{a}_y^\dagger \hat{a}_x\right) \approx \frac{A_x}{\sqrt{2}}\left(\frac{\hat{a}_y + \hat{a}_y^\dagger}{\sqrt{2}}\right) = \frac{A_x}{\sqrt{2}}\hat{a}_S^c, \\
\hat{S}_y(z,t) &= \frac{1}{2}\left(\hat{a}_x^\dagger \hat{a}_y + \hat{a}_y^\dagger \hat{a}_x\right) \approx \frac{A_x}{\sqrt{2}}\left(\frac{\hat{a}_y - \hat{a}_y^\dagger}{\sqrt{2}i}\right) = \frac{A_x}{\sqrt{2}}\hat{a}_S^s,
\end{aligned}
\tag{3.18}
$$

where $\hat{a}_S^c(t)$ and $\hat{a}_S^s(t)$ represent the cosine and sine quadrature operators of the y-polarized light, respectively, with reference to the x-polarization carrier phase, as we introduced earlier, alongside the commutation relations $[\hat{a}_S^c(t), \hat{a}_S^c(t')] = i\delta(t-t')$. Since the light in y polarization lacks classical DC components, we can omit the relative minor effect of vacuum noise in x polarization. A more comprehensive explanation of this detection method and the general framework that relates the variance of Stokes operators to two-mode quadrature operator variances can be found in the references [62, 63]. In our experiment, we normally utilize a linearly polarized probe light. Assuming this probe is linearly polarized at an angle α relative to the macroscopic spin component F_x, which is defined by the DC magnetic field. We can redefine the quantum stokes operators in a basis parallel and perpendicular to the linearly polarized probe field as:

$$
\begin{aligned}
&\hat{S}_0, \\
&\hat{S}_\parallel = \hat{S}_x\cos(2\alpha) - \hat{S}_y\sin(2\alpha), \\
&\hat{S}_\perp = \hat{S}_x\sin(2\alpha) + \hat{S}_y\cos(2\alpha), \\
&\hat{S}_z.
\end{aligned}
\tag{3.19}
$$

Since we assume a perfect linearly polarized light, where all the photons are linearly polarized along the parallel axis with an average photon number N_{photon}: $S_\parallel \equiv \langle \hat{S}_\parallel \rangle \approx \langle \hat{S}_0 \rangle = \frac{N_{photon}}{2} = \frac{A_x^2}{2}$, it allows us to treat this operator as a classical variable $\hat{S}_\parallel \to S_\parallel$. We only need to consider other two quantum stokes operators $\hat{S}_\perp$ and $\hat{S}_z$ with zero mean and quantum fluctuations. Similarly, we can also map the light stokes operators in the rotated basis to the approximated canonical phase and amplitude operators[64]:

$$
\begin{aligned}
\hat{X}_L &= \hat{S}_z/\sqrt{S_\parallel} \approx \hat{a}_S^c, \\
\hat{P}_L &= -\hat{S}_\perp/\sqrt{S_\parallel} \approx \hat{a}_S^s, \\
\left[\hat{X}_L(t), \hat{P}_L(t')\right] &= i\delta(t-t').
\end{aligned}
\tag{3.20}
$$

---

^{2}This relative phase will add $\pi/2$ to the polarization homodyne detection angle.

3.4 light-atom interaction, QND and high order tensor

Building on collective spin operators and light stokes operators previously defined, we now initiate an analysis of light-atomic dipole interactions within our experimental framework. The vector Faraday interaction[65], introduced in the previous chapter in the context of quantum noise reduction via an effective negative mass oscillator, will be revisited. Now, we will try to expand the effective interaction Hamiltonian by incorporating the high-order terms due to the fact that Cesium is not a mere spin-1/2 system.

Consider a scenario where a probe laser propagate through a dilute gas of Cs atoms, detuned by Δ relative to the atomic transition $F = 4 \rightarrow F' = 5$, as depicted in Fig.3.1. This probe laser is deliberately detuned far from the atomic transition to ensure that the dispersive coupling ($\propto \frac{1}{\Delta}$), commonly known as the stark shift [66], is the predominant interaction, while the absorption ($\propto \frac{1}{\Delta}^2$) becomes almost negligible. The combination of far-off-resonant weak interaction, rapid decay of excited states[3], and the slow evolution of the ground states, facilitates the implementation of adiabatic elimination. This method enables the disregard of transitions from the ground to excited states and ignore populations in the excited states, as illustrated in Fig.3.3 [a, b]. Consequently, this allow us to narrow down focus on the coupling between light and ground states of atoms. A detailed derivation of our system with the adiabatic elimination can be found in our group's previous PhD thesis [49, 61], where the extended effective interaction Hamiltonian for Cesium D2 line structure, F = 4, is expressed in terms of the collective spin oscillator and light stokes operators:

$$
\begin{aligned}
\hat{H}_{S,L}/\hbar = g_{\mathrm{S}} \Big(& a_0 \hat{S}_0 + a_1 \hat{S}_z \hat{F}_z + \\
& 2a_2 \left[\hat{S}_0 \left(3\hat{F}_z^2 - \hat{F}_0(\hat{F}_0+1) \right) /3 - \hat{S}_x \left(\hat{F}_x^2 - \hat{F}_y^2 \right) - \hat{S}_y \left(\hat{F}_x \hat{F}_y + \hat{F}_y \hat{F}_x \right) \right] \Big),
\end{aligned}
$$
$$(3.21)$$

where g_{S} represents a single photon and single atom coupling rate. In the limit of large probe detuning $\Delta \gg \gamma_{cs}$, this coupling rate can be expressed as follows:

$$
g_{\mathrm{S}} = -\frac{c\gamma_{\mathrm{cs}}}{8A\Delta} \frac{\lambda^2}{2\pi}.
$$
$$(3.22)$$

Here γ_{cs} is the spontaneous emission rate of excited state, with $\gamma_{cs}/2\pi = 5.22\mathrm{MHz}$ for D2 line. Additionally, λ denotes the optical wavelength, A refers to the cell transverse area and c represents the speed of light. The coefficients a_i (i = 0, 1, 2) correspond to different types of light-atom interactions: the scalar a_0, vector

---

[3]The life time of excited state is around 35 ns, contrasted with the ground state's life time of several milliseconds, according to[ref] alkali data sheet

a_1, and tensor a_2 , respectively.

$$a_0 = \frac{1}{4} \left(\frac{1}{1 - \Delta_{35}/\Delta} + \frac{7}{1 - \Delta_{45}/\Delta} + 8 \right) \xrightarrow[\Delta \to \infty]{} 4,$$

$$a_1 = \frac{1}{120} \left(\frac{-35}{1 - \Delta_{35}/\Delta} - \frac{21}{1 - \Delta_{45}/\Delta} + 176 \right) \xrightarrow[\Delta \to \infty]{} 1, \qquad (3.23)$$

$$a_2 = \frac{1}{240} \left(\frac{5}{1 - \Delta_{35}/\Delta} - \frac{21}{1 - \Delta_{45}/\Delta} + 16 \right) \xrightarrow[\Delta \to \infty]{} 0.$$

In this context, Δ_{35} represents the detuning between the excited states F'= 3 and F'= 5, with a value of $\Delta_{35}/2\pi = 452.24$ MHz. Similarly, Δ_{45} is the offset between F' = [4,5], with $\Delta_{45}/2\pi = 251.09$ MHz. Now let's take a close look at these light-atom interaction terms. The first term a_0 gives a scalar light shift that is independent on the internal atomic states but only proportional to the total photon number and light detuning.

The vector term a_1, on the other hand, represents the coupling between the light stokes and collective spin operators, reflecting the electron-dipole interactions dynamic as depicted in Fig.3.3 (a, b)). This interaction, known as our favorite Faraday interaction(see [64]), involves the probe light undergoing circular birefringence. This phenomenon entails the rotation of linearly polarized light due to differential phase shifts arising from distinct refractive indices for two circular polarization modes. Consequently, the light stokes operator $\hat{F}_x$ is rotated around the z-axis by an amount proportional to the number of atomic spins along the F_z axis. Additionally, there is back action rotation effect on the spin component around the same z-axis can be influenced by the fluctuations in probe light polarization. Notably, this back action noise is particularly interest to our experiments, as it can contribute to the reduction of quantum backaction noise in other quantum systems, such as the LIGO interferoemter, thereby enhancing precision in gravitational wave measurements.

The last terms associated with a_2 introduce higher-order couplings that were not discussed in previous chapter. The physical interpretation of this high-order terms in the Hamiltonian can be understood through the scattering interactions. In the context of collective spins with high spin numbers (larger than 1/2), an interaction resembling light-quadruple effects emerges. This interaction can be characterized by atoms transitioning from the ground state to a excited state, and subsequently decaying to a different ground state, as exemplified by multiple Zeeman levels transitions from $m_F : 4 \to 3 \to 2$, depicted in Fig.3.3 (a or b). The tensor polarizability of multilevel atoms during dispersive measurements has been thoroughly documented in the literature[64, 67–69]. This tensor interaction can lead to the scattering of elliptically polarized photons as a result of additional linear birefringence. Simultaneously, these tensor terms contribute to the tensor dynamic stark shift in neighbouring sub-Zeeman levels, and also plays a role in the dynamic cooling and broadening of the atomic spin system.

To achieve a through understanding of the tensor contributions to the interaction dynamics, consider a scenario with ideally linearly polarized probe light and the redefined light stokes operators $\hat{S}_0, \hat{S}_\parallel, \hat{S}_\perp, \hat{S}_z$. In this context, the input polarization is positioned at an angle α relative to the DC magnetic field orientation, characterized by $\langle \hat{S}_\parallel \rangle \approx \langle \hat{S}_0 \rangle$. Consequently, the operators including the tensor interaction terms can be reformulated. Specifically, $\hat{S}_x$ is recast as $\hat{S}_\parallel \cos(2\alpha) \sim \hat{S}_0 \cos(2\alpha)$, and a similar relationship applies to $\hat{S}_y :\sim \hat{S}_0 \sin(2\alpha)$. We could rewrite the tensor interaction Hamiltonian as:

$$\hat{H}_{tensor}/\hbar = g_S 2a_2 \hat{S}_0 \cdot \left(\underbrace{\hat{F}_z^2 - \left[\hat{F}_x^2 - \hat{F}_y^2 \right] \cos(2\alpha)}_{tensor\ shift} - \underbrace{\left[\hat{F}_x \hat{F}_y + \hat{F}_y \hat{F}_x \right] \sin(2\alpha)}_{tensor\ cooling/broadening} \right).$$
(3.24)

Upon calculating the expectation values of this Hamiltonian for the collective spin components along the quantized x-axis, we obtain:

$$\begin{aligned}
\left\langle m \left| \hat{F}_z^2 \right| m \right\rangle &= \frac{F(F+1) - m^2}{2}, \\
\left\langle m \left| \hat{F}_x^2 \right| m \right\rangle &= m^2, \\
\left\langle m \left| \hat{F}_y^2 \right| m \right\rangle &= \frac{F(F+1) - m^2}{2}, \\
\left\langle m \left| \hat{F}_x \hat{F}_y + \hat{F}_y \hat{F}_x \right| m \right\rangle &= 0.
\end{aligned}$$
(3.25)

The detailed calculation is provided page 155 of Jacob sherson's PhD thesis[70]. As a result, the energy shift for each Zeeman sub level induced by the tensor interaction terms can be expressed as:

$$E_m^{tensor}/\hbar = g_S a_2 \cdot S_0 \cdot \left[\frac{1 + 3\cos(2\alpha)}{2} \cdot m^2 - \frac{1 + \cos(2\alpha)}{2} F(F+1) \right]. \quad (3.26)$$

In addition to the Zeeman splitting induced by a bias magnetic field, it becomes apparent that the light-induced tensor Stark shift also influences the Zeeman transition frequency, denoted as Ω_t:

$$\frac{\Omega_{tensor}}{2\pi} = \frac{E_{m+1} - E_m}{\hbar} = \frac{\gamma_{cs} \lambda_{cs}^2}{32\pi} \frac{a_2}{\Delta} \frac{S_0}{A} (1 + 3\cos 2\alpha) [2m + 1]. \quad (3.27)$$

The magnitude of the tensor stark shift can be adjusted through various parameters, such as the laser power S_0, the detuning of probe light Δ, and the input polarization angle α. Interestingly, this light-induced tensor shift can be zeroed by selecting the angle at $\alpha \sim 54.7°$. Furthermore, this shift can also be employed to counterbalance the quadratic Zeeman splitting at higher Larmor frequencies where the multiple atomic resonances emerge. This approach effectively simplifies the atomic spin to resemble a two-level system, despite the presence of non-degenerate splitting within Zeeman sublevels [71].

Although the leftover term $(\hat{F}_x\hat{F}_y + \hat{F}_y\hat{F}_x)$ in the tensor interaction doesn't contribute to an additional light shift, it indicates distinct dynamics on atomic spins. Considering the atomic spins that are perfectly polarized at F =4, $m_F = 4$, the transition between $m_F = [4,3]$ acts as an ideal negative mass spin oscillator, the high-order components $(\hat{F}_x\hat{F}_y + \hat{F}_y\hat{F}_x)$ can be approximated as $(2m + 1)\hat{F}_y = 7\hat{F}_y$. Consequently, the detailed light-atom interaction Hamiltonian, including the oscillation, vector, and tensor terms, can be approximately described as follows:

$$\hat{H}_{L,S}/\hbar = \Omega_S F_x - \frac{\Omega_S}{2}(\hat{X}_S^2 + \hat{P}_S^2) + g_S\left(a_1\hat{S}_z\hat{F}_z - 14a_2\hat{S}_y\hat{F}_y\right). \qquad (3.28)$$

The aforementioned Hamiltonian, excluding the initial spin energy $\Omega_S F_x$, can be reformulated based on the previously defined quadrature operators $\hat{X}_S$, $\hat{P}_S$, $\hat{X}_L$, $\hat{P}_L$. It is important to note the inclusion of a negative sign in photon-atom coupling factor g_S (3.22) [43] :

$$\hat{H}_{L,S}/\hbar = -\frac{\Omega_S}{2}(\hat{X}_S^2 + \hat{P}_S^2) - \sqrt{\Gamma_S}(\hat{X}_S\hat{X}_L + \epsilon_S\hat{P}_S\hat{P}_L). \qquad (3.29)$$

Here we introduce the spin vector readout rate Γ_S and tensor interaction strength ϵ_S for simplicity:

$$\begin{aligned} \Gamma_S &= g_S^2 a_1^2 S_{\parallel} F_x, \\ \epsilon_S &= -14\frac{a_2}{a_1}\cos(2\alpha). \end{aligned} \qquad (3.30)$$

As illustrated in the Eq.(3.30), the strengths of the vector and tensor interactions,
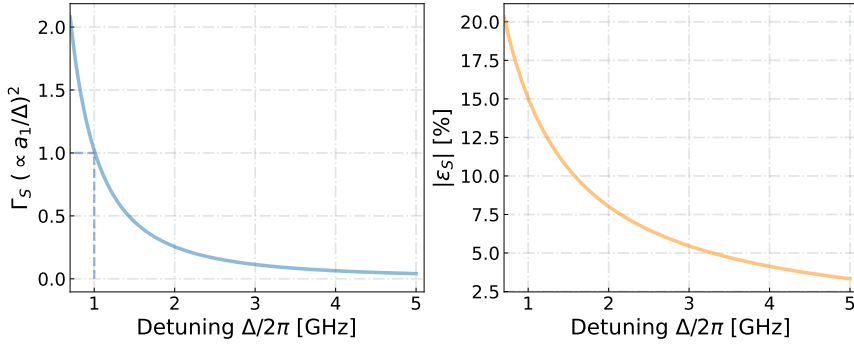
Figure 3.5: The readout rate and tensor interaction strength as functions of probe detuning. The blue curve on the left represents the dependency of the vector readout rate Γ_S varying with the probe detuning, used in our experiment, normalized to the readout rate at a 1 GHz detuning for clear visualization. The orange curve on the right indicates the tensor interaction strength relative to the vector readout rate at each corresponding detuning, $|\epsilon_S|$, over the same detuning range. It's noteworthy that the sign of ϵ_S can be adjusted based on the input polarization angle.

normalized to the vector readout rate as functions of the blue detuning with respect to the D2 line $F = 4 \to F' = 5$, are shown in Fig.3.5. Moreover, the sign of the tensor interaction can be controlled by the input polarization angle

α, enabling the adjustment of the light-atom interaction from the pure Quantum Non-Demolition (QND) vector interaction to the dynamic beam splitter (BS: cooling) or two-mode squeezing (TMS: anti-damplng) interaction, which can be described as follows: [72, 73].

$$\hat{H}_{L,S} / \hbar = -\sqrt{\Gamma_S} \left((1 + \epsilon_S) \underbrace{(\hat{a}_L \hat{b}_S^\dagger + \hat{a}_L^\dagger \hat{b}_S)}_{BS} + (1 - \epsilon_S) \underbrace{(\hat{a}_L \hat{b}_S + \hat{a}_L^\dagger \hat{b}_S^\dagger)}_{TMS} \right). \quad (3.31)$$

These high-order tensor terms are important in some quantum protocols, as they enable the achievement of quantum teleportation between two remote quantum systems. Further details on this topic can be found in the study on two atomic ensembles [53, 74] and spin-membrane entanglement [44, 75].

3.5 Quantum Heisenberg Langevin equation and I/O relationship

Given the above introduced systems along with their interaction Hamiltonian, we can now calculate the dynamics of spin oscillator and probe light influenced by the Hamiltonian. But before we delve into these calculations, we have to acknowledge that in practical experiments, both spins and light fields are unavoidably coupled to the environment. This interaction can lead to unanticipated 'loss' of the spin and optical variables. Taking atomic spins as example, various decay mechanism can happen through intrinsic decay like spin-wall collisions, atom losses to cell stem, atom-atom collision and light power dependent decay due to the spontaneous emission during the light-atom interaction. These mechanisms were discussed in detail on page 60 of Hanna's PhD thesis [72]. The complexity of properly accounting for all forms of dissipation and modeling associated interactions between the system and its surrounding bath environment is non-trivial. However, the challenge of dealing such open quantum system can be effectively addressed by using the quantum Langevin equation. This approach allows us to concentrate on deriving the target system dynamic under the effect of the environmental baths, without the necessity of solving the dynamics of the baths. In our analysis, the environmental thermal bath acts as an infinite thermal reservoir, without the temporal memory throughout the dynamic evolution. Such assumption can be mathematically characterized by a zero mean and delta-correlated noise in time. The Heisenberg equation of motion that describes a system operator $\hat{A}$ in a quantum system as it dissipates to a Markovian reservoir with decay rate $\hat{L}_k$, and experiences the stochastic driving force of a Langevin source $\hat{f}$, can

be written as (adapted from page 137 of Rodrigo's PhD thesis [49]):

$$\frac{\mathrm{d}}{\mathrm{d}t}\hat{A} = \frac{i}{\hbar}\left[\hat{H}_{L,S}, \hat{A}\right] + \sum_k \left[\hat{L}_k^+ \hat{A}\hat{L}_k - \frac{1}{2}\left\{\hat{L}_k^+\hat{L}_k, \hat{A}\right\}\right] + \sum_k \left[\hat{f}^\dagger\left[\hat{A}, \hat{L}_k\right] - \left[\hat{A}, \hat{L}_k^+\right]\hat{f}\right],$$
(3.32)

where $\hat{L}_k$ is the Lindblad operator that represents the decay of a quantum system into the environment through various channels, indexed by k. This operator specifies the dynamics of real physical dissipative processes, such as spontaneous emission or collective spin dephasing [76]. Correspondingly, these decay processes are associated with their respective Langevin noise forces $\hat{f}$. Consequently, we expect that the spin operators will decay in accordance with the Heisenberg-Langevin equation [77]:

$$\frac{d\hat{A}}{dt} = \frac{i}{\hbar}[\hat{H}, \hat{A}] - \frac{\gamma}{2}\hat{A} + \sqrt{\gamma}\hat{f}.$$
(3.33)

Now, if we start with a simple case including only the scalar and vector interaction terms, denoted as $\sim g_S(\hat{S}_0 + a_1\hat{S}_z\hat{F}_z)$, we proceed to calculate the time evolution of spin dynamics in the following manner (based on the derivation on page 29 of Rodrigo's thesis [49]):

$$\begin{aligned}
\frac{\mathrm{d}}{\mathrm{d}t}\hat{F}_x &= g_\mathrm{S}\hat{S}_z\hat{F}_y - \frac{\gamma_\mathrm{S}}{2}S_0\hat{F}_x + \sqrt{\gamma}\hat{f}_{Fx}, \\
\frac{\mathrm{d}}{\mathrm{d}t}\hat{F}_y &= -g_\mathrm{S}\hat{S}_z\hat{F}_x - \frac{\gamma_\mathrm{S}}{2}S_0\hat{F}_y + \sqrt{\gamma}\hat{f}_{Fy}, \\
\frac{\mathrm{d}}{\mathrm{d}t}\hat{F}_z &= -\frac{\gamma_\mathrm{S}}{2}\hat{S}_z\hat{F}_0 - \frac{\gamma_\mathrm{S}}{2}S_0\hat{F}_z + \sqrt{\gamma}\hat{f}_{Fz}, \\
\frac{\mathrm{d}}{\mathrm{d}t}\hat{F}_0 &= 0,
\end{aligned}$$
(3.34)

in the regime of QND interactions and assuming the depumping effect of circular component of probe is negligible, we can disregard the $\gamma_S/2\hat{S}_z\hat{F}_0$ component. In this context, the dynamic of each spin operators decay at the identical total decoherence rate γ_S. This total decay rate can be described as $\gamma_S = \gamma_0 + \gamma_{op} + \gamma_{pb}$, which encapsulates contribution from various sources: the intrinsic decay in the absence of light γ_0, optical pumping effects γ_{op}, and probe power broadening γ_{pb}, see further details on page 60 of Hanna thesis [72]. Notably, the decay rate attributable to power broadening is solely dependent on the total probe power $\hat{S}_0$ and is inversely proportional to the square of the probe detuning $\gamma_{pb} \sim 1/\Delta^2$.

Then we can perform the similar calculations to analyze the probe light operators. The rapid propagation speed of light allows us to neglect the retardation effects, thereby leaving out the time derivation $\frac{\mathrm{d}}{\mathrm{d}t}$ term as discussed in page 29 of Rodrigo's PhD thesis[49]. Consequently, the evolution of light variables can

be described as:

$$\frac{\mathrm{d}}{\mathrm{d}z}\hat{S}_x = -g_S\hat{S}_y\hat{F}_z,$$
$$\frac{\mathrm{d}}{\mathrm{d}z}\hat{S}_y = g_S\hat{S}_x\hat{F}_z,$$
$$\frac{\mathrm{d}}{\mathrm{d}z}\hat{S}_z = 0, \tag{3.35}$$
$$\frac{\mathrm{d}}{\mathrm{d}z}\hat{S}_0 = 0.$$

In this interaction scenario, the decay effects on light operators and their associated noise forces are neglected due to minimal absorption. Meanwhile, the detailed equations of motion, incorporating complex higher-order interaction terms, are elaborated in Brain Julsgaard PhD's thesis.[4].

Considering the above scenario where symmetric decay is present in both canonical position ($\hat{X}_S$) and momentum ($\hat{P}_S$) operators (derived from $\hat{F}_z$ and $\hat{F}_y$), it is feasible to formulate these complex equations of motion. Moreover, by applying the effective quadrature interaction Hamiltonian eq.(3.28), inclusive of the tensor term, together with the introduced rotating wave approximated Heisenberg-Langevin equations eq.(3.33) , the equation of motion for atomic spin operators can now be re-expressed in a matrix form[5]:

$$\frac{\mathrm{d}}{\mathrm{d}t}\begin{pmatrix} \hat{X}_{\mathrm{S}}(t) \\ \hat{P}_{\mathrm{S}}(t) \end{pmatrix} = \begin{pmatrix} -\gamma_{\mathrm{S}}/2 - \epsilon_S\Gamma_{\mathrm{S}} & \Omega_{\mathrm{S}} \\ -\Omega_{\mathrm{S}} & -\gamma_{\mathrm{S}}/2 - \epsilon_S\Gamma_{\mathrm{S}} \end{pmatrix}\begin{pmatrix} \hat{X}_{\mathrm{S}}(t) \\ \hat{P}_{\mathrm{S}}(t) \end{pmatrix}$$
$$+ \sqrt{\Gamma_{\mathrm{S}}}\begin{pmatrix} 0 & -\epsilon_S \\ 1 & 0 \end{pmatrix}\begin{pmatrix} \hat{X}_{\mathrm{L}}(t) \\ \hat{P}_{\mathrm{L}}(t) \end{pmatrix} + \sqrt{\gamma_{\mathrm{S}}}\begin{pmatrix} \hat{F}_{\mathrm{S}}^X(t) \\ \hat{F}_{\mathrm{S}}^P(t) \end{pmatrix}, \tag{3.36}$$

where $\hat{F}_S^X$ and $\hat{F}_S^P$ are the effective Langevin noise forces. The first matrix on the right side of the equation indicates the Larmor precession (oscillation) of the spin operators and their associated decoherence. The decay rate now described as $\gamma_{\mathrm{S}}/2$ after the Holstein-Primakoff approximation includes the intrinsic decay of the spin and the broadening effects due to the QND probe power and optical pumping. The term $\epsilon_S\Gamma_S$ denotes the tensor dynamic broadening. The second matrix corresponds to the vector (or QND) and tensor back-action perturbation from the light operators. The final terms represent the decay-associated Langevin force, also referred to as the spin projection and thermal forces. As the integration along z-axis is reflected by the collective properties of atomic spins, the output light operator can be acquired from the input variables combined with the terms

---

[4]The comprehensive propagation equations for the spin operators can be found in Brian Julsgaard PhD thesis in page 42. The decoherence aspects can be found on page 27 of Rodrigo thesis, along with the Quantum noise for Faraday light matter interfaces paper

[5]Here we assume the tensor term only impacts the spin oscillation and dynamic back action but not the coupling to thermal baths

recorded from the atomic spins:

$$
\begin{pmatrix} \hat{X}_{\mathrm{L}}^{\mathrm{out}}(t) \\ \hat{P}_{\mathrm{L}}^{\mathrm{out}}(t) \end{pmatrix} = \begin{pmatrix} \hat{X}_{\mathrm{L}}^{\mathrm{in}}(t) \\ \hat{P}_{\mathrm{L}}^{\mathrm{in}}(t) \end{pmatrix} + \sqrt{\Gamma_{\mathrm{S}}} \begin{pmatrix} 0 & -\epsilon_S \\ 1 & 0 \end{pmatrix} \begin{pmatrix} \hat{X}_{\mathrm{S}}(t) \\ \hat{P}_{\mathrm{S}}(t) \end{pmatrix}. \tag{3.37}
$$

Then we can apply the Fourier transformation: $[\mathrm{F}(\frac{\mathrm{d}}{\mathrm{d}t}\hat{X}_S(t)) = -i\Omega\hat{X}_S(\Omega),$ $\mathrm{F}(\frac{\mathrm{d}}{\mathrm{d}t}\hat{P}_S(t)) = -i\Omega\hat{P}_S(\Omega)]$ to the above equations of motion. The input-output relationship in frequency domain for spin operators facilitates a more detailed understanding of the system's dynamics. For simplicity, $\hat{P}$ will be used hereafter instead of $\hat{P}(\Omega)$:

$$
\begin{pmatrix} \gamma_{\mathrm{S}}/2 + \epsilon_S\Gamma_{\mathrm{S}} - \mathrm{i}\Omega & -\Omega_{\mathrm{S}} \\ \Omega_{\mathrm{S}} & \gamma_{\mathrm{S}}/2 + \epsilon_S\Gamma_{\mathrm{S}} - \mathrm{i}\Omega \end{pmatrix} \begin{pmatrix} \hat{X}_{\mathrm{S}} \\ \hat{P}_{\mathrm{S}} \end{pmatrix} = \sqrt{\Gamma_{\mathrm{S}}} \begin{pmatrix} 0 & -\epsilon_S \\ 1 & 0 \end{pmatrix} \begin{pmatrix} \hat{X}_{\mathrm{L}}^{in} \\ \hat{P}_{\mathrm{L}}^{in} \end{pmatrix} + \sqrt{\gamma_{\mathrm{S}}} \begin{pmatrix} \hat{F}_{\mathrm{S}}^{\mathrm{X}} \\ \hat{F}_{\mathrm{S}}^{\mathrm{P}} \end{pmatrix}.
$$
$$\tag{3.38}$$

We are now in a position to represent the matrix in a more compact notation:

$$
\begin{pmatrix} \hat{X}_{\mathrm{S}} \\ \hat{P}_{\mathrm{S}} \end{pmatrix} = \sqrt{\Gamma_{\mathrm{S}}}\mathbf{L}\mathbf{Z} \begin{pmatrix} \hat{X}_{\mathrm{L}}^{\mathrm{in}} \\ \hat{P}_{\mathrm{L}}^{\mathrm{in}} \end{pmatrix} + \mathbf{L}\sqrt{\gamma_{\mathrm{S}}} \begin{pmatrix} \hat{F}_{\mathrm{S}}^{X} \\ \hat{F}_{\mathrm{S}}^{P} \end{pmatrix}, \tag{3.39}
$$

In this equation, the matrices within the above formula are defined as follows:

$$
\mathbf{Z} = \begin{pmatrix} 0 & -\epsilon_S \\ 1 & 0 \end{pmatrix}, \tag{3.40}
$$

and the matrix $\mathbf{L}$ indicates the spin oscillator dynamics within frequency domain, and can be written in a more transparent form through susceptibilities $\chi_S(\Omega)$ and $\rho_S(\Omega)$, which describe the response of spin oscillator to the external forces. [6]:

$$
\mathbf{L} = \begin{pmatrix} \gamma_{\mathrm{S}}/2 + \epsilon_S\Gamma_{\mathrm{S}} - i\Omega & \Omega_{\mathrm{S}} \\ -\Omega_{\mathrm{S}} & \gamma_{\mathrm{S}}/2 + \epsilon_S\Gamma_{\mathrm{S}} - i\Omega \end{pmatrix}^{-1} = \begin{pmatrix} \rho_{\mathrm{S}}(\Omega) & \chi_{\mathrm{S}}(\Omega) \\ -\chi_{\mathrm{S}}(\Omega) & \rho_{\mathrm{S}}(\Omega) \end{pmatrix}.
$$
$$\tag{3.41}$$

The spin susceptibilities $\chi_S(\Omega)$ and $\rho_S(\Omega)$ are defined as:

$$
\chi_{\mathrm{S}}(\Omega) = \frac{\Omega_{\mathrm{S}}}{\Omega_{\mathrm{S}}^2 - \Omega^2 - i\Omega\left(\gamma_{\mathrm{S}} + 2\Gamma_{\mathrm{S}}\epsilon_S\right) + \left(\gamma_{\mathrm{S}} + 2\Gamma_{\mathrm{S}}\epsilon_S\right)^2/4},
$$
$$
\rho_{\mathrm{S}}(\Omega) = \frac{\left(\gamma_{\mathrm{S}} + 2\Gamma_{\mathrm{S}}\epsilon_S\right)/2 - i\Omega}{\Omega_{\mathrm{S}}^2 - \Omega^2 - i\Omega\left(\gamma_{\mathrm{S}} + 2\Gamma_{\mathrm{S}}\epsilon_S\right) + \left(\gamma_{\mathrm{S}} + 2\Gamma_{\mathrm{S}}\epsilon_S\right)^2/4},
$$
$$\tag{3.42}$$

---

[6]The inverse of a matrix can be calculated based on the following formula:
$\mathbf{L} = \begin{bmatrix} a & b \\ c & d \end{bmatrix}^{-1} = \frac{1}{ad-bc}\begin{bmatrix} d & c \\ b & a \end{bmatrix}$

the total spin linewidth now includes the tensor dynamic broadening, expressed as $\gamma_S/2 + \Gamma_S\epsilon_S$. As shown in eq.(3.39), the matrix $\mathbf{L}$ helps to map the input light noise and atomic thermal/projection noise forces onto the output spin oscillator. Similarly, we can achieve the equation of motion for light variables within the frequency domain, reads as:

$$
\begin{aligned}
\begin{pmatrix} \hat{X}_{\mathrm{L}}^{\mathrm{out}} \\ \hat{P}_{\mathrm{L}}^{\mathrm{out}} \end{pmatrix}
&= [\mathbf{1}_2 + \Gamma_{\mathrm{S}}\mathbf{ZLZ}]\begin{pmatrix} \hat{X}_{\mathrm{L}}^{\mathrm{in}} \\ \hat{P}_{\mathrm{L}}^{\mathrm{in}} \end{pmatrix} + \sqrt{\Gamma_{\mathrm{S}}\gamma_{\mathrm{S}}}\mathbf{ZL}\begin{pmatrix} \hat{F}_{\mathrm{S}}^X \\ \hat{F}_{\mathrm{S}}^P \end{pmatrix} \\
&= \left[\mathbf{1}_2 + \Gamma_{\mathrm{S}}\begin{pmatrix} -\epsilon_{\mathrm{S}}\rho_{\mathrm{S}} & -\epsilon_{\mathrm{S}}^2\chi_{\mathrm{S}} \\ \chi_{\mathrm{S}} & -\epsilon_{\mathrm{S}}\rho_{\mathrm{S}} \end{pmatrix}\right]\begin{pmatrix} \hat{X}_{\mathrm{L}}^{\mathrm{in}} \\ \hat{P}_{\mathrm{L}}^{\mathrm{in}} \end{pmatrix} \\
&\quad + \sqrt{\Gamma_{\mathrm{S}}\gamma_{\mathrm{S}}}\begin{pmatrix} \epsilon_{\mathrm{S}}\chi_{\mathrm{S}} & -\epsilon_{\mathrm{S}}\rho_{\mathrm{S}} \\ \rho_{\mathrm{S}} & \chi_{\mathrm{S}} \end{pmatrix}\begin{pmatrix} \hat{F}_{\mathrm{S}}^X \\ \hat{F}_{\mathrm{S}}^P \end{pmatrix}.
\end{aligned}
\tag{3.43}
$$

Then, we could incorporate the Stokes operator detection scheme demonstrated in Fig.3.4 to select the measured Stokes operators or quadrature operators. With the application of quarter and half wave-plates, we can adjust the polarization ellipticity, thereby allowing for the mixing of two quadrature operators. The rotation matrix, indicating the homodyne detection angle ϕ, is defined as follows:

$$
\mathbf{R}_\phi = \begin{pmatrix} \cos(\phi) & -\sin(\phi) \\ \sin(\phi) & \cos(\phi) \end{pmatrix}.
\tag{3.44}
$$

The detected quadrature operators $\hat{\mathbf{X}}_L^{det}$ are now described as follows:

$$
\hat{\mathbf{X}}_{\mathbf{L}}^{\mathrm{det}} = \begin{pmatrix} \hat{X}_{\mathrm{L}}^{\mathrm{det}} \\ \hat{P}_{\mathrm{L}}^{\mathrm{det}} \end{pmatrix} = \mathbf{R}_\phi\begin{pmatrix} \hat{X}_{\mathrm{L}}^{\mathrm{out}} \\ \hat{P}_{\mathrm{L}}^{\mathrm{out}} \end{pmatrix} = \begin{pmatrix} \cos(\phi)\hat{X}_{\mathrm{L}}^{\mathrm{out}} - \sin(\phi)\hat{P}_{\mathrm{L}}^{\mathrm{out}} \\ \sin(\phi)\hat{X}_{\mathrm{L}}^{\mathrm{out}} + \cos(\phi)\hat{P}_{\mathrm{L}}^{\mathrm{out}} \end{pmatrix}.
\tag{3.45}
$$

We have successfully derived the final expressions for the equations of motion for the light and spin oscillators within frequency domain. This includes the input-output relationship that describes the dynamics of atomic spins are recorded by the output of light, as well as the Stokes detection mechanism that can facilitate the interference of two quadrature components. In the coming section, we will explore a new technique named spin noise spectroscopy (SNS) that can enhance our understanding of the dynamic of steady-state atomic spins.

3.6 Spin noise spectrum

Given that measurements of spin systems in our experiments are inherently constrained by the quantum mechanical uncertainty (3.12) and involve a finite number of atomic spins, confined with the vapor cell, undergoing stochastic motion (to maintain the thermal equilibrium of the system), they inevitably exhibit pro-

jection fluctuations in the recorded spin signal. Spin noise spectroscopy (SNS) is a powerful approach to obtaining insights into the dynamics of such spin fluctuations, as outlined in the work [78]. We now turn our attention to analyzing the power spectral density (PSD) of the detected light quadrature for a better understanding of spin fluctuations. The PSD of light phase quadrature is given by the symmetrized correlation function:

$$\overline{S}_{\text{pp}}^{det}\delta(\Omega - \Omega') = \frac{1}{2}\left\langle \hat{P}_{\text{L}}^{det}(\Omega)\hat{P}_{\text{L}}^{det,\dagger}(\Omega') + \hat{P}_{\text{L}}^{det,\dagger}(\Omega')\hat{P}_{L}^{det}(\Omega) \right\rangle. \qquad (3.46)$$

In this context, the notation $\langle \cdot \rangle^{\dagger}$ denotes the Hermitian conjugate of a quadrature operator (or complex conjugate transposition in the matrix representation). By combining the symmetrized power spectral density with the linear matrix equations of motion for light and spin operators, we can calculate the PSD of detected light quadrature once the fluctuation of input noise operators are known. Fortunately, the input light fluctuation and thermal baths can be deduced from the commutation relations, providing a foundational basis for these calculations:

$$\overline{S}_{\text{X}_{\text{L}}\text{X}_{\text{L}}^{\dagger}}^{\text{in}} = \overline{S}_{\text{P}_{\text{L}}\text{P}_{\text{L}}^{\dagger}}^{\text{in}} = \frac{1}{2}\delta(\Omega - \Omega'), \qquad (3.47)$$

$$\overline{S}_{F_{\text{S}}^{\text{X}}F_{\text{S}}^{\text{X},\dagger}}^{\text{in}} = \overline{S}_{F_{\text{S}}^{\text{P}}F_{\text{S}}^{\text{P},\dagger}}^{\text{in}} = \gamma_{\text{S}}(n_S + \frac{1}{2})\delta(\Omega - \Omega'). \qquad (3.48)$$

In this case, n_S signifies the effective thermal occupation, which is directly linked to the degree of spin polarization. This relationship will be further explored in the subsequent section. The inclusion of the factor $\frac{1}{2}$ accounts for the ground state of spin thermal fluctuations, commonly known as the projection noise. This term represents the inherent quantum mechanical uncertainty in the spin state, serving as a fundamental limit to the precision in projective spin measurements [79]. Hence, we can write down the complete model for the recorded spin oscillator as follows:

$$\overline{S}_{\text{L},\phi}^{\text{det}} =$$

$$\overbrace{\left(1 + \Gamma_S^2\epsilon_S^2|\rho_S|^2 - 2\Gamma_S\epsilon_S\,\text{Re}\,[\rho_S]\right)\sin\phi^2 + \left(\Gamma_S\,\text{Re}\,[\chi_S] - \Gamma_S^2\epsilon_S\,\text{Re}\,[\chi_S\rho_S^*]\right)\sin 2\phi + \Gamma_S^2|\chi_S|^2\cos\phi^2}^{\left\langle \hat{X}_{\text{L}}^{\text{in}}\hat{X}_{\text{L}}^{\text{in},\dagger} \right\rangle} +$$

$$\overbrace{\left(1 + \Gamma_S^2\epsilon_S^2|\rho_S|^2 - 2\Gamma_S\epsilon_S\,\text{Re}\,[\rho_S]\right)\cos\phi^2 + \left(-\Gamma_S\epsilon_S^2\,\text{Im}\,[\chi_S] + \Gamma_S^2\epsilon_S^3\,\text{Im}\,[\chi_S\rho_S^*]\right)\sin 2\phi + \Gamma_S^2\epsilon^4|\chi_S|^2\sin\phi^2}^{\left\langle \hat{P}_{\text{L}}^{\text{in}}\hat{P}_{\text{L}}^{\text{in},\dagger} \right\rangle}$$

$$+ \underbrace{\Gamma_{\text{S}}\left(|\rho_{\text{S}}|^2 + |\chi_{\text{S}}|^2\right)\gamma_{\text{S}}\left(n_{\text{S}} + \frac{1}{2}\right)\left(\cos^2(\phi) + \epsilon_{\text{S}}^2\sin^2(\phi)\right)}_{\left\langle F_{\text{S}}^{\text{X}}F_{\text{S}}^{\text{X},\dagger} \right\rangle = \left\langle F_{\text{S}}^{\text{P}}F_{\text{S}}^{\text{P},\dagger} \right\rangle}.$$

$$(3.49)$$

To understand the preceding complex expression, we can deconstruct the detected noise spectra into three primary contributions: shot and backaction noise, which stem from the X quadrature of y-polarized light; shot and back-action noise originating from the P-quadrature, and spin thermal noise imprinted onto the output

quadrature. Notably, both the X and P quadrature contributions are influenced by terms proportional to $\sin(2\phi)$. By carefully selecting the detection angle, it is possible to induce destructive interference that mitigates the impact of light shot and quantum backaction noise associated with respective light sources.

An important scenario occurs when the spin oscillator functions within the Quantum Non-Demolition (QND) interaction regime-where the light only measures the position X of the spin oscillator with $\epsilon_S = 0$. This constitutes a complete QND measurement considering a harmonic oscillator with zero oscillation frequency, and is scheduled for the quantum noise reduction [45]. In this case, the equation can be simplified to:

$$
\overline{S}_{\text{QND},\phi}^{\text{det}} = \overbrace{(1)\sin\phi^2 + \Gamma_{\tilde{S}}^2|\chi_{\text{S}}|^2\cos\phi^2 + \Gamma_S\,\text{Re}\,[\chi_{\text{S}}]\sin 2\phi}^{\left\langle \hat{X}_{\text{L}}^{\text{in}}\hat{X}_{\text{L}}^{\text{in},\dagger}\right\rangle} + \overbrace{(1)\cos\phi^2}^{\left\langle \hat{P}_{\text{L}}^{\text{in}}\hat{P}_{\text{L}}^{\text{in},\dagger}\right\rangle}
$$
$$
+ \underbrace{\Gamma_{\text{S}}\left(|\rho_{\text{S}}|^2 + |\chi_{\text{S}}|^2\right)\gamma_{\text{S}}\left(n_{\text{S}} + \frac{1}{2}\right)\left(\cos^2(\phi)\right)}_{\left\langle \hat{F}_{\text{S}}^{\text{X}}\hat{F}_{\text{S}}^{\text{X},\dagger}\right\rangle = \left\langle \hat{F}_{\text{S}}^{\text{P}}\hat{F}_{\text{S}}^{\text{P},\dagger}\right\rangle}.
$$

(3.50)

Simplifying the expression, we are left with the shot noise of light from the phase quadrature contribution, which is rescaled by $\cos\phi^2$. From the light amplitude quadrature, we could observe that both the shot and backaction noise can interfere via the cross correlation term $\Gamma_{\text{S}}\text{Re}[\chi_{\text{S}}]\sin 2\phi$. By appropriately selecting the detection angle ϕ, it is possible to achieve noise levels below the angle-independent shot noise of light, expressed as $\overline{S}_{\text{X}_{\text{L}}\text{X}_{\text{L}}^{\dagger}}^{\text{in}}\cos\phi^2 + \overline{S}_{\text{P}_{\text{L}}\text{P}_{\text{L}}^{\dagger}}^{\text{in}}\sin\phi^2$, thereby enabling light squeezing. Furthermore, this cross-correlation emerges from the motion of collective spin oscillator, primarily driven by the intensity fluctuation in the light-induced radiation pressure, as evident from its transfer through the real part of atomic susceptibility. This phenomenon, also known as ponderomotive squeezing [80], arising from the light fluctuation induced quantum cross-correlation, provides a useful tool for calibrating the quantum backaction noise in our spin systems. When the PSD is normalized to the light shot noise $\overline{S}_{\text{P}_{\text{L}}\text{P}_{\text{L}}^{\dagger}}^{\text{in}}$, denoted as $1/2$, the expression for the spin noise spectrum with the Quantum Non-Demolition (QND) regime, in terms of shot noise units[7], can now be articulated as follows:

$$
\overline{S}_{QND,\phi}^{\text{det}}/\text{SN} = 1 + \overbrace{\Gamma_{\text{S}}^2\,|\chi_{\text{S}}(\Omega)|^2\cos^2(\phi)}^{\text{QBAN}} + \overbrace{\Gamma_{\text{S}}\,\text{Re}\,[\chi_{\text{S}}(\Omega)]\sin(2\phi)}^{\text{Correlations}}
$$
$$
+ \underbrace{2\gamma_{\text{S}}\Gamma_S\left(|\rho_{\text{S}}(\Omega)|^2 + |\chi_{\text{S}}(\Omega)|^2\right)\left(n_{\text{S}} + \frac{1}{2}\right)\cos^2(\phi)}_{\text{TN}}.
$$

(3.51)

---

[7]Although the PSD is normalized to shot noise, it is worth noting the shot noise originates from two distinct quadratures

Furthermore, when the detection angle is set at $\phi = 0$, such that we are only monitoring the phase quadrature of light, we can observe the maximum atomic spin thermal noise and induced quantum backaction noise. The equation now reads as :

$$\overline{S}_{QND,\phi\to0°}^{\det}/\mathrm{SN} = 1 + \overbrace{\Gamma_{\mathrm{S}}^2 |\chi_{\mathrm{S}}(\Omega)|^2}^{\mathrm{QBAN}} + \overbrace{2\gamma_{\mathrm{S}}\Gamma_S \left(|\rho_{\mathrm{S}}(\Omega)|^2 + |\chi_{\mathrm{S}}(\Omega)|^2 \right) \left(n_{\mathrm{S}} + \frac{1}{2} \right)}^{\mathrm{TN}}. \tag{3.52}$$

Now we approach the scenario desirable for canceling quantum noise in gravitational wave detectors, as previously discussed at the end of Chapter Two. The contributors to the spin noise spectrum, presented in Fig.3.6 (a), from the left to right, are: the light shot noise from the light phase (P) quadrature (illustrated by the blue curve), quantum backaction noise from the light amplitude (X) quadrature (depctied by the purple curve), and atomic spin thermal noise (represented by the green curve). Considering the proposal of the quantum noise reduction, only the shot noise (SN) and quantum backaction noise (QBAN) are entangled with the quantum noise in other interferometer arms via the produced entangled source. In contrast, the intrinsic atomic thermal fluctuations will incoherently imprint on the spin noise signal, compromising the quantum noise cancellation. Consequently, it becomes crucial to introduce a new quantity termed quantum cooperativity C_q^S, which quantifies the dominance of quantum backaction noise in the spin noise spectrum over spin thermal noise by comparing their ratio.

Assume we only evaluate around the atomic Larmor frequency ($\Omega \approx \Omega_S$), with the spin decoherence being significantly smaller (by an order of magnitude) compared to the atomic resonance ($\gamma_S \ll \Omega_S$). In this scenario[8], we can make the following approximation, such that $|\chi_S|^2 + |\rho_S|^2 \sim 2|\chi_S|^2$, then we arrive at the expression for quantum cooperativity as follows:

$$C_q^S = \frac{\overline{S}_{\mathrm{QBAN}}}{\overline{S}_{\mathrm{TN}}} = \frac{\Gamma_{\mathrm{S}}^2 |\chi_{\mathrm{S}}|^2}{2\Gamma_{\mathrm{S}}\gamma_{\mathrm{S}} \left(|\chi_{\mathrm{S}}|^2 + |\rho_{\mathrm{S}}|^2 \right) (1/2 + n_S)} = \frac{\Gamma_S}{4\gamma_S(1/2 + n_S)} \sim \rho\sigma_0 L. \tag{3.53}$$

We assume a perfect polarized atomic ensemble probed with a large-detuned, intensely linearly polarized light, and consider a scenario where probe power decoherence dominates other decay mechanisms. The total decoherence can be approximated as probe power broadening $\gamma_S \sim \gamma_{prob}$, scaling similarly to the readout rate Γ_S. In this case, the quantum cooperativity can be approximately expressed in terms of absorption cross section $\sigma_0 = \frac{3\lambda^2}{2\pi}$, atomic vapor density ρ

---

[8]As previously described, focusing only around the spin resonance ($\Omega \sim \Omega_S$), the susceptibilities above can be further simplified to:

$$\chi_S(\Omega) \approx \frac{1}{2} \frac{1}{\Omega_S - \Omega - i(\frac{\gamma_S}{2})},$$
$$\rho_S(\Omega) \sim -i\chi_S(\Omega),$$

Consequently, the absolute squares of these equations follow a Lorentzian function.

and the length of the vapor cell L (detailed on page 37 of Rodrigo's thesis [49]). Therefore, the quantum cooperativity can be enhanced by increasing either the atomic density or the length of the vapor cell.

As presented in eq.(3.51), a deviation from $\phi = 0$ introduces the cross-correlation term $\Gamma_S \operatorname{Re} \chi_S(\Omega)$, a proper choice of $\sin 2\phi$ makes the correlation term negative, facilitating destructive interference between the shot and backaction noise. This interference manifests as a dispersive feature in spin noise spectrum, illistrated in Fig.3.6 (b). With sufficiently small atomic thermal noise-as depicted by the down-scaled green curve, the total detected spin noise drops below the shot noise within a specific sideband frequency range, thereby producing pondermotive squeezing, as seen in the purple curve in the same figure. However, finite detection efficiency and optical loss η during the propagation will replace the recorded spin noise signal with the uncorrelated vacuum noise. This loss inevitably reduces the measured level of pondermotive squeezing:

$$\frac{\overline{S}_{\mathrm{QND}}^{\mathrm{det}}}{\mathrm{SN}} \gtrsim \eta \frac{\overline{S}_{\mathrm{QND},\phi}^{\mathrm{out}}}{\mathrm{SN}} + (1 - \eta). \tag{3.54}$$

In the regime where $\gamma_S \ll \Gamma_S, \Omega_S$, the maximal pondermotive squeezing achievable[81], given an optimized detection phase, can be attainable in terms of quantum cooperativity and finite overall detection efficiency. This maximum observable squeezing bound can be approximately by the following expression (adapted from the expressions described on page 103 of Muller's PhD [20] and page 22 of Junxing's PhD thesis [82]). As indicated by the purple curve in Fig.3.6 (b), the measured ponder-motive squeezing can closely approach this bound with sufficiently high quantum cooperativity:

$$\frac{\overline{S}_{\mathrm{sq}}^{\mathrm{det}}}{\mathrm{SN}} \gtrsim 1 - \eta \frac{\Gamma_S}{\Gamma_S + 4\gamma_S(1/2 + n_S)} \gtrsim 1 - \eta \frac{C_q^S}{1 + C_q^S}. \tag{3.55}$$
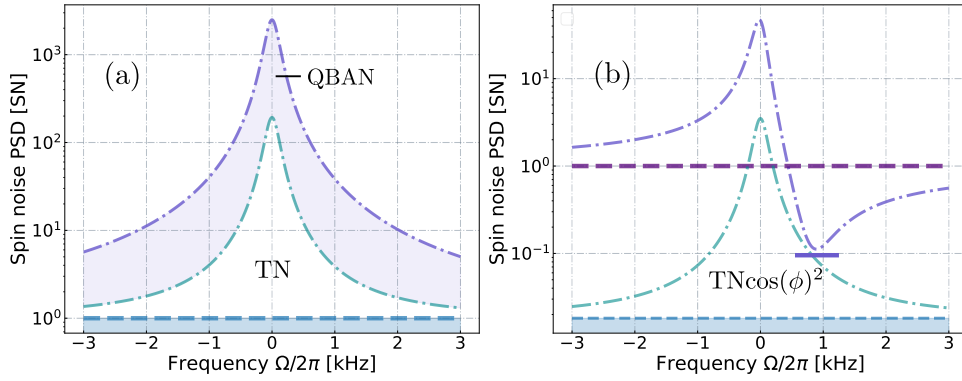
Figure 3.6: Spin noise spectrum and pondermotive squeezing. The power spectrum density of the recorded spin oscillator in shot noise units, is analyzed for detection angle $\phi = 0$ (a) and $\phi = 0.45\pi$ (b). The phase quadrature's shot noise is represented by the blue curve, while the quantum backaction noise from amplitude quadrature, highlighted by the purple area between the total spin noise (the purple curve) and atomic thermal noise (area below the green curve). Altering the detection angle reduces the effective thermal noise and the original shot noise from the phase quadrature but introduce the shot noise from amplitude quadrature, thereby facilitating the interference among the amplitude shot noise and backaction noise, leading to ponderomtive squeezing, as illustraed in Fig.(b). In this analysis, the quantum cooperativity C_q is set to 10, with a readout rate of 12kHz, total decay rate is 0.3 kHz, and an applied thermal occupation of approximately $n_S : 0.5$.

We have discussed that optimal pondermotive squeezing is attained by selecting the appropriate detection phase for specific sideband frequencies, which directly links to the crucial parameter-quantum cooperativity. Therefore, in our experiments, this relation also facilitates a cross-validation method for calibrating the quantum backaction noise. For readers seeking further details on the maximum achievable squeezing across various Fourier frequencies, the corresponding detection phases, and the bandwidth of pondermotive squeezing, we would direct them to the following literature [83, 84].

3.7 Projection noise and effective thermal occupation

As we just demonstrated, in addition to quantum noise (shot and backaction) transferred from the light fluctuations, the total spin noise spectrum also includes atomic thermal noise (shown as the area below the green curve in Fig.3.6). This additional uncorrelated noise projects onto the entangled light and impacts its ability to reduce broadband quantum noise as a noise eater. We now revisit the atomic total noise to explore its origin and provide a method to characterize this supplementary thermal noise.

First, we review the concept of 'shot noise' for atom, also known as projection noise. This entails performing a projective measurement of the transverse component of collective atomic spins, with the atomic system's quantum state initially

aligned along the longitudinal axis. This projection noise results from the collapse (knowledge lost) of the prepared two-level superposition quantum state in the transverse basis (comprising ground and excite states) into one of two states (either ground or excite state) [85]. Assume a simplistic two-level system consisting of N independent electron spins (1/2), the mean measurement outcome will be binomially distributed, with its variance, indicative of uncertainty, being proportional to $\sqrt{N\hbar/2}$ (assuming $\hbar = 1$ for simplicity). However, in the context of our actual experiments, the cesium atomic ensemble cannot be simply modeled as two-level systems. The presence of large total angular momentum, coupled with a nonzero nuclear spin $I = \frac{7}{2}$, complicates the modeling. Preparing atoms in other hyperfine (or even Zeeman) manifolds can introduce additional thermal noise during projection measurement, causing the uncertainty of projective measurement to conform to a complex multinomial distribution. Furthermore, atoms in a thermal state that remain unpolarized are not sensitive to the probe light fluctuation of interest. This significantly reduces the quantum backaction, thereby decreasing the quantum cooperativity that is crucial for our project.

In practice experiments, spin relaxation and dephasing are induced by inevitable environmental interactions, such as inhomogeneous magnetic fields and collisions with spins and anti-relaxation coatings. These interactions randomly perturb the prepared quantum atomic state, resulting in dynamic resembling diffusive spin behavior driven by random Langevin forces, as detailed in the study on [64]. According to the fluctuation-dissipation theorem in eq.(3.36), this relaxation related dissipation 'amplifies' the atomic thermal noise with decoherence rate γ_S, contributing to the overall observed total spin noise.
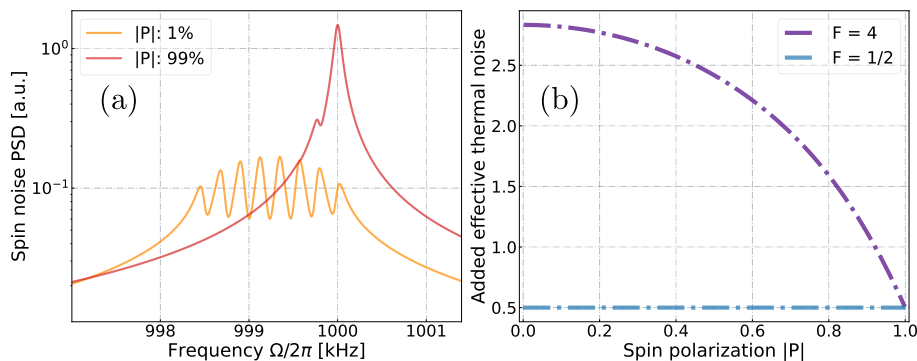
Figure 3.7: The spin noise spectrum density (a), along with added atomic thermal noise as function of spin polarization (b). Fig.(a) illustrates the atomic spin noise signals for atoms with total spin F = 4, depicted in an orange curve for a thermal state with spin polarization of $|P| \sim 1\%$ and in a red curve for nearly coherent spin state with $|P| \sim 99\%$. Fig.(b) reveals that additional spin thermal noise arises due to large total spin and imperfect spin polarization. In scenarios of perfect spin polarization, atomic spins exhibit minimal projective atomic noise, characteristic of a pure spin-1/2 system.

In our experiment, we could apply optical pumping to excite spin electrons among different electronic levels before or during the probe interaction, eventually transferring all electrons to one of extreme Zeeman levels. This process can be linked to creating an effective two-level system, as the simulated spin noise signal with two different degrees of spin polarization demonstrated in Fig.3.7 (a), where the orange and red curve represent a nearly atomic thermal state or an ideal coherent spin state, respectively. A high degree of spin polarization, indicative of the optical pumping 's efficiency, helps to mitigate this additional atomic thermal noise. This optical pumping method enables us to prepare the atomic states that closely mimic a coherent atomic state, even for large total spins like F =4 in our project. The relationship between the measured atomic thermal noise and the degree of atomic spin polarization has been extensively studied on page 55 of Rodrigo PhD thesis [49] and page 231 of Gorgios PhD thesis [86]. Under the condition that there are no coherence among atomic spins in the quantization basis, which is achieved by the spin-exchange collisions or damping of spin via the optical pumping, the atomic ground-state population attains thermal equilibrium, as discussed on page 47 of Lee's PhD thesis [87]. This equilibrium can be described by the Boltzmann distribution, allows us to define the Zeeman level populations according to the spin temperature distributions:

$$\rho_{th}(F,m) = \frac{e^{\beta m}}{Z},\tag{3.56}$$

where $Z = \sum_{m=-F}^{F} e^{\beta m}$ is the partition normalization function, and $\beta = 1/k_B T_S$ incorporates the effective spin temperature T_S with Boltzmann constant k_B. This parameter β is linked to another important parameter-spin polarization P, which quantifies the relative ratio of the mean atomic spin along the prepared quantization x-axis (bias magnetic field) to the total atomic spin F, as shown below:

$$P = \frac{\langle F_x \rangle}{F} = \frac{1}{ZF} \sum_{m=-F}^{F} m e^{\beta m},$$
$$\beta = \log\left(\frac{1 + |P|}{1 - |P|}\right).\tag{3.57}$$

Thus, in a real spin F =4 atomic system, the variance of the transverse components and the effective atomic thermal occupation n_s, influenced by the atomic spin polarization, can be expressed as follows (the detailed derivation is provided

on page 56 of Rodrigo's PhD thesis) [49]:

$$\left\langle \hat{F}_z^2 \right\rangle = \left\langle \hat{F}_y^2 \right\rangle = \frac{1}{4Z} \sum_{m=-F}^{F} e^{\beta m} \left[F(F+1) - m^2 \right]$$

$$= \begin{cases} \frac{F}{4}, & \text{for } |P| \to 1, \\ \frac{F(F+1)}{3}, & \text{for } |P| \to 0, \end{cases} \qquad (3.58)$$

$$n_S = \frac{\left\langle \hat{F}_z^2 \right\rangle + \left\langle \hat{F}_y^2 \right\rangle}{\langle F_x \rangle} - \frac{1}{2} = \begin{cases} 0, & \text{for } |P| \to 1, \text{normalize to } F = 4, \\ \frac{17}{6}, & \text{for } |P| \to 0, \text{normalize to } F = 4. \end{cases}$$

This conversion is illustrated in Fig.3.7. The plot facilitates an estimation of the additional atomic thermal noise by calibrating the atomic spin polarization. The experimental details regarding the preparation of coherent atomic state with optical pumping will be presented in Chapter 4, further experimentally characterization of spin polarization can be found in Chapter 5.

3.8 Atomic motional average and broadband noise

Our previous investigations concentrated on the internal dynamics of atomic spins. Nevertheless, practical experiments with atom ensembles in hot vapor cells reveal the influence of the external factors: such as atom's relative positions and their thermal motion-further complicate interactions between light and spins, thereby influencing the observed spin noise spectrum's shape. In scenarios where the probe beam does not entirely cover the vapor cell, and assuming decoherence is mainly driven by atomic spin relaxation, we temporarily neglect probe intensity broadening effects. Hence, probe intensity primarily affects light-atom coupling strength.

During the interaction, the atomic signal, mainly from spin relaxation, originates from atoms within the probe area for the entire interaction duration. However, some atoms initially within the probe area contributing to the spin signal might diffuse out of the beam's area due to the thermal motion, whereas others, not initially observed after collisions with the relaxation coating or other atoms, might re-enter the interaction zone, as depicted in Fig.3.8 (a). These conditions contribute to the spin noise signal but have shorter coherence times than the main spin relaxation time, introducing additional broadband atomic responses as shown in the frequency spectrum domain. This is distinct from the primary narrowband atomic signal, as illustrated in Fig.3.8 (c).
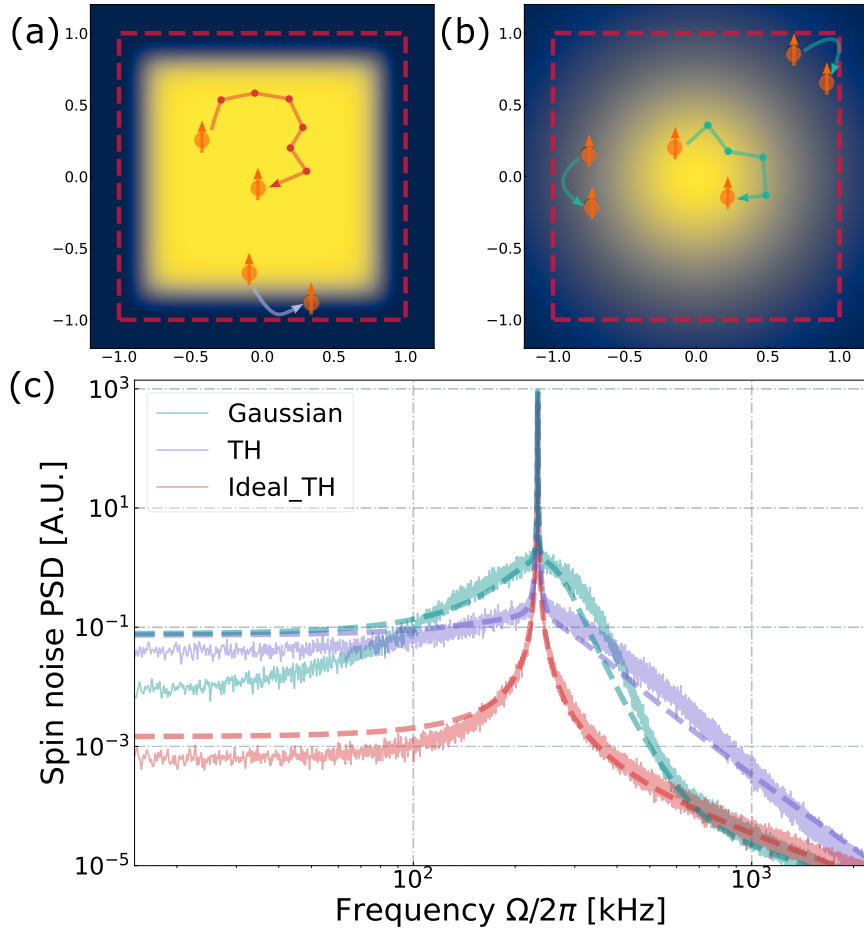
Figure 3.8: Numerically simulation of Spin Broadband Noise as detected by Gaussian and Square Top Hat (TH) Beams. This simulation models a thermal gas of Cs atoms confined within a $2*2*80mm^3$ rectangle channel. Within this channel, atoms can freely move across the cell, experiencing collisions with both the channel walls and neighbouring atoms. The diffusion mode of thermal atoms is governed by the cell geometry, leading to a scenario where an ideal top hat beam with 100% filling factor yields a Lorentzian line shape (red curve). In this context, the spin noise decoherence(line-width) is predominantly affected by spin-spin collisions. An imperfect filling factor introduces coupling to high-order atomic diffusion modes, resulting in broadband (fast decay) responses due to the atoms moving in and out of the probe beam (purple curve). Probing with a Gaussian beam leads to different high-order interactions, manifesting as another broadband response composed of complex Lorentzian functions with different decoherence rates (teal curve). The Gaussian probe beam has a diameter of 1.8mm, whereas the square top hat beam, generated from a Super-Gaussian function with order of n = 12, has an equivalent diameter. The signals are rescaled to equalize the narrow band responses, thereby more effectively illustrating the broadband noise. The numerical simulation program were implemented using program written by Christian Baerentsen.

Furthermore, the light and collective spin interactions are influenced not only by atomic thermal motion but also by the optical mode of the probe light. As Fig.3.8 (c) shows, numerically simulated spin noise spectra reveal variations in

the shape of the spin noise signal due to the differences in the probe beam profile and filling factor. The red curve illustrates an interaction with a square top-hat beam, assuming full illumination where the spin behavior is determined solely by spin relaxation rate, yielding an exponential decay in time or a lorentzian function in frequency domain. An imperfect filling factor, approximately 90 %, introduces additional broadband noise, as shown by the purple curve in Fig.3.8 (a), allowing atoms to move in and out of the probe beam area diffusely or ballistically, depending on their mean free path relative to the cell cross-section, Using a standard Gaussian beam further complicates the interaction between atoms and light by varying the atom-light coupling strength with the atom's position relative to the Gaussian beam profile within the cell. This situation, depicted by the teal curve, with enlarged dark area, results in distinct broadband noise with a higher amplitude and narrower bandwidth. The hypothesis assumes thermal atoms average out the light coupling across various diffusion modes, including our the narrow band spin signal of interest. Overall, given the rapid decay of these broadband modes compared to the spin readout rate Γ_S, which is significantly smaller under our experimental conditions, this broadband noise acts as additional uncorrelated spin noise, thereby undermining quantum noise reduction efforts.

Numerous PhD candidates in our group have contributed to the study of thermal atom motion during light-spin ensemble interactions.[33, 49, 50, 55, 56, 72, 88]. An intriguing feature, termed 'atomic motional averaging', arises as the duration of light-atom interaction increases, helping to mitigate the effect of inhomogeneous coupling, such as that introduced by Gaussian probe beam or inhomogeneous bias-magnetic fields. This method, which averages out the inhomogeneous coupling effect, has been shown to enhance the efficiency of writting single photon into thermal atomic vapors, as discussed in [89, 90].
However, accurately modeling the interaction between light and thermal atomic ensemble is never trivial. In the work of [91], a theoretically analysis of spin noise in anti-relaxation coated cell, accounting for different atomic diffusion modes, was presented. It demonstrated that the choice between Ballistic flight and Langevin diffusion modes for modeling thermal atoms depends on the comparison of the atom's mean free path with the cell's cross section. The similar numerical simulation of atomic responses, both narrow and broadband, to various probe profiles, are well elaborated in Chapter 9, page 81 of Christian's thesis in our group [50]. Here the thermal motion of atoms is simulated via a Monte Carlo method employing the Euler approach, with atom-atom collisions modeled using the Langevin stochastic forces and the spin-wall collision assumes resulting in reversing the direction of the momentum without causing spin decoherence. Decoherence is attributed solely to atom-atom collisions and is uniformly modeled during the probe light interactions, adhering to the QND (quantum nondemolition) input-output relations. Additionally, the readout rate is influenced by the atoms' relative position within the probe beam profile.

Further improvement in our simulations would require us to adjust the probe-dependent interaction, addressing not just the coupling strength but also spin decoherence. Additionally spin-wall (anti-relaxation coating) collision decay should also be included, as discussed by Shaham et al. (2020) [92], their research provides a insightful analysis of decay and fluctuation within the Langevin diffusion formalism, including the case when spins interacts with anti-relaxation coatings governed by the cell geometry. Their approach enables the decomposition of light-atomic spin interactions into distinct spin diffusion and wall collision processes with multi-modes evolution, allowing the each mode to accumulate different quantum noise during the light interactions.

Despite the current model's limitations, the numerical simulation of the spin noise spectrum, including the atomic thermal motion and varying probe beam profile, suggests using a collimated top-hat beam that fully covers the interaction cross-section for minimal atomic broadband noise when probing our collective atomic spin oscillator within a hot vapor cell. Further details on the experimental setup of the top-hat beam and analyze of its impact on spin noise will be presented in Chapter 4 and Chapter 5, respectively.

3.9 Quantum noise engineering with cross-correlation: virtual rigidity

Until now, we have studied various sources contributing to the observed spin noise spectrum. These noise components can be in principle characterized by a crucial parameter: quantum cooperativity (C_q), This parameter represents the ratio of quantum backaction noise, originated from the light radiation pressure noise perturbing the spin oscillator, to the atomic intrinsic thermal noise when the system interacts with environmental thermal baths. We have demonstrated that in real experiments with hot vapor gas, the external thermal motion of atoms induces the location-dependent light-atom coupling, thereby generating additional atomic broadband noise. In the original proposal for the broadband quantum noise reduction via an effectively negative mass spin oscillator [45], achieving such noise reduction necessitates a perfect matching of susceptibilities between the Laser Interferometer Gravitational-Wave Observatory (LIGO) and the atomic spin oscillator, alongside minimal intrinsic atomic thermal noise. This requirement imposes a demanding quantum cooperativity value of approximately 100. Additionally, operating the atomic oscillator at ultra-low audio sideband frequencies-a regime technically challenging to maintain-requires dominance of the quantum noise due to the increased environmental classical noise at such frequencies.

Based on the above limitations, one may consider tailoring the optical rigidity by adjusting the dispersive and dissipative coupling to enhance sensitivity in weak force measurement [93], such as tensor stark shift and cooling within atomic

systems. However, this adjustment significantly complicates the atomic spin system's dynamics. Fortunately, Emil.e.c.t. [46]] introduces an additional concept-virtual frequency shift (or rigidity)- that may relax the demanding requirement on quantum cooperativity and induce an effective frequency shift without complicating light-matter interaction dynamics. The approach of a virtual frequency shift, initially proposed in the Chapter 4.4 of quantum measurement theory [16], describing that constructing a cross-correlation between the measurement impression(shot noise) and quantum backaction noise can modify the dynamic properties of the quantum probe system, via introducing additional effective rigidity (stiffness). This modification can be applied to surpass the standard quantum limit (SQL), thereby enhancing sensitivity in devices like spin ensembles or gravitation wave interferometers.

In the context of the QND measurement of the collective atomic spin oscillator, we have identified a similar cross-correlation, as discussed in Chapter 3.6. This correlation facilitates quantum noise cancellation (ponderomotive squeezing) in the spin noise spectrum through engineering of the homodyne detection angle. To further elucidate this virtual frequency shift and the introduced stiffness, as we in-depth analysis the spin noise, incorporating the cross-correlation term into the total quantum noise (TQN) against the spin thermal noise coefficient:

$$\frac{\overline{S}_{\text{TQN}}}{\overline{S}_{\text{TN}}} = \frac{\overbrace{1}^{\text{SN}} + \overbrace{\Gamma_{\text{S}}^2 |\chi_{\text{S}}(\Omega)|^2 \cos^2(\phi)}^{\text{QBAN}} + \overbrace{\Gamma_{\text{S}} \operatorname{Re}[\chi_{\text{S}}(\Omega)] \sin(2\phi)}^{\text{Correlations}}}{\underbrace{4\gamma_{\text{S}}\Gamma_S |\chi_{\text{S}}(\Omega)|^2 \cos^2(\phi)}_{\text{TN}}}. \tag{3.59}$$

The simulated noise spectra for the pondermotive squeezing of light across diverse polarimetric homodyne phases, alongside their corresponding thermal force normalized noise curve, are plotted in Fig.3.9. The red dash-dotted line, representing the detection of phase quadrature of light $\phi = 0$ without cross-correlation, serves as a baseline for comparative analysis. A deviation from this pure phase quadrature $\phi = 0$ towards the amplitude quadrature ($\phi = \pi/2$) introduces a cross-correlation term, resulting in ponderomotive squeezing. Moreover, normalizing the total quantum noise for each detected light quadrature against the respective atomic thermal noise, as illustrated in Fig.3.9 (b), reveals distinct phase-dependent frequency shifts, evidenced by the shift of dip for each parabolic shape curve. Compared to the referenced red dash-dotted line, centered around 15 kHz, we expect to observe a maximal downshift of parabola's depth is noted in the light purple curve, with a maximum shift around 3 kHz-indicated by two dashed vertical lines (orange and red), approximately a quarter of spin readout rate Γ_S. Notably, this shift can be reversed up-shift by altering the sign of the detection phases ($\sin 2\phi$).

The concept of this virtual frequency shift, detailed in references [33, 46, 94], can
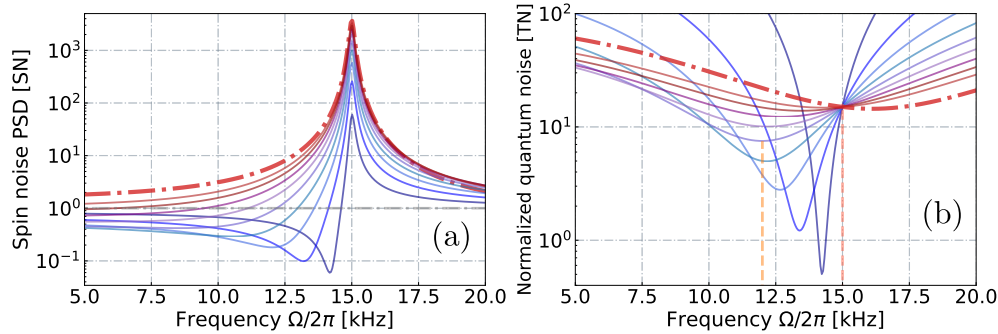
Figure 3.9: Ponderomotive squeezing and virtual frequency (virtual rigidity) shifts across homodyne detection phases. (a) The red dash-dotted line corresponds to the detection of phase quadrature of light $\phi = 0$ with maximum atomic signal. Deviation from the pure phase quadrature $\phi = 0$ towards the amplitude quadrature $\phi = \pi/2$ introduces cross-correlation term, resulting in ponderomotive squeezing. The detection angle varies by $\pi/20$ increments. (b) This quantum cross-correlation adjusts the frequency response of the atomic oscillator to the probe light quantum fluctuation, creating a virtual frequency shift. Compared to the pure phase quadrature detection (as the red dash-dotted line), a noticeable frequency downshift (around 3kHz, presented with two dashed vertical lines (orange and red) and an increased sensitivity of the thermal noise with a narrow band near the Larmor frequency are observed. It is interesting to note that deep in force normalization plot does not coincident with the frequency of maximum pondermotive squeezing. These effects are demonstrated at a fixed center frequency Ω_S of 15 kHz, a readout rate Γ_S of 12 kHz (~ 3mW probe power), a linewidth (FWHM) γ_S of 200Hz and a thermal occupation of $n_s = 0.5$.

be understood through the effective frequency response (susceptibility) of spin oscillators to the quantum noise across different probe quadrature bases. Assuming the total quantum noise, including cross-correlation, can be redefined whenever the detection changes into a new quadrature basis where the shot noise (SN) and quantum backaction noise (QBAN) remain uncorrelated. Consequently, in this new detection basis, the effective susceptibility of the spin oscillator to the light fluctuations is modified, as described by the following equation:

$$\chi_{\text{eff}}^{-1}(\Omega) = \chi_{S}^{-1} + \frac{\Gamma_S}{2}\sin 2\phi. \tag{3.60}$$

Here, $\frac{\Gamma_S}{2}\sin 2\phi$ is the virtual stiffness added by the underlying quantum cross-correlation. This adjustment yields a new effective oscillator frequency that is now written as: $\Omega_{S,eff} = \Omega_S\sqrt{1 + \frac{\Gamma_S}{2}\sin 2\phi/\Omega_S}$. As we can modify the sign of this stiffness though the detection phase, such adjustment allows for an effective shift in atomic response, based on the selected uncorrelated quadrature basis. Through this mechanism does not substantially modify the spin response to atomic thermal force noise-the detection angle still rescales the recorded atomic thermal noise by $\cos\phi^2$. Thus, leveraging quantum correlation enables the engineering of the atomic frequency responses of the spin oscillator to uncorrelated quantum shot and backaction noise of the probe field.

Apart from that, we observed the variations in the steepness of the parabolic curves across different detection phases. The physical meaning of this phenomenon becomes more apparent upon normalizing the spin thermal noise term against the total recorded spin noise (both quantum noise and atomic thermal noise) without altering the parameters, as illustrated in Fig.3.10 (a). Here, the vertical axis represents the proportion of thermal noise within the total recorded spin noise at each Fourier frequency. The effective shift induced by cross-correlation can increase the atomic response to external force signals (here is the thermal forces), via increasing the proportion of atomic thermal noise where the quantum noise cancellation emerges, thereby improving the signal (thermal forces) to noise (quantum noise) ratio and enhancing the sensing sensitivity. This is particularly relevant if the external force signal shares dynamics similar to thermal Langevin forces, as seen in Mz or My magnetometry [95]. However, it's important to note that these sensitivity gains are achieved at the expense of reduced bandwidth as shown in Fig.3.9 (b).

Moreover, for effective quantum noise reduction with the atomic spin oscillators, it is crucial to prepare the system with sufficient large quantum cooperativity, therefore the influence of atomic thermal noise becomes negligible. Instead of focusing on the virtual frequency shift occurring below the Larmor frequency, we now concentrate on the red shaded area depicted in Fig.3.10 (a), particularly above the atomic Larmor frequency, where this virtual frequency shift also plays an important role in minimizing thermal noise contributions. This minimization occurs in the frequency regime where the constructive interference between quantum backaction and shot noise arises, allowing the atomic system to operate with what can be considered as effective enhanced quantum cooperativity. This phenomenon emphasizes the balance between different noise sources through the probe detection phases to achieve optimized quantum sensing performance.
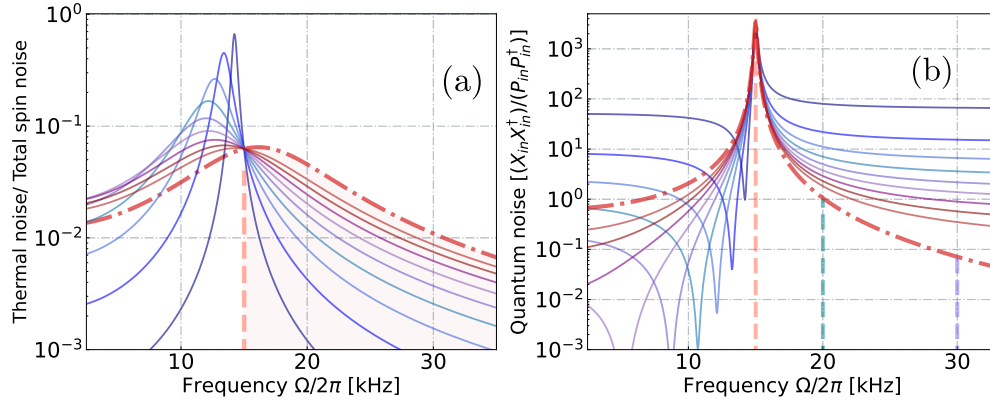
Figure 3.10: Analysis of thermal noise and quantum noise (amplitude and phase quadrature) contributions across various detection phases. (a) This analysis examines the proportion of thermal noise within the total spin noise, highlighted by a dash dotted red curve represents atomic signal detection exclusively at light phase quadrature. An alteration from the phase quadrature shows increased thermal noise contributions within a specific frequency band, alongside a decrease above the Larmor frequency. (b) Examining the ratio of quantum backaction and shot noise from the amplitude quadrature to the phase shot noise reveals transitions from backaction dominance (illustrated by the orange line) to shot noise dominance (depicted by the purple line). Implementing virtual rigidity mitigates thermal noise while elevating shot noise contributions from the amplitude quadrature, particularly at high frequencies. Additionally, virtual rigidity facilitates a tunable transition in quantum noise, from backaction dominance to shot noise dominance, below the Larmor frequency, with the option to adjust the transition bandwidth. The parameters are consistent with those in the preceding figure.

However, one need to be more cautious when directly utilizing the effectively increased total quantum noise that arises as we engineer the detection angle. While virtual rigidity plays a role to reduce the thermal noise fraction, it simultaneously introduces shot noise from the amplitude quadrature of light, which ultimately becomes predominant at higher Fourier frequencies. This introduction of additional shot noise may compromise the quantum noise reduction effort at high Fourier frequencies, where the phase quadrature shot noise should dominant. Hence, we calculate the ratio of these two noise contributions and examine its variation as a function of frequency to better understand and mitigate these effects.

$$\frac{\overline{S}_{\hat{X}_{\mathrm{L}}^{\mathrm{in}}\hat{X}_{\mathrm{L}}^{\mathrm{in},\dagger}}}{\overline{S}_{\hat{P}_{\mathrm{L}}^{\mathrm{in}}\hat{P}_{\mathrm{L}}^{\mathrm{in},\dagger}}} = \frac{(1)\sin\phi^2 + \Gamma_S^2|\chi_{\mathrm{S}}|^2\cos\phi^2 + \Gamma_S\,\mathrm{Re}\,[\chi_{\mathrm{S}}]\sin 2\phi}{(1)\cos\phi^2}. \tag{3.61}$$

The findings are plotted in Fig.3.10 (b), where the red curve without the quantum cross-correlation serves as our benchmark. The orange, teal, and purple vertical lines present the three transitions through the quantum noise spectrum- from backaction noise dominance, through equal contributions, to phase shot noise dominance, respectively. While the virtual rigidity shift reducing the thermal

noise contribution above the atom resonance frequency in Fig.(a), it also introduces additional shot noise from the orthogonal light amplitude quadrature as in Fig.(b). This, in turn, may obstructs the third regime, wherein the light shot noise from phase quadrature (the gravitational wave signal also encoded into this quadrature) should predominant the total quantum noise at higher frequencies, thereby impairing the efficiency of broadband quantum noise cancellation.

Conversely, below the Larmor frequency, virtual rigidity not only facilitates an adjustment of the ratio for backaction noise and shot noise but also allows for the fine-tuning of bandwidth (from the back action dominance to shot shot in phase quadrature dominance) utilizing the detection angle. Notably, in this regime, the virtual frequency shift plays a crucial role in tailoring the frequency bandwidth to achieve simultaneous quantum backaction and shot noise reduction. This is evidenced by the gradually shift of the minimal dips from the Larmor frequency, as illustrated in Fig.3.10 (b). Meanwhile, this of course comes at the cost of an increased thermal noise effect, depicted in Fig.3.10(a). Assume the atomic spins can maintain quantum noise-limited behavior at ultra low frequencies with sufficiently small thermal noise, one could invert the detection phase and unitize the virtual rigidity up-shift approach to better match the bandwidth of the quantum backaction to shot noise transition in GWD system.

This section elaborates on the subtle advantages and challenges associated with the complex virtual frequency shifts, induced by cross-correlation, to modify frequency responses, enhancing sensitivity within specified bandwidths, and effectively enhance quantum cooperativity for refined broadband quantum noise reduction management. Although this approach offers several benefits, it also encounters notable limitations, including a reduced effective readout rate and a restricted bandwidth of the sensitivity improvement, emerges only around the center frequency. The effectiveness of this method depends solely on the real component of the susceptibility, and the inherent dissipation in measurement configurations leads to additional noise, undermining this virtual effect. Furthermore, virtual rigidity introduces quantum noise from orthogonal quadrature, altering the quantum noise ratio across the frequency spectrum. In the extreme scenarios, this could prevent reaching the tuning point where phase shot noise prevails, thereby limiting the potential for optimizing broadband quantum noise reduction strategies.

In this chapter, we have undertaken a thorough analysis of the theory of light and atomic spin operators, delving into the light-atom interactions, from QND interaction to more complex higher-order tensor interactions. Our exploration extended further into the study of the effective atomic masses and analyzing the spin noise spectrum to understand the dynamics of atomic systems. Furthermore, we investigated the light ponderomotive squeezing, resulting from quantum cross-

correlations, alongside investigating the impacts of uncorrelated atomic thermal noise and fast decay broadband noise in practical experiments that involve atomic thermal motion. Lastly, we introduced the concept of virtual frequency shift (optical rigidity) and explored its application in release certain experimental constraints. Now we finish the theory introduction, let us move on to the experiments.

Part II

Preparation of atomic spin oscillator

Experimental setup

In this chapter, we explore the detailed experimental setup involving atomic components for our project. We describe the fabricated atomic vapor cell designed specifically for the GWD experiments. Subsequently, we delve into the heater system, which is crucial for regulating the atomic density without introducing additional magnetic noise. We also cover the implementation of magnetic shielding alongside a home-designed printed circuit board (PCB) coil system. This system produces a homogeneous magnetic field, achieving magnetic inhomogeneity of less than 0.4‰. This level of precision allows us, for the first time, to observe the quadratic Zeeman splitting in an 8cm-long atomic vapor cell. Additionally, we present the generation of a collimated square top hat beam, which facilitates homogeneous coupling. We conclude this chapter with an overview of the laser systems applied for the optical pumping.

4.1 Cell fabrication and anti-relaxation coating

In our work, the atomic hot vapour cell is deployed to produce the collective spin oscillator and to achieve the optimal quantum noise reduction for gravitational wave detection systems. The selection of cells have to fulfill certain requirements. such as increased length to enhance the interaction readout rate and quantum cooperativity under the same condition-owing to the proportionality of C_q to the length of cell rather than the volume. Higher working temperatures can result in increased atomic vapor density. It is also crucial to minimize decoherence, as the imaginary part of the spin's response will degrade the quantum noise reduction performance, given that the gravitational wave detectors have negligible dissipation. Furthermore, the cell's transmission should be well controlled to protect the signal and entanglement. With all these prerequisites in mind, we introduce our specially fabricated vapor cell used in our experiments.

The vapour cells fabricated for our experiment, presented in fig.4.3, feature a

8cm long rectangle channel with varying cross sections ranging from 1*1 to 5*5 mm^2. The channels are placed inside a half-inch glass tube employed as the cell body. The cesium atoms, in golden color, are contained within the narrow curved tube called the cell stem, which is glass-blown to the cell body. The micro-holes among the cell stem, cell body, and the inner rectangle channel allow atoms to enter the rectangle channel, facilitating interaction with the probe light. The cell channel, with its rectangle geometry, is designed to minimize the lens effect during optical pumping. All these parts were made of Borofloat, the rectangle channel were ordered from Vitrocom. The cell windows on both sides were ordered from Foctek company and later were antire-reflective (AR) coated on both sides by the Company Ferroperm with on average 99.5% transmission and then degrade 1 % after repolishing them for easier glass blowing [1].

When polarized atomic spins are confined within the cell channel, collisions with the cell wall surface may lead atoms to be absorbed into the wall surface and experience local magnetic or electric fluctuating fields produced by the glass molecules. Consequently, the spins-wall collision interaction can randomize electron and nuclear spins, leading to atomic spins depolarization. To mitigate spin-wall collisions, one approach is to introduce high-pressure buffer N_2 gas, which causes atoms to undergo diffusive motion and delays their contact with the wall [96]. In our laboratory, we employ an anti-relaxation coating made with paraffin to prevent direct interactions between alkali atoms and the walls. [97]. I was fortunate to participate in the fabrication of generation O and assist in testing the performance of some vapor cells, as shown in Fig.4.3. The anti-relaxation coating for this generation is based on normal AlphaPlus C30+HA from Chevron Phillips Chemical-CPChem company[56](the credit for these cell components management should go to Rebecca, pg76). Mikhail (our cell fabrication master) prepared the coating by setting the coating evaporation temperature to approximately 120 ~150 $°C$, then collected the C30+ mixture, which contains over 95% of carbon chains with at least 30 carbon atoms. The cells for this generation were then deposited at significantly higher temperatures, around $320 \sim 330 \, °C$. The mixture coating enables us to maintain efficient spin coherence time at working temperature up to 60 $°C$, as demonstrated by the cells labeled O7-O21. Details are provided in tab.4.2. The mixture coating can also be collected at higher evaporation temperature using shorter carbon chains (C20+), which contain unsaturated hydrocarbons with double bounds between carbon atoms. As described in the studies on cell generation N and L [97], this coating enables atoms to undergo up to 10,000 wall collisions without spin depolarization, significantly extending spin coherence time as much as minutes [98]. However, this particular coating is only recommended to work at temperature below 30$°C$.

---

[1]Most components of the cell were ordered by Rebecca
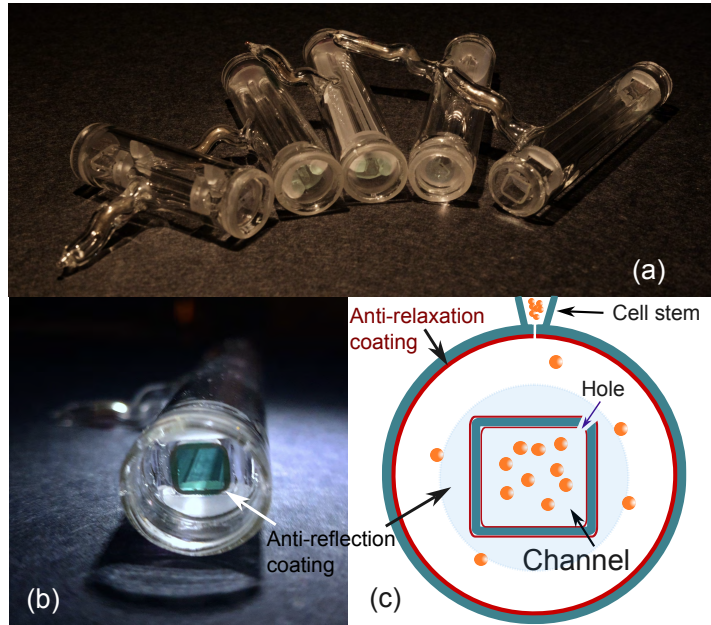
Figure 4.1: Cesium contained in a vapor glass cell. (a) Photo of our latest fabricated atomic vapor cell exhibiting different geometries. Each cells features a square inner channel with different cross-sectional dimensions (varying from 1*1 mm^2 to 5*5 mm^2). (b) Both the input and output windows are coated with anti-reflective coatings for 852 nm, optimizing probe transmission. In addition, the entire vapor cell has also been coated with an anti-relaxation paraffin layer to prevent the atoms losing their spin polarization. (c) A droplet of cesium in the cell stem serves as an atomic reservoir, allowing cesium atoms to move in and out of the inner channel through a tiny scratch hole. All cells were crafted by Mikhail Balabas.

		GWD Experiment Cell Characterization			
Cell	**Size [mm^3]**	**Coating**	**FWHM [Hz]**	**Trans [%]**	**Density [$10^{16}/m^3$]**
L3	5×5×80	C20+	7	95	3.05±0.04
N12	3×3×80	C20+	13	91	-
O19	3×3×80	C30+	28	94.8	3.78±0.04
O21	3×3×80	C30+	48	95.3	4.80±0.40
O7	2×2×80	C30+	54	96.7	2.65±0.04
O8	2×2×80	C30+	32	96.3	2.95±0.11
O12	2×2×80	C30+	43	95.2	2.77±0.09
O13	2×2×80	C30+	46	95.4	2.39±0.15
O15	2×2×80	C30+	35	95.8	2.90±0.10

Table 4.2: Characterized cell parameters that might be relevant for gravitational wave experiments. C20+ and C30+ represent two different paraffin coatings, C20+ normally operates below 30°C, while C30+ is capable of working up to 60°C. The cells characterization was measured together with Ryan, while the characterization of atomic density were done by Rebecca.schmieg and Issac Caritg

However, the fabrication process inevitably introduces imperfections, such as accidental scratches on the windows (a) or condensation of the paraffin coating (b). Therefore, it is essential to characterize their cell performance before integrating them into our experiments. This characterization entails assessing the transmission, optical depth (density) for interaction strength, and measuring T1 and T2 to better understand the mechanisms behind the decoherence. Interested readers can find further details on the absorption and DC Faraday calibration methods in Chapter7 of Rebecca's PhD thesis[56]. Additionally, in our experiments over the past year, we have occasionally observed a decrease in cell transmission. Using a high resolution camera, we detected atoms clusters on the cell windows (dark spots blocking the probe light). Fortunately, we managed to remove these clusters by applying a carefully controlled temperature gradient curing, exceeding 15 °C, between the cell stem and body.
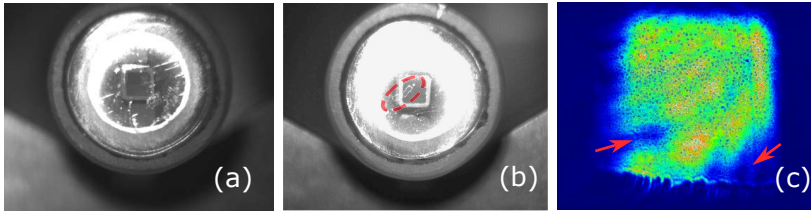
Figure 4.3: Cesium contained in a vapour glass cell. (a) Scratched cell windows observed during the fabrication process. (b) Over-condensation of paraffin wax on the cell windows (c) After a year of usage, we observed atom clusters and condensation, marked with red arrows within the channel, leading to a degradation in cell transmission.

4.2 Temperature and Vapor cell density control

To increase the temperature of the atomic system, a high-resistance heating ribbon wire, as shown in the Fig.4.4, is utilized. This wire, made from the non-magnetic material Nickel-Chromium (ordered from Omega), is double-folded and then wrapped around the central aluminum layer. The temperature is regulated via the current flow, which also minimize the influence of low frequency classical noise that may be produced from the heater power supply. The entire magnetic shield is covered with neoprene rubber (depicted as the black cover in Fig.4.4 (b)) to reduce heat dissipation into the surrounding environment. Consequently, once the equilibrium temperature is reached, the cell can sustain the working temperature for approximately an hour without the need to reactivate the heater.

The relationship between the fractional increase in the total atom number-a parameter of significant interest -and the cell's working temperature is presented in Fig.4.4 (c). This relationship is normalized to the atomic density at room temperature, 20 °C as a baseline. The graph demonstrates that we can increase the total number of atoms (and, notably, quantum cooperativity) by a factor of 34 via

94

increasing the temperature from 20 °C to 60 °C. In addition to enhancing atomic
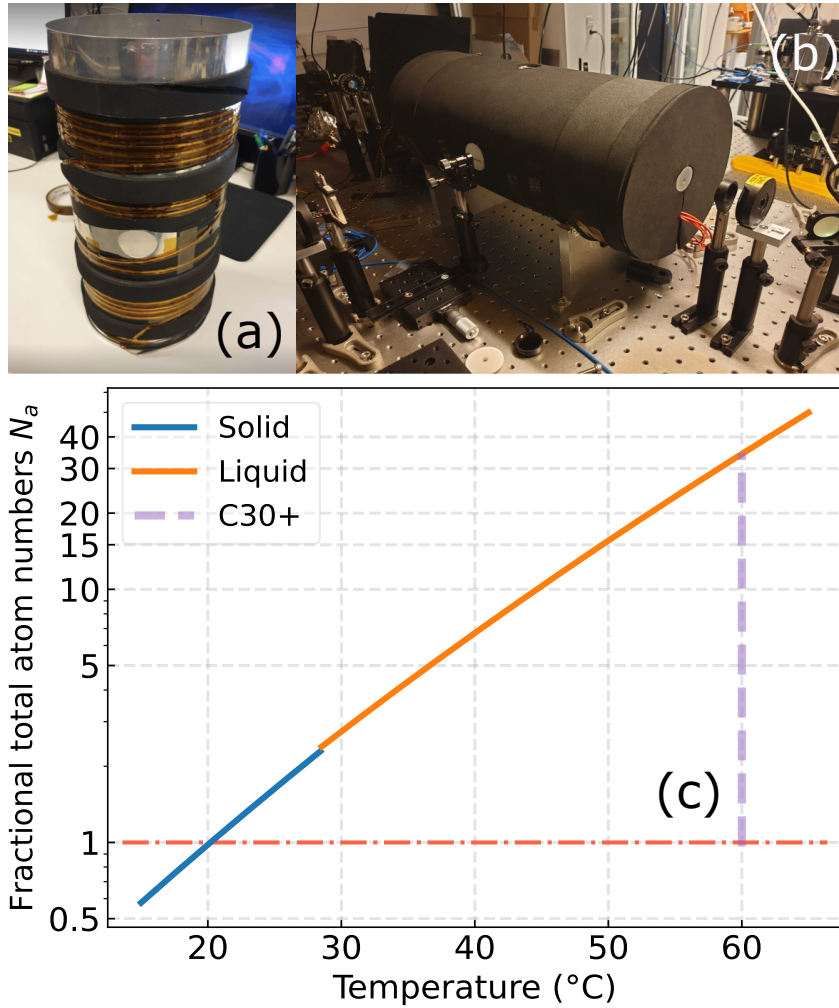
Figure 4.4: Temperature control system. (a) The middle layer is wrapped with a double-folded Nickel-Chromium heating ribbon wire. (b) The whole setup is then insulated with Neoprene, commonly used in diving suit, to preserve temperature stability even when the heater is deactivated. This strategy mitigates additional RF noise generated by the heater. (c) The graph illustrates the fractional increase in the total numbers of atoms as function of the cell temperature. The reference for comparison is the atom density at the room temperature, which is approximately $3 \times 10^{16}/mm^3$ at 20 °C. It is noted that the phase transition for cesium atom occurs at 28.5 ∘C.

density by heating the atomic vapor cell, one can also employ the method known as light-induced atomic desorption (LIDA). This approach temporarily releases the atoms absorbed by the cell surface and paraffin coating, thereby increasing the total atom number within a short time [99].

4.3   Magnetic shield

In order to protect the spin oscillator from environmental perturbations, such as Earth's magnetic field and low-frequency noise, we employed 5 layers of magnetic shielding which can in principle achieve comparable shielding factor to that of single thick shield [100], consisting of 3 layers of Mu metal together with a layer of aluminum and iron.

Mu metal, known for its high permeability, is ideal for isolating the DC magnetic field. The iron layer targets the isolation of acoustic radio frequencies, while Aluminum (Al), due to its good conductivity, shields against high radio frequency influences. Subsequently, the magneto-optical resonance spectroscopy (MORS) measurements [101] were conducted to quantify the residual magnetic field by monitoring the atom Larmor frequency, which was identified to be around 270 Hz as presented by blue curve in Fig.4.5. A demagnetization process (discussed in Hans master thesis, appendix C) [102] was then applied to randomize the dipoles orientation through the shielding material using a saturated sinusoidal magnetic field. Gradually decreasing this field further helps in diminishing the residual magnetic field contribution down to approximately 70 Hz. Considering the Copenhagen's earth magnetic field of 0.5 G, our magnetic shielding configuration achieved a shielding factor of $\approx 2000 \sim 3000$. These curves also present the lowest feasible working larmor frequency achievable with the current shielding configuration, without additional coil compensation.
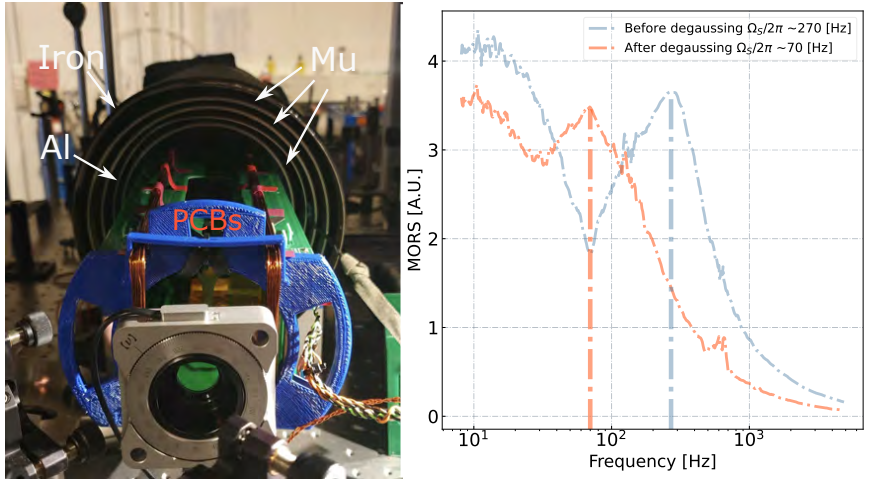
Figure 4.5: Magnetic shield and residual magnetic field. The atomic vapor cell and coil systems are protected by five layers of magnetic shielding, designed to isolate the cell from Earth's magnetic field and classical noise perturbation from environments. The residual magnetic field are detected through magneto-optical resonance spectroscopy (MORS) measurements shown by the blue and orange curves. A degaussing approach is commonly applied to minimize the strength of these residual magnetic fields.

4.4 PCB and Rectangle coils

Having fabricated anti-relaxation coated vapor cells with substantial optical depth and a 'quiet' residual magnetic environment, shielded by our magnetic enclosure, our next objective is to manipulate the atomic spins within the vapor cell. As previously outlined in Chapter 3.1, the orientation and strength of the internal bias magnetic field within the magnetic shield around the cell's location determine the spin quantization axis and the resonance frequency of the spin oscillator, respectively. A collective spin oscillator, encompassing all Cs atoms in the cell channel, is subject to slight Larmor frequency variations due to inhomogeneous field strength, leading to additional atomic dephasing and reduced spin intrinsic lifetime. To mitigate this effect, it is imperative to ensure a uniform magnetic field across the cell volume, thereby imposing stringent requirements on the bias magnetic field's uniformity. In previous PhD work, bias fields were typically oriented along the longitudinal axis of the cylindrical magnetic shield, produced by a Lee-Whiting configuration as the main coil, and compensated by saddle or Helmholtz coils, as detailed in [55, 56]. This setup achieved a homogeneous magnetic field optimized for 1cm-long atomic vapor cells. However, the broadband quantum noise reduction project necessitated redesigning the vapor cell to enhance optical depth and quantum cooperativity C_q, extending the cell length up to 8cm. This modification requires us to either scaling up the entire previous shield and coil systems or devising a new magnetic coil system for improved magnetic homogeneity for a larger volume.

Fortunately, around the same time, Jürgen Appel began investigating alternative methods for producing the magnetic field, different from the Helmholtz or saddle coil configurations. He explored the potential of leveraging the current flow in copper traces on 2D printed circuit boards (PCBs), offering unprecedented design freedom for much more complex magnetic field distributions. This approach, optimized through coil design, enables the production of significantly more homogeneous magnetic fields with compact coils geometries, fitting within our existing magnetic shield.
During his time at NBI, Appel developed a script for modeling the magnetic field generated by surface currents, leading to the fabrication of the first-generation test coil. This valuable work was further refined by Ryan Yde, with Michael Zugenmaier's assistance, tailoring the coil designs towards our specific requirements. I later joined the project, collaborating with Ryan to characterize the performance of the second generation PCB coils, with results demonstrated in Ryan thesis [103]. We finished the first long cell characterization measurement within the magnetic shield, although the generated field's homogeneity (~ 3 ‰) was insufficient for resolving the quadratic Zeeman splitting and performing the atomic state calibration. Recognizing the shield's influence on field inhomo-

geneity, Ryan and I shifted our target from achieving a uniform distribution via the perfect design to obtaining first and second-order parabolic profiles through optimal current ratios among the coils. This strategy, employing multiple coil pairs, can produce enhanced magnetic field homogeneity even with the shielding effects. In the next section, we will delve into the experimental characterization of our latest coil system generation in more detail.

4.4.1 Magnetic profile and its optimization

The fabricated PCBs coil system can be seen in Fig.4.8 (a), where the front image shows the Bz coil, our excitation RF coil. Three pairs of bias coils, marked with white arrows and orthogonal to the RF coil, are spaced at a specific distance apart. These coils are assembled and mounted on a 3D-printed round holder, colored red, designed to position the coils at the center of the magnetic shield as shown in Fig.4.5. The three pairs of bias coils, ordered by their separation from nearest to farthest, are the linear gradient coil, the convex (or 'cup') coil, and concave (or 'cap') coil, respectively. The distribution of copper traces and the produced magnetic profile are visible in Fig.4.6. Each coil features a rectangular aperture serving as the simulation's inner boundary and is sized to allow the propagation of optical pumping lasers.

Before introducing the long cell into the coil setup, it is necessary to characterize the magnetic profile across the transverse axis within the cell's volume. To achieve this, a cubic 5*5*5 mm^3 cell is installed on a 3D printed cell holder, as seen in Fig.4.8 (b), and attached to a glass tube. This allows to the longitudinal movement within the shield while enabling atomic signal detection via colinear MORS measurement [103], with a constant current of 100mA flowing through each coil pair. Subsequently, the atomic Larmor frequency is extrapolated by fitting the signal to a Lorentzian function. Detail calibration procedures are outlined in chapter 4.2 of Ryan's thesis and Chapter 7.2 of Christian thesis. [50, 103], . To optimize the magnetic field homogeneity for an 8 cm long cell, we monitored the variation of Larmor frequency near the shield center, across a 100mm span. Given the magnetic shield's influence varies with its distance to the PCBs, we measured each coil at multiple distances to ascertain the optimal profile for the designed coils. The finalized magnetic profile, derived from the optimal coil separation distances for each PCB coil, is presented in the Fig.4.6. Notably, the difference between the blue and green profiles resulted from flipping the orientation of the bias magnetic field, employing the mean Larmor frequency at each position to mitigate the residual magnetic field's effect along the same bias-axis.
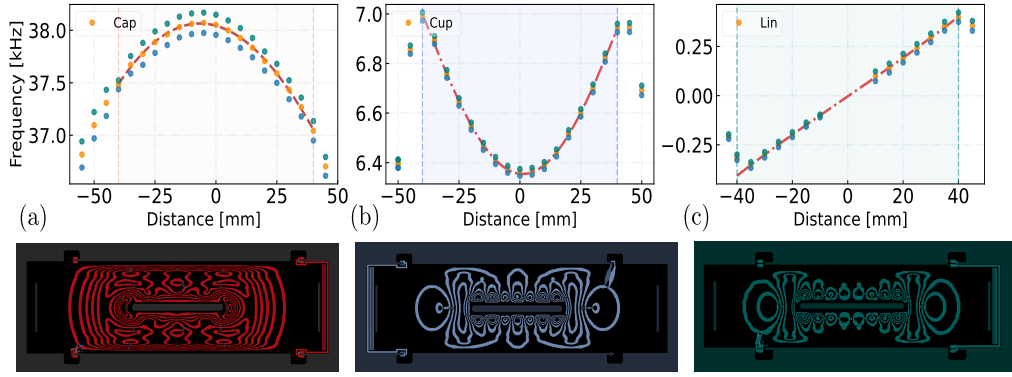
Figure 4.6: Bias magnetic fields produced by the final version of PCB coils. This coil design incorporates concave (cap) and convex (cup) parabolic shapes, along with a linear gradient coil, to generate the specified magnetic profiles. Measurements were taken with 100mA of current flowing through each coil, with all coil pairs placed at their optimal separation distances. The distribution of copper traces, which are crucial for producing each magnetic field profile, is also presented below. The coil designs were developed by Ryan.

| Coil Separation [mm] | Coil Profiles Fitted with Polynomial Function | | | | |
	$\mathbf{a_0}$	$\mathbf{a_1}$	$\mathbf{a_2}$	$\mathbf{a_3}$	$\mathbf{a_4}$
Cap: 43	38.0	$-6.5 \cdot 10^{-3}$	$-4.9 \cdot 10^{-4}$	$6.7 \cdot 10^{-7}$	$4.1 \cdot 10^{-9}$
Cup: 39	6.3	$-1.1 \cdot 10^{-3}$	$4.6 \cdot 10^{-4}$	$2.18 \cdot 10^{-7}$	$-4.8 \cdot 10^{-8}$
Linear: 35	0.0	$9.6 \cdot 10^{-3}$	$2.2 \cdot 10^{-6}$	$2.8 \cdot 10^{-7}$	$-1.1 \cdot 10^{-9}$
Rectangle: 55	553	$-2.5 \cdot 10^{-3}$	$1.3 \cdot 10^{-4}$	$4.3 \cdot 10^{-6}$	$3.5 \cdot 10^{-7}$

Table 4.7: Fitted Parameters of Magnetic Inhomogeneity. the measured coil profiles have been fitted using a fourth-order polynomial function, $f(x) = a_0 + a_1 x + a_2 x^2 + a_3 x^3 + a_4 x^4$, to facilitate the estimation of the optimal current ratio to effectively mitigate the magnetic inhomogeneity.

The optimal separation distances for our PCBs coils have been determined as follows: 43mm for the concave ('cap') coil with red traces, 39mm for the convex ('cup') coil with blue traces, and 35mm for the linear gradient coil with green traces. To identify the best combination of currents through each pair, we fitted the magnetic profiles using a multi-order polynomial function. This approach allowed us to estimate the linear current ratio essential for minimizing magnetic inhomogeneity. The results of these fittings are shown in tab.4.7. Using the cap coil as a reference point, we then adjusted the current ratio of the cup and the linear gradient coils simultaneously. This process helps us find the configuration that minimizes the standard deviation of the combined magnetic profile over an 8cm span, thus optimizing field uniformity. The outcomes of these adjustments, represented as a 2D contour map varying according to the two different coil ratio, are depicted in Fig.4.8.
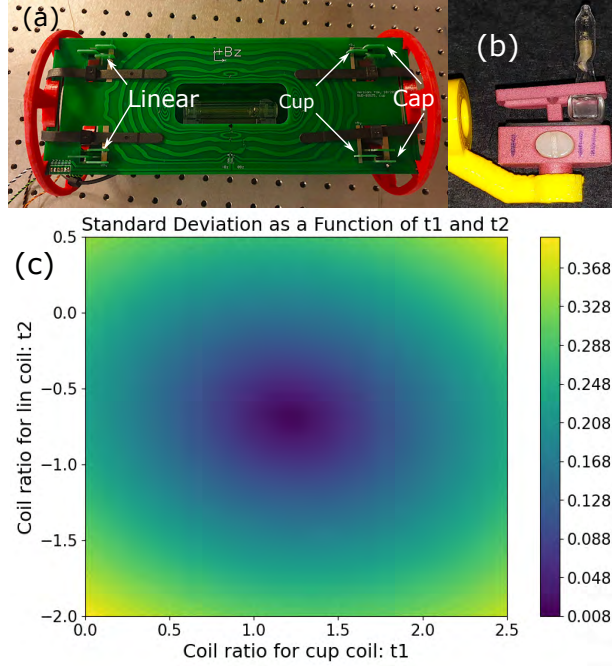
Figure 4.8: PCBs coil system and the optimal current ratio estimation. (a) A photo of the assembled PCB coil system. (b) A 5*5*5 mm^3 cubic cell, serves for calibrating the magnetic field profile. (c) A 2D counter map illustrates the combined magnetic field inhomogeneity, quantified by the standard deviation, as a function of current ratios for the cup and linear gradient coils, (denoted as t1 and t2, respectively). This map illustrates the improvement in magnetic field uniformity achieved by integrating all three PCB coils.
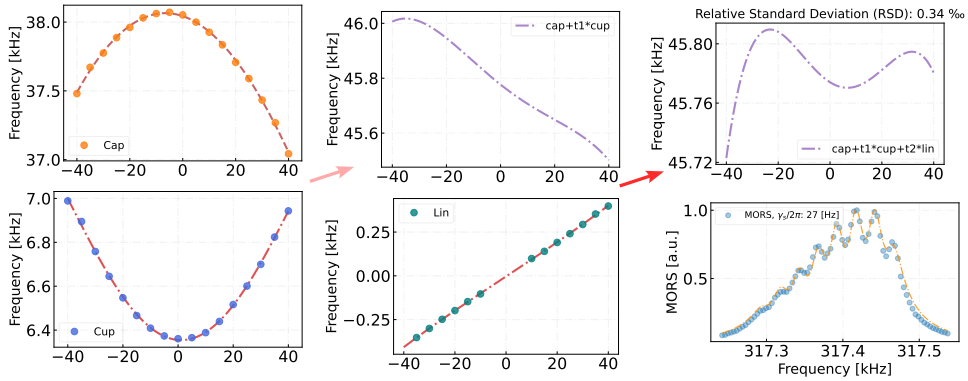
Figure 4.9: Magnetic profile achieved through the integration of three printed circuit board (PCB) coils. The combination of cap and cup coils results in a magnetic field with linear gradient component, optimized by current ratio t1. This configuration is then maximally compensated by the linear gradient PCBs coil with ratio t2. By integrating all three coils, we achieve a magnetic field with a relative standard deviation around 0.34 ‰. This coils configuration allows the observation of a partially resolved Magneto-Optical-Resonance-Signal (MORS) at 317 kHz using an 8cm long cell.

Based on the estimated coil current ratios t1 and t2, the improvement in the pro-

duced magnetic field profile through proper integration of all three pairs of PCBs coil can be found in Fig.4.9. With the help of all three 'cap', 'cup', and 'linear gradient' coils, we have managed to produce a field with relative homogeneity (~ 0.3 ‰), an order of magnitude better than that of our previous generation. Such field uniformity has, for the first time, allowed us to observe a partially resolved quadratic Zeeman splitting for the D2 line, F =4 transition, with a linewidth (full width half maximal) of 27Hz for each peak. Considering the cell (L3) used, with an intrinsic transverse life time around 7 Hz, this magnetic field only contributes additional 20Hz to the total spin relaxation time at a 300 kHz larmor procession frequency. Compared to the probe power broadening of around 150 Hz in our normal operating configuration, a 20Hz magnetic field contribution is significant achievement in our lab. At the Larmor frequency of around 10kHz, where we aim to perform the proof-of-principle experiment, this additional magnetic field broadening can be maximally reduced to ~ 2Hz. Given that the splitting between each peak shown in Fig.4.9 MORS signal scales quadratically with the strength of the bias magnetic field, but not with the spin decoherence, we should increase the magnetic field to better resolve the quadratic Zeeman splitting signal. However, the PCBs coils were originally designed to produce fine tune-able magnetic fields, not strong field. The limited current to magnetic field conversion efficiency and non-ideal heat dissipation prevent us from further increasing the atomic Larmor frequency.

Aiming for improved current-to-field convert efficiency, our colleague Sergey A. Fedorov camp up with the idea of designing a Rectangle coil, where the size of the coil is elongated close to the boundary of the inner cylindrical shield. The designed rectangle coil was then simulated using the open-source coil design python package bfieldtools [104, 105]. This simulation allowed us to model the magnetic profile within a simulated magnetic shield close to our real geometry and determine the estimated optimal separation distance and coil profile. After fabrication, the coil was installed around our PCB coil, as seen in Fig.4.10 (a), with the measured profile presented in Fig (c). The discrepancy between the real and experimentally measured magnetic profiles indicates distortion due to the magnetic shield (we couldn't find the right specification of our magnetic shield). With the same 100 mA current flowing through the rectangle coil, the larmor frequency can be shifted up to 550 kHz. By incorporating the PCB 'cap' coil with slight optimization of the current ratio as in Fig.4.10 (d), we achieved a completely resolved atomic spin signal at 1.033 MHz. The additional broadening due to the magnetic field inhomogeneity is 100 Hz. We also observe a tiny bump next to the extreme Zeeman level, as depicted in blue area in Fig.4.10 (b), which we assume is produced by the magnetic inhomogenity, as its height can be modified through the cap coil current ratio in Fig (d). In the next chapter, we will elaborate more on the atomic state characterization based on this resolved MORS signal.
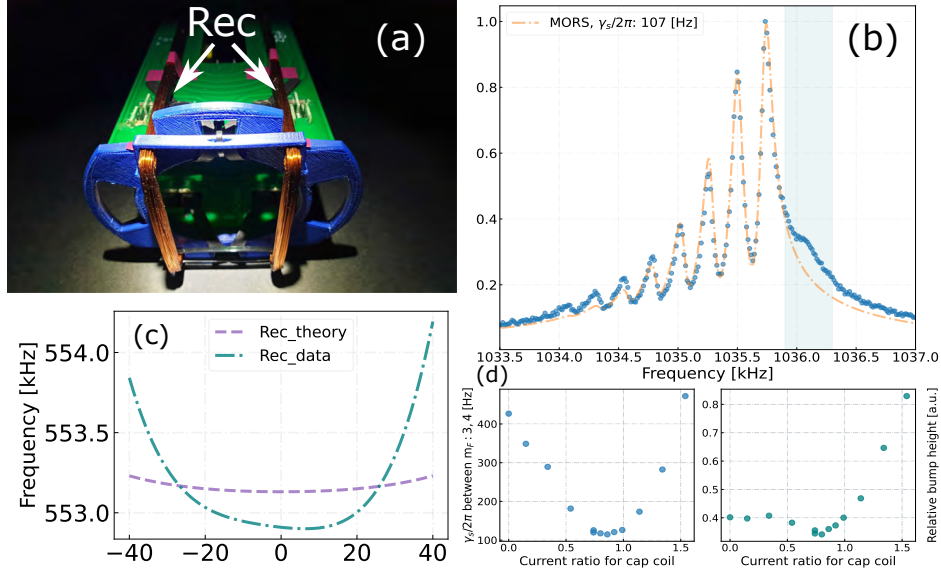
Figure 4.10: Resolved MORS signal with additional Rectangle coil for operating the system at high larmor frequency. (a) A photograph of our final assembled coil system. (b) The completely resolved atom MORS signal. (c) The comparison between the simulated and measurement rectangle coil. (d) The optimization of spin coherence time and homogeneity bump height with the current ratio. The calibration of rectangle coil was performed by Sergey A. Fedorov .

4.4.2 Modeling spin dynamics with magnetic Inhomogeneity

To enhance our understanding of the additional tiny bump observed in previous atomic MORS signals, as well as the atomic motional average limit in our system-where atoms' thermal motion averages out the magnetic field's non-uniformity-we conducted another numerical simulation. This simulation, described in the broadband noise section, utilized parameters such as cell temperature and geometry to close mirror our real experimental conditions. However, this time, we applied a bias magnetic field with three distinct magnetic profiles, with the relative standard deviation (RSD) ranging from 0 to 0.8‰(to simulate the suboptimal gradient field and the second bump observed in the atomic signal at 23 kHz) and up to 3.5 ‰, as shown in Fig.4.11. We then analysis the simulated spin noise spectrum to gauge the impact of magnetic inhomogeneity on the spin signal. The findings, illustrated in Fig..4.11, reveal that the recorded spin noise signal maintain a clear Lorentzian shape with a decoherence of 54Hz, obtained under a magnetic profile depicted by the blue curve in the bottom panel. Under this field profile, an additional minor bump is observed at a slight higher Larmor frequency next to the main atomic signal, attributed to the increased magnetic field strength on the cell's left side, where the atom's thermal motion is insufficient to average out such a field difference, leading to the separated atomic resonances-a similar deviation also noted at 1MHz in the resolved MORS atomic

signal, Fig.4.10 (b), aligning with our numerical simulations in middle plot. The slight difference in frequency between this deviation and the main signal, along with a linewidth of (40 Hz)- slightly narrower than the experimental recorded data- suggests a slightly larger mean free path (MFP) for atoms than in actual experiment conditions. Enhancing the magnetic field's homogeneity can narrow the signal bandwidth and eliminate the inhomogeneity bump, as demonstrated by the purple curve in the right figure. Conversely, reducing the field uniformity to 3.5 ‰severely disrupts the coherence of spin signal; in such a case, the atomic spin's thermal motion fails to average out the field strength's gradient, deviating the signal from a Lorentzian shape. Therefore, for experiments using an 8cm long cell, maintaining magnetic inhomogeneity below 0.8 ‰is advisable. Considering the optimized field inhomogenity of 0.34 ‰, the collective spin oscillator is not limited by our field non-uniformity. This numerical simulation of thermal atoms elucidates the impact of the magnetic field uniformity on our system's spin noise spectrum, offering valuable insights into the homogeneity requirements for future work with varying vapor cell geometries. Additionally, refining the mean free path parameter- or atom velocity-changing collision rate-in our simulation (discussed in the faster decay chapter of Christian thesis)[50] can further align the simulation with the experimental observations.
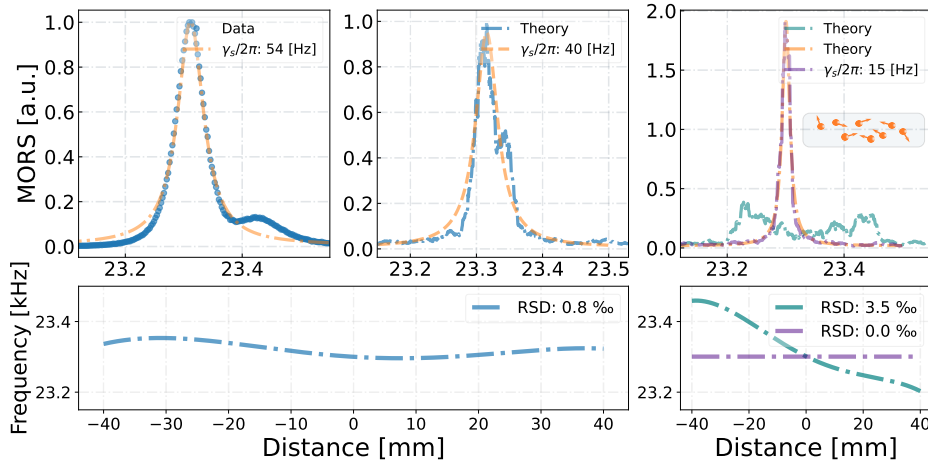
Figure 4.11: Monte-Carlo Simulation of collective thermal atoms experiencing magnetic inhomogeneity. The atomic signal, characterized by a Lorentzian shape (purple), without the influence of bias field inhomogeneity, is primarily limited by the atoms' intrinsic relaxation time. The introduction of an inhomogeneous field, quantified by the Relative Standard Deviation (RSD), along with the assistance of the thermal motional average, results in the broadening of the line-width of atomic signal. However, surpassing a certain threshold of field inhomogeneity leads to the emergence of a second atomic response. This phenomenon is illustrated by a comparison between the experimental observed MORS signal in the upper left plot and the numerically simulated atomic signal in the upper center plot under the identical bias magnetic field (blue curve in bottom left figure) with 0.8 ‰ uniformity, where the second bump in both plots signifies the impact of field inhomogeneity. Increasing the field gradient further (green curve) up to 3.5 ‰ completely exceeds the motional averaging capacity, severely disrupting the coherent dynamic of atomic spins.

4.5 Square top hat beam and beam shaper
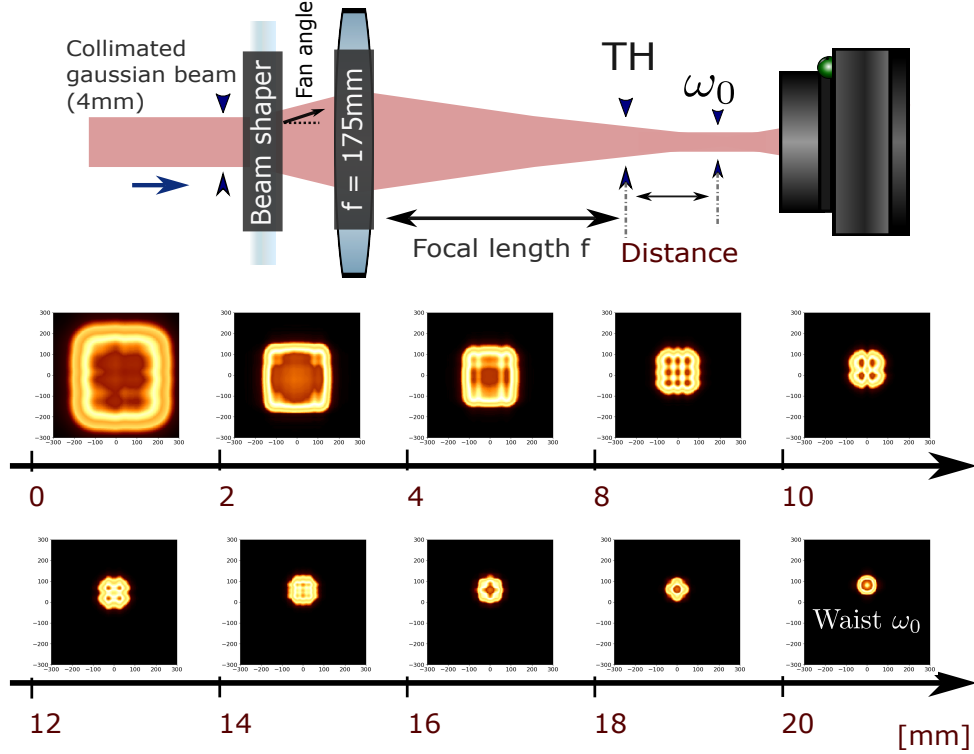
Figure 4.12: **Top Hat Beam generated from a Top hat beam shaper.** This figure illustrates a top hat beam profile with a size of ~ 370 mm produced by a beam shaper in conjunction with a single focusing lens system. The fan angle of the top hat beam shaper results in a displacement ($\sim 20mm$) between the ideal top hat profile and the position of minimal beam waist ω_0. Furthermore, the top hat beam profiles undergo rapid alternations during propagation, attributable to the diffractive beam shaping and convergence.

We have demonstrated that an insufficient beam filling factor and inhomogeneous light-atom coupling can lead to an additional 'fast' decay in spin dynamics, contributing to the broadband noise observed in the spin noise spectrum. Therefore, to counteract the influence of this fast decay mode, and given the geometry of our atomic vapor cell, the atoms are ideally probed by a square top hat beam. This beam's intensity profile, resembling a flat square over the interaction cross section, is similar to the top hat beam implemented in an atom interferometer as presented in [106] to improve the interference contrast, and can also be employed to enhance the quality of biomedical microscopy [107]. In experiments, a flat-top hat beam is obtained by transforming a Gaussian beam from a laser into a flat-top profile using optical elements. This transformation can be realized through the refractive beam shaping, such as using Pi shaper [91, 107]; diffractive beam shaping with a top hat beam shaper from Holor and aspherico company, or

by merging arrays of smaller beams at the target plane. Each method presents unique advantages and disadvantages [108]. In our group, considering factors such as propagation loss, beam uniformity, and the need for compact setup, we decided to generate the square top hat with a diffractive optics element (DOE): GTH-4-2.2 beam shaper, with $\sim 99\%$ transmission efficiency, manufactured by TOPAG Lasertechnik company. This configuration requires us to concentrate only on the beam alignment, divergence, and precise positioning of the target top hat beam. As illustrated in Fig.4.12, a collimated Gaussian with a 4mm diameter (with a tolerance of $\sim 5\%$) is required as the input into this beam shaper. Subsequently, the produced beam diverges at a constant 2.2 mrad fan angle. A focal lens (175mm) is utilized to reduce the propagation distance from infinity down to the focal length, yielding a square top beam with dimensions of 370mm ($\frac{2.2}{1000} \cdot f$). Due to the fan angle, the top hat beam is not collimated and rapidly collapses back to a Gaussian beam at the beam waist ω_0 position, which is now positioned after the square top hat beam as shown in Fig.4.12. In practical applications, a camera is utilized backwards from the beam waist position to ascertain the optimal position for achieving a uniform top hat beam.
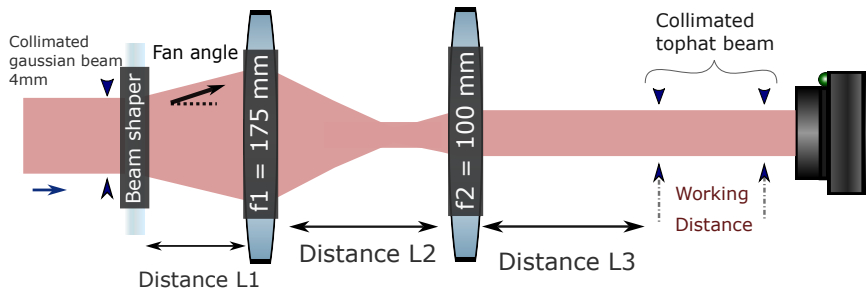
Figure 4.13: Optical setup for generating a collimated tophat beam. To produce a collimated top hat beam, we introduce a second lens with a focal length f2 = 100 mm. By adjusting three tunable distances, L1, L2, and L3, we can establish an effective 4f optical system, counteracting this fan angle effect, aligning the optimal top hat beam closer to the minimal waist, and extending the effective working distance of the collimated top hat beam. In our experimental configuration, the optimal distances between three optical elements are determined to be 606mm, 296mm, and 567mm, respectively.

Analyzing the recorded images of the top hat beam, it becomes apparent that a single lens following the beam shaper is not enough for generating a collimated top hat beam capable of illuminating the whole elongated cell. An initial attempt involved inserting a negative lens at the position of the optimal top hat beam. This arrangement was intended to compensate for the beam's fan angle and relocate the top hat beam closer to the beam waist, thereby, maintaining a top hat beam over a longer distance with a reduced converging angle (details on calculating the second focal length are available in the page 71 of Christian Baerentsen's thesis [50]. Subsequently, a 4f telescope system can be employed to adjust the top hat beam size in accordance with varying cell geometries.

Taking into account practical experimental conditions-such as the preference for

optics placement outside the magnetic shield and the selection of minimal commercially available optics to control the propagation losses-the entire collimation optical system was simplified to an effective '4f' configuration. The setup relies on the relative distances from the beam shaper to the first optical lens, between the two focal lenses, and from the last lens to the target top hat beam position. With the two focal lengths determined, we adjusted three relative distances, to substitute the original arrangement and achieve a collimated top hat beam with an adjustable beam size, as depicted in Fig.4.13. Detailed calculations involving the ABCD ray transfer matrix to determine lens distances based on beam shaper parameters (input beam diameter and fan angle) and desired top hat beam size are beyond the scope of this discussion. However, interested readers are recommended to Christian's thesis Chapter 8.2 [50] for an in-depth exploration. For more precise positioning of each real optical component and quantifying the top hat beam aberration due to the selection of lenses, employing Zemax with actual beam shaper blackbox optics and lens data is recommended [109].

The creation of collimated top hat beam is illustrated in Fig.4.14 , where we monitor the beam's evolution and their intensity profiles along the horizontal axis by adjusting the camera position every 10mm. The optimal top hat beam is located approximately in the center (100-110 mm) of the monitored working distance. To evaluate the quality of the top hat beam, we fit the observed intensity profile with a super-Gaussian function:

$$I(x,y) = A_x A_y \exp\left(-2(\frac{x-x_0}{w_{r_x}})^2\right)^n \exp\left(-2(\frac{y-y_0}{w_{r_y}})^2\right)^n, \qquad (4.1)$$

where the $\omega_{(x,y)}$ denotes the $1/e^2$ radius of the intensity distribution, and the exponent order n characterizes the beam quality, ranging from a standard Gaussian beam (n = 1) to an ideal square top hat beam (n $\to \infty$). As illustrated in Fig.4.15, the analysis reveals that, with the aid of the 4f optical system, the top hat beam's size can be expanded by approximately a factor of 5 up to around 1.5mm, achieving a fitted super-Gaussian order of $n > 5$ in both horizontal and vertical axes. Although slightly convergence is observed during propagation, we have successfully demonstrated the production of an enlarged collimated top hat beam that exceeds the cell's length. When considering the beam size in relative to the 2*2 mm cross-section of the atomic vapor cell, this achievement significantly contributes to mitigating the broadband noise.
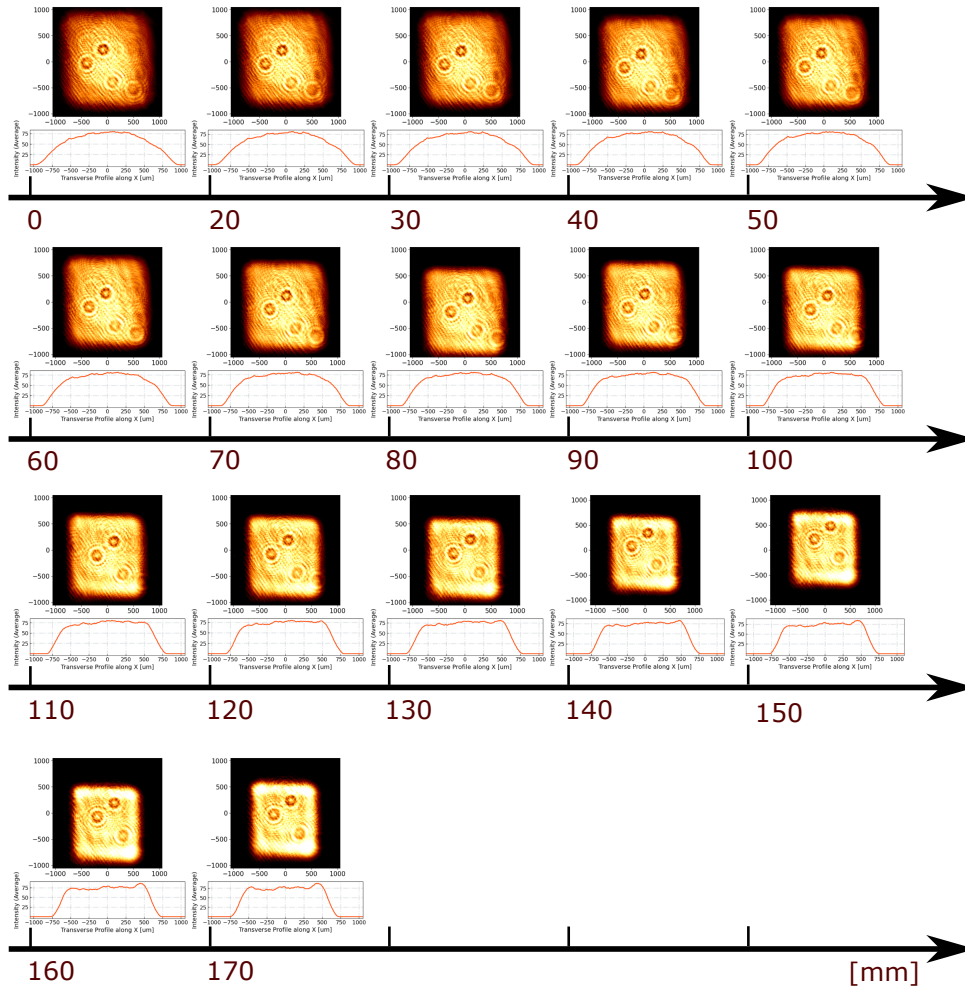
Figure 4.14: Collimated top hat beam. Utilizing a properly designed 4f telescope system allows for optimal compensation of the beam shaper's fan angle, yielding a collimated top hat beam with a tailored beam size. The figures present a top-hat beam with a size of approximately 1.6 mm over a working distance of 170 mm. This span effectively covers the length of the 80mm long atomic vapor cell utilized in our experiment. Notably, the observed spots and patterns in the intensity profile can be attributed to dust and camera-related interference.
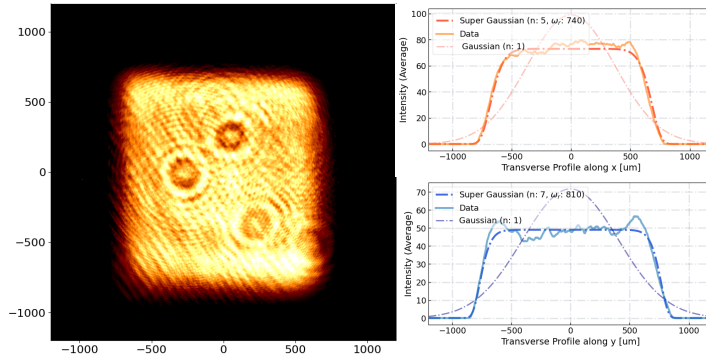
Figure 4.15: Collimated Top hat beam analyzed with high order super Gaussian function. Here we focus on the top hat beam photos (on the left) located at the center working distance (center position of cell), with the goal of evaluating its quality by fitting to a super-Gaussian profile. Illustrated on the right are the intensity profiles of this top hat beam along the horizontal (orange curve) and the vertical (blue curve) axes. Each profile is fitted with super gaussian function characterized by exponent orders n =5 and n = 7, and $1/e^2$ beam radius of 740 um and 810um, respectively. For comparative analysis, the corresponding normal Gaussian beams, with identical radius and n =1, are also presented.
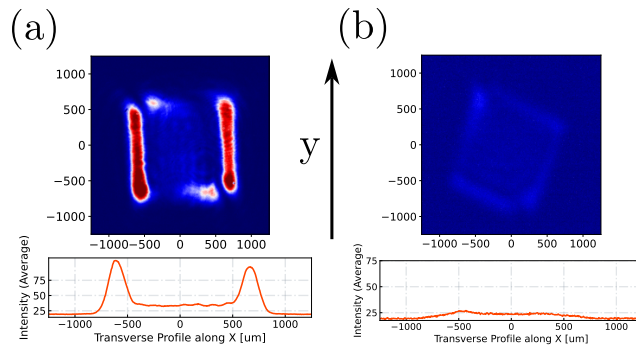
Figure 4.16: Birefringence induced by the top hat beam shaper. The probe laser, vertical linearly polarized, propagates through the beam sharper. The quality of the top hat beam's linear polarization is characterized by monitoring the beam intensity profile with a polarizer inserted before camera. In the figure (a), a clear birefringence effect is observed as the intensity can not be attenuated homogeneously. Fortunately, this birefringent effect can be significantly reduced by aligning the input polarization along the beam shaper's off-diagonal axis (as we demonstrated by rotating the beam shaper by 45 degree in figure (b)). Consequently, the quality of the extinction ratio improves dramatically, from 800 to 8000, maintaining good linear polarization.

We then try to quantify the birefringence induced by the top hat beam shaper, we inserted a high extinction-ratio polarizer before the camera and monitor its maximal attenuation. This characterization is crucial for QND light-atom interactions, which necessitate the use of clean, linearly polarized probe light, as the ellipticity component can induce additional decoherence and spin thermal noise.

We observed inhomogeneous attenuation when the input polarization was aligned either vertically or horizontally with the beam shaper, indicating spatially dependent birefrigence. The degree of polarization ellipticity, inferred by comparing the maximal transmission to attenuation, was around 800. Fortunately, we can substantially reduce the effect-by a factor of 10-by aligning the input polarization along the off-diagonal axis of the beam shaper or by rotating the beam shaper by 45 degrees as in Fig.4.16. This adjustment significantly improves the quality of the probe light polarization, making it more suitable for probing the collective atomic spins.

4.6   Optical pumping and Laser system

We have demonstrated that imperfect atomic spin polarization of the collective spin oscillator consisting of cesium atoms contributes to additional atomic thermal noise. Therefore, preparing the atomic state closer to a two level system is essential. In this section, I will introduce the optical pumping laser system designed to prepare such atomic state for our experiment.

In our experiment, the optical pumping is performed using one or two lasers, depending on practical experimental conditions, which involve balancing the reduction of atomic thermal noise, pumping power broadening, and classical intensity noise. To prepare the negative atomic spin oscillator, we aim to accumulate all atoms eventually in the F =4, m_f =4 dark ground state. Therefore, the selection of optical pumping and repumping transitions within the cesium electronic energy levels structure is presented in Fig.4.17 (b), where the pump laser is locked to the D1 line transition from F =4 →F' = 4 to prepare the atoms to the target Zeeman level, while the repump laser, recycling the atoms from unused F =3 back to F =4 ground state, is locked to D2 line transition from F =3 → F' = 3,4 cross over. It is also interesting to mention **in section** 5.2 of Rodrigo thesis[49], selecting F' = 2 might further enhance the maximal achievable spin polarization using re-pumping only.

To achieve this, the pump and repump laser are generated from Toptica DFB and DL pro tunable diode lasers installed on a separate breadboard as depicted in Fig.4.17. Both lasers are frequency-stabilized using the polarization spectroscopy method [110–112], differing from frequency stabilization via the saturated absorption spectroscopy [113, 114], where a frequency modulation on the probe light is required to extrapolate the error signal. The principle of polarization spectroscopy is to induce a frequency dependent circular birefringence with a circularly polarized pump beam. Linearly polarized light from the same laser source counter-propagates to measure this birefringence, monitored by a balanced polarimeter that includes a half-wave plate, a polarizing beam splitter, and a balanced detector. This setup provides a signal with a dispersive shape, as illustrated by the red curves in Fig.4.17 (c), corresponding to the derivative

of the sub-Doppler line-width of saturated absorption shown as the green curves. This signal can be used directly as an error signal, sent to a PID locking box (in our lab we normally use redpitaya) to stabilize the frequency. Furthermore, the strength and shape of the error signal can be optimized further by adjusting the pump intensity and the bias magnetic field. [115].
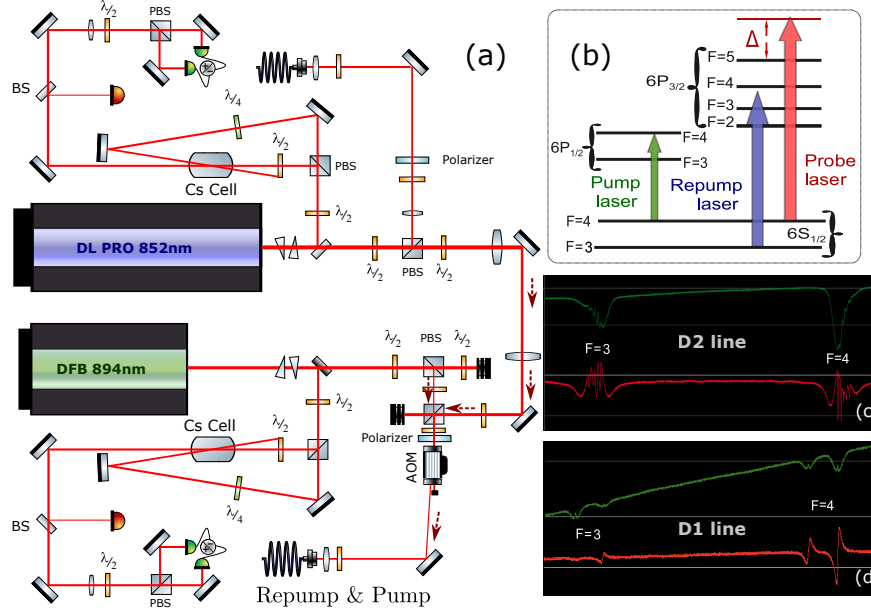
Figure 4.17: Optical pumping & repumping locking system with polarization spectroscopy. (a) The optical pumping and repumping lasers, produced by two diode lasers (Toptica DL pro for 852 nm and DFB for 894 nm), have a tiny fraction split by a polarizing beam splitter (PBS) for wavelength locking. The main outputs from both optical paths are combined via a PBS, a polarizer and an acoustic-optic modulator (AOM), then directed into a polarization-maintaining (PM) fiber for atom pumping. Within the polarization spectroscopy setup, the locking beam is divided by a PBS into a linearly polarized probe and a circularly polarized, counter-propagating pump. The probe beam passes through a beam sampler, where a tiny amount is sent to a single-diode detector to monitor the atomic saturated absorption, while the remainder is directed to a PBS and a balanced detector to acquire an error signal. (b) Optical pumping and repumping energy structure. The pump and repump laser are stabilized at the D1 and D2 line atomic transitions, while the probe in our experiment is off-resonantly tuned with a certain detuning Δ from the D2 line transition. (c) The recorded atomic saturated absorption signals for each laser (green curve) and the corresponding error signals (red curve) are also presented.

After stabilizing the optical pumping lasers, both the pump and repump lasers are combined using a PBS and polarizer, allowing for an adjustable power ratio. They are then directed through an acoustic-optic modulator (AOM) to switch between continuous pumping with adjustable power or pulsed configuration. Subsequently, both beams are sent into a polarization-maintaining (PM) fiber, which is utilized for optical pumping on the atomic setup. Given the 80 mm long cell used in our experiments, the atomic thermal motion along the elongated longitu-
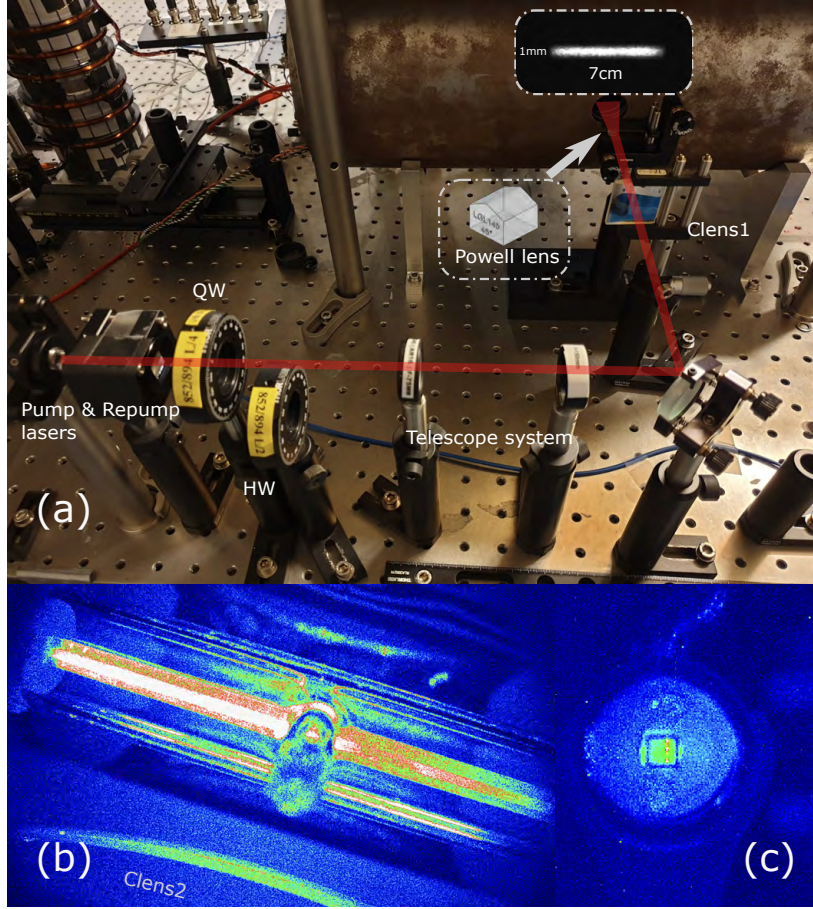
Figure 4.18: Optical pumping setup and enlargement of pumping laser with powell lens. (a) After passing through the PM fiber, the combined pumping & repumping lasers pass through achromatic quarter- and half-wave plates, and are subsequently enlarged into a 7cm*1mm laser line beam using a Powell lens and telescope system. The spontaneous emission fluorescence of atoms, observed as the laser scans across the atomic resonance transitions, facilitates the quantification of both the vapor cell's full illumination and the divergence of laser beams.

dinal axis of cell is insufficient. Therefore, it is necessary for both optical pumping lasers to illuminate the largest possible cross section (for example 2*80 mm^2) of the atomic ensemble. In our atomic setup, as shown in Fig.4.18 (a), the limited space within the magnetic shield necessitates the use of a telescope system, incorporating a cylindrical lens and a Powell lens (line generator). This system create a diverging, homogeneous laser line with a constant fan angle ($\tilde{3}0$ degree) but a variable beam width (from 500um to 5 mm), and a second cylindrical lens (c-lens) to collimate the laser line (here is 1mm*7cm) at the position of the atomic vapor cell. The alignment of pump light propagation, coinciding with the bias magnetic field. can influence the quality of spin polarization, as discussed in section 3.3 of Karsten thesis [55]. In our pumping beam alignment, we normally monitor the spontaneous emission fluorescence of atoms while scanning the optical pumping

112

lasers across the atomic resonant transition. This approach helps to quantify the illumination cross section (b) and beam collimation, as depicted in Fig (c). This method also help us analysis the origin of the degradation of atomic signal such as when the small exchange hole becomes clogged with atoms.

With the experimental setup and preparation outlined above, we are now positioned to advance to the next chapter, where we will commence the calibration of the state of the collective spin oscillator.

Characterization of atomic spin oscillator

In this chapter, we introduce the experimental characterization of the prepared atomic spin oscillator. We will explore methods to extract the effective atomic thermal occupation from the spin polarization, the readout rate of light-atom interactions, and the decoherence rate. We will discuss how to quantify the effective mass of the spin oscillator and strategies to operate the interaction in a quantum non-demolition (QND) configuration, avoiding tensor effects. Moreover, we will demonstrate the cross-validation of extrapolated parameters through observed ponderomotive squeezing and the virtual frequency shift induced by its cross-correlation.

5.1   Calibration of atomic spin polarization, MORS

We have demonstrated that the necessity for atomic ensembles to closely mimic a two-level system to function effectively as collective spin oscillators. This emulation in our experiment is achieved through optical pumping, a technique detailed in Section 4.6 of the previous chapter. We now focus on a critical experimental method for quantifying the performance of optical pumping via the spin polarization, which is known as the Magneto Optical Resonance Signal (MORS). This method, presented in Julsgaard's work from 2003 [116] , enables the direct extraction of steady-state atomic information such as the decoherence rates among Zeeman sublevels and their associated atomic population distributions once equilibrium is reached with certain probe and pumping power. As presented in Fig.5.1, this MORS process involves applying a continuous RF magnetic field close to the Zeeman transition energy to induce a coherent displacement in the collective atomic spin oscillator or more specifically a coherent coupling between the adjacent magnetic sublevels. Following this, the dynamics of the displaced spin oscillator's information are encoded onto the polarization rotation of a far-
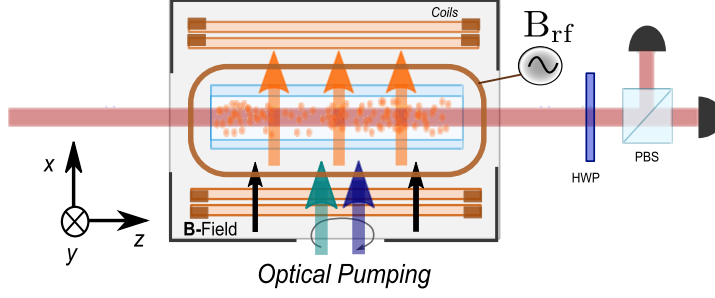
Figure 5.1: Experimental setup for characterizing spin polarization. The atomic ensemble is positioned inside a magnetic shield, surrounded by bias magnetic coils, producing the field along the x-axis. Circularly polarized optical pump and re-pump lasers, co-propagating along the quantization x-axis, prepare the polarized atomic ensemble. An RF coil, orthogonal to the bias coils, produces an oscillating magnetic field along the y-axis, driving the atomic spins. The resulting atomic signal is imprinted on the polarization rotation of the probe light, which is then directed to the polarimetry for further analysis.

off-resonant, linearly polarized weak probe light through the ensembles' circular birefringence. The resultant photo-current is directed into a polarimetry detection system, then demodulated using a lock-in amplifier synchronized with the RF signal. This allows us to extract the atomic frequency response to the applied RF magnetic field that can later be used to extrapolate the atomic population distribution.

Considering atomic ensembles with N total atoms, this MORS signal spectrum can be described by the following expression (a brief derivation of the MORS signal from equation of motion can be found on page 65 of Michael's thesis) [88]:

$$\text{MORS}\left(\Omega_{RF}\right) = A(N) \cdot \left| \sum_{m=-F}^{F-1} C(F,m)\chi\left(\Omega_{RF},m\right)\left(P_{m+1} - P_m\right) \right|^2. \quad (5.1)$$

Here, A is a signal strength that depends on the total atom number, and $C(F,m)$ is the Clebsch-Gordan coefficients for cesium atoms, which quantify the probability of each quantum states in the total angular momentum basis. The atomic susceptibility function, $\chi(\Omega_{RF,m})$, represents the frequency response of each pair of Zeeman sub-levels to the applied RF magnetic field. It can be expressed as a function of the scanning RF frequency, Ω_{RF}, and spin decoherence rate, $\gamma_{m+1,m}$, as follows: $\chi\left(\Omega_{RF,m}\right) = \frac{g_F\mu_B B_{RF}}{4\hbar} \cdot \frac{1}{(\Omega_{m+1,m}-\Omega_{RF})-i\gamma_{m+1,m}}$. The last part in MORS theory is of our interest as it reflects the atomic population distribution within the i-th Zeeman sub-level. As discussed in section 3.7, when the dynamic of atomic ground state approaches thermal equilibrium and experience equally decoherence, denoted by γ_S , the populations of the Zeeman levels can be modeled according to an effective Boltzmann distribution. This leads us to a commonly used thermal MORS model with significantly less free parameters,

which is written as:

$$\text{MORS}(\Omega_{RF}) = A(N) \cdot \left| \sum_{m=-F}^{F-1} \frac{(F(F+1) - m(m+1))\left(e^{\beta(m+1)} - e^{\beta m}\right)}{(\Omega_{\text{S}} + m\Omega_{\text{qzs}} - \Omega_{\text{RF}}) - i\gamma_S/2} \right|^2.$$

(5.2)

For the parameter β, which represents the spin temperature, it is used to estimate the atom spin polarization P, according to the expression: $P = \frac{1}{ZF}\sum_{m=-F}^{F} me^{\beta m}$, which was also presented in Eq.(3.57).

Figure.5.2 compares the recorded atomic signal (blue curve) in the frequency regime where quadratic Zeeman splitting is resolved, alongside the fitted orange curves that align with the thermal equilibrium model. With an increase in re-pump power targeted at the D2 line transition from F = 3 to F' =4, the atom populations at F =3 are observed to gradually deplete, as evidenced by a decreasing atomic signal at higher response frequencies (0.3 ‰) and an increasing atomic signal at low frequencies, indicating atoms being recycled back to the F =4 ground state. Concurrently, the re-pumping process assists in enhancing the spin polarization, which eventually stabilizes at 80%. We also observe additional peaks next to both F =3 and F =4 response signals. These signals can be attributed to the same Zeeman level but exhibit slightly higher Larmor frequency due to the magnetic in-homogeneity.

To further increase spin polarization, we incorporate an optical pumping laser, as depicted in Fig.5.3. In our experiments, we select the optical pumping transition on the D1 line from F = 4 to F' = 4 , achieving an improvement in spin polarization up to 98% while requiring significantly less optical power relative comparing to the repump laser. However, the pumping laser can also lead to noticeable power broadening due to spontaneous emission [49], a phenomenon that will be addressed in subsequent Coherently Induced Faraday rotation (CIFAR) section. Thus, optimizing atom quantum cooperativity C_q, necessitates a careful balance between minimizing atomic thermal noise with sufficient spin polarization and mitigating the broadening effect introduced by optical pumping. Another potential approach to improve this most critical quantum cooperativity (the ratio between coherent backaction and atomic thermal noise) involves modifying the pumping transition in the excited state from F' = 4 to F' =3. This adjustment, as presented in page 51 of Rodrigo and page 55 of Hanna thesis [49, 72], results in significantly less broadening on the coherence of $m_F = (3, 4)$ Zeeman transition. The impact of this modification on atomic spin polarization P and even light-atom interaction strength- readout rate Γ_S, remains an interesting area for future exploration.
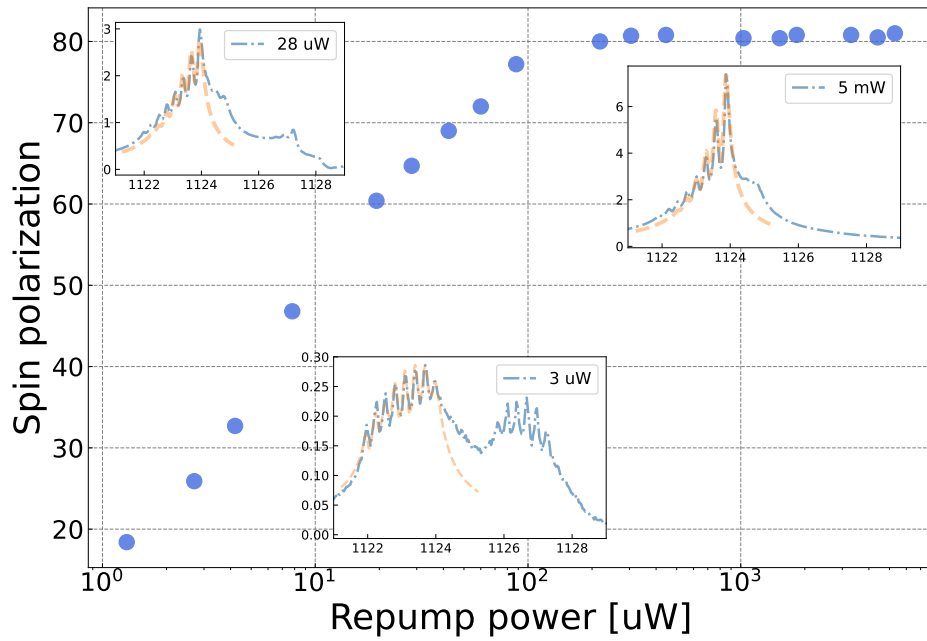
Figure 5.2: Optimization of the spin polarization with repump laser power.
In the quadratic Zeeman splitting resolved frequency regime, observations show that
atoms are almost equally distributed between the F = 3 and F = 4 hyperfine states at
a repump power of 3 uW. Increasing the $\sigma+$ repump power leads to a gradual depletion
of atoms from the F =3 state, effectively recycling them back to the F =4 ground state.
Meanwhile, the process enhances the atomic spin polarization, achieving up to 80% solely
with the re-pump laser.
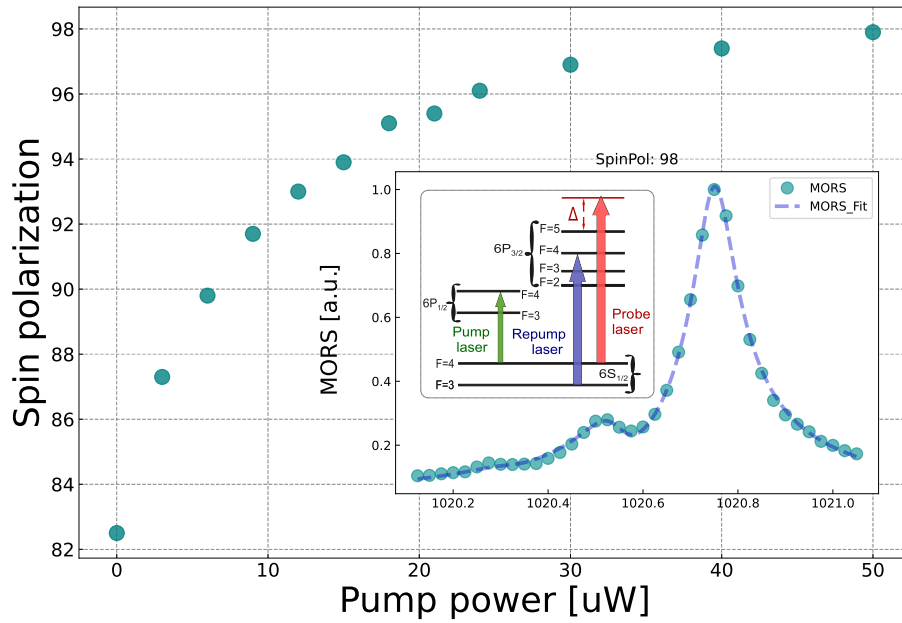
Figure 5.3: Improvement of the spin polarization with optical pumping beam. Integrating the pumping laser significantly improves atomic spin polarization from 82 % up to 98%. However, the pumping laser directly couples to the Zeeman transition coherence in the F =4 ground state, inevitably introducing decoherence through the pump power broadening. This additional effect will be explored in the next CIFAR section.

5.2 Calibration of interaction readout rate- CIFAR

After preparing atomic ensembles with high spin polarization, which enables us to treat the atomic system as collective spin oscillators, our next goal is to precisely calibrate the light-atom interaction strength. This strength is quantified by the measurement readout rate, symbolized as $\Gamma_S \propto g_S(\Delta)^2 S_x F_x$, and is influenced by the collective spin length, polarized photon number, and the probe detuning. We introduce an additional calibration technique-known as Coherently Induced Faraday Rotation (CIFAR) [117], which facilitates the extrapolation of the spin readout rate Γ_S and the spin linewidth γ_S. This calibration method allows direct access to the light-atom interaction strength and total spin decay rate while optimizing key parameters such as probe and optical pumping power, atomic density, etc. Alongside the previously calibrated spin polarization from the MORS measurement, these two methods collectively enable us to estimate the quantum cooperativity parameter, C_q. Our aim is to predominantly prepare the atomic spin oscillator to be influenced by the light quantum fluctuation-induced backaction noise, rather than langevin thermal noise, assuming the system operates within the quantum regime. However, classical noise can often dominate in practical experiments, making the CIFAR measurement a vital method for calibrating essential system parameters without operation in the quantum regime. Further discussion on the couplings of classical noise will be presented in the following chapter.

 The method for quantum cooperativity calibration, as presented in the Appendix D of Rodrigo's thesis [49], was conducted by analyzing the increased spin noise strength, which was dominated by classical backaction noise driven by calibrated white probe polarization noise as a function of varying modulated white levels. This method allows for the extraction of quantum cooperativity from the proportionally increased spin noise amplitude. However, it requires accurate knowledge of both the detection efficiency and the white noise modulation value, which are challenging to measure experimentally. On the other hand, the CIFAR method introduced here enables the direct extraction of interaction strength from a distinct dispersion signal, independent of the accuracy of the detection efficiency and modulation strength. This CIFAR method is inspired by the Optomechanically-Induced Transparency (OMIT) method detailed on the page 54 in William's PhD thesis [118], a calibration widely utilized in optomechanics community. The core principle of the CIFAR method is to analyze the induced interference between two classical drive modulations-both in phase and amplitude- through the spin oscillator's frequency responses. This generated interference, akin to ponderomotive squeezing, generates a dispersive signal.

Let us briefly review the CIFAR calibration setup and signal model. As depicted in Fig.5.4 , the experimental setup employs a strong linearly polarized local oscillator (LO) to interact with atoms, defining the spin readout rate and establishing the steady state of atomic spins. Meanwhile, a significantly weaker drive beam,
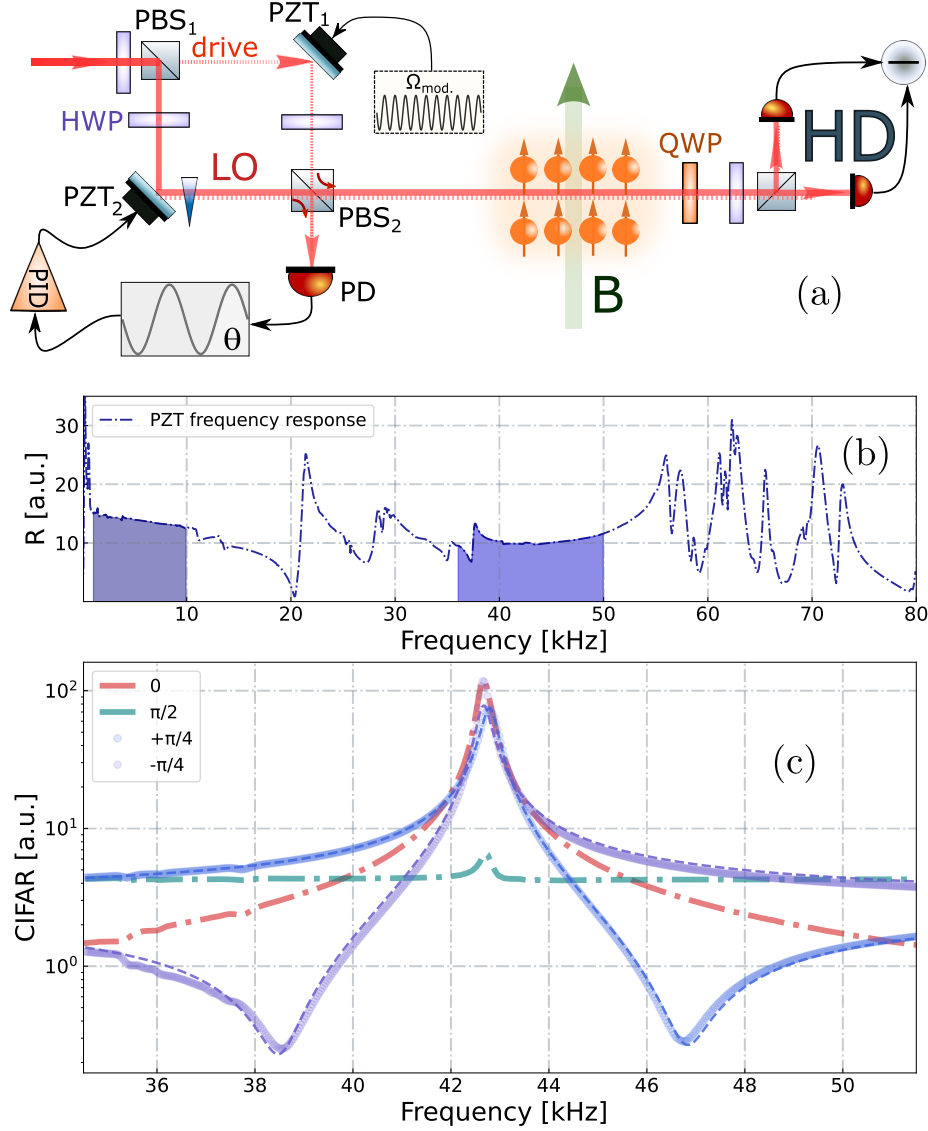
Figure 5.4: Readout rate calibration with Coherent Induced Faraday Rotation (CIFAR). (a) Diagram of the calibration setup. The probe laser is split into a strong local oscillator (LO) arm and a weak phase modulation arm. Both lasers are recombined at a polarizing beam splitter (PBS) and locked with a relative phase θ. After interacting with atoms, the combined light is directed into a balanced polarimeter and demodulated at the same modulation frequency. This modulation is scanned across the atomic Larmor frequency to acquire CIFAR signals for further analysis. (b) Calibration of the piezo frequency response $G(\Omega)$ in modulation arm. (c) CIFAR signals driven with the modulation arm at $\pm 45°$ relative to the LO arm. The red and teal curves represent the Lorentzian and flat atomic responses, respectively, and are used as references to calibrate the locking phases. The two mirrored dispersion curves (blue and purple) illustrate the extrapolated readout rate of 7740 , 8070 Hz, with decay rates of 320 Hz and 310 Hz, respectively.

experiencing phase modulation G, and overlapping orthogonally with the LO

light at a tunable relative phase θ, acts solely as a classical modulation and does not affect the readout rate. Such phase modulation can be accomplished using either an Electro-optic modulator (EOM) or Piezoelectric Chips. In our work, we utilize a high resonant frequency ring pizeo up to 515kHz from thorlabs (PA44LE) to cover our frequency range of interest. The calibrated piezo (PZT) frequency response curve is presented in Fig.5.4(b), two shaded areas with relative flat response are considered as optional work frequency regime.

The input light phase and amplitude quadratures, with classical phase modulation, are expressed in the frequency domain as:

$$\left(\begin{array}{c} X_{\mathrm{L}}^{\mathrm{in}}(\Omega) \\ P_{\mathrm{L}}^{\mathrm{in}}(\Omega) \end{array} \right) = \left(\begin{array}{cc} \cos\theta & -\sin\theta \\ \sin\theta & \cos\theta \end{array} \right) \left(\begin{array}{c} 0 \\ G(\Omega) \end{array} \right) = \left(\begin{array}{c} -\sin\theta \\ \cos\theta \end{array} \right) G(\Omega). \quad (5.3)$$

Let's consider the simplest QND interaction configurations, where all tensor dynamic contributions previously discussed are neglected. Additionally, we neglect the atomic thermal baths, as the system is predominantly influenced by classical polarization modulation:

$$\left(\begin{array}{c} X_{\mathrm{L}}^{\mathrm{det}}(\Omega) \\ P_{\mathrm{L}}^{\mathrm{det}}(\Omega) \end{array} \right) = \left(\begin{array}{cc} \cos\phi & -\sin\phi \\ \sin\phi & \cos\phi \end{array} \right) \left(\begin{array}{cc} 1 & 0 \\ \Gamma_{\mathrm{S}}\chi_S(\Omega) & 1 \end{array} \right) \left(\begin{array}{c} X_{\mathrm{L}}^{\mathrm{in}}(\Omega) \\ P_{\mathrm{L}}^{\mathrm{in}}(\Omega) \end{array} \right). \quad (5.4)$$

Assuming we lock the relative phase θ such that the input light amplitude and phase polarization quadratures have identical modulation strengths, satisfying $X^{in} = \pm P^{in} = G(\Omega)$. We evaluate the phase quadrature of light ($\phi = \pi/2$) via the half-wave plate in the balanced detection setup , as shown in Fig. 5.4 (a). In this configuration, the quarter-wave plate is utilized solely to compensate for the half wave plate imperfections. As this modulation frequency scans across the atomic resonance, we can observe and reformulate the signal equation in terms of the modulation $G(\Omega)$ as follows:

$$P_L^{out} = (1 \pm \Gamma_S\chi_S(\Omega)G(\Omega), \quad (5.5)$$

from the above signal equation, we notice that the atomic response term with $\chi_S(\Omega)$ is now decoupled from the modulation $G(\Omega)$. Based on this, we can calculate the spectrum of CIFAR signal, normalized to the modulation drive $G(\Omega)$, as shown in the presented Piezo frequency response curve:

$$\mathrm{CIFAR}(\Omega) = \left| P_L^{out}(\Omega)/G(\Omega) \right|^2 = 1 + \Gamma_S^2 |\chi_S(\Omega)|^2 \pm \Gamma_S \mathrm{Re}[\chi_S(\Omega)]. \quad (5.6)$$

Therefore, we can acquire the signal without being influenced by the detection efficiency or the modulation strength G. Similar to the quantum backaction noise driven by the quantum fluctuation of the probe light's orthogonal polarization component, as discussed in Chapter 3, the CIFAR signal contains a constant offset, indicating the classical modulation ('1' after the normalization), a Lorentzian

function, and a more interesting dispersive term that represents the interference between the two classical quadratures of light through the motion of the spin oscillator. This interference can be either destructive or constructive, leading to two distinct signal bumps that indicates maximum transparency or opaqueness, as shown in Fig.5.4 (c). In the limit of high Q and focusing solely around the atomic resonance frequency, we could apply the simplified spin susceptibility function $\chi_S(\Omega) \sim \frac{1}{2(\delta\Omega - i\frac{\gamma_S}{2})}$ (here, $\delta\Omega$ is $(\Omega_S - \Omega)$). Therefore, with the relative phase locked at $\theta = \pi/4$, and the input drive satisfying $X^{in} = -P^{in} = G(\Omega)$, we have:

$$\left|P_L^{out}\right|^2 \approx 1 + \frac{\Gamma_S(\Gamma_S - 4\delta\Omega)}{\gamma_S^2 + 4\delta\Omega^2}. \tag{5.7}$$

After performing a simple derivation with respect to $\delta\Omega$, one can identify the frequencies $\delta\Omega$ corresponding to the minimal and maximal CIFAR signals:

$$\begin{aligned} \delta\Omega_{max} &= \frac{1}{4}(\Gamma_S - \sqrt{\Gamma_S^2 + \gamma_S^2}), \\ \delta\Omega_{min} &= \frac{1}{4}(\Gamma_S + \sqrt{\Gamma_S^2 + \gamma_S^2}), \\ \delta\Omega_{max} - \delta\Omega_{min} &= \frac{1}{2}\sqrt{\Gamma_S^2 + \gamma_S^2} \sim \frac{1}{2}\Gamma_S. \end{aligned} \tag{5.8}$$

Therefore, in the limit of $\Gamma_S \gg \gamma_S$, based on the frequency difference between the minimal and maximal peaks in CIFAR signal, one can make a reliable estimation of the interaction readout rate. More accurate readout rates (Γ_S) and linewidths (γ_S) can be extrapolated from the fitted CIFAR signal.

In Fig.5.4 (c), we present examples of recorded CIFAR signals with varying phase θ of overlap between the LO and driven beams, where the homodyne detection phase is set at the phase quadrature. The selection around 40kHz is due to the flat frequency response, ensuring that the piezo resonance doesn't significantly affect the fitting precision. As discussed in the signal model, the accurate readout rate is acquired when the relative phase is locked at $\pi/2$. Therefore, in our experiments, the target phase is calibrated by identifying the symmetric Lorentzian (red curve) and flat atomic responses (teal curve), which correspond to the pure P and X quadratures of of light (A tiny bump in the flat response quadrature indicates the leftover tensor contribution), while scanning the locking phase. The correct locking phase for the CIFAR signal is typically in the mid-range(sometimes not precisely $\pi/4$ due to instrument imperfections). one can also flip the locking phase to acquire a mirrored CIFAR signal. Using the weighted mean of two CIFAR signals can further enhance the precision of the precision of parameters. With the newly introduced CIFAR calibration method that enables us to efficiently extrapolate the interaction readout rate and decoherence, we can now explore two examples-optical pumping and probe- that will help us better optimize the atomic system during the preparation stage. In the MORS section, we presented that optical pumping can enhance the spin polarization from 82%
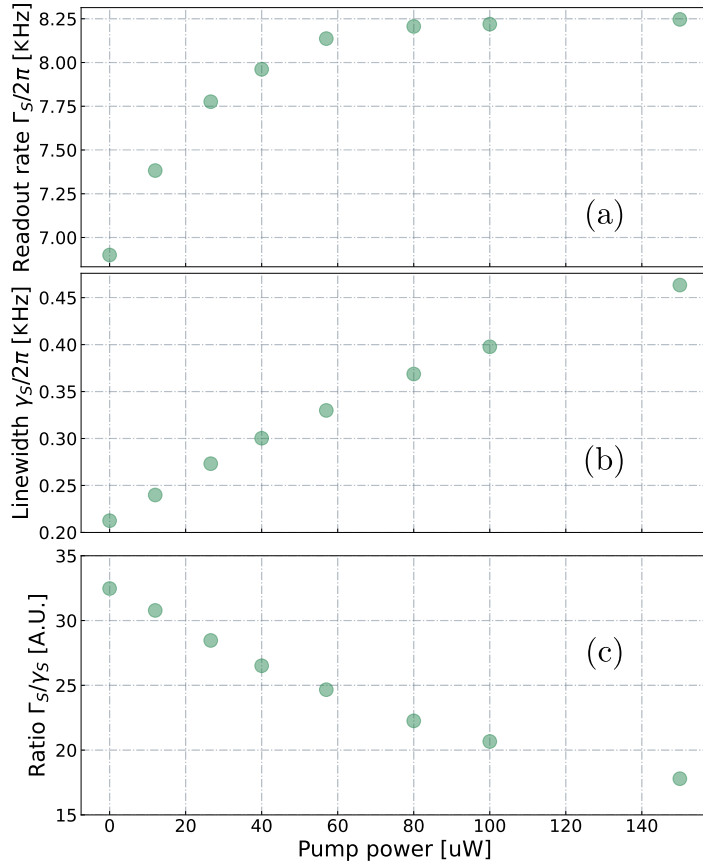
Figure 5.5: Calibrated spin readout rate and linewidth as functions of pump power. We observe a faster increment in the decay rate compared to the spin readout rate, indicating a gradual reduction in the classical cooperativity $\frac{\Gamma_S}{\gamma_S}$. In this experiments, atoms operated at 39° are probed with 1mW detuned by 1.6GHz, the repump laser is set at 5 mW, and we vary the pump power to quantify its influence on spin readout rate and decoherence.

up to 98% at the cost of additional pump power broadening. With the CIFAR calibration, we now acquire more detailed information about the steady-state spin oscillator under varying pumping power; the results are displayed in Fig.5.5. In this strong probe ($\sim$ 1mW) power regime, we observe a slight increase in the spin readout rate with the pumping power, this suggests that the pumping power attempts to return collective atoms back to the desired spin oscillator state, acting as the repumping beam. However, this increase is not comparable with the pump power broadening, and it then reaches a plateau, indicating the interaction is limited by insufficient probe power. On the other hand, we note a continues increase in pump power broadening, which further decreasing the classic cooperativity, denoted as $\frac{\Gamma_S}{\gamma_S}$. A complete analysis of quantum cooperativity should also consider the degradation of the atomic thermal noise.

Moreover, we observe a change in the ratio of readout rate to linewidth as we optimize the probe power during the interaction. It is worth noting that these

124
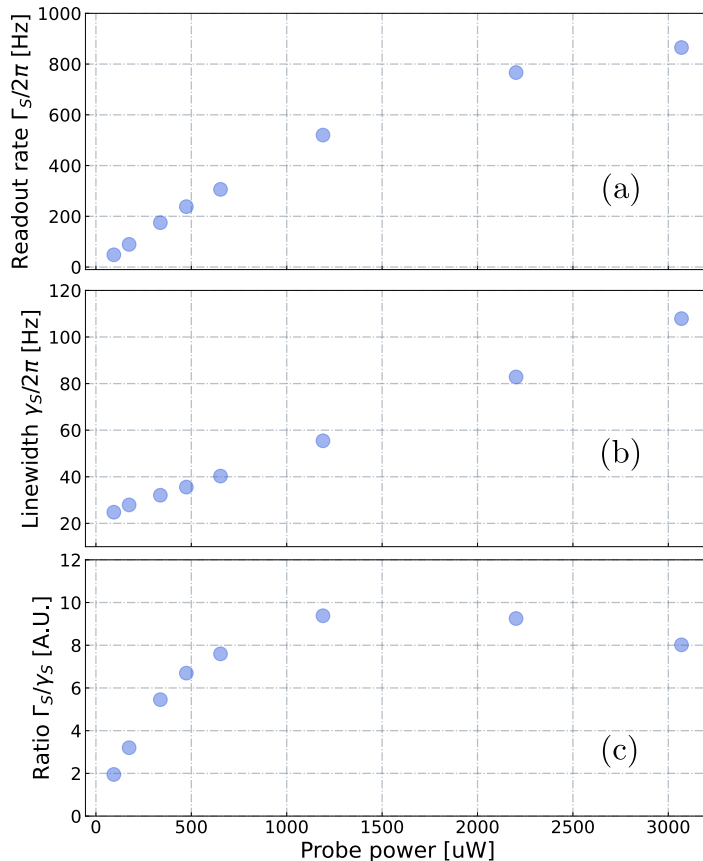
Figure 5.6: Calibrated readout rate and linewidth as functions of probe power. We observe different scaling behaviors for the readout and decay rate as functions of probe power from the pumping laser. The classical cooperativity $\frac{\Gamma_S}{\gamma_S}$ increases until the probe power saturates the atoms; after this point, it begins to degrade. These measurements were performed using a cell with dimensions $3*3*80$ mm^3 at an operating temperature of $\sim 23°C$. This trend can also be extrapolated to other cell geometries and temperatures. The repumping power was carried out with a power of 5 mW, while the pump was conducted with a power of 50 uW.

experiments were performed with different cells at different times under different temperature conditions; however, the scaling of the ratio remains constant. We observe an enhancement in the spin readout rate with increased probe power, accompanied by the associated power broadening. Different from the case with the pump beam, here, we notice a rise in classical cooperativity, reaching a maximum plateau that represents the saturation of atomic spins during the interaction. Beyond this point, further increasing the probe power leads to a slower rise in the readout rate and begins to degrade this cooperativity. This indicates that there is an optimal probe power for each experimental condition to achieve maximum classical cooperativity.

In this section, we only cover the CIFAR calibration in the QND interaction configuration, readers interested into the general CIFAR expression including the

tensor and broadband contribution calibrations, are recommended to refer to section 8.2 of Rodrigo's thesis [49].

5.3   Experimental setup for spin noise measurement
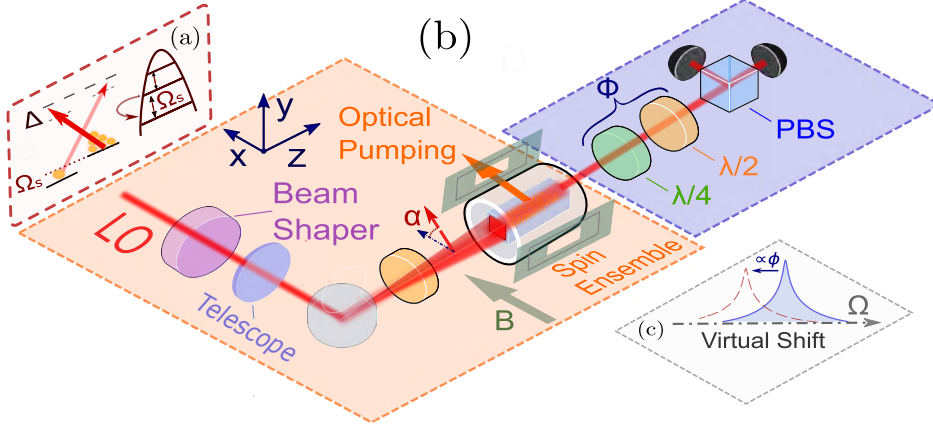
Figure 5.7: Setup scheme for spin noise measurement. (a) Probe light frequency and atomic energy structure. (b) The atomic ensemble is probed by a linearly polarized, collimated top hat beam, generated from a beam shaper and telescope system. This beam is detuned by $\Delta/2\pi \sim 1.6$ GHz relative to the D2 line F = 4 → F' = 5 transition, with the power set at 1 mW. The input polarization, at an angle α with respect to the quantized magnetic axis, can be adjusted via a half-wave plate. The effective mass of the spin oscillator can be altered by changing the direction ($\sigma+$ or $\sigma-$) of the circularly polarized optical pumping beams, or the orientation of the bias magnetic field **B**. After interacting with the atoms, the probe light is analysed using a balanced polarimetry, where the detection phase is selected through a combination of half and quarter wave plates. (c) Adjusting the detection phase also facilitates the realization of a virtual frequency shift in the oscillator's resonant frequency.

With the atomic spin oscillator prepared and the strength of the light-atom interaction optimized, we now concentrate on analyzing the spin noise spectrum. Before proceeding, it is essential to briefly review the setup for measuring spin noise. As illustrated in Fig.5.7, the spin oscillator is established through optical pumping of the atomic ensemble into either the highest $|F = 4, m_F = 4\rangle$ or the lowest $|F = 4, m_F = -4\rangle$ Zeeman sublevels, determining the effective oscillator masses, and achieving a spin polarization of 98% as verified by MORS measurement. The Larmor frequency of the spin oscillator, controlled by the bias magnetic field strength, is adjustable from MHz down to a few Hz. A linearly polarized top hat probe beam, with its preparation detailed in section 4.5, labeled as LO and set to atomic vapour cell with an optical power of 1 mW, is aligned at an angle α relative to the magnetic field along the x-axis. This beam interacts with atoms detuned by $\Delta/2\pi$ from the D2 line $6S_{1/2}$, F =4 → 6 $S_{3/2}$, F' = 5 transition, with the detuning set at 1.6 GHz for most analyses in this chapter. Following the interaction, the probe beam, now carrying information on the spin dynamics, is

126

directed into a balanced polarimeter. The phases of detection in the polarimeter are adjusted via a quarter-wave and a half-wave plates. The recorded photocurrent is sent to a low-noise 16-bit vertical resolution analog-to-digital converter (ADC) with sampling rates up to 125 MS/s (Spectrum M2p5913-x4), enabling a Fast Fourier Transform (FFT) for further analysis of the captured spin noise spectrum.

5.4   Calibration of atomic spin broadband noise
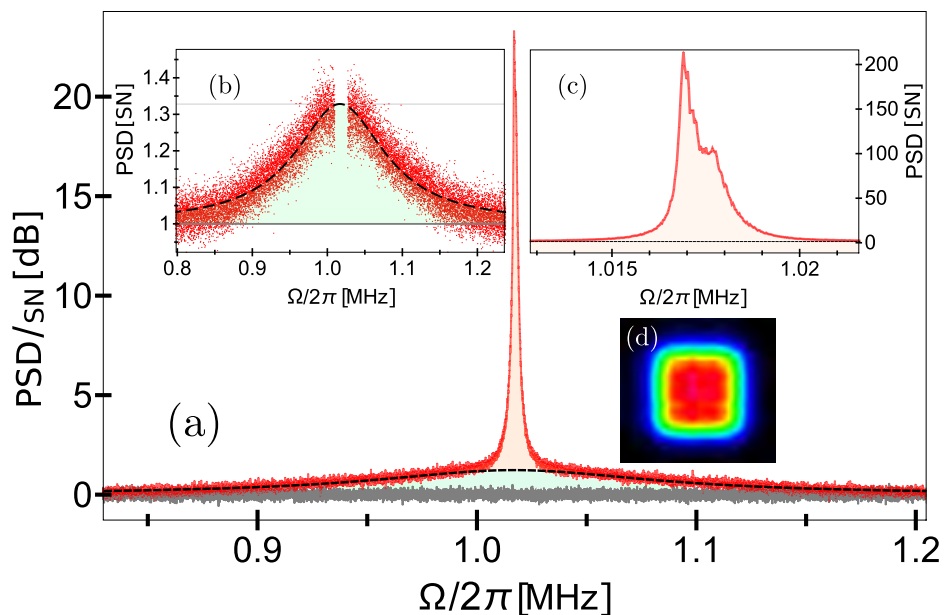
Figure 5.8: Spin noise spectra recorded with a square top hat beam. (a) The measured spin noise spectra of atomic spin oscillator precessing at 1 MHz showing (b) broadband and (c) narrowband noise contributions. The estimated ratio of the narrow band to broadband amplitude is $\tilde{8}00$. These results were obtained using a $1.65*1.65 mm^2$ square top hat beam.

In Section 3.8, we discussed how the thermal motion of atomic spins leads to spin-locality dependent interaction strength. This dependency varies with the uniformity of the probe spatial intensity, and sub-optimal filling factors, which can modify the shape of the recorded spin noise spectrum, introducing additional broadband noise. In our experiments, this broadband noise can be significantly reduced by employing a square top hat laser beam for probing atoms.

The result depicted in Fig.5.8 shows the recorded spin noise spectrum using a $1.65*1.65 mm^2$ square top hat beam, as illustrated in Fig (d). The spectrum was acquired with the atomic cell operating at $39°$ and precessing at approximately 1 MHz. From the plot, we can distinguish the Zeeman splitting resolved narrow band spin responses in orange and a broadband noise floor marked in green. The level of broadband noise is 0.3 in shot noise (SN) units, and the ratio of narrow-

band to broadband noise is ~ 800, a substantial enhancement over the results of about ~ 100 reported in page 72 of Rodrigo's thesis [49], which the measurements were performed with a Gaussian beam. By fitting the broadband noise with the complex susceptibility function introduced in Chapter 3, we extract a bandwidth for the broadband contribution of ~ 150 kHz.

Moreover, we also compare the numerically simulated and experimentally recorded
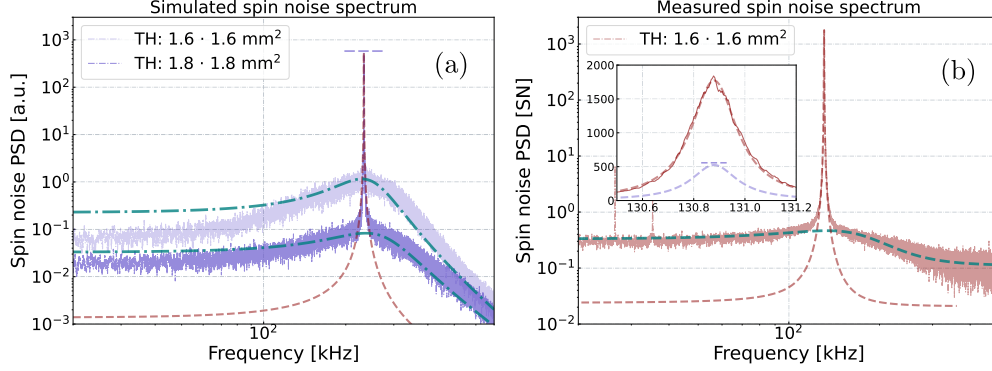
Figure 5.9: Comparison of numerically simulated (purple curve) and experimentally acquired (tomato curve) spin noise signals The numerically simulated spin noise signals are re-scaled based on the extrapolated atomic thermal noise shown in Fig.(b) inner plot. This adjustment yields a good match between the dynamics of the spin noise in the simulation and the experimental data. The extrapolated linewidth of the simulated broadband noise is approximately 180 kHz, closely aligning with the 150 kHz measured in the experimental data.

spin noise spectra to quantify our understanding of the theoretical model, as demonstrated in Fig.5.9. Since our simulation only accounts for the atomic thermal noise without incorporating the quantum backaction noise, the spin noise depicted in Fig.(a) has been re-scaled based on the constructed atomic thermal noise from experiments. This reconstruction is linked to the observed ponderomotive squeezing, which will be elaborated upon in the following ponderomotive squeezing section. The predicted broadband noise from the simulation closely matches our observed spin broadband noise in both height and bandwidth, providing an effective instruction to minimize the broadband contribution with the right top hat size. It is also worth noting that the broadband noise increases more at ultra low Larmor frequency as contributions from the negative sideband frequency can add up to the spin noise spectrum.

Regarding the proposed application of the broadband quantum noise reduction, since the broadband noise acts as additional uncorrelated spin noise due to the relatively large decoherence rate, it is crucial that this contribution remains less than 1 unit of shot noise across our frequency band of interest (30 kHz around the Larmor frequency), this enabling the entangled light in the atomic reference arm to assist the joint measurement of the hybrid system in surpassing the standard quantum limit (SQL) without being overwhelmed by this broadband noise. With the observed maximum of 0.3 shot noise (SN) contribution, we are now prepared

to proceed to the next section.

5.5   Spin noise spectra with effective mass

After characterizing the atomic broadband noise, we shift our focus to the most relevant, quadratically resolved narrow-band spin response at around 1MHz. Fig.5.10 displays quantum noise measurements in the MHz frequency range, showcasing the quantum backaction (QBA)-dominated spin response in both the positive- and negative-mass configurations. Imperfect optical pumping results in significant populations of levels other than $|F = 4, m_F = -4\rangle$ (or $|F = 4, m_F = 4\rangle$), leading to multiple peaks in the Zeeman-splitting-resolved spectrum. This aids in distinguishing the effective oscillators' mass. Specifically, we observe two peaks around $\Omega/(2\pi) \approx 960$ kHz, identified as the transitions $|m_F = \pm 4\rangle \leftrightarrow |m_F = \pm 3\rangle$ for $\Omega_{S1,(a,d)}$, and $|m_F = \pm 3\rangle \leftrightarrow |m_F = \pm 2\rangle$ for $\Omega_{S2,(b,c)}$ within the $F = 4$ hyperfine multiplets. We also notice a third unresolved signal remains at higher frequency for both cases that are attributed to the magnetic field inhomogenity as we discussed in previous Section 4.4.3 . In Fig.5.10 (c), the highest atomic population at lower energy (frequencies) indicates a spin prepared in the positive mass configuration, whereas Fig.5.10 (d), represents a negative mass configuration, with the populations prevailing at the highest energy state. Additionally, residual atoms in the $|F = 4, m_F = \pm 3\rangle \leftrightarrow |F = 4, m_F = \pm 2\rangle$ transitions and the third atomic signal at $\Omega_S/(2\pi) \approx 1$ MHz necessitate an extension of the model to multiple oscillators. These oscillators' QBA noise contributions, driven by the vacuum fluctuations of probe light orthogonal components, can even interfere with each other with varying phases, as each spin oscillator has slightly different Larmor frequency.

$$\overline{S}_{\Sigma}^{\text{det}}/\text{SN} = 1 + \overbrace{\sum_{i=1}^{n=3} e^{i\phi_{S,i}} \Gamma_{\text{S,i}}^2 |\chi_{\text{S,i}}(\Omega_i)|^2}^{\text{QBAN}} + \overbrace{\sum_{i=1}^{n=3} 4\gamma_{\text{S,i}} \Gamma_{S,i} |\chi_{\text{S,i}}(\Omega_i)|^2 \left(n_{\text{S,i}} + \frac{1}{2}\right)}^{\text{TN}}.$$
(5.9)

Using this multi-oscillator model, we estimate the overall integrated areas of QBA noise and thermal noise, respectively. We find a quantum cooperativity $C_q = 2.7 \pm 0.3$ for the positive-mass oscillator, focusing on the largest atomic signal in Fig.(c). We also extract effective thermal occupation of $n_S \sim 0.6$ for this signal, which aligns with the corresponding thermal occupancy of ~ 0.55 based on Fig.3.7 estimated from the 89% spin polarization measured with high probe power, as discussed in [94]. The estimated ponderomotive squeezing $\overline{S}_{sq} = -4.8$ dB based on the quantum cooperativity correlates well with the observed squeezing in Fig.5.10(e). The negative-mass oscillator exhibits slightly reduced ponderomotive squeezing, likely due to a sub-optimal current ratio between the magnetic coils causing additional inhomogeneous broadening and increased spin

damping rate. These calibration results indicate that the spin oscillator is primarily influenced by the quantum shot noise, backaction and atomic thermal noise in this frequency regime.
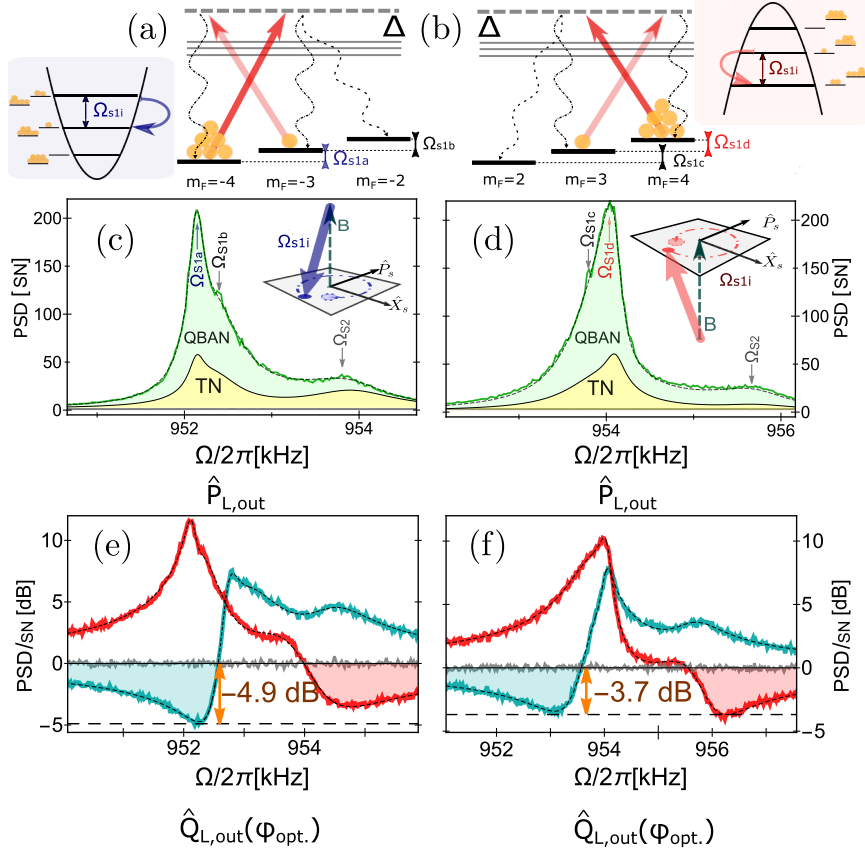
Figure 5.10: Spin noise spectra with effective positive and negative mass spin oscillators (a,b) The cesium atomic ensemble in our experiments is modeled as a harmonic oscillator using a 2-level-system approximation. The spin oscillator exhibits an effective negative mass (or frequency) when the atoms are prepared at $m_F = 4$, and a single excitation lowers the energy of the atomic state in (b). Conversely, the oscillator in (a) shows a positive mass when the excitation increases the energy. The recorded spin noise spectra are processed at 0.96 MHz. In real experiments, the effective mass is identified in the non-ideal spin polarization within the quadratic Zeeman splitting resolved regime. By observing the frequency of the second resonant signal $\Omega_{S2,(b,c)}$, which indicates the $m_F = (-3, -2)$ *or* $(3, 2)$ Zeeman sublevels, relative to the main spin oscillator frequency $\Omega_{S,(a,d)}$, one can distinguish between a positive spin oscillator with the Larmor frequency of largest signal ($\Omega_{S1,a}$) lower than the second resonant peak ($\Omega_{S1,b}$) (c), or a negative spin oscillator with a higher procession frequency ($\Omega_{S1,d}$) (d) in the noise spectrum. The observed ponderomotive squeezing in fig.(e,f) for both configurations indicates that the atomic systems are predominantly influenced by the quantum backaction noise. The reconstruct atomic thermal noise (TN) and quantum backaction noise (QBAN), based on the spin noise fit, are also presented in (c, d) for clearer illustration. In this frequency regime, a third peak, presumably arising from the magnetic field inhomogeneity, is also observed. The spectra demonstrate readout rates of $\sim$3.6 kHz and $\sim$2.7 kHz for the largest $\Gamma_{S,1}$ and second $\Gamma_{S,2}$ spin signals, respectively, with an effective thermal occupation of $n_S : \approx 0.6$.

130

5.6 Calibration of QND and tensor interaction

As we analyze the measured spin noise spectrum, we aim to utilize the quantum backaction noise acquired from the light-atomic spin vector Faraday interaction as a quantum noise 'eater' to cancel noise in other quantum systems. However, for real cesium atoms used in our experiments, which have nonzero nuclear spins, we must also be aware of another tensor alignment interaction. Although it can be small, this interaction further complicates the light-spin interaction through linear birefringence, and even involves quantum back-action noise from unwanted orthogonal components of the probe light, as shown in eq.(**??**). This can compromise the dominance of Faraday back-action in the atomic system. Therefore, it is crucial to calibrate the light-atom interaction and choose an appropriate experimental configuration beforehand. In this section, we will explore the influence of the tensor interaction term on the spin dynamics around the atomic Larmor frequency and introduce two calibration methods that can minimize these higher-order terms, ensuring the atoms operate maximally close to the QND interaction regime.

The measured tensor Stark shift and its induced effects on dynamic broadening or cooling of the collective spins, as introduced in Section 3.4, are shown in fig.5.11. These parameters are extracted by fitting the MORS signals at varying input polarization angles, as exemplified in the inner plots. More specifically, the light-induced tensor stark shift is derived from the frequency difference between two fitted atomic resonant signals. after subtracting the Zeeman splitting component. Subsequently, this extrapolated energy shift, which results from different input polarizations, is modeled with the following function:

$$\Omega_{tensor}/2\pi = A(1 + 3\cos 2\alpha).\qquad(5.10)$$

In particular, this sinusoidal scaling of the input polarization angle enables us to zero this tensor stark shift by setting this angle to approximately $\alpha \sim 54.7$, as indicated by the dashed horizontal line in purple. The discrepancy between the fitted tensor shift and the extrapolated shift is primarily due to the imperfectly resolved atomic signals around these polarization angles, which increases the uncertainty of the estimation. Meanwhile, in eq.(**??**), we introduce the tensor interaction that couples through the spin's quadrupole transition, potentially altering the decoherence of the spin dynamic around the Larmor frequency. This can lead to additional light-atom interaction such as beam-splitter or two-mode squeezing configuration, affecting the spin decoherence rate as: $\gamma_S/2 + \epsilon_S\Gamma_S$. The tensor term ϵ_S here scales with the input polarization angles as: $\epsilon_S \propto -A'\cos 2\alpha$. This inverse scaling of the spin decoherence relative to the Stark shift with the input polarization angle α is also observed in the two bottom plots in Fig.5.11.

The influence of the tensor interaction can also be observed in spin noise measurements at very low Larmor frequencies, where the quadratic Zeeman splitting
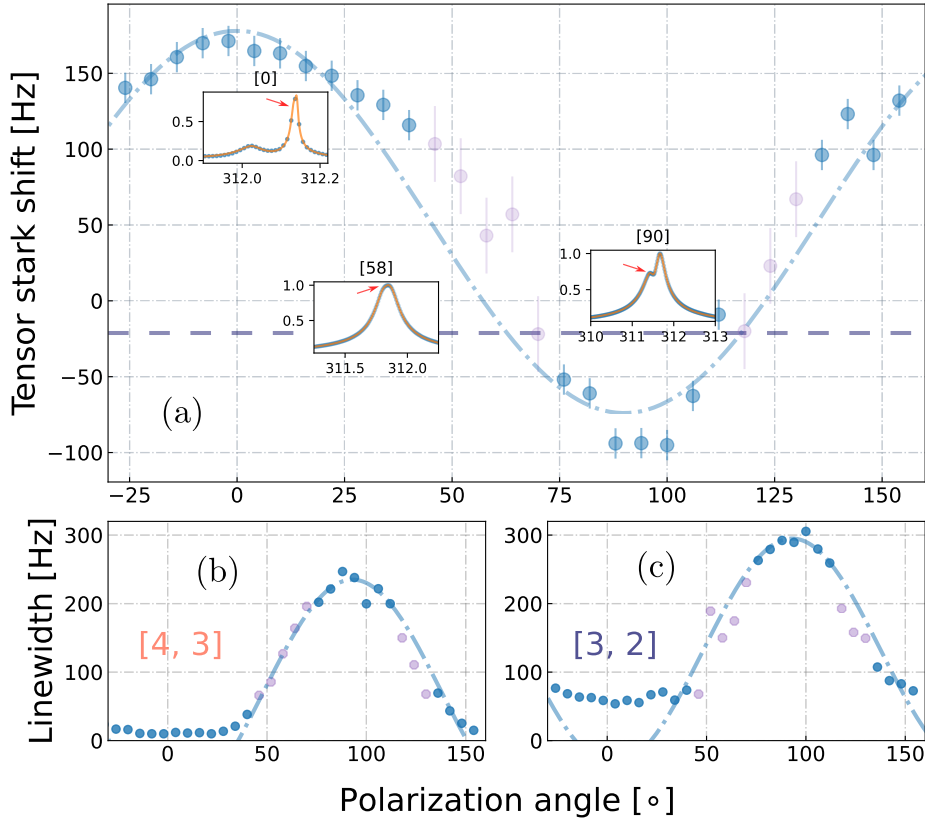
Figure 5.11: Tensor stark shift and broadening as a function of input polarization angle. (a) The extracted tensor stark shift from the fitted MORS signal as a function of the input polarization angle α. Several raw MORS signals are also presented for clarity.(b,c) Tensor broadening for the large population atomic state and second-neighbour response as a function of the polarization angle. The probe detuning is set at 800 MHz for better presenting the tensor effect.

is unresolved. In Fig.5.12 (a), the spin dynamics are monitored at the phase quadrature (difference between the $\pm$ 45 ° linear polarizations) of light detected with a polarimeter controlled solely by a half-waveplate. The recorded spin noise exhibits a clear modification as the tensor term-quantified by the tensor readout rate ϵ_S-varies with the input polarization angle. This effect is attributed to the additional dynamic quantum back-action noise driven by quantum noise from the orthogonal light quadrature, as predicted in theoretical model described in (3.49).

Furthermore, the inclusion of a quarter-wave plate in the detection setup allows for monitoring the orthogonal amplitude (or $\sigma\pm$ polarization difference), as shown in Fig.(c). Here, while the Faraday interaction doesn't appear, the tensor contribution can prevail. This difference in amplitude quadrature enables maximal minimization of the tensor contribution by achieving a flat spin noise signal through varying the input polarization at lower probe detuning ($\sim$ 800MHz). It is also noteworthy that, despite the more complex interaction dynamics, the

tensor alignment term offers new potential to observe enhanced ponderomotive squeezing of light in Fig (b).
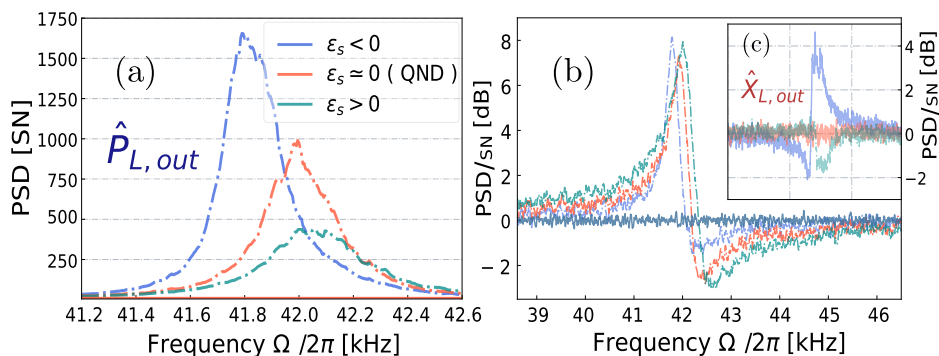
Figure 5.12: Spin noise spectra with tensor effect in the unresolved frequency regime. At low Larmor frequencies where the quadratic Zeeman splitting is unresolved, we notice that the width of the acquired spin noise spectra is modified by the tensor readout rate ϵ_S via the input polarization angle α. We observe different magnitude of spin noise signals in light phase quadrature ($\hat{P}_{L,out}$) (a) as well as different ponderomotive squeezing (b). This effect is more clear visualized in light amplitude quadrature $\hat{X}_{L,out}$ (c) where the QND contribution is not presented. Here the probe detuning remains at 1.6 GHz.

5.7 Ponderomotive squeezing- calibration of quantum cooperatively

When the Larmor frequency is reduced to 130 kHz while all other experimental conditions remain the same, the quadratic Zeeman splitting becomes negligible, and the spin ensemble behaves as a single spin oscillator with a significantly enhanced spin signal, as presented in Fig.5.13. From the fits of the pure phase quadrature $\overline{S}_{QND,P}^{det}$ and the quadrature $\overline{S}_{QND,sq}^{det}$ yielding the strongest ponderomotive squeezing, we extract the essential parameters of the atomic spin dynamics, to prevent the overestimation of model parameters, both the readout rate and linewidth are set based on the results in CIFAR measurement with 10 % confinement, while the thermal occupancy remains free. We extracted the readout rate $\Gamma_S/(2\pi) = 7.8\,\mathrm{kHz}$ and the linewidth $\gamma_S/(2\pi) = 0.23\,\mathrm{kHz}$, whereas the amount of thermal noise, encoded in the thermal occupation $n_S = 3.7$, is a significantly higher than the value $n_S \approx 0.6$ measured at $\Omega_S/(2\pi) \approx 1\,\mathrm{MHz}$ [1]. Following this, we estimate the quantum cooperativity $C_q \approx 1.9$ with the corresponded ponderomotive squeezing $\overline{S}_{sq}^{det} = -4.0\,\mathrm{dB}$, which matches well with

---

[1] Here we use the parameter-thermal occupancy n_s to quantify the reduction of ponderomotive squeezing, therefore, the increased thermal noise is not only due to the imperfect spin polarization, we will elaborate on more details about several additional sources in the next chapter.

the experimentally observed $-4.2\,\mathrm{dB}$ value and thus validating the agreement of the theory model. Meanwhile, the calibration of the quantum cooperativity C_q cross-validated with the measured ponderomotive squeezing enables us to precisely quantify the amount of the quantum backaction together with the non-correlated effective thermal noise. This can later be utilized for better performance estimation of the broadband quantum noise reduction.
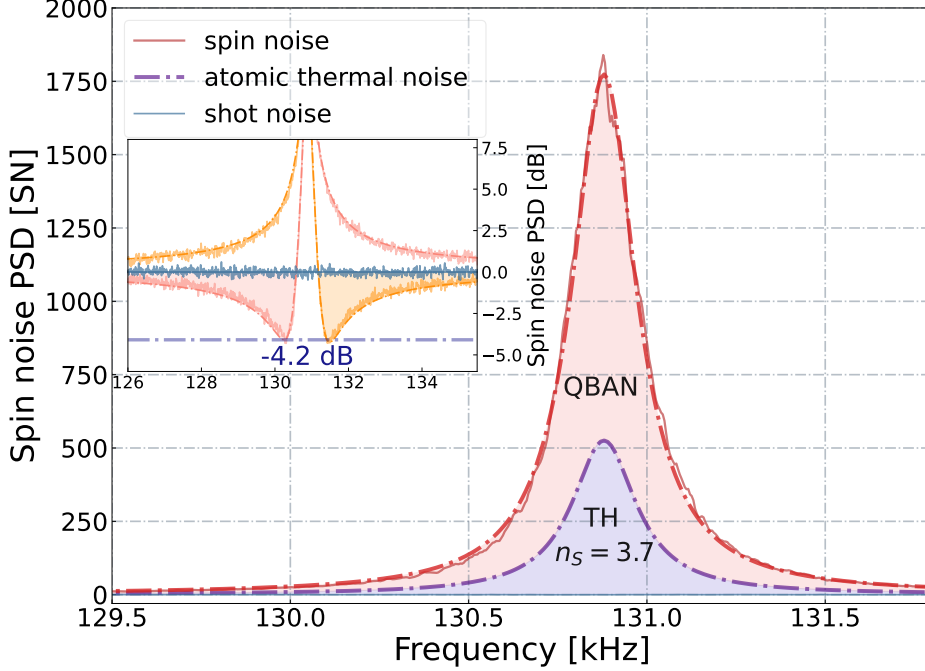
Figure 5.13: Quantum noise calibration for spin oscillator at 130 kHz. The measured spin noise and two largest ponderomotive squeezing curves at 130 kHz Larmor frequency are fitted with the QND spin noise model. The extracted parameters enable us to distinguish and reconstruct the amount of quantum backaction noise (colored in red area) and effective atomic thermal noise (colored in purple) in the total spin noise. The fitted parameters are: readout rate $\Gamma_S/2\pi$: 7.8 kHz , decay rate $\gamma_S/2\pi$: 0.23 kHz. The extrapolated quantum cooperativity from the spin noise data is $C_q \sim 1.9$.

5.8 Calibration of virtual frequency shift

We continue characterizing the atomic system, extending into the upper range of the acoustic frequency regime, with the Larmor frequency approximated at $\Omega_S/2\pi \approx 18\,\mathrm{kHz}$. By fitting the measured spin noise spectrum, we extract critical parameters of the atomic spin oscillator. The readout rate $\Gamma_S/2\pi$: 8.1 kHz, and the decay rate, $\gamma_S/2\pi$: 0.21 kHz. These values are still consistent with the CIFAR calibration results. The extracted thermal occupation, n_S : 3.5, is slightly better than the 120 kHz result. These parameters enable us to estimate the quantum cooperativity of $C_q \approx 3$, corroborated by the observed -5 dB pon-

deromotive squeezing shown in Fig.5.14 (b). Furthermore, Fig.5.14 (a) presents both the reconstructed quantum backaction noise and the atomic thermal noise contributions to the overall spin noise.

As anticipated at the conclusion of Chapter 3, the cross-correlation between shot noise and quantum backaction can alter the spectrum of the light noise, mimicking a probe system with a virtually downshifted resonance frequency. Following the thermal force noise normalization process described in Eq.(3.59), we extracted the total quantum noise component from the experimental data using the extrapolated parameters. We then normalize the total quantum noise of the spin oscillator at 18 kHz to the coefficient of atomic thermal noise, represented as $4\gamma_S\Gamma_S|\chi_S|^2\cos\phi^2$. As depicted in Fig5.14 (c), we observe a frequency shift of $\Delta\Omega_S/2\pi \leq -2.0\mathrm{kHz}$ in our experimental data. The maximal frequency downshift occurred at a homodyne phase set to $\phi = \pi/4$, closely matching the predictions based on the extracted readout rate $\sim \Gamma_S/4$. This demonstration supports the feasibility of a real spin oscillator operating in the few kHz range, employing the virtual frequency shift method to align with the frequency response of free mass gravitational wave detectors (GWDs) operating at near-DC frequencies.
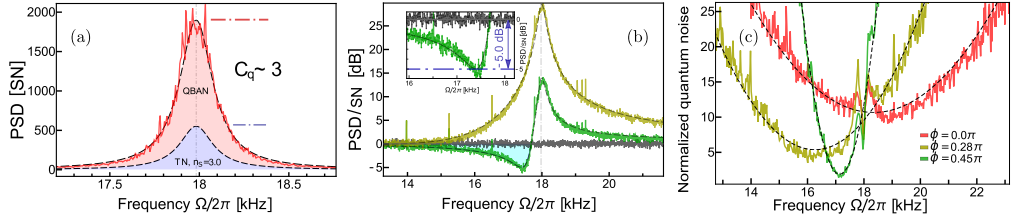
Figure 5.14: Calibrating the effective frequency downshift via the virtual frequency shift. (a) The spin noise spectrum, recorded at 18 kHz, shows the reconstructed atomic backaction noise (in red) and effective thermal noise (in purple), based on the extrapolated quantum cooperativity $C_q :\sim 3$. (b) Adjusting the homodyne phase facilitates the generation of maximum ponderomotive squeezing, $\overline{S}_{sq} \sim -5\,\mathrm{dB}$ (illustrated by the green curve), which aligns well with the predictions from the theoretical model. The yellow curve represents detection at another phase close to $\phi \sim -\pi/4$. Axes are normalized to the shot noise of light, presented on linear (SN) or decibel scale (dB). (c) Normalization of the total spin noise to the atomic thermal force coefficient, as described in eq.(3.59), exhibits the virtual frequency shift of the atomic resonance frequency $\Omega_{S,eff}$. This effective frequency shift is depicted through the frequency downshift of the minimum dip of the thermal force-normalized quantum noise, as shown in the yellow ($\Delta\Omega_s/2\pi \sim -2.0\mathrm{kHz}$) and green curves ($\Delta\Omega_s/2\pi \sim -1.2\mathrm{kHz}$) relative to the reference red curve. Apart from that, this normalized quantum noise reduces the vertical offset, indicating an enhancement of sensitivity to the force signal, and increases the curve steepness, which corresponds to a reduced sensitivity bandwidth. The extract readout rate is $\Gamma_S/2\pi : 8.1\,\mathrm{kHz}$, and the decay rate is $\gamma_S/2\pi : 0.21\,\mathrm{kHz}$. The overall efficiency is 92%.

We have now completed the experimental calibration of the atomic spin oscillator, successfully demonstrating an atomic system dominated by quantum back-action noise. Moving forward, we will continue to reduce the atomic Larmor frequency and explore its noise performance at significantly lower acoustic frequencies.

Towards the gravitation wave frequency range

Having explored the spin noise spectra in the upper audio band, we have now shifted the Larmor frequency to the much lower acoustic range, extending to sub-kHz frequencies. We anticipate observing similar quantum noise-limited spin responses in this frequency regime. However, in real experiments, the atoms in this frequency band were overwhelmed by the classical noise environments. To address these issues, we updated our system and improved the noise performance of our electronics such as current source, balanced detector, and optical pumping lasers, to minimize their influences at low acoustic band. Additionally, we detected another atomic response at the near-DC sidebands frequency independent of the atomic Larmor frequency, fortunately, we notice such DC atomic noise scales down much faster than the QND backaction noise, thus we can effectively minimize such noise by carefully choosing the detuning of the probe light without significantly affecting the quantum backaction noise. These methods enabled us to re-observe ponderomotive squeezing as low as approximately 900 Hz when probing the atoms with a diode laser at 4 GHz detuning. Subsequently, to better match the atomic system with the entangled light source for our proof-of-principle experiment, we transitioned the probe light from the diode laser to the Ti:Sapphire laser. This change initially resulted in significantly higher amplitude noise that dominated all quantum dynamics. However, through collaboration with my colleague Alkiviadis Zoumis and Tulio Brito Brasil, we successfully mitigated this probe amplitude noise using a homemade active noise eater, thereby restoring the -3.5 dB ponderomotive squeezing at 5 kHz.

6.1 Reduction of RF current noise

To achieve quantum noise-limited performance down to such a low acoustic Larmor frequency, one experimental improvement involves reducing the current noise

from the bias coil current supply. Classical current noise around the Larmor frequency can significantly excite the spin oscillators more than the quantum backaction from vacuum fluctuations. Therefore, after evaluating various current sources, including the bipolar triplet current source [102], and the MLD203CLN - Constant Current driver from thorlabs, we selected the low noise laser diode drive from Koheron, this device characterized by a current noise of 50 pA with a 40mA output down to 100 Hz, and we powered it with a DC battery. This configuration allows us to operate an atomic system at an acoustic frequency without significant influence from current noise, thereby achieving the experimental results that will be presented. In our proof-of-principle experiment, we hypothesized that overall quantum noise reduction would be more effective in cells with much less decoherence, such as a 7Hz intrinsic decay rate for a 5mm cross-section cell. However, such a cell would require substantially higher probe power to achieve the necessary readout rate, placing more challenging requirements on the maintenance of shot noise and magnetic shielding quality. After careful calibration of spin noise for various atomic vapor cells with our current experimental setup, we decided on a 2*2 mm^2 cross-section cell with an intrinsic decay rate of 36Hz, which proved to be the optimal candidate for our current experiment.

6.2 Observation of noise coupling through optical pumping & repumping

During our measurement, to maintain sufficient spin polarization while probing with a high-power probe, we employed continuous pump and repump lasers. However, we observed that both the pumping and repumping could influence the spin noise spectra when the atomic system operates closer to the DC spectrum frequency, potentially compromising the measured ponderomotive squeezing. As discussed in Chapter 5.1, the repump laser prepares the collective spin oscillator with a spin polarization up to 80%. Consequently, we normally operate the system with a continuous 5 mW repumping laser. When the Larmor frequency is reduced to the lower acoustic frequency band ($\leq$ 20 kHz), electronic modulation spikes begin to appear around the atomic signal, as presented in Fig.6.1 (c). These spikes were simultaneously observed in the intensity noise of the previous diode laser from Toptica DL100, as shown in Fig.6.1 (a), and were confirmed to originate from the electronic noise in the locking system. Replacing the repumping laser with cleaner DL pro laser, as in Fig.6.1 (b), coupled with an improved locking system (from redpitaya STEMlab 125-14), allows us to achieve a much cleaner spectrum around the atomic signal, as demonstrated by the orange curve in Fig.(d).

Regarding the optical pumping laser, its influence is more complex. On one hand, we can employ the pumping laser to further improve the spin polarization
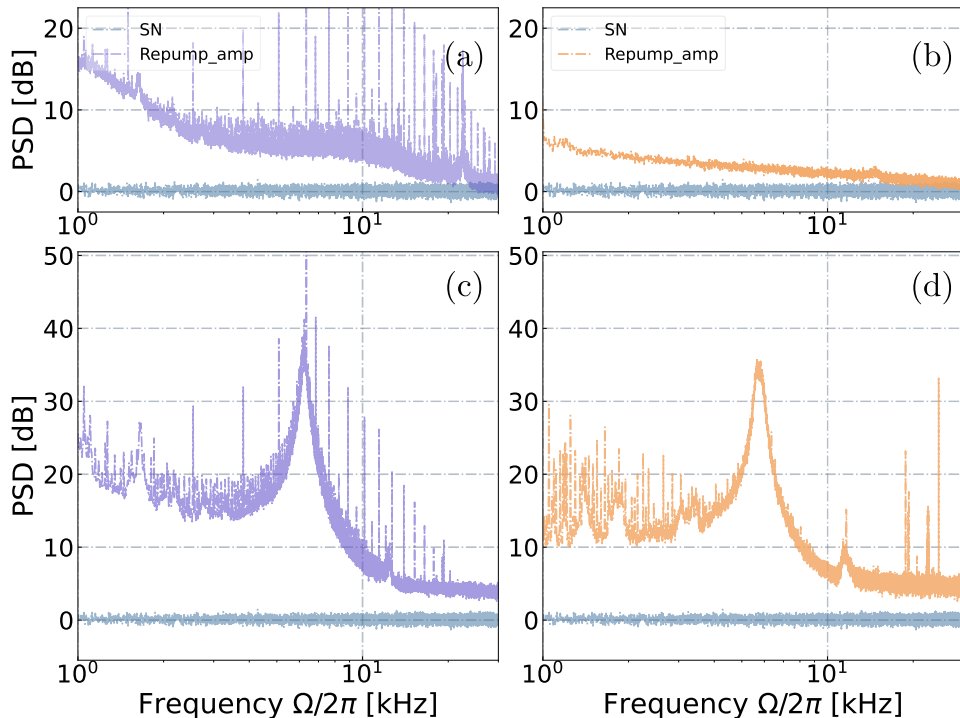
Figure 6.1: Spin noise spectra influenced by repump laser amplitude noise.
At lower acoustic frequencies, repump laser amplitude noise impacts the recorded spin
noise spectra. Classical noise from the Toptica DL100 laser in Fig.(a), attributable to its
noisy control electronics, is evident with identical noise spikes in the spin noise spectrum
as shown in Fig.(c). These noise spikes around the atomic signal disappear when the
repump laser is replaced with the quieter DLpro laser in Fig.(b), equipped with a superior
locking system, as demonstrated in Fig.(d).

up to 98 % and even recycle some atoms back to the Zeeman sub-levels of inter-
ests. On the other hand, as the optical pumping directly couples to the atomic
transitions interacting with the probe light, it introduces additional decoherence
in the spin oscillator. In our experimental conditions, the increase in the deco-
herence rate surpasses the benefits from the larger interaction readout rate, thus
reducing classical cooperativity as previously discussed in the CIFAR calibration
(excluding the reduction of thermal noise). This influence is further evidenced in
the spin noise measurement shown in Fig.6.2, where we observe a reduction in
ponderomotive squeezing around 16 kHz with the pumping laser activated. Ad-
ditionally, from the acquired spin noise, we notice an increment in spin noise as
we approach the DC frequency range, which is even enhanced by the application
of the optical pumping. One presumed origin of this DC noise is attributed to the
intensity noise of the pumping laser; we will elaborate more on this 'DC noise'
and explore the method to minimize its contribution in the following section.
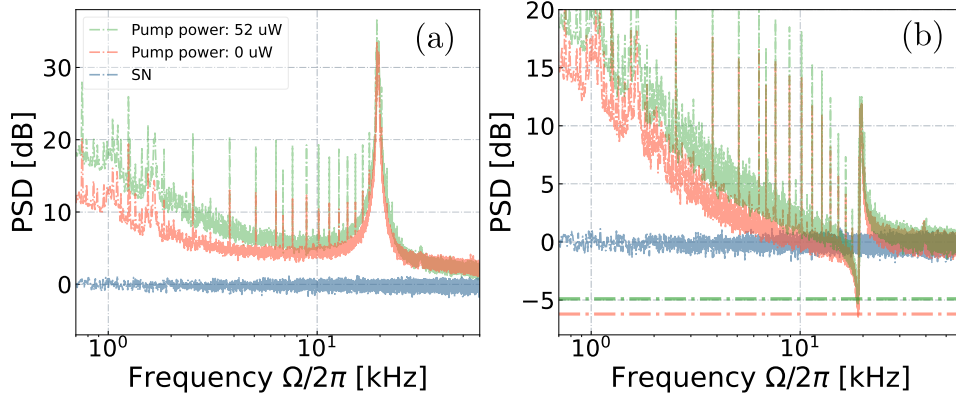
Figure 6.2: Spin noise spectra influenced by pump power. The introduction of repump power results in pump power broadening, which slightly reduces the level of ponderomotive squeezing, as evidenced by transition from the tomato curve to the green curve. Additionally, the increased pump power induces additional spin noise near the DC frequency, observable in both the spin noise (phase quadrature of light) and the ponderomotive squeezing (mixed light quadrature). During the measurement, the probe was set at 1 mW with a detuning of 1.6 GHz, and the repump power was set at 5 mW.

6.3 Observation of atomic DC noise and its minimization

As we now target low acoustic frequencies, aiming even for sub-kHz range, we observe a dramatic reduction in the ponderomotive squeezing level with decreasing of the Larmor frequency, initially disappearing at 10 kHz. In our theory, such reduction is characterized by a boost of the atomic thermal occupation n_S, thereby reducing the quantum cooperativity C_q. This additional noise becomes more apparent as we increase the Larmor frequency up to 40 kHz, as shown in Fig.6.3. When selecting the ponderomotive squeezing quadrature, we observed two additional atomic signals centered near DC and twice the Larmor frequency in the spectrum domain, which are beyond the ponderomotive squeezing frequency band. All these noise contributions accumulate with the reduction of the Larmor frequency.

In searching for an physical explanation, we hypothesize that the presence of the nonzero nuclear spin in Cesium atoms requires extending the model beyond the QND vector interaction with a two-level harmonic oscillator to incorporate alignment interaction operators $\hat{j}_x^2 - \hat{j}_y^2$, and $\hat{j}_x\hat{j}_y + \hat{j}_y\hat{j}_x$ as discussed in Eq.(3.24) in Chapter 3. These extensions can influence the spin oscillators via the tensor stark shift and tensor dynamic cooling or broadening around the Larmor frequency Ω_S. However, upon revisiting the first tensor alignment term, we notice that this term also affects the spin noise at $\Omega = 0$ and $\Omega = 2\Omega_S$, as the expectation $\langle m_{F,f}|\hat{j}_x^2 - \hat{j}_y^2|m_{F,i}\rangle$ is nonzero when $|f - i| = 0, 2$. Therefore, we could explain the observed atomic signal at 2Ω and 0 spectrum frequency with the

tensor alignment terms. Similar atomic responses have been observed for cesium vapor operating in Voigt geometry [119], and more detailed theoretical explanations are provided in three papers on spin alignment noise [69, 120, 121]. For our experiment, we will focus only on the zero frequency component, which we refer to as "DC noise", as it directly deteriorate the level of our measured ponderomotive squeezing in our interest frequency band.
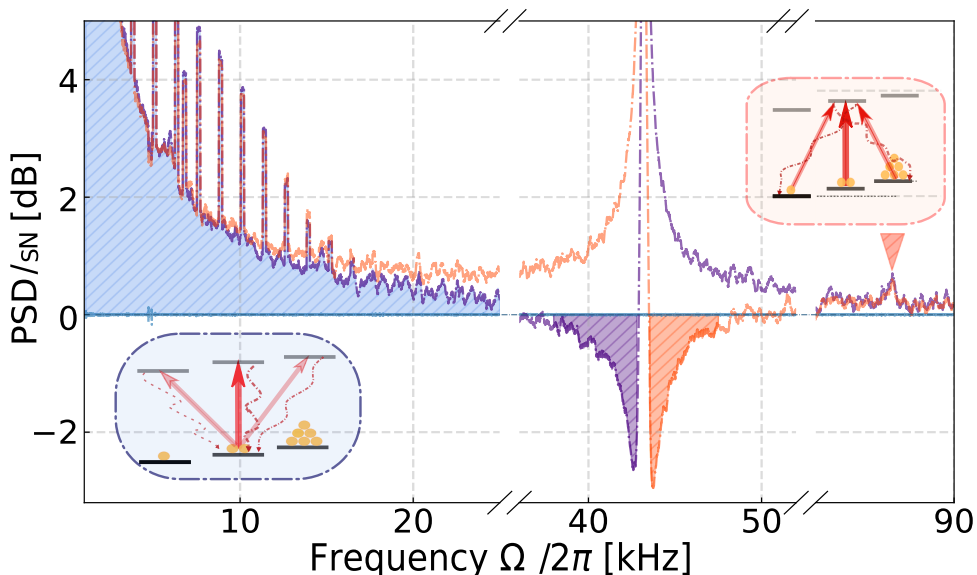
Figure 6.3: Influence of spin alignment noise beyond Larmor frequency. Beyond the vector and tensor interaction centered at Larmor frequency $\Omega_S/2\pi \sim 42\,\mathrm{kHz}$, a second peak emerges at twice the Larmor frequency. Additionally, there is enhanced noise towards the DC frequency regime, as indicated by the dashed blue area. These two effects presumably originate from tensor interactions. Axis are normalized to the shot noise of light on a decibel scale.

Crucially, we find that such DC noise can be strongly suppressed by minimizing the alignment term, in particular, one can increase the optical detuning Δ and benefit from the fast decline of a_2 coefficient, which governs the alignment interaction strength without significantly compromising the Faraday (QND) interaction strength as presented in Fig.6.4(a). A detailed analysis of the integrated areas of the QND quantum bakcaction noise, the reconstructed atomic thermal noise, and the DC noise as a function of the probe detuning is shown in Fig.6.4 (a) . The dramatically reduction of this DC noise enables us to predict the optimal detuning Δ_{opt} for the largest quantum cooperativity based on the equation described in Eq.(3.53) and even the best ponderomotive squeezing from Eq.(3.55). Such improvements can be observed through several example trances in Fig.6.4(d). We then extracted the recorded minimal noise level for each experimental trace and plotted it as a function of detuning. This nicely matches the predicted ponderomotive squeezing (light blue curve) derived from the integration of each noise

141

areas. The more detailed analysis can be found in paper [94]

It is also interesting to note that the amount of DC noise can be adjusted via the selection of the detection quadrature. In particular, we observe that this noise is maximized in the amplitude quadrature of light, thereby having a direct impact on the amount of ponderomotive squeezing. Conversely, this noise is barely noticeable when observing the phase quadrature of the probe light. With
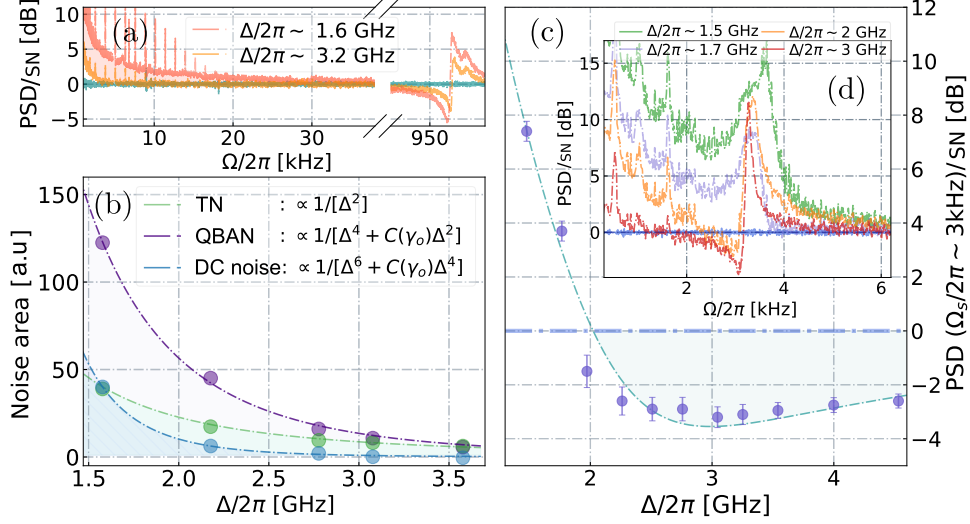
Figure 6.4: Various contributions to the total spin noise budgets with different probe detunings. (a) Spectra of the light probing the spin ensemble reveal strong near-DC noise contributions below 20 kHz while the spin oscillator operates at $\Omega_S/2\pi \sim 1\,\mathrm{MHz}$, which in principle leads to reduced measured ponderomotive squeezing when operating in the acoustic frequency range. This DC-noise contribution decreases with an increase in the probe light detuning Δ from 1.6 GHz to 3.2 GHz. (b) Comparison of the atomic thermal noise (TN), quantum backaction noise (QBAN), and DC-noise integrated areas as a function of detuning Δ . (c) The larmor frequency is then reduced down to the acoustic frequency band to explore the effect of probe detuning Δ on the observed ponderomotive squeezing at $\Omega_S/2\pi \sim 3\,\mathrm{kHz}$, where the DC noise now significantly influences the spin noise budget. At detunings around 3∼3.5 GHz, where the ratio between QBAN and all uncorrelated noise sources (including DC noise) is maximized. We observe optimal squeezing $\overline{S}_{sq} \sim -3\,\mathrm{dB}$ at 3kHz. Error bars represent the uncertainty of extracted pondermotive squeezing for each detuning value. (d) Illustration of the recorded spin noise spectra, especially the ponderomotive squeezing quadrature, optimized with different probe detuning Δ.

the optimization of the probe detuning, we can experimentally observe a maximal level of -3 dB ponderomotive squeezing when the spin oscillator operates at $\Omega_S = 3\,\mathrm{kHz}$, achieved by increasing the detuning from 1.6 to 3 GHz. Further increments in detuning, allowing for lower Larmor frequencies, result in -2 dB and -1.3 dB of noise below the shot noise limit at around 2 kHz and 1kHz, respectively, as demonstrated in the low panels of Fig.6.5 (d, e, and f).
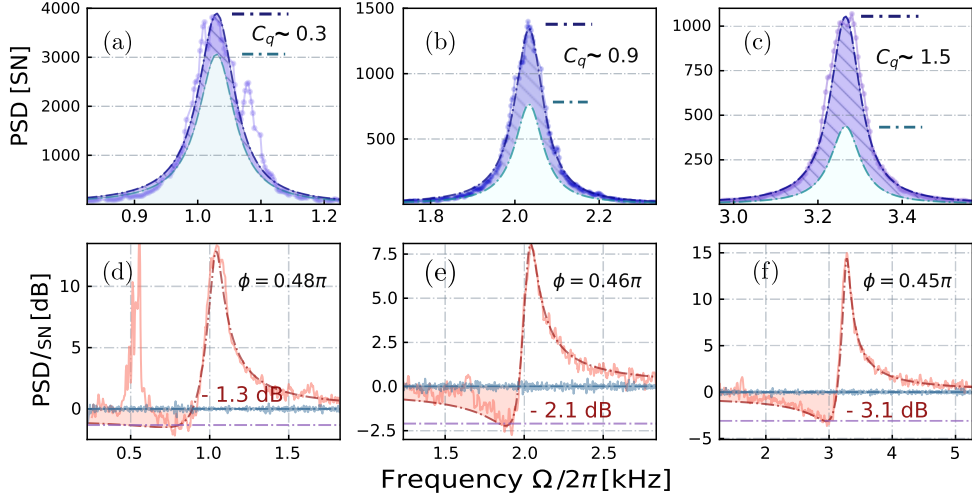
Figure 6.5: Spin noise spectra recorded at lower audio sideband frequencies. Panels (a-c) display the spectra of the light phase quadrature; the reconstructed quantum backaction noise (QBAN) and thermal noise (TN) are represented by the purple dashed area and the light green area, respectively. Panels (d-f) show detections optimized for maximal squeezing, corresponding to the experimental conditions described above. The ponderomotive squeezing level is optimized by adjusting the probe detuning across Larmor frequencies, gradually increasing from $\Delta/2\pi = 3\,\mathrm{GHz}$ at 3 kHz Larmor frequency up to $\Delta/2\pi = 4\,\mathrm{GHz}$ at 1 kHz. Axes are normalized to the shot noise of light, and represented in either a linear or decibel scales.

6.4 Observation of probe amp noise coupling-diode and Ti laser

We have developed an negative mass spin oscillator operating within the acoustic frequency band. We demonstrated quantum backaction-dominated spin noise with -3.0 dB ponderomotive squeezing using a quiet diode laser as a probe light. The amplitude noise of probe is depicted by the blue curve in Fig.6.6 (a). For the proposed broadband quantum noise reduction experiments, it is necessary to probe the atoms with light that is combined with one of the generated EPR entangled pairs, as well-demonstrated in the PhD thesis of Valeriy [33] and Tulio [122] from our group. This process requires both spatial and frequency matching of the probe light (or local oscillator) with the entangled arm, necessitating a switch from the Topitca DL pro diode laser to a titanium-sapphire laser from M Squared, which is pumped by a 8W 532nm laser from Sprout [20]. One advantage of the titanium-sapphire laser is its typically superior phase noise performance, narrow linewidth, and precise wavelength control when locked to a High-Finesse WS-600 wavemeter. However, its amplitude noise, as illustrated by the orange curve in Fig.6.6 (b), is significantly worse compared to the diode laser. Even after adjusting the Ti pump power to shift the relaxation oscillation frequency up to 800 kHz, a significant noise bump at around 3 kHz, attributed to the pump noise as also discussed in page 44 of Tulio's thesis [122]. The presence

of this 3 kHz amplitude noise bump, along with the increased noise at acoustic frequencies, can drive the atomic spin oscillator classically, projecting 'classical backaction' into the recorded spin noise spectrum, which cannot be cancelled by the common mode rejection of the balanced detection as shown in Fig.6.6 (d). We observed that the ponderomotive squeezing is overwhelmed by the presence of strong amplitude noise.
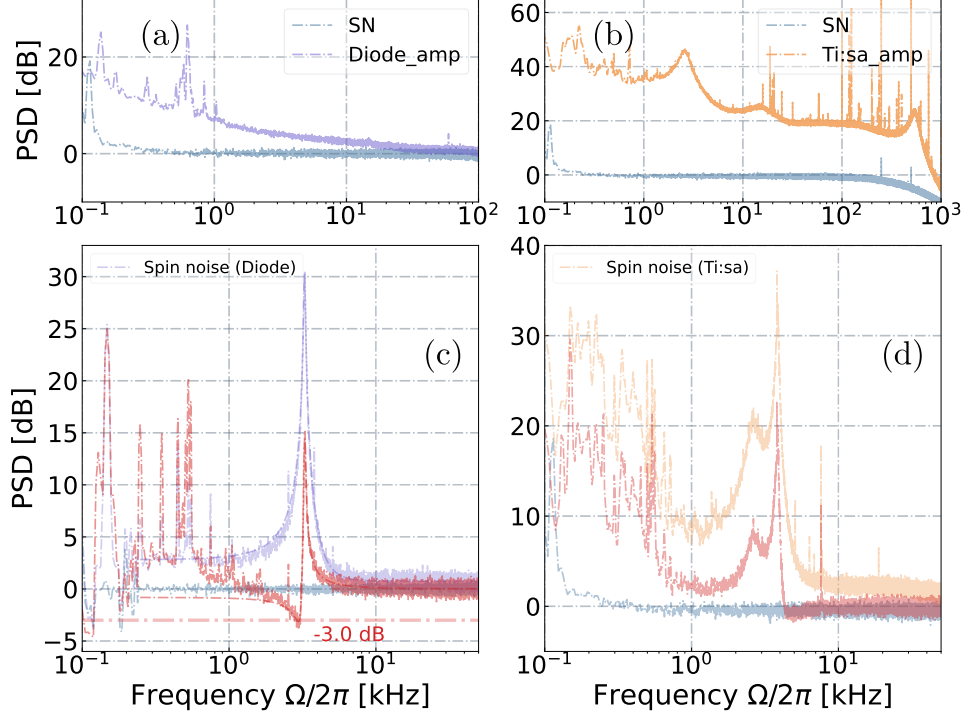
Figure 6.6: **Spin noise spectra influence by the probe amplitude noise.** We observe -3 dB ponderomotive squeezing when a spin oscillator operates at 3 kHz, probed by a diode laser, as shown in left bottom panel (c), the reduction in squeezing can attribute to the light intensity noise, as shown in (a), evidenced by the noise spikes around 800 Hz in both results (panel a and c). When the probe is replaced with a Ti:sapphire laser to better overlap with the entanglement pair, the light intensity noise significantly increases, even as the relaxation oscillation spectrum shifts up to 800 kHz. A noise peak at 3 kHz, due to Ti:sapphire pump laser noise, is observed. This increased amplitude noise dramatically raises the recorded spin noise spectrum and washes out the ponderomotive squeezing, as demonstrated in (d).

Furthermore, we observed a even substantial increase in amplitude noise when sending the local oscillator through a mode cleaner cavity (MCC) to mitigate the beam pointing effect and facilitate better spatial overlap with the EPR mode produced by the optical parametric oscillator (OPO) cavity. Unfortunately, this arrangement also converted these instabilities into the amplitude fluctuations in the transmitted light as described on page 49 of Valeriy thesis [33]. Consequently, implementing an active intensity stabilization system in optical path is essential.

144

6.5 Reduction of probe amplitude noise coupling with active noise eater

The implementation of an active noise eater to reduce the effect of amplitude noise on atomic spins was a collaboration with Tulio Brito Brasil and Alkiviadis Zoumis. The detailed preparation is well-documented on page 30 to 38 of Alkis's master thesis [123]. In our experiment, the intensity fluctuations mentioned above are maximally compensated via the zero-order scattering efficiency of an acoustic optic modulator (AOM) [124], where this scattering efficiency is controlled by the power of the 87 MHz RF drive. Active control is established by the Proportional Integral Derivative (PID) module in PyRPL using a Red Pitaya STEMlab 125-14 DAC, which was re-modified to produce less noise [125]. This setup facilitates us to interact with atoms using even more probe power and an enhanced readout rate, The reduction of light intensity fluctuation is illustrated by the green curve in Fig.6.7 (a), compared with the yellow curve with the noise eater off, demonstrating a reduction of at least 20dB in the amplitude noise of 2 mW probe power within the 10 kHz frequency band and maintaining around 10dB reduction up to 50 kHz.

Interestingly, when the intensity-noise mitigated probe is used to interact with atoms at a 2 GHz detuning, we observe a clear decrease in the overall spin noise comparable to the reduction in the light intensity noise, and the original noise bump that drives oscillator at 3 kHz can be completely removed. This improvement enables us to achieve -3.5 dB ponderomotive squeezing, slightly better than that recorded with a diode laser. Meanwhile, the noise spikes observed predominantly below 2 kHz are assumed to arise from amplitude noise introduced by the acoustic-optics modulator, which necessitates the use of a cleaner RF drive. The extrapolated effective thermal occupation of 5 also suggests that the squeezing level could be further improved by reducing more amplitude noise. Overall, the current experiments provide sufficient results to progress to the next stage and begin integration with the entangled light source. We also observe that the atomic response at twice the Larmor frequency (due to transitions between two Zeeman sublevels) is significantly increased with the doubled probe power; this double-frequency peak could potentially compromise the performance of the broadband quantum noise above the Larmor frequency.

In this chapter, we have discussed several noise sources that can effect the atomic responses and thus compromise the measured ponderomotive squeezing in low acoustic sideband frequency regime. We have presented methods such as probe detuning, optimization of the optical pumping laser amplitude noise, and noise eater for probe light, which can help us to maintain the observed level of ponderomotive squeezing even when the probe laser transitions from diode laser to a noisy Ti;sapphire probe laser. Now, with the quantum noise dominant spin oscil-

lator optimized, we will move to the next exciting chapter where we will integrate the probe local oscillator with entangled pairs and perform joint measurements.
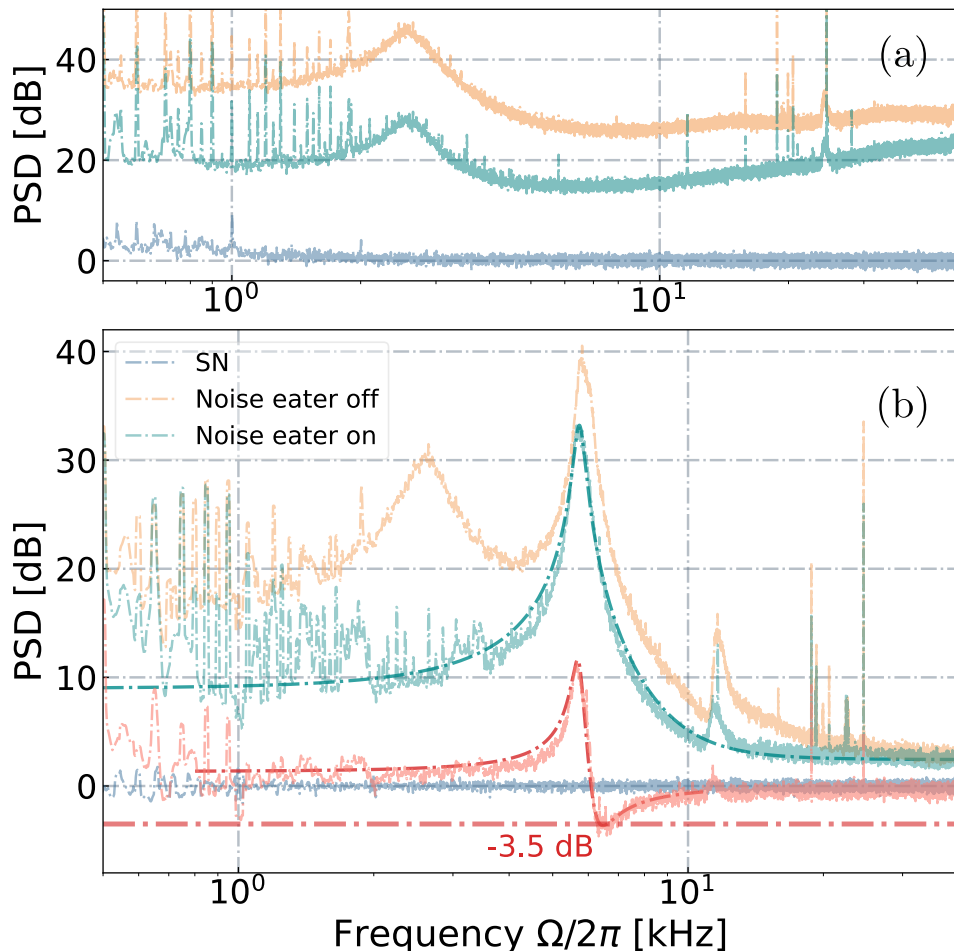
Figure 6.7: Reduction of classical intensity noise using an active noise eater. Panel (a) shows the enhanced intensity noise of a Ti laser, represented by the yellow curve, which is effectively reduced by our homemade active noise eater (green curve). This significant reduction minimizes the classical amplitude noise that could drive the spin oscillator, and eliminates the noise peak at 3 kHz. Consequently, this enables -3.5 dB ponderomotive squeezing using a 2 mW probe light. From the analysis, we extract several parameters, a thermal occupation number n_S of 5, a spin readout rate Γ_S : 12.0 kHz, and a spin decoherence rate γ_S : 0.33 kHz. The expected quantum cooperativity C_q is 1.64, aligning with the observed -3.5 dB squeezing. This data was acquired using a 2 mW probe light at 2.1 GHz detuning, in collaboration with Alkis and Tulio.

Part III

Towards broadband quantum noise reduction with conditional negative mass spin oscillator

Atomic spin oscillator enhanced conditional frequency dependent squeezing

In this chapter, we will discuss the generation of enhanced frequency-dependent squeezed entangled source achieved by a negative mass atomic ensemble. Building on the previously calibrated atomic system and concurrently calibrated Einstein Podolsky Rosen (EPR) entangled beams by my colleagues Tulio Brito Brasil, Valerii Novikov and Andrea Grimaldi, we will emulate predictions from our proof-of-principle experiments. These include the demonstration of the frequency dependent rotation on the phase of one of the entangled pairs and the expected achievable maximal squeezing when two correlative quadratures are detected and combined with an optimal wiener filter 'g'.

We will also address several potential limitations of our current experiments and propose methods to further improve our system, in particularly close to the frequency range where both the gravitational wave signals and quantum noise reside. Additionally, we will elaborate on some intriguing alternative directions based on our hybrid quantum system, which combines the atomic spin oscillator operation in quantum regime with the non-degenerate two-color (852 nm and 1064 nm) entangled light sources.

7.1 Hybrid atom-entanglement experimental setup

Before exploring the atom-induced, frequency dependent EPR squeezing, let us first introduce our experimental setup for the hybrid system, as shown in Fig.7.1. In our experiment, we utilize the Innolight Mephisto ND:YAG laser, emitting at 1064 nm, as one light source for the potential interferometer arm, achieving maximally output power of up to 10 W after amplification by a Nufern fiber amplifier (PSFA-1064-50-10W-2-1). Conversely, the 852 nm laser light is generated by an

M-Squared Ti:Sapphire (SolsTiS PSX-R) with a power up to 2 W. The associated relaxation oscillation spectrum and the amplitude noise were discussed in previous chapter.

The two color EPR entangled vacuum fields are generated using a non-degenerated optical parametric oscillator (OPO), which includes a custom-designed PPKTP nonlinear crystal within a bow-tie cavity. The crystal's design was discussed in Chapter 5 (page 45) of Tulio's PhD thesis [122] and Chapter 3 page 38 of valeriy's PhD thesis [33], along with the design of the OPO cavity. The OPO is pumped by a 473 nm laser from a sum-frequency generation (SFG) and is double-resonant locked to produce two-color entangled lights. The resulting entangled photon pairs are spatially separated by a dichroic mirror and merged with their corresponding Local oscillators (LOs).

An additional frequency-shifted beam, slightly detuned from the 1064 nm carrier but still within the OPO bandwidth, and the parametrically down-converted 852 nm beam with opposite detuning, co-propagate with the entangled sources. This arrangement facilitates phase locking relative to the LOs without the pollution of the vacuum quantum correlation at ultra low acoustic sideband frequency due to the locking beam, as detailed on page 43 of Valeriy's thesis [33]. The 1064 nm arm is detected using standard homodyne detection, with quadrature is adjusted accordingly. The 852 nm entangled arm is combined with an orthogonally polarized local oscillator (LO) via a polarizing beam splitter to measure the polarization stokes quadrature of light. The relative phase is locked at $\pi/2$, allowing the LO to measure the amplitude quadrature of the 852 nm arm.

The combined beam is then shaped by a top hat beam shaper for homogeneous interaction with the prepared negative mass spin oscillator. A half-wave plate, set before the atoms at an input polarization angle α, is adjusted specifically to facilitate only the QND Faraday interaction. The light, carrying the atomic signal, is then directed to a balanced polarimeter to measure the phase quadrature of light. During data processing, the two photon currents are summed or subtracted with an optimal filter 'g' , based on the homodyne detection phase of the 1064 nm arm and sideband frequency Ω. Subsequently, we utilize the Welch's method from scipy to perform a fast Fourier transform of the combined power spectrum density and analyze the quantum correlation.
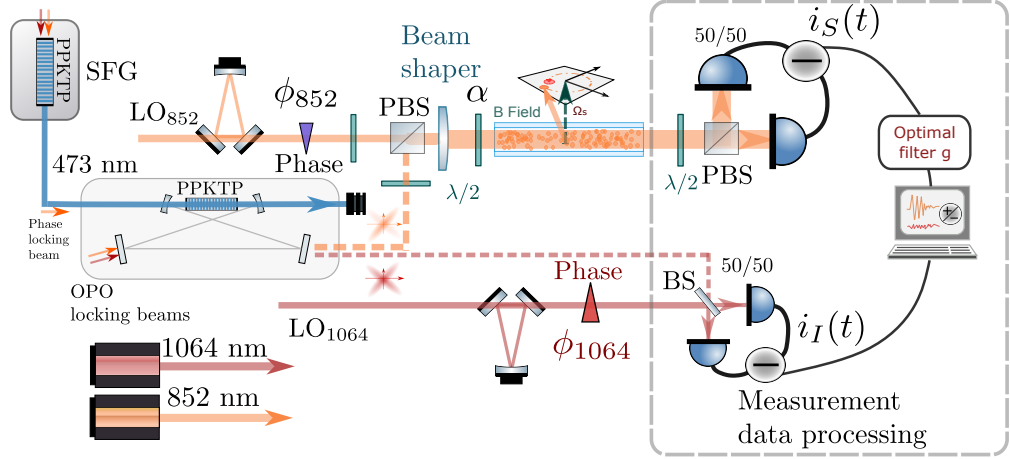
Figure 7.1: Scheme of negative mass spin oscillator enhanced EPR entanglement. The 852 nm and 1064 nm lasers serve as local oscillators and generate the 473 nm pump laser for the nondegenerate optical parametric oscillator (NOPO) via the sum frequency generator (SFG). The produced two color entangled beams from NOPO are separated by a dichroic mirror. The 852 nm mode is combined with a filtered local oscillator from a mode cleaner and is locked with a $\pi/2$ phase shift. These two beams maintain orthogonal polarization relative to each other at the output of a polarizing beam splitter, then the combined beams are shaped into a top hat beam to homogeneously interact with the atomic ensemble prepared in a negative mass configuration. The light and atomic interaction is chosen at QND interaction via the input polarization angle α, and finally detected with a balanced polarimeter. Meanwhile, the 1064 nm entangled mode is combined with another local oscillator using a beam splitter, where the relative phase can be adjusted accordingly. The detected two photocurrents from both modes are then processed with an optimal weight 'g'; the choices for the subtraction or summation are selected based on the detected 1064 nm quadrature. See text for more details.

7.1.1 EPR entanglement source
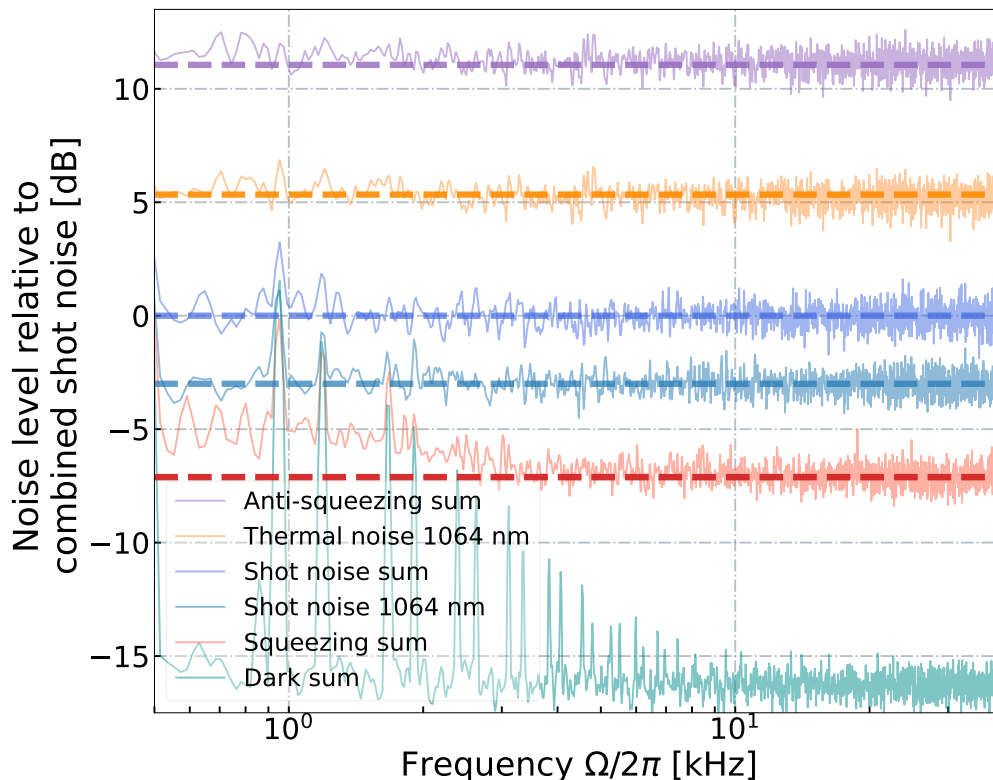
Figure 7.2: Performance of the measured EPR entangled source. Noise levels are scaled relative to the combined shot noise of signal and idler fields. From top to bottom, the curves represent: maximum anti-squeezing (purple curve), thermal noise with 1064 nm (or 852 nm) one arm only (orange curve), combined shot noise and single arm shot noise (dark and light blue, respectively), and squeezing with red color and electronic noise level with teal color. By fitting the above noise traces , we extracted a common squeezing parameter r of 1.34 and total losses (balanced) of around 86.5% . These measurements were performed by Valeriy, Tulio, and Andrea.

Now, let us first review the performance of our entangled source. Figure.7.2 illustrates the noise spectrum of the combined two-photon current without interacting with atomic ensemble. These spectra serve as calibrations for assessing the performance of the entangled source. The noise level depicted is normalized to the combined shot noise (dark blue curve), which is 3 dB above the single-arm shot noise (light blue curve). The electronic noise is -15 dB relative to the combined shot noise. Based on the measured -7 dB EPR squeezing and 11 dB antisqueezing, and considering approximately ~ 5.1 dB of thermal noise from one arm of EPR source, we estimate a squeezing factor $r \approx 1.34$, as introduced in the first chapter, with a detection efficiency of approximately 86.5% for each arm. In this measurement, the phase noise associated with the pump gain for the OPO can be considered negligible as discussed in page 56 of Valeriy's PhD thesis [33]. It

is also important to note that for proper quantification of the quantum enhancement with an EPR entangled source, one should compare the combined quantum noise to the one-arm shot noise level (light blue). Thus, the 3dB penalty can be accounted for during the sensitivity analysis.

7.1.2 Atomic spin ensemble

We will then revisit the calibrated atomic system. To model the atomic spin noise as depicted in Fig.7.3, we utilize parameters observed at -5 dB pondermotive squeezing, combined with an effective thermal occupation of $n_S \approx 3.5$ and 1.5 dB of atomic broadband noise (teal curve). By replacing the input noise from vacuum with the previously calibrated EPR thermal noise, we emulate the spin noise driven by one of the EPR pair. As shown in the red curve, this noise is significantly greater than the observed EPR entangled noise due to the ponderomotive effect of the spin oscillator. Consequently, it becomes necessary to apply specific post-processing techniques to accurately present our intriguing frequency-dependent rotation of the EPR entangled light with the atomic spin oscillator.
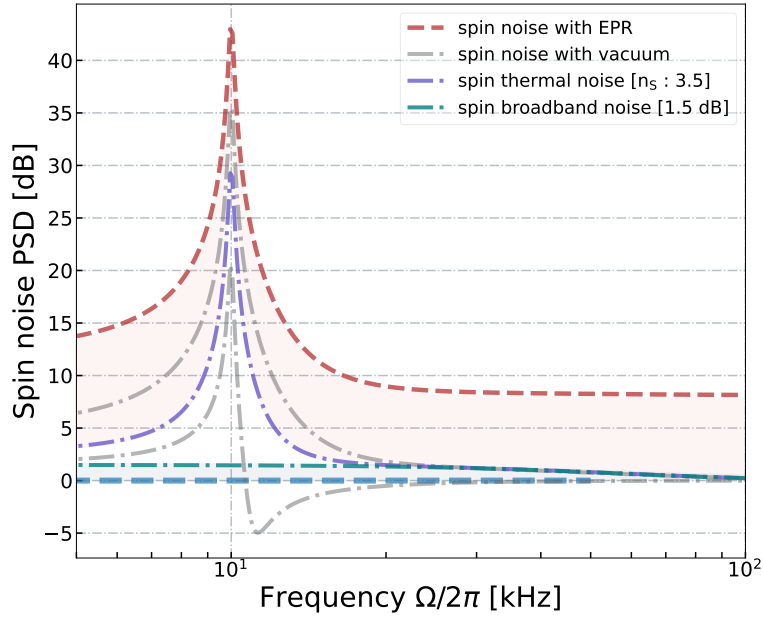
Figure 7.3: Simulation of spin noise with the injection of EPR thermal noise.
Utilizing the calibrated atomic parameters extrapolated from previously measured -5 dB pondermotive squeezing and a squeezing factor r = 1.34, we predict the spin noise when the vacuum is replaced with one arm of the entangled pair, represented by red dashed curve. The original spin noise and -5 dB pondermotive squeezing are depicted in grey. Additionally, the reconstructive atomic thermal noise and broadband noise, which do not correlate with the other entangled arm, are shown in purple and teal color, respectively. The model parameters include a measurement readout rate Γ_S of 12kHz, linewidth γ_S of 200 Hz, atomic thermal occupation n_S: 3.5, 1.5 dB of atomic broadband noise with an overall bandwidth of 150 kHz, and a total measurement efficiency of 86.5%.

7.2   Theoretical model
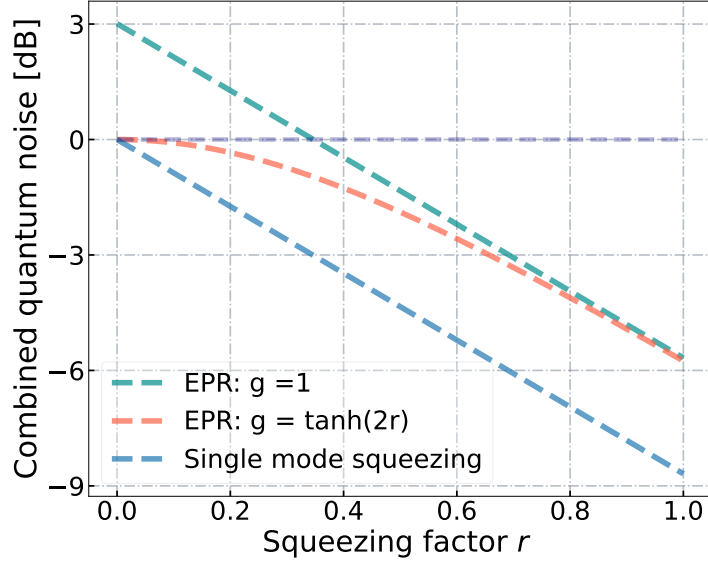
Figure 7.4: EPR correlations as a function of squeezing factor r. The observed EPR squeezing from the combined entanglements faces a 3 dB penalty due to doubled shot noise or uncorrelated sidebands associated with each entangled mode of EPR pair, as depicted by the teal curve. This contrasts with the level of single-mode squeezing, represented by the blue curve, under the identical squeezing factor r condition. However, this 3 dB penalty of the combined EPR-correlated quantum noise can be effectively mitigated, as shown by the orange curve, via the application of an optimized filter gain g on one arm of the entangled pair, particularly at lower squeezing factor.

Let us elaborate a bit more on the optimal filter gain 'g'. While we do not currently have a gravitational wave interferometer to directly demonstrate the broadband quantum noise reduction via the joint measurement of the hybrid system, we can reformulate our proof-of-principle experiment in terms of producing conditional, frequency-dependent EPR squeezing. This process can be analogous to monitoring the quantum noise of EPR-entangled fields reflected from a detuned filter cavity [29], which selectively reduces quantum backaction noise (from the amplitude quadrature) and shot noise (from the phase quadrature) while the detuned filter cavity rotates the relative phases of entangled fields. This frequency-dependent reduction in quantum noise results from the ponderomotive squeezing effect in atomic spin oscillator, suggesting that the atomic frequency response, given sufficient optical depth, can both amplify and rotate the quantum noise beyond the merely cavity's linear phase dispersion. Such pondermotive effect enables significant quantum noise cancellation at low frequency where the quantum backaction is predominant. However, our focus currently remains on the frequency-dependent rotation.

To effectively demonstrate this rotation as a filter cavity, it is crucial to employ

a Wiener filter gain 'g' in processing the recorded photocurrents. This filter gain $g(\Omega)$, presented here in frequency domain for clarity, will be applied to the time domain photon current. By adjusting this weighted gain in the 852 nm arm, we can maximize the quantum correlation between the two correlated photocurrents. Considering the high sideband frequency in the absence of additional spin noise (atomic thermal noise, backaction noise, and broadband noise) introduced by atoms, this gain $g(\Omega)$, helps mitigate the inherent 3 dB penalty associated with the conditional squeezing measurements, as shown in Fig.7.4. This approach is particularly effective when the squeezing factor r is low and also compensates for varying losses in each arm.

Integrating the atomic spin noise, we proceed to represent the previously introduced spectral densities for the interferometer (1064 nm) and atomic spin ensembles (852 nm), denoted as σ_I and σ_S, respectively. The expressions $\left\langle \hat{X}_L^{\text{in}} \hat{X}_L^{\text{in},\dagger} \right\rangle$ and $\left\langle \hat{P}_L^{\text{in}} \hat{P}_L^{\text{in},\dagger} \right\rangle$ indicate the input quantum noise for the amplitude and phase quadratures. Additionally, σ_{IS} corresponds to the cross-spectral density between the two EPR pairs and is influenced by the detection phase. The following calculations have been modified based on the joint measurement discussed at the end of chapter 3. Assuming the Larmor frequency significantly exceeds the spin decay term $\Omega_S \gg \gamma_S$, the thermal noise component can be simplified with one susceptibility function $\chi_S(\Omega)$:

$$\sigma_I(\Omega) = [\underbrace{\sin^2 \phi_{1064}}_{\left\langle \hat{P}_L^{\text{in}} \hat{P}_L^{\text{in},\dagger} \right\rangle} + \underbrace{\cos^2 \phi_{1064}}_{\left\langle \hat{X}_L^{\text{in}} \hat{X}_L^{\text{in},\dagger} \right\rangle}] \cosh 2r,$$

$$\sigma_S(\Omega) = [\underbrace{1}_{\left\langle \hat{P}_L^{\text{in}} \hat{P}_L^{\text{in},\dagger} \right\rangle} + \underbrace{\Gamma_S^2 |\chi_S(\Omega)|^2}_{\left\langle \hat{X}_L^{\text{in}} \hat{X}_L^{\text{in},\dagger} \right\rangle}] \cosh 2r + 4\Gamma_S \gamma_S |\chi_S(\Omega)|^2 (1/2 + n_S),$$

$$\sigma_{IS}(\Omega) = \sigma_{SI}^*(\Omega) = [\underbrace{\sin \phi_{1064}}_{\left\langle \hat{P}_L^{\text{in}} \hat{P}_L^{\text{in},\dagger} \right\rangle} + \underbrace{\Gamma_S \chi_S(\Omega) \cos \phi_{1064}}_{\left\langle \hat{X}_L^{\text{in}} \hat{X}_L^{\text{in},\dagger} \right\rangle}] \sinh 2r. \tag{7.1}$$

Here the value of filter gain, $g(\Omega)$ is strategically selected to minimize the spectrum density of the combined noise. This optimization is achieved by taking the derivative of combined spectrum with respect to g and aligns with the criteria detailed in [30, 45]:

$$g(\Omega) = \frac{\sigma_{IS}^*}{\sigma_S(\Omega)} = \frac{\sigma_{SI}}{\sigma_S(\Omega)} = \frac{[\sin \phi_{1064} + \Gamma_S \chi_S(\Omega)^* \cos \phi_{1064}] \sinh 2r}{\left[1 + \Gamma_S^2 |\chi_S(\Omega)|^2\right] \cosh 2r + 4\Gamma_S \gamma_S (|\chi_S(\Omega)|^2)(1/2 + n_S)}. \tag{7.2}$$

This selected filter gain $g(\Omega)$ optimizes the alignment of noise at 852 nm with the quantum noise at 1064 nm, thereby facilitating the demonstration of frequency dependent rotation of EPR correlations while minimizing the influence of uncorrelated quantum noise, such as atomic thermal noise (or broadband noise), particularly in the backaction-dominant frequency band. Incorporating this optimized filter gain into the combined photo currents enables us the calculation

of the power spectral density (PSD) for the joint measurement of the hybrid light-atomic system, provided that the parameters for each individual system are known. Additionally, the PSD incorporates separated losses, η_I and η_S, integrating them into the combined noise spectrum as follows:

$$
\begin{aligned}
\overline{S}_{\text{combined}}(\Omega) &= \eta_I \sigma_I(\Omega) + \eta_S |g(\Omega)|^2 \sigma_S(\Omega) \\
&\quad - \sqrt{\eta_I \eta_S} g(\Omega) \sigma_{IS}(\Omega) - \sqrt{\eta_I \eta_S} g(\Omega)^* \sigma_{SI}(\Omega) \\
&\quad + (1 - \eta_I) + |g(\Omega)|^2 (1 - \eta_S) \\
&= \eta_I \sigma_I(\Omega) + \eta_S |g(\Omega)|^2 \sigma_S(\Omega) \\
&\quad - 2\sqrt{\eta_I \eta_S} \operatorname{Re}\left(g(\Omega) \sigma_{IS}(\Omega)\right) \\
&\quad + (1 - \eta_I) + |g(\Omega)|^2 (1 - \eta_S),
\end{aligned}
\tag{7.3}
$$

and the new optimal weight, including the losses, will be expression as:

$$
g(\Omega) = \frac{\sqrt{\eta_I \eta_S}\left[\sin \phi_{1064} + \Gamma_S \chi_S(\Omega)^* \cos \phi_{1064}\right] \sinh 2r}{\eta_S \left[\left(1 + \Gamma_S^2 |\chi_S(\Omega)|^2\right) \cosh 2r + 4\Gamma_S \gamma_S (|\chi_S(\Omega)|^2)(1/2 + n_S)\right] + (1 - \eta_S)}.
\tag{7.4}
$$

Upon analyzing the spectrum of the combined photo currents, the shifts of the minimal squeezing observed in noise spectrum across various homodyne phases at 1064 nm can be attributed to the atomic spins functioning as a detuned filter cavity that frequency dependently rotating the squeezing angle. In this configuration, the spin oscillator selectively rotates the 852 nm light quadrature across different sideband frequencies, resulting in a frequency shift of the maximal conditional EPR squeezing.

7.3 Simulations based on current calibrated experiments parameters

Fig.7.5 illustrates how quantum backaction noise in amplitude noise projects into the light phase quadrature via the pondermotive atomic frequency response. On the phasor diagram, the small arrow on the dotted circle represents the selection of the homodyne detection phase. The amplitude quadrature occurs when the small arrow (local oscillators, LOs) aligns with the large dotted arrow indicating the carrier of entangled arm, while the phase quadrature is when the small arrow is orthogonal to the large arrow. The homodyne measurement sums the projection of quantum noise from the two $\Omega_{carrier} \pm \Omega$ sidebands onto the LO's direction. To observe EPR squeezing, it is necessary to subtract the 852 nm and 1064nm photo currents when both quantum noise circles along the LO direction, and to sum the currents when one arm is out of phase (along negative direction) relative to the aligned LO arm. More details will be presented in the follow section, combined with specific configurations.
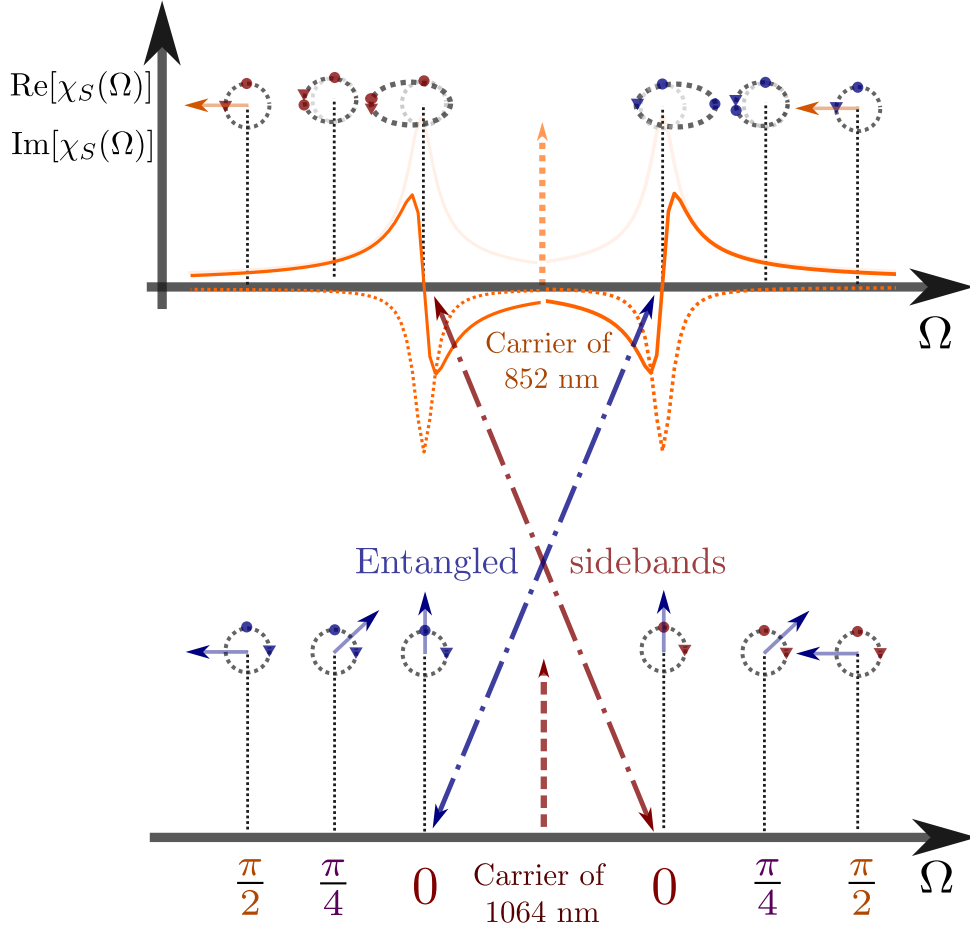
Figure 7.5: Phasor representation of two-mode entangled states after interaction with an atomic spin oscillator. The stick-dashed circles indicate the entangled sidebands around carrier frequency marked by corresponding colors, for example, a red small circle at 852 nm for one negative frequency correlates with a similar red circle for 1064 nm for the corresponding positive frequency. These small circles represent the quantum noise in amplitude quadrature of the entangled fields (in phase with carrier of 852 nm mode), while the small triangles represent the phase quadrature of the same fields. The small arrows indicate the selected homodyne detection phases: the 852 nm arm is set at the phase quadrature of light (sum of two $\pm$ sidebands), while the quadrature on 1064 nm is adjusted based on the frequency response of the atomic oscillator. The dispersion, $\mathrm{Re}[\chi_s(\Omega)]$, and dissipation, $\mathrm{Im}[\chi_s(\Omega)]$, frequency responses of negative mass spin oscillator to the quantum noise of probe light are presented as solid and dotted orange curves,respectively; The $|\chi_s(\Omega)|$, reflecting the measured spin noise, is shown with a transparent orange curve. The ponderomotive squeezing effect of spin oscillator on the quantum noise in the quadrature sidebands of the 852 arm is also depicted. See text for more details.

7.3.1 Combined quantum noise with real optimal filter $\mathrm{Re}(g(\Omega))$

The ideaa of presenting the frequency-dependent squeezing in this manner was developed together with Valeriy Novikov. The noise spectrum density of the com-

bined two simulated photon currents is depicted in Fig.7.6. We adjust only the relative weight of the two current in the time domain, representing the real part of the optimal Wiener gain $\text{Re}(g(\Omega))$. Initially, we consider a scenario where the sideband frequency is sufficiently high such that the atomic frequency response has minimal impact. For simplicity, we also neglect the broadband noise in the current simulation. The homodyne measurement is set at the phase quadrature of light, where the real gravitational wave signal would reside. In this high frequency regime, the quantum noise of current GWDs is the light shot noise in the observed phase quadrature. To reduce this shot noise, the detection phase is set at $\pi/2$, measuring the anti-correlated sidebands. The sum of two signals with optimized weight results in quantum noise reduction at this frequency rang, as indicated by the red dash curve, which the combined quantum noise is 6 dBbelow the one arm 1064 nm shot noise. At low frequencies, combined noise aligns with the level of one arm's EPR thermal noise. This is because the influence of uncorrelated quantum noise in 852 nm is mitigated by setting the optimized wiener gain at $g \sim 0$.

Reducing the sideband frequency involves the quantum backaction on the light due to the interaction with the atomic spin oscillator. At a certain frequency where only the dispersion effect emerges, the spin oscillator begins accumulating quantum noise from the amplitude quadrature of light and project it directly into the phase quadrature with amplification of 1. To simultaneously reduce this equally existing phase and amplitude noise in the output phase quadrature, we adjust the homodyne phase for 1064 nm to $\pi/4$, and select the wiener gain on 852 arm to optimized the measured quantum noise as shown in Fig.7.5. The combined quantum noise in this configuration now changes to the purple curve, with the minimal squeezing now shifting to a lower frequency. The slight reduction in maximal squeezing is due to the uncorrelated atomic thermal or (projection) noise. Overall, the shift in maximal squeezing can be understood as the atomic spin effectively rotating the phase of correlated quantum noise at the 852 arm relative to 1064 nm arm by $\pi/4$ at this specific sideband frequency.

Keep reducing the frequency will effectively rotate the phase of correlated quantum noise even further. In reality, the spin oscillator also pondermotively amplifies the quantum fluctuations and projects them onto the light phase quadrature, but this process also incorporates the imaginary frequency response of spin oscillator. In particular when the frequency is near atomic resonance where the dissipation coupling dominates, adjusting the relative weight $\text{Re}(g(\Omega))$ is not sufficient to cancel quantum noise in this regime as shown by the orange curve in Fig.7.6. Nevertheless, the observation of tiny squeezing around the Larmor frequency indicates the atoms can still rotate the quantum noise by nearly $\pi/2$. Moreover, when we scan each homodyne readout angle along with their combined quantum noise, these arrangements enable us to construct a 2D color plot where we can observe the shift of the minimal squeezing for each detection angle at different sideband frequencies, effectively presenting our targeting frequency-

dependent rotation.
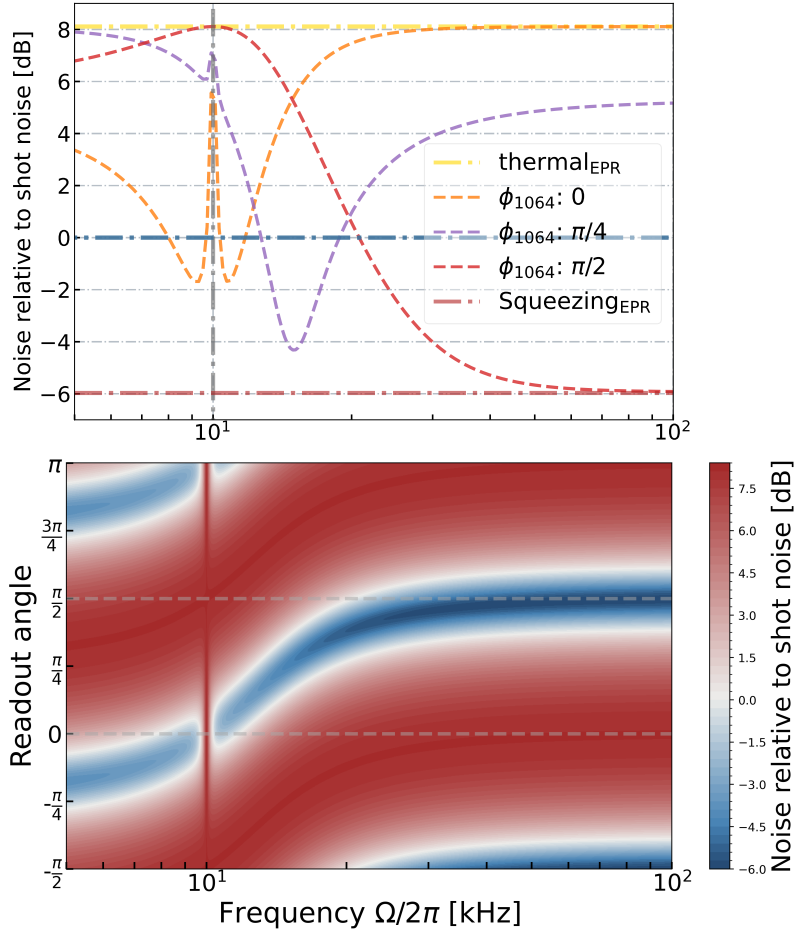
Figure 7.6: Spectra of combined quantum noise and demonstration of frequency dependent squeezing angle optimized with real number filter gain $\text{Re}[g(\Omega)]$**.** Noise levels are scaled relative to the 1064 nm arm shot noise. Upper plot: Spectra of combined quantum noise for three different readout angles (0, $\pi/4$ and $\pi/2$) of 1064 nm arm. Each spectrum is combined with the associated optimal filter gain 'g' for two correlated photon currents. The maximal noise level of each curve aligns with the one arm EPR thermal noise, while the anti-squeezing is around 14dB above the shot noise. Lower plot: Simulated noise spectrum as a function of the readout detection angle at the 1064 nm arm and its sideband frequency. The frequency-dependent phase transition of the maximal entanglement squeezing, indicated by the blue area, demonstrates the frequency dependent rotation of the phase of 852 nm entangled mode due to the atomic ponderomotive squeezing effect. However, at around 10 kHz near the atomic Lamor frequency, the quantum noise cannot be fully canceled due to the dominant imaginary dissipation response of the spin oscillator. The detailed parameters for this simulation are presented in tab.7.9.

7.3.2 Combined quantum noise with complex optimal filter $g(\Omega)$
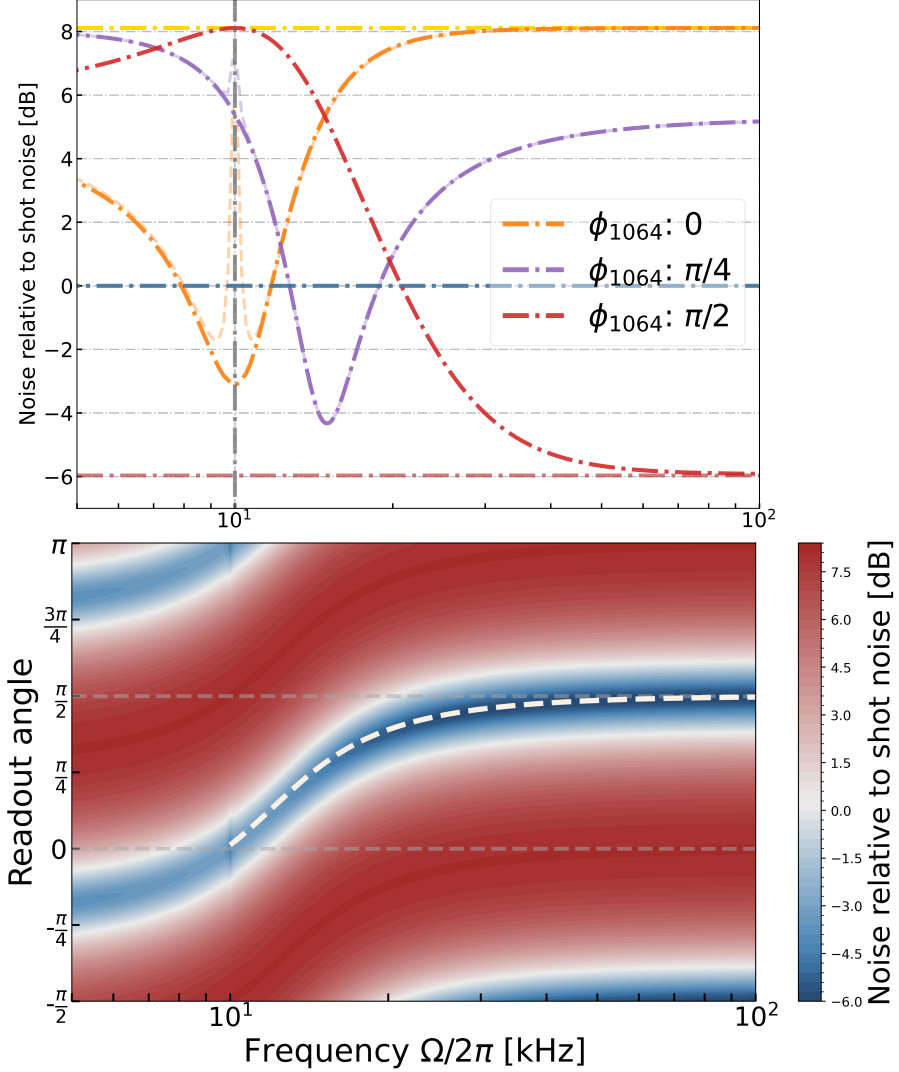
Figure 7.7: Spectra of combined quantum noise and demonstration of frequency dependent squeezing angle with optimized complex filter g(Ω). Noise levels are scaled relative to the 1064 nm arm shot noise. The plots illustrate how two photocurrents, when combined with a complex filter gain, effectively minimize the quantum noise across the wide range of the sideband frequencies. This reduction is especially significant around the atomic Larmor frequency, where the quantum noise is primarily driven by the imaginary part of the atomic response. By fitting the simulated readout phase as a function of sideband frequency to a filter cavity expression, the resulting frequency-dependent squeezing can be seen as the reflection of the squeezed light from a detuned filter cavity. The rotation presented in this plots can be achieved by means of a filter cavity with an effective bandwidth of 5 kHz, with the carrier light detuned by 11 kHz from the cavity's resonant frequency. Moreover, this effective bandwidth can be further reduced by adjusting the spin readout rate and total spin decoherence rate.

In revisiting the theory model for optimal gain as in eq.(7.4), we notice that the optimal wiener gain should be a complex number. Incorporating the imaginary part into the filter gain 'g' facilitates the full reduction of quantum noise around the atomic resonant frequency, as shown in the top plot of Fig.7.7. The result illustrated in the bottom figure now clearly demonstrates the rotation of the maximal EPR squeezing, marked with the blue area. This phenomenon is further analyzed by fitting the read out detection angle as a function of the sideband frequency, using the introduced detuned filter cavity function:

$$\phi_{opt}(\Omega) = \text{arccot}\left[\frac{2\delta_f\gamma_f}{\gamma_f^2 - \delta_f^2 + \Omega^2}\right]. \tag{7.5}$$

Here δ_f represents the cavity detuning and γ_f denotes the cavity's full width half maximal (FWHM) bandwidth. Interestingly, our analysis reveals that the atomic spin oscillator effectively functions as detuned squeezing light, reflected from a filter cavity with 11kHz detuning and a 5 kH bandwidth (FWHM). Though with our current atomic vapor cell configuration does not yet meet the gravitational wave observatory's stringent filter cavity requirement, which typically demands a 50 Hz bandwidth, met by an approximately 300 m long filter cavity with a Finesse of ≈ 5000 [126] . our hybrid system offers a substantial reduction in physical size. Additionally, we can effectively address the atomic damping rate by redesigning the cell geometry, such as using a vapor cell with a increased 5mm cross-section. Our proposal introduces a completely different approach to implementing the frequency-dependent quantum noise rotation. In our setup, this effective cavity detuning in our system can be finely controlled by adjusting the atomic Larmor frequency via the bias magnetic field, greatly simplifying the technique challenge of maintaining the probe light detuning relative to a super narrow filter cavity over long-durations.

Furthermore, exploring the imaginary part of the optimal gain 'g' in the time domain indicates the need to apply a frequency-dependent phase shift to compensate the phase lag introduced by the damping of the atomic spin oscillator. This aspect becomes particularly intriguing when the sideband frequency is slightly off the atomic resonant frequency, where both the real and imaginary response manifest, creating complex quantum correlations. Proper manipulation of these correlation would require heterodyne measurement, which would entail additional image vacuum costs [127], or synodyne detection, where one could adjust the relative phase of two frequency sidebands separately [31, 128]. The fully reduction of these complex quantum correlations will be very interesting to explore in our future experiments.

7.3.3 Combing with broadband atomic noise
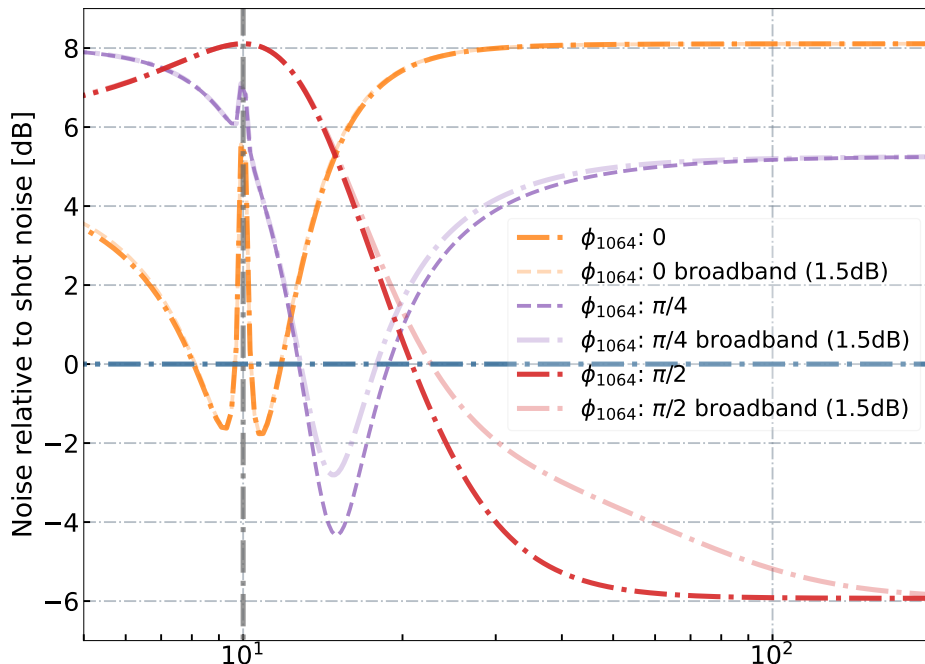
Figure 7.8: Spectra of the simulated frequency dependent squeezing with atomic broadband noise. Assuming that the two correlated photocurrents are combined with only the real part of the optimal filter, and +1.5 dB of atomic broadband noise is introduced into the simulation, we observe a upward frequency shift for minimal squeezing when detection phase is locked at $\pi/2$. This shift results from the uncorrelated broadband noise deteriorating the EPR entanglement. Additionally, the broadband noise influences the level of the maximal squeezing in a mixed homodyne quadrature $\pi/4$, and it is barely noticeable close to the amplitude quadrature of light at 0. The squeezing factor used for simulation is r: 1.34, with a total efficiency of 86.5% .

To better predict with practical experimental conditions, we have incorporated 1.5dB of atomic broadband noise into the combined quantum noise spectrum. This inclusion allows us to explore its effect on the observed squeezing, in particularly we observe the shot noise dominant at higher frequency is strongly impacted by the broadband noise, which also compromise the narrow frequency band of the frequency dependent rotation. At an angle of $\pi/4$, while the broadband noise influence the level of squeezing, it does not alter the frequency where maximal squeezing is observed, indicating a consistent rotation angle by the spin oscillator. This influence is further reduced when approaching atomic resonance, where the quantum backaction noise predominates over other uncorrelated atomic thermal and broadband noise. Fortunately, the influences of both atomic thermal noise and broadband noise can be mitigated by employing the virtual frequency shift, as discussed at the end of the Chapter 3. The reduction of uncorrelated quantum noise through the application of virtual frequency shift presents another

| | Parameters for GW configurations | |
Parameter	Notation	Value
EPR squeezing factor	r	1.34
losses for 1064 nm	η_I	0.86
losses for 852 nm	η_S	0.86
Larmor frequency	Ω_S	10 kHz
Atomic readout rate	Γ_S	12 kHz
Atomic decay rate	γ_S	200 Hz
Atomic thermal occupation	n_S	3.5
Atomic broadband noise		1.5 dB
Atomic broadband noise decay rate	γ_{bb}	150 kHz
Maximal pondermotive squeezing	$\overline{S}_{sq}$	-5 dB

Table 7.9: Parameters used for modelling frequency dependent EPR squeezing source

interesting avenue for future theoretical and experimental research.

Conclusion and Outlook

In this thesis, we have described the presence of the quantum noise in the gravitational wave signal regime, which limits the performance of current gravitational wave observatories. We also reviewed several quantum noise engineering approaches, primarily based on the frequency-dependent phase rotation of the quantum squeezed states, aimed at achieving broadband quantum noise reduction across the gravitational wave detection bandwidth. Additionally, we introduced an alternative approach that, instead of using filter cavities, proposes the preparation of an auxiliary quantum system, such as atomic spins operating in a negative mass reference frame. This joint measurement of GWDs and atomic spins opens up the possibility of evading quantum backaction noise [43], which can be further enhanced with single-mode vacuum squeezed states. To match the wavelengths of the atomic transition and gravitational observatory, this scheme is modified to include a parallel measurement using a nondegenerate EPR entangled source as proposed by Eugene and Khalili [45]. This thesis discusses the experimental preparation and calibration necessary to demonstrate the proof-of-principle of this concept.

To enhance the light atom interaction strength for better matching with the frequency responses of GWDs, we redesigned and significantly enlarged the cell channel to 2*2*80 mm^3. This was followed by the implementation of a new bias coil systems that provide the homogeneous magnetic fields within the interaction channel area. We also apply a top hat beam to interact homogeneously with atoms and maximally mitigate the broadband atomic responses. After years of improvement, we successfully demonstrated -5 dB ponderomotive squeezing of light, corresponding an observed quantum cooperativity of 3. Meanwhile, after mitigating additional atomic responses at near-DC sideband frequencies and applying an active noise eater, we showed that this quantum backaction noise dominated spin oscillator can maintain squeezing down to sub-kHz. This observed quantum noise limited spin oscillator operates in the gravitional wave signal regime even when the probe light is transitioned to a more noisy Ti:sappire laser, setting the stage for incorporation with EPR entangled source.

Building on the calibrated atomic spin oscillator prepared in a negative mass reference frame [94] and the produced nondegenerate EPR entanglement [129], we present numerical simulations demonstrating that these hybrid atom-EPR quantum systems, combined with an optimized weight g, pave the road for generating a frequency-dependent EPR squeezing source. This development opens up the opportunity to improve the gravitational wave observatory sensitivity beyond the standard quantum limit (SQL) over a broadband frequency range.

Beyond enhancing the sensitivity for gravitational wave signals, the presented hybrid system can also be applied to magnetic field sensing. The entangled 1064 nm arm provides an additional degree of freedom to conditionally reduce the quantum shot noise and backaction noise of the 852 nm atomic beam when the spin system functions as an optically pumped magnetometer, as demonstrated in [130, 131]. Moreover, the atomic ensemble demonstrated here can serve as a long coherence time quantum memory system [90]. With the entanglement channel built between the 1064 nm and 852 nm fields, this hybrid system can potentially enable quantum teleportation between the telecom wavelength and an auxiliary atomic system. This opens up the possibility of further enhancing the precision of quantum sensing by extending the coherence lifetime of the sensors, such as optically levitated nanoparticle [132], operating in 1064 nm arm through a quantum memory via our auxiliary atomic ensemble [133].

8.1   Last Minute Experimental Achievement
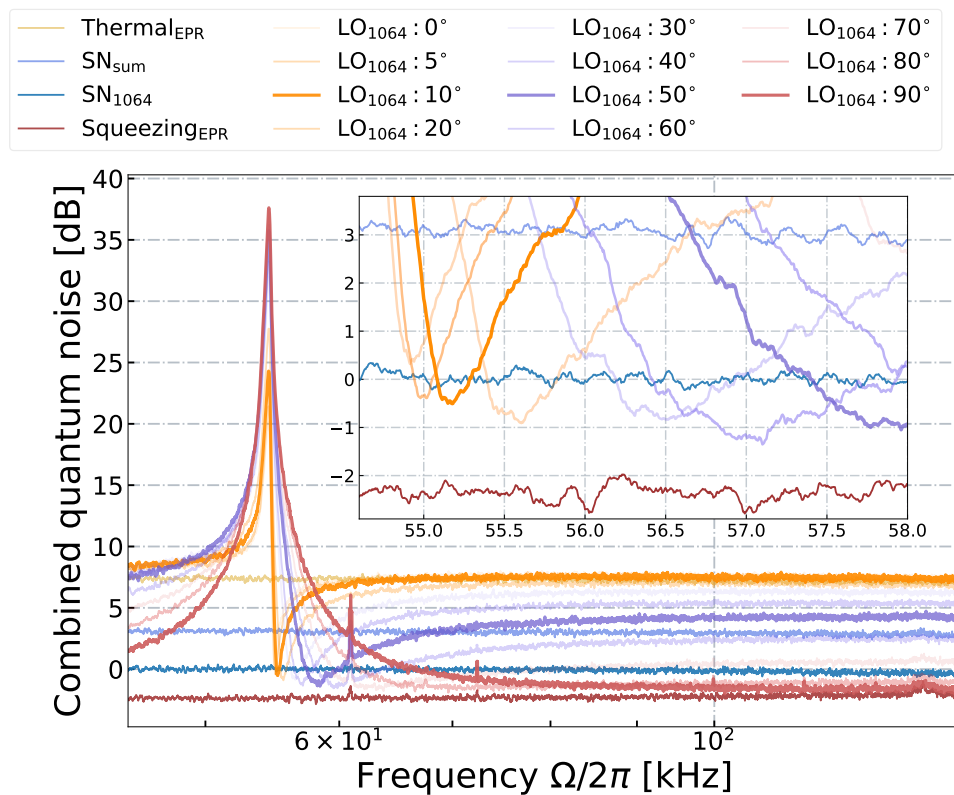
Figure 8.1: Spectra of combined quantum noise with the atomic spin oscillator operating at 55 kHz are presented. These curves demonstrate the combined quantum noise with numerically optimized weight gain g for each homodyne detection phase at 1064 nm arm. All noise traces are normalized to the 1064 nm shot noise (light blue curve) while the combined shot noise is 3 dB above (royal blue curve), the measured EPR squeezing (dark red curve) is 2.5 dB below the one arm shot noise and the thermal noise noise (sand curve) is around 8 dB above the one arm shot noise. The combined quantum noise being less than 0 indicates the conditional quantum noise enhancement for the 1064 nm mode. From the figure, we can clearly observe the shift of minimal quantum noise for the joint measurement among red, purple, and orange curves, representing the atomic response frequency dependently rotating the phase of 852 nm entangled field. In the inner plot, we observe the combined quantum noise falls below the one-arm shot noise from 5° (close to amplitude quadrature) to 90° (phase quadrature) homodyne detection angles, indicating a wide range of quantum noise reduction (or sensitivity improvement). These measurement was performed with -4 dB ponderomotive squeezing of light with the spin oscillator and -5.5 dB EPR squeezing without the influence of atoms. Credit for this work goes to my wonderful GWD team: Valerii Novikov, Maïmouna Bocoum, Tulio Brasil, Andrea Grimaldi.

Meanwhile, in alignment with the conclusions of this PhD work, our experiments have yielded a significant achievement by demonstrating the frequency-dependent phase rotation of the EPR entangled pairs, as shown in Fig.8.1, when the atomic

spin oscillator operates at 55 kHz with -4dB ponderomotive squeezing and -5.5 dB EPR squeezing including the cell transmission. These preliminary results are achieved by combining two recorded photo-currents with the numerically optimized constant gain g (optimized for one sideband frequency only) for each 1064 nm homodyne phases across the sideband frequency. Then we compute the power spectral density of the combined signal using Wlech's method. These results clearly show the atomic spin ponderomotively 'rotate' the phase of the 852 nm entanged arm, which is evidenced by the shifts of the maximal quantum correlation in Fourier frequency as we scan the 1064 nm homodyne angle to mimic the interferometer optomechancis responses.

From the inner plots, the observed quantum noise of the joint system goes below the 1064 nm shot noise level, indicating the quantum correlation enhancement once this arm is used in combination with the probe in gravitational wave interferometer. Though it is still a bit far from the low acoustic frequency range ($\leq$ 10 kHz) [134], where the gravitational wave signal resides. At moment, the main limitation that prevents us from reaching acoustic frequency range is the classical amplitude noise which originates from the ti: sapphire pump laser intensity noise. Additionally, low-frequency phase modulation, utilized to lock the laser wavelength, is also converted into amplitude modulation after mode cleaner that deteriorates the quantum noise dominant performance of probe light, reducing the observed atomic ponderomotive squeezing down to -2 dB.

The next improvement involves modifying the noise eater to better attenuate the amplitude noise and mitigate the phase modulation, with the well controlled classical noise in this frequency range, we can also explore possible methods to reduce atomic thermal noise via spin squeezing while maintaining the quantum backaction noise, which can further improve our quantum cooperativity. Ultimately, once we manage to recover the -4 dB ponderomotive squeezing at this acoustic band, we will demonstrate the predicted frequency dependent rotation of the EPR entangled source, resulting in a wide range of quantum sensitivity enhancements.

Part IV

Appendix

Supplementary information

Spin and density operators

In our experiment, the atomic spins are prepared along the quantization axis in the x-axis, while we probe the transverse component along the z-axis. In this basis, the relations between the collective spin operators and the density operators $\hat{A}_{m,m}$ are established:

(Here, we provide both the both the collective spin operators and density operators, as the spin operators are more intuitive to understand the interaction Hamiltonian, while the density operators are more convenient to derive the equations of motions [49, 50, 61])

$$\hat{F}_x = \sum_m m \hat{A}_{m,m},$$

$$\hat{F}_y = \frac{1}{2} \sum_m \sqrt{F(F+1) - m(m+1)} \left(\hat{A}_{m+1,m} + \hat{A}_{m,m+1} \right),$$

$$\hat{F}_z = \frac{1}{2i} \sum_m \sqrt{F(F+1) - m(m+1)} \left(\hat{A}_{m+1,m} - \hat{A}_{m,m+1} \right),$$

$$\hat{F}_0 = \sum_m \left(\hat{A}_{m,m} \right),$$

$$\hat{F}_+ = \sum_m \sqrt{F(F+1) - m(m+1)} \left(\hat{A}_{m+1,m} \right),$$

$$\hat{F}_- = \sum_m \sqrt{F(F+1) - m(m+1)} \left(\hat{A}_{m,m+1} \right),$$

We also provide the high order components, which will be helpful for calculating

the tensor noise and energy shifts:

$$\hat{F}_x^2 = \sum_m m^2 A_{mm},$$

$$\hat{F}_y^2 = \frac{1}{4}\left(\hat{F}_+\hat{F}_+ + \hat{F}_-\hat{F}_- + \hat{F}_+\hat{F}_- + \hat{F}_-\hat{F}_+\right),$$

$$\hat{F}_z^2 = -\frac{1}{4}\left(\hat{F}_+\hat{F}_+ + \hat{F}_-\hat{F}_- - \hat{F}_+\hat{F}_- - \hat{F}_-\hat{F}_+\right),$$

$$\left(\hat{F}_x^2 + \hat{F}_y^2 + \hat{F}_z^2\right) = F(F+1),$$

$$\left(\hat{F}_x^2 - \hat{F}_y^2\right) \approx \left(\hat{F}_x^2 - \hat{F}_z^2\right) \approx F\left(F - \frac{1}{2}\right),$$

$$\hat{F}_y\hat{F}_z + \hat{F}_z\hat{F}_y = \frac{1}{2i}\sum_m \sqrt{(F-m)(F+m)(F+1+m)(F+1-m)},$$

$$\times \left(\hat{A}_{m+1,m-1} - \hat{A}_{m-1m+1}\right) \approx 0,$$

$$\hat{F}_x\hat{F}_y + \hat{F}_y\hat{F}_x = \frac{1}{2}\sum_m \sqrt{F(F+1) - m(m+1)}(2m+1)\left(\hat{A}_{m+1,m} + \hat{A}_{m,m+1}\right)$$

$$\approx \mathrm{sgn}(F_x)(2F-1)\hat{F}_y,$$

$$\hat{F}_x\hat{F}_z + \hat{F}_z\hat{F}_x = \frac{1}{2i}\sum_m \sqrt{F(F+1) - m(m+1)}(2m+1)\left(\hat{A}_{m+1,m} - \hat{A}_{m,m+1}\right)$$

$$\approx \mathrm{sgn}(F_x)(2F-1)\hat{F}_z,$$

where $\mathrm{sgn}(F_x)$ is the sign of F_x. For the work described in this thesis, we normally work with the ground state of atomic spin F = 4.

Commutations between spin operators

Here we also provide the the commutators between different spin operators that can be useful when deriving the equations.

$$\left[\hat{F}_x, \hat{F}_y\right] = i\hat{F}_z$$

$$\left[\hat{F}_x, \hat{F}_-^2\right] = +\left(\hat{F}_x\hat{F}_z + \hat{F}_z\hat{F}_x\right) - i\left(\hat{F}_y\hat{F}_z + \hat{F}_z\hat{F}_y\right)$$

$$\left[\hat{F}_x, \hat{F}_+^2\right] = -\left(\hat{F}_x\hat{F}_z + \hat{F}_z\hat{F}_x\right) - i\left(\hat{F}_y\hat{F}_z + \hat{F}_z\hat{F}_y\right)$$

$$\left[\hat{F}_x, \hat{F}_z^2\right] = -i\left(\hat{F}_y\hat{F}_z + \hat{F}_z\hat{F}_y\right)$$

$$\left[\hat{F}_y, \hat{F}_-^2\right] = -i\left(\hat{F}_x\hat{F}_z + \hat{F}_z\hat{F}_x\right) - \left(\hat{F}_y\hat{F}_z + \hat{F}_z\hat{F}_y\right),$$

$$\left[\hat{F}_y, \hat{F}_+^2\right] = -i\left(\hat{F}_x\hat{F}_z + \hat{F}_z\hat{F}_x\right) + \left(\hat{F}_y\hat{F}_z + \hat{F}_z\hat{F}_y\right),$$

$$\left[\hat{F}_y, \hat{F}_z^2\right] = +i\left(\hat{F}_x\hat{F}_z + \hat{F}_z\hat{F}_x\right),$$

$$\left[\hat{F}_z, \hat{F}_-^2\right] = -2\hat{F}_-^2,$$

$$\left[\hat{F}_z, \hat{F}_+^2\right] = +2\hat{F}_+^2,$$

$$\left[\hat{F}_z, \hat{F}_z^2\right] = 0.$$

Transfer functions of magnetic coils
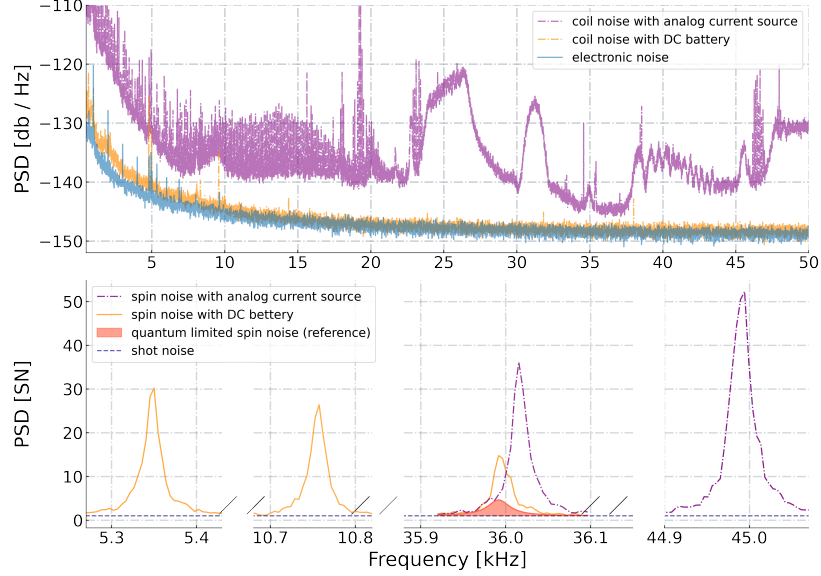
Figure A1: Impact of classical noise on atomic spin noise spectra due to bias magnetic noise from noisy current sources. We present the two different current supplies. For the current source that contains the audio/radio current noise, this noise subsequently converts to RF magnetic fields that drive the atomic spin oscillator. Consequently, the recorded atomic spin noise is predominantly influenced by classical noise. We also plot the predicted quantum noise-limited spin noise from previous calibration used as a reference for comparison.

We have demonstrated that, in order to observe the quantum dynamics of atomic system, it is crucial to mitigate various sources of classical noise across the frequency band of interest. One of the major sources in our experiments was the audio current noise from the bias coils' current supply. As shown in Fig.A1, the non-ideal DC current supply generates audio current noise, which converts to ultra-low frequency magnetic fields that excites the atomic spin oscillators and overwhelm the quantum noise we aim to explore. Therefore, After the upgradation of our current source, we dramatically reduce the level of classical modulations on atoms, as shown in orange curves in bottom plots. However, the residual can still drive the atomic spins as the system reaches the lower acoustic frequency band. Consequently, a future improvement for the atomic system would be to design a proper low-pass filter to cut off the current noise and to en-

gineer the impedance transfer functions, as shown in Fig.A2, of our coil systems to maximally attenuate the current noise across the acoustic frequency band.
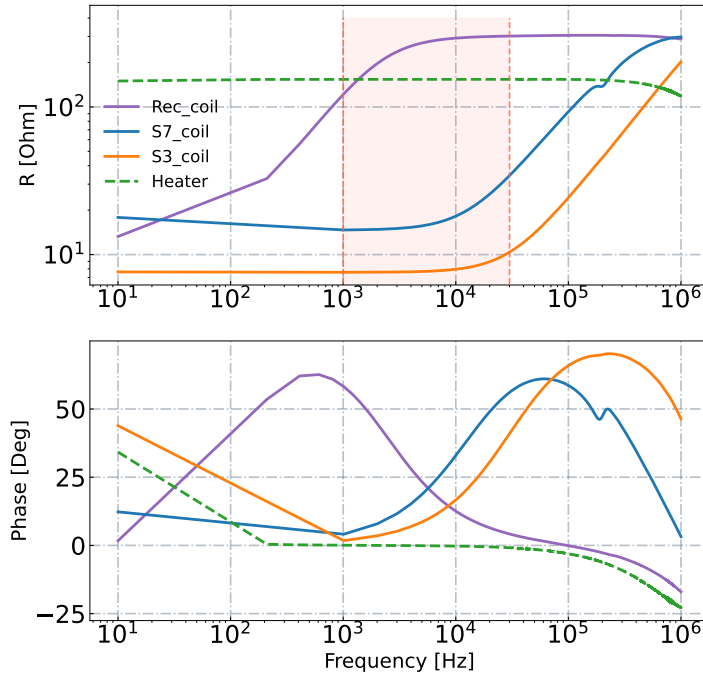
Figure A2: Impedance transfer functions of the magnetic coils and heater system. To better quantify the influence of classical current noise in the audio band due to the coils and heater, we measure the transfer functions of each coil's impedance with a locking-in amplifier. Higher impedance in the frequency range indicates minimal current passing through, which in turn reduces the generation of the audio/radio magnetic fields. We observed the heater has a relative constant resistance across the frequency band of interest, as we use the non-magnetic material to heat the system. The purple curve (Rec coil) shows a significant increase in impedance above 500 Hz, while the blue and orange curves for other coils attenuate more current noise at much higher frequencies ($\geq$ 100kHz). Since we typically need to combine both Rec and PCBs coils to produce a homogeneous magnetic field, it would be more beneficial to apply low-pass filter on PCBs coils to block noise at audio frequencies.

Bibliography

[1] David E McClelland, Nergis Mavalvala, Yanbei Chen, and Roman Schnabel. Advanced interferometry, quantum optics and optomechanics in gravitational wave detectors. *Laser & Photonics Reviews*, 5(5):677–696, 2011.

[2] Craig Cahillane and Georgia Mansell. Review of the advanced ligo gravitational wave observatories leading to observing run four. *Galaxies*, 10(1):36, 2022.

[3] Carlton M Caves. Quantum-mechanical noise in an interferometer. *Physical Review D*, 23(8):1693, 1981.

[4] Vladimir B Braginsky and F Ya Khalili. Quantum nondemolition measurements: the route from toys to tools. *Reviews of Modern Physics*, 68(1):1, 1996.

[5] Vladimir B Braginsky, Yuri I Vorontsov, and Kip S Thorne. Quantum nondemolition measurements. *Science*, 209(4456):547–557, 1980.

[6] H Jeff Kimble, Yuri Levin, Andrey B Matsko, Kip S Thorne, and Sergey P Vyatchanin. Conversion of conventional gravitational-wave interferometers into quantum nondemolition interferometers by modifying their input and/or output optics. *Physical Review D*, 65(2):022002, 2001.

[7] Ling-An Wu, HJ Kimble, JL Hall, and Huifa Wu. Generation of squeezed states by parametric down conversion. *Physical review letters*, 57(20):2520, 1986.

[8] Keisuke Goda, Osamu Miyakawa, Eugeniy E Mikhailov, Shailendhar Saraf, Rana Adhikari, Kirk McKenzie, Robert Ward, Steve Vass, Alan J Weinstein, and Nergis Mavalvala. A quantum-enhanced prototype gravitational-wave detector. *Nature Physics*, 4(6):472–476, 2008.

175

[9] Junaid Aasi, Joan Abadie, BP Abbott, Richard Abbott, TD Abbott, MR Abernathy, Carl Adams, Thomas Adams, Paolo Addesso, RX Adhikari, et al. Enhanced sensitivity of the ligo gravitational wave detector by using squeezed states of light. *Nature Photonics*, 7(8):613–619, 2013.

[10] A gravitational wave observatory operating beyond the quantum shot-noise limit. *Nature Physics*, 7(12):962–965, 2011.

[11] Fausto Acernese, M Agathos, L Aiello, A Allocca, A Amato, S Ansoldi, S Antier, M Arène, N Arnaud, S Ascenzi, et al. Increasing the astrophysical reach of the advanced virgo detector via the application of squeezed vacuum states of light. *Physical review letters*, 123(23):231108, 2019.

[12] M e Tse, Haocun Yu, Nutsinee Kijbunchoo, A Fernandez-Galiana, P Dupej, L Barsotti, CD Blair, DD Brown, SE Dwyer, A Effler, et al. Quantum-enhanced advanced ligo detectors in the era of gravitational-wave astronomy. *Physical Review Letters*, 123(23):231107, 2019.

[13] CM Mow-Lowry, BS Sheard, Malcolm B Gray, DE McClelland, and Stanley Ernest Whitcomb. Experimental demonstration of a classical analog to quantum noise cancellation for use in gravitational wave detection. *Physical review letters*, 92(16):161102, 2004.

[14] D Ganapathy, W Jia, M Nakano, V Xu, N Aritomi, T Cullen, N Kijbunchoo, SE Dwyer, A Mullavey, L McCuller, et al. Broadband quantum enhancement of the ligo detectors with frequency-dependent squeezing. *Physical Review X*, 13(4):041021, 2023.

[15] Lee McCuller and Lisa Barsotti. Design requirement document of the a+ filter cavity and relay optics for frequency dependent squeezing. *T1800447*, (T1800447):63, 2020.

[16] Stefan L. Danilishin and Farid Ya. Khalili. Quantum measurement theory in gravitational-wave detectors. *Living Reviews in Relativity*, 15(1):5, 2012.

[17] Bonny L Schumaker and Carlton M Caves. A new formalism for two-photon quantum optics. In *Coherence and Quantum Optics V: Proceedings of the Fifth Rochester Conference on Coherence and Quantum Optics held at the University of Rochester, June 13–15, 1983*, pages 743–750. Springer, 1984.

[18] Carlton M Caves and Bonny L Schumaker. New formalism for two-photon quantum optics. i. quadrature phases and squeezed states. *Physical Review A*, 31(5):3068, 1985.

[19] Thomas Corbitt, Yanbei Chen, and Nergis Mavalvala. Mathematical framework for simulation of quantum fields in complex interferometers using the two-photon formalism. *Physical Review A*, 72(1):013818, 2005.

176

[20] Christoffer Østfeldt. *Quantum Optomechanics for Hybrid Spin–Membrane Entanglement.* PhD thesis, 2022.

[21] Gianfranco Cariolaro and Gianfranco Pierobon. Bloch-messiah reduction of gaussian unitaries by takagi factorization. *Physical Review A*, 94(6):062109, 2016.

[22] DB Horoshko, L La Volpe, F Arzani, N Treps, C Fabre, and MI Kolobov. Bloch-messiah reduction for twin beams of light. *Physical Review A*, 100(1):013837, 2019.

[23] Mikhail Korobko. *Taming the quantum noise: How quantum metrology can expand the reach of gravitational-wave observatories.* PhD thesis, Staats- und Universitätsbibliothek Hamburg Carl von Ossietzky, 2020.

[24] Jan Gniesmer. Advanced techniques for squeezed-light-enhanced gravitational-wave detection. 2019.

[25] Carlton M Caves. Quantum-mechanical radiation-pressure fluctuations in an interferometer. *Physical Review Letters*, 45(2):75, 1980.

[26] B Garaventa, M Bawaj, M De Laurentis, S Di Pace, B D'Angelo, I Khan, L Naticchioni, C Nguyen, V Sequino, F Sorrentino, et al. Frequency-dependent squeezing generation with epr entanglement. In *Journal of Physics: Conference Series*, volume 1548, page 012013. IOP Publishing, 2020.

[27] Min Jet Yap. *Quantum noise reduction for gravitational-wave interferometers with non-classical states.* PhD thesis, The Australian National University (Australia), 2020.

[28] Thomas Randall Corbitt. *Quantum noise and radiation pressure effects in high power optical interferometers*, volume 69. 2008.

[29] Yiqiu Ma, Haixing Miao, Belinda Heyun Pang, Matthew Evans, Chunnong Zhao, Jan Harms, Roman Schnabel, and Yanbei Chen. Proposal for gravitational-wave detection beyond the standard quantum limit through epr entanglement. *Nature Physics*, 13(8):776–780, 2017.

[30] Stefan Danilishin, Farit Khalili, and Haixing Miao. Advanced quantum techniques for future gravitational-wave detectors. *Living Reviews in Relativity*, 22, 04 2019.

[31] LF Buchmann, S Schreppler, J Kohler, N Spethmann, and DM Stamper-Kurn. Complex squeezing and force measurement beyond the standard quantum limit. *Physical review letters*, 117(3):030801, 2016.

[32] NS Kampel, RW Peterson, R Fischer, P-L Yu, K Cicak, RW Simmonds, KW Lehnert, and CA Regal. Improving broadband displacement detection with quantum correlations. *Physical Review X*, 7(2):021008, 2017.

[33] Valeriy Novikov. *Entangled states of light and atomic spin oscillators for quantum noise reduction in Gravitational Wave Detectors*. PhD thesis, 2021.

[34] H. J. Kimble, Yuri Levin, Andrey B. Matsko, Kip S. Thorne, and Sergey P. Vyatchanin. Conversion of conventional gravitational-wave interferometers into quantum nondemolition interferometers by modifying their input and/or output optics. *Phys. Rev. D*, 65:022002, Dec 2001.

[35] M. Evans, L. Barsotti, P. Kwee, J. Harms, and H. Miao. Realistic filter cavities for advanced gravitational wave detectors. *Phys. Rev. D*, 88:022002, Jul 2013.

[36] LIGO SCIENTIFIC COLLABORATION. Lsc instrument science white paper (2024 edition).

[37] Riccardo Maggiore, Paolo Ruggi, Andreas Freise, Daniel Brown, Jonathan W Perry, Enzo N Martín, Conor M Mow-Lowry, Maddalena Mantovani, Julia Casanueva Diaz, Diego Bersanetti, et al. Angular control noise in advanced virgo and implications for the einstein telescope. *arXiv preprint arXiv:2401.13013*, 2024.

[38] Yi Pan. Optimal degeneracy for the signal-recycling cavity in advanced ligo. *arXiv preprint gr-qc/0608128*, 2006.

[39] Min Jet Yap, Paul Altin, Terry G McRae, Bram JJ Slagmolen, Robert L Ward, and David E McClelland. Generation and control of frequency-dependent squeezing via einstein–podolsky–rosen entanglement. *Nature Photonics*, 14(4):223–226, 2020.

[40] Jan Südbeck, Sebastian Steinlechner, Mikhail Korobko, and Roman Schnabel. Demonstration of interferometer enhancement through einstein–podolsky–rosen entanglement. *Nature photonics*, 14(4):240–244, 2020.

[41] Eugene S Polzik and Klemens Hammerer. Trajectories without quantum uncertainties. *Annalen der Physik*, 527(1-2):A15–A20, 2015.

[42] Klemens Hammerer, Markus Aspelmeyer, Eugene Simon Polzik, and Peter Zoller. Establishing einstein-poldosky-rosen channels between nanomechanics and atomic ensembles. *Physical review letters*, 102(2):020501, 2009.

[43] Christoffer B. Møller, Rodrigo A. Thomas, Georgios Vasilakis, Emil Zeuthen, Yeghishe Tsaturyan, Mikhail Balabas, Kasper Jensen, Albert

Schliesser, Klemens Hammerer, and Eugene S. Polzik. Quantum back-action-evading measurement of motion in a negative mass reference frame. *Nature*, 547(7662):191–195, 2017.

[44] Rodrigo A. Thomas, Michał Parniak, Christoffer Østfeldt, Christoffer B. Møller, Christian Bærentsen, Yeghishe Tsaturyan, Albert Schliesser, Jürgen Appel, Emil Zeuthen, and Eugene S. Polzik. Entanglement between distant macroscopic mechanical and spin systems. *Nature Physics*, 17(2):228–233, 2021.

[45] F. Ya. Khalili and E. S. Polzik. Overcoming the standard quantum limit in gravitational wave detectors using spin systems with a negative effective mass. *Phys. Rev. Lett.*, 121:031101, Jul 2018.

[46] Emil Zeuthen, Eugene S. Polzik, and Farid Ya. Khalili. Gravitational wave detection beyond the standard quantum limit using a negative-mass spin system and virtual rigidity. *Phys. Rev. D*, 100:062004, Sep 2019.

[47] Emil Zeuthen, Eugene S Polzik, and Farid Ya Khalili. Trajectories without quantum uncertainties in composite systems with disparate energy spectra. *PRX Quantum*, 3(2):020362, 2022.

[48] Klemens Hammerer, Anders S. Sorensen, and Eugene S. Polzik. Quantum interface between light and atomic ensembles. *Rev. Mod. Phys.*, 82:1041–1093, Apr 2010.

[49] Rodrigo Adriano Thomas. *Optical spin-mechanics quantum interface: entanglement and back-action evasion.* PhD thesis, 2020.

[50] Christian Folkersen Barentsen. *Quantum Optomechanics for Hybrid Spin–Membrane Entanglement.* PhD thesis, 2023.

[51] Kasper Jensen, Michael Zugenmaier, Jens Arnbak, Hans Stærkind, Mikhail V Balabas, and Eugene S Polzik. Detection of low-conductivity objects using eddy current measurements with an optical magnetometer. *Physical Review Research*, 1(3):033087, 2019.

[52] Nabeel Aslam, Hengyun Zhou, Elana K Urbach, Matthew J Turner, Ronald L Walsworth, Mikhail D Lukin, and Hongkun Park. Quantum sensors for biomedical applications. *Nature Reviews Physics*, 5(3):157–169, 2023.

[53] H. Krauter, D. Salart, Christine Muschik, J. Petersen, Heng Shen, T. Fernholz, and E. Polzik. Deterministic quantum teleportation between distant atomic objects. *Nature Physics*, 9:400, 12 2012.

[54] Brian Julsgaard, Jacob Sherson, J Cirac, Jaromír Fiurásek, and E. Polzik. Experimental demonstration of quantum memory for light. *Nature*, 432:482–6, 12 2004.

[55] Karsten Bjerrum Dideriksen. *A room-temperature single-photon source with built-in memory*. PhD thesis, 2021.

[56] Rebecca Schmieg. *Collective Spin-Oscillators for Light-Atom Interfaces*. PhD thesis, 2023.

[57] Steven R Jefferts, Thomas P Heavner, Thomas E Parker, and Jon H Shirley. Nist cesium fountains: current status and future prospects. *Time and Frequency Metrology*, 6673:63–71, 2007.

[58] Daniel A Steck. Cesium d line data. 2003.

[59] Scott Jeffrey Seltzer. *Developments in alkali-metal atomic magnetometry*. Princeton University, 2008.

[60] Theodore Holstein and Henry Primakoff. Field dependence of the intrinsic domain magnetization of a ferromagnet. *Physical Review*, 58(12):1098, 1940.

[61] Brian Julsgaard. *Entanglement and Quantum Interactions with Macroscopic Gas Samples*. PhD thesis, 2003.

[62] Roman Schnabel, Warwick P Bowen, Nicolas Treps, Timothy C Ralph, Hans-A Bachor, and Ping Koy Lam. Stokes-operator-squeezed continuous-variable polarization states. *Physical review A*, 67(1):012316, 2003.

[63] Warwick P Bowen, Roman Schnabel, Hans-A Bachor, and Ping Koy Lam. Polarization squeezing of continuous variable stokes parameters. *Physical Review Letters*, 88(9):093601, 2002.

[64] D. V. Vasilyev, K. Hammerer, N. Korolev, and A. S. Sørensen. Quantum noise for faraday light–matter interfaces. *Journal of Physics B: Atomic, Molecular and Optical Physics*, 45(12):124007, jun 2012.

[65] W Happer and BS Mathur. Off-resonant light as a probe of optically pumped alkali vapors. *Physical Review Letters*, 18(15):577, 1967.

[66] William Happer. Light propagation and light shifts in optical pumping experiments. *Progress in quantum electronics*, 1:51–103, 1970.

[67] DV Kupriyanov, OS Mishina, IM Sokolov, Brian Julsgaard, and ES Polzik. Multimode entanglement of light and atomic ensembles via off-resonant coherent forward scattering. *Physical Review A*, 71(3):032348, 2005.

[68] JM Geremia, John K Stockton, and Hideo Mabuchi. Tensor polarizability and dispersive quantum measurement of multilevel atoms. *Physical Review A*, 73(4):042112, 2006.

[69] Giorgio Colangelo, Robert J Sewell, Naeimeh Behbood, Ferran Martin Ciurana, Gil Triginer, and Morgan W Mitchell. Quantum atom–light interfaces in the gaussian description for spin-1 systems. *New Journal of Physics*, 15(10):103007, 2013.

[70] Jacob F. Sherson. *Quantum Memory and Teleportation Using Macroscopic Gas Samples*. PhD thesis, 2006.

[71] Witold Chalupczak, Adam Wojciechowski, Szymon Pustelny, and Wojciech Gawlik. Competition between the tensor light shift and nonlinear zeeman effect. *Physical Review A*, 82(2):023417, 2010.

[72] Hanna Krauter. *Generation and application of entanglement of room temperature ensembles of atoms*. PhD thesis, 2011.

[73] Heng Shen. *Spin squeezing and entanglement with room temperature atoms for quantum sensing and communication*. PhD thesis, 2014.

[74] Hanna Krauter, Christine A. Muschik, Kasper Jensen, Wojciech Wasilewski, Jonas M. Petersen, J. Ignacio Cirac, and Eugene S. Polzik. Entanglement generated by dissipation and steady state entanglement of two macroscopic objects. *Phys. Rev. Lett.*, 107:080503, Aug 2011.

[75] Xinyao Huang, Emil Zeuthen, Denis V Vasilyev, Qiongyi He, Klemens Hammerer, and Eugene S Polzik. Unconditional steady-state entanglement in macroscopic hybrid systems by coherent noise cancellation. *Physical Review Letters*, 121(10):103602, 2018.

[76] Florian Marquardt. An introduction to the basics of dephasing, 2001.

[77] Warwick P Bowen and Gerard J Milburn. *Quantum optomechanics*. CRC press, 2015.

[78] Valerii S Zapasskii. Spin-noise spectroscopy: from proof of principle to applications. *Advances in Optics and Photonics*, 5(2):131–168, 2013.

[79] Anton Konstantinovich Vershovskii, Sergey Pavlovich Dmitriev, Gleb Gennadevich Kozlov, Anatoly S Pazgalev, and Mikhail Valer'evich Petrenko. Projection spin noise in optical quantum sensors based on thermal atoms. *Technical Physics*, 65:1193–1203, 2020.

[80] Daniel WC Brooks, Thierry Botter, Sydney Schreppler, Thomas P Purdy, Nathan Brahms, and Dan M Stamper-Kurn. Non-classical light generated by quantum-noise-driven cavity optomechanics. *Nature*, 488(7412):476–480, 2012.

[81] William Hvidtfelt Padkær Nielsen, Yeghishe Tsaturyan, Christoffer Bo Møller, Eugene S Polzik, and Albert Schliesser. Multimode optomechanical system in the quantum regime. *Proceedings of the National Academy of Sciences*, 114(1):62–66, 2017.

[82] Junxin Chen. *Quantum Correlations Generated by a Soft-Clamped Membrane-in-the-Middle System.* PhD thesis, 2019.

[83] Jacob L Beckey and Haixing Miao. Ponderomotive squeezing of light. 2017.

[84] Christian Bærentsen, Sergey A Fedorov, Christoffer Østfeldt, Mikhail V Balabas, Emil Zeuthen, and Eugene S Polzik. Squeezed light from an oscillator measured at the rate of oscillation. *Nature Communications*, 15(1):4146, 2024.

[85] Wayne M Itano, James C Bergquist, John J Bollinger, JM Gilligan, DJ Heinzen, FL Moore, MG Raizen, and David J Wineland. Quantum projection noise: Population fluctuations in two-level systems. *Physical Review A*, 47(5):3554, 1993.

[86] Georgios Vasilakis. *Precision measurements of spin interactions with high density atomic vapors.* Princeton university, 2011.

[87] Wonjae Lee. *Ultra-high sensitivity atomic magnetometers.* PhD thesis, Princeton University, 2022.

[88] Michael Zugenmaier. *Towards a room temperature single photon source based on atomic vapour.* PhD thesis, 2018.

[89] J Borregaard, M Zugenmaier, JM Petersen, H Shen, G Vasilakis, K Jensen, ES Polzik, and AS Sørensen. Scalable photonic network architecture based on motional averaging in room temperature gas. *Nature communications*, 7(1):11356, 2016.

[90] Karsten B Dideriksen, Rebecca Schmieg, Michael Zugenmaier, and Eugene S Polzik. Room-temperature single-photon source with near-millisecond built-in memory. *Nature communications*, 12(1):3699, 2021.

[91] Yuanjiang Tang, Ya Wen, Ling Cai, and Kaifeng Zhao. Spin-noise spectrum of hot vapor atoms in an anti-relaxation-coated cell. *Phys. Rev. A*, 101:013821, Jan 2020.

[92] Roy Shaham, Or Katz, and Ofer Firstenberg. Quantum dynamics of collective spin states in a thermal gas. *Phys. Rev. A*, 102:012822, July 2020.

[93] Alexandr Karpenko and Sergey P Vyatchanin. Dissipative coupling, dispersive coupling, and their combination in cavityless optomechanical systems. *Physical Review A*, 102(2):023513, 2020.

[94] Jun Jia, Valeriy Novikov, Tulio Brito Brasil, Emil Zeuthen, Jörg Helge Müller, and Eugene S Polzik. Acoustic frequency atomic spin oscillator in the quantum regime. *Nature Communications*, 14(1):6396, 2023.

[95] EB Alexandrov and AK Vershovskiy. Mx and mz magnetometers. *Optical Magnetometry*, page 60, 2013.

[96] V. G. Lucivero, N. D. McDonough, N. Dural, and M. V. Romalis. Correlation function of spin noise due to atomic diffusion. *Phys. Rev. A*, 96:062702, Dec 2017.

[97] SJ Seltzer, DJ Michalak, MH Donaldson, MV Balabas, SK Barber, SL Bernasek, M-A Bouchiat, A Hexemer, AM Hibberd, DF Kimball, et al. Investigation of antirelaxation coatings for alkali-metal vapor cells using surface science techniques. *The Journal of chemical physics*, 133(14), 2010.

[98] MV Balabas, Todor Karaulanov, MP Ledbetter, and Dmitry Budker. Polarized alkali-metal vapor with minute-long transverse spin-relaxation time. *Physical review letters*, 105(7):070801, 2010.

[99] Lara Torralbo-Campo, Graham D Bruce, Giuseppe Smirne, and Donatella Cassettari. Light-induced atomic desorption in a compact system for ultracold atoms. *Scientific reports*, 5(1):14729, 2015.

[100] Xiaojun Di. *Magnetic shielding using electrical steel panels at extremely low frequencies*. Cardiff University (United Kingdom), 2008.

[101] B Julsgaard, J Sherson, J L Sørensen, and E S Polzik. Characterizing the spin state of an atomic ensemble using the magneto-optical resonance method. *Journal of Optics B: Quantum and Semiclassical Optics*, 6(1):5, sep 2003.

[102] Hans Chr. Straekind. Optical magnetometry for biomedical applications, 2016.

[103] Ryan Yde. Room temperature spin ensembles for precision measurements. Master's thesis, 2020.

[104] Antti J. Mäkinen, Rasmus Zetter, Joonas Iivanainen, Koos C. J. Zevenhoven, Lauri Parkkonen, and Risto J. Ilmoniemi. Magnetic-field modeling with surface currents. part i. physical and computational principles of bfieldtools. *Journal of Applied Physics*, 128(6):063906, 2020.

[105] Rasmus Zetter, Antti J. Mäkinen, Joonas Iivanainen, Koos C. J. Zevenhoven, Risto J. Ilmoniemi, and Lauri Parkkonen. Magnetic field modeling with surface currents. part ii. implementation and usage of bfieldtools. *Journal of Applied Physics*, 128(6):063905, 2020.

[106] N Mielec, M Altorio, R Sapam, D Horville, D Holleville, LA Sidorenkov, A Landragin, and R Geiger. Atom interferometry with top-hat laser beams. *Applied Physics Letters*, 113(16), 2018.

[107] Alexander Laskin, Peter Kaiser, Vadim Laskin, and Aleksei Ostrun. Laser beam shaping for biomedical microscopy techniques. In *Biophotonics: Photonic Solutions for Better Health Care V*, volume 9887, pages 251–260. SPIE, 2016.

[108] Edmund. *Laser Beam Shaping Overview*. Edmund Optics, 2024.

[109] Holor. *How to build basic setup using ZEMAX Black Box of Top Hat beam shaper*. Holor/or, 2019.

[110] CP Pearman, CS Adams, SG Cox, PF Griffin, DA Smith, and IG Hughes. Polarization spectroscopy of a closed atomic transition: applications to laser frequency locking. *Journal of Physics B: Atomic, Molecular and Optical Physics*, 35(24):5141, 2002.

[111] Joshua S Torrance, Ben M Sparkes, Lincoln D Turner, and Robert E Scholten. Sub-kilohertz laser linewidth narrowing using polarization spectroscopy. *Optics Express*, 24(11):11396–11406, 2016.

[112] ML Harris, CS Adams, SL Cornish, IC McLeod, E Tarleton, and IG Hughes. Polarization spectroscopy in rubidium and cesium. *Physical Review A*, 73(6):062509, 2006.

[113] Experiment SAS. *Saturated Absorption Spectroscopy*. University of Florida, 2020.

[114] E de Carlos López and JM López Romero. High resolution spectroscopy in gases and its application on the frequency stabilization of semiconductor lasers. *Revista mexicana de física*, 50(6):569–578, 2004.

[115] Oliver Schmidt, K M Knaak, Robert Wynands, and D Meschede. Cesium saturation spectroscopy revisited: How to reverse peaks and observe narrow resonances. *Applied Physics B*, 59:167–178, 1994.

[116] B. Julsgaard, Jacob Sherson, J. Sorensen, and E. Polzik. Characterizing the spin state of an atomic ensemble using the magneto-optical resonance method. *Journal of Optics B Quantum and Semiclassical Optics*, 6, 07 2003.

[117] Rodrigo A. Thomas, Christoffer Østfeldt, Christian Bærentsen, Michał Parniak, and Eugene S. Polzik. Calibration of spin-light coupling by coherently induced faraday rotation. *Opt. Express*, 29(15):23637–23653, Jul 2021.

[118] William H. P. Nielsen. *Quantum Cavity Optomechanics with Phononic Bandgap Shielded Silicon Nitride Membranes*. PhD thesis, 2016.

184

[119] A. A. Fomin, M. Yu. Petrov, G. G. Kozlov, M. M. Glazov, I. I. Ryzhov, M. V. Balabas, and V. S. Zapasskii. Spin-alignment noise in atomic vapor. *Phys. Rev. Research*, 2:012008, Jan 2020.

[120] Gleb Kozlov, Aleksei Fomin, Mikhail Petrov, Ivan Ryzhov, and Valerii Zapasskii. Raman scattering model of the spin noise. *Optics Express*, 29, 02 2021.

[121] Marcin Kozbial, Lucy Elson, Lucas M Rushton, Ali Akbar, Adil Meraki, Kasper Jensen, and Jan Kolodynski. Spin noise spectroscopy of an alignment-based atomic magnetometer. *arXiv preprint arXiv:2312.05577*, 2023.

[122] Tulio Brito (Catalogo USP) Brasil. *Entanglement and Quantum Interactions with Macroscopic Gas Samples*. PhD thesis, 2021.

[123] Alkiviadis Zoumis. Laser noise stabilisation for low frequency quantum back action cancellation, 2023.

[124] F Tricot, DH Phung, M Lours, S Guérandel, and E De Clercq. Power stabilization of a diode laser with an acousto-optic modulator. *Review of Scientific Instruments*, 89(11), 2018.

[125] LNEUHAUS. Red pitaya dac performance. `https://ln1985blog.wordpress.com/2016/02/07/red-pitaya-dac-performance/`, 2016. Accessed: 2016-02-07.

[126] L. Barsotti L. McCuller. Design requirement document of the a+ filter cavity and relay optics for frequency dependent squeezing. *LIGO*, 63:022002, Jul 2015.

[127] Teng Zhang, Philip Jones, Jiří Smetana, Haixing Miao, Denis Martynov, Andreas Freise, and Stefan W Ballmer. Two-carrier scheme: evading the 3 db quantum penalty of heterodyne readout in gravitational-wave detectors. *Physical review letters*, 126(22):221301, 2021.

[128] N. S. Kampel, R. W. Peterson, R. Fischer, P.-L. Yu, K. Cicak, R. W. Simmonds, K. W. Lehnert, and C. A. Regal. Improving broadband displacement detection with quantum correlations. *Phys. Rev. X*, 7:021008, Apr 2017.

[129] Tulio Brito Brasil, Valeriy Novikov, Hugo Kerdoncuff, Mikael Lassen, and Eugene S Polzik. Two-colour high-purity einstein-podolsky-rosen photonic state. *Nature Communications*, 13(1):4815, 2022.

[130] Morgan W. Mitchell and Silvana Palacios Alvarez. Colloquium: Quantum limits to the energy resolution of magnetic field sensors. *Rev. Mod. Phys.*, 92:021001, Apr 2020.

185

[131] C. Troullinou, R. Jiménez-Martínez, J. Kong, V. G. Lucivero, and M. W. Mitchell. Squeezed-light enhancement and backaction evasion in a high sensitivity optically pumped magnetometer. *Phys. Rev. Lett.*, 127:193601, Nov 2021.

[132] Felix Tebbenjohanns, M. Luisa Mattana, Massimiliano Rossi, Martin Frimmer, and Lukas Novotny. Quantum control of a nanoparticle optically levitated in cryogenic free space. *Nature*, 595:378, 07 2021.

[133] Sebastian Zaiser, Torsten Rendler, Ingmar Jakobi, Thomas Wolf, Sang-Yun Lee, Samuel Wagner, Ville Bergholm, Thomas Schulte-Herbrüggen, Philipp Neumann, and Jörg Wrachtrup. Enhancing quantum sensing sensitivity by a quantum memory. *Nature communications*, 7(1):12279, 2016.

[134] Nancy Aggarwal, Odylio D Aguiar, Andreas Bauswein, Giancarlo Cella, Sebastian Clesse, Adrian Michael Cruise, Valerie Domcke, Daniel G Figueroa, Andrew Geraci, Maxim Goryachev, et al. Challenges and opportunities of gravitational-wave searches at mhz to ghz frequencies. *Living reviews in relativity*, 24:1–74, 2021.